Characterisation of Hydrogen Trapping in Steel by Atom Probe Tomography

Yi-Sheng Chen

Department of Materials

St Edmund Hall

University of Oxford

A thesis submitted for the degree of

Doctoral of Philosophy

Michaelmas Term, 2017/2018

To my family,

who have been the support of my life.

Abstract

Hydrogen embrittlement (HE), which results in an unpredictable failure of metals, has been a major limitation in the design of critical components for a wide range of engineering applications, given the near-ubiquitous presence of hydrogen in their service environments. However, the exact mechanisms that underpin HE failure remain poorly understood. It is known that hydrogen, when free to diffuse in these materials, can tend to concentrate at a crack tip front. In turn, this facilitates crack propagation. Hence one of the proposed strategies for mitigating HE is to limit the content of freely diffusing hydrogen within the metal atomic lattice via the introduction of microstructural hydrogen traps. Further, it is empirically known that the introduction of finely-dispersed distribution of nano-sized carbide hydrogen traps in ferritic steel matrix can improve resilience to HE. This resilience has been attributed to the effective hydrogen trapping of the carbides. However, conclusive atomic-scale experimental evidence is still lacking as to the manner by which these features can impede the movement of the hydrogen. This lack of insight limits the further progress for the optimisation of the microstructural design of this type of HE-resistant steel.

In order to further understand the hydrogen trapping phenomenon of the nano-sized carbide in steel, an appropriate characterisation method is required. Atom probe tomography (APT) has been known for its powerful combination of high 3D spatial and chemical resolution for the analysis of very fine precipitates. Furthermore, previous studies have shown that the application of isotopic hydrogen (^{2}H) loading techniques, combined with APT, facilitates the hydrogen signal associated to fine carbides to be unambiguously identified. However, the considerable experimental requirements as utilised by these previous studies, particularly the instrumental capability necessary for retention of the trapped hydrogen in the needle-shaped APT specimen, limits the study being reproduced or extended.

In this APT study, a model ferritic steel with finely dispersed V-Mo-Nb carbides of 10-20 nm is investigated. Initially, existing specialised instrumentation formed the basis of a cryogenic specimen chain under vacuum, so as to retain loaded hydrogen after an electrolytic charging treatment for APT analysis. This work confirms the importance of cryogenic treatment for the retention of trapped hydrogen in APT specimen. The quality of the obtained experimental data allows a quantitative analysis on the hydrogen trapping

mechanism. Thus, it is conclusively determined that interior of the carbides studied in this steel acts as the hydrogen trapping site as opposed to the carbide/matrix interface as commonly expected. This result supports the theoretical investigations proposing that the hydrogen trapping within the carbide interior is enabled by a network of carbon vacancies.

Based on the established importance of the specimen cold chain in these APT experiments, this work then successfully develops a simplified approach to cryo-transfer which requires no instrumental modification. In this approach there is no requirement for the charged specimen to be transferred under vacuum conditions. The issue of environmental-induced ice contamination on the cryogenic sample surface in air transfer is resolved by its sublimation in APT vacuum chamber. Furthermore, the temperature of the transferred sample is able to be determined independently by both monitoring changes to vacuum pressure in the buffer chamber and also the thermal response of the APT sample stage in the analysis chamber. This simplified approach has the potential to open up a range of hydrogen trapping studies to any commercial atom probe instrument. Finally, as an example of the use of this simplified cryo-transfer technique, targeted studies for determining the source of hydrogen adsorption during electropolishing and electrolytic loading process are demonstrated.

This research provides a critical verification of hydrogen trapping mechanism of fine carbides as well as an achievable experimental protocol for the observation of the trapping of individual hydrogen atoms in alloy microstructures. The methods developed here have the potential to underpin a wide range of possible experiments which address the HE problem, particularly for the design of new mitigation strategies to prevent this critical issue.

Preface

This original work had been conducted at the Department of Materials, University of Oxford from October 2014 to January 2018, under the supervision of Prof. Michael P. Moody, Dr. Paul A.J. Bagot, and Dr. Daniel J. Haley. No part of this thesis has been submitted for a degree at this or any other university. Part of this work has been published in journals and presented at conferences and meetings as detailed below:

Journals:

Chen, Y.-S., Haley, D., Gerstl, S. S. A., London, A. J., Sweeney, F., Wepf, R. A., Rainforth, W. M., Bagot, P. A. J., Moody, M. P. (2017). Direct observation of individual hydrogen atoms at trapping sites in a ferritic steel. *Science*, 355, 1196-1199. doi:10.1126/science.aal2418

Chen, Y.-S., Haley, D., Bagot, P. A. J., Moody, M. P. (2017). Simplifying Observation of Hydrogen Trapping in Atom Probe Tomography. *Microscopy and Microanalysis*, 23(S1), 620-621. doi:10.1017/S1431927617003774

Conferences and meetings:

Chen, Y.-S., Haley, D., Bagot, P. A. J., Moody, M. P. Simplifying Observation of Hydrogen Trapping in Atom Probe Tomography. *Microscopy & Microanalysis*. St. Louis, Missouri, USA (2017)

Chen, Y.-S., Haley, D., Bagot, P. A. J., Moody, M. P. Direct Observation of Hydrogen Atoms at Trapping Sites in a Ferritic Steel by Atom Probe Tomography. *The challenges of hydrogen and metals – Discussion meeting by the Royal Society*. London, UK (2017)

Chen, Y.-S., Haley, D., Bagot, P. A. J., Moody, M. P. Characterization of Hydrogen Trapping in Steels by Atom Probe Tomography. *Atom Probe Tomography & Microscopy*. Gyeongju, Korea (2016)

Chen, Y.-S., Haley, D., Bagot, P. A. J., Moody, M. P. Atom Probe Characterization of Hydrogen Trapping in Hydrogen-Resistant Steels via Electrolytic Route. *International Hydrogen Conference*. Moran, Wyoming, USA (2016)

Chen, Y.-S., Haley, D., Bagot, P. A. J., Moody, M. P. Direct Observation of Hydrogen Atoms at Trapping Sites in a Ferritic Steel by Atom Probe Tomography. *European Atom Probe Workshop*. Oxford, UK (2016)

Acknowledgement

EPSRC programme Grant, EP/L014742/1, *Hydrogen in metal–from fundamentals to the design of new steels* (HEmS) was acknowledged for the experimental and most of the travel costs. Taiwan Ministry of Education was appreciated for my university fees.

The following people are deeply appreciated due to their noticeable helps: Prof. Michael P. Moody set off this ambitious project and gave both mental and practical supports when I was in need. Dr. Paul A.J. Bagot provided precious advice. Dr. Daniel J. Haley guided me through the whole journey and taught me all the essential knowledge about atom probe, about hydrogen, and about how to be a good researcher. Dr. Stephan S.A. Gerstl lighted up this work when it was still in dark by letting us test the key concept in his masterpiece VCT. Prof. W. Mark Rainforth provided the right material perfectly fitting our need. Profs. Alan C.F. Cocks and A. Tony Paxton demonstrated incredible leadership in this EPSRC programme. Dr. Andrew J. London generously shared his genius knowledge and transformed this wormy work into a dragon (Chinese idiom). Dr. Tomas L. Martin provided heart-warming technical support and encouragement. Last but not least, Prof. Julie Cairney, Dr. Brent Grocholski, as well as the anonymous reviewers made my meaningful first scientific publication an unbelievably good one.

I would like to thank my parents and parents-in-law, Fang-Ling, Jui-Sung, Fu-Chin, and Shu-Nien, who full-heartedly supported me and my family's living in both mental and financial perspectives. This thesis could not be done without you all.

I am very grateful that my daughter Shin-Yen has tremendous self-discipline and tenacity in learning a completely new language tirelessly and blending herself into this strange country. Moreover, she has been an amazing role-model sister who takes great care of her little sister when her parents were not available. Also, I am thankful that my little Shin-Ni has grown herself nicely and has never worried her parents so far.

Lastly, the most special thanks go to my most-beloved wife, Ya-Hsuan, who has been my best partner, best friend, best lover, best listener, best believer, and best supporter. During the time in Oxford, we have been through such an extraordinary journey together that we may not believe when we look back. This journey was such full-of-challenge, but we somehow made it. We sacrificed so much but we learned so much. I know all of these are because you always put yourself after us and let us shine our own lights. These will not be forgotten or taken for granted. I will always love you and support you back whenever you are in need, promised in the name of Jesus Christ.

Table of Contents

1. Introduction

The characteristic embrittling phenomenon due to the presence of hydrogen in metal is known as 'hydrogen embrittlement' (HE) or hydrogen-induced/assisted/enhanced cracking/fracture/failure, or sometimes also referred to as the origin of stress corrosion cracking [1]. In 1874, Johnson first reported the effect of hydrogen on metals, the toughness of which was significantly reduced after hydrogen loading [2]. Since this pioneering work, for over one hundred years the HE problem has been investigated and discussed in 38,000 papers [3], with this number still increasing at the current rate of few hundred per year. Such a large number of papers in the literature is indicative of the impact that this problem has across a range of research area. It also reflects the complexity, controversy, tenacity that the HE problem is difficult to solve, as well the high interest in both scientific and industrial perspectives. Recently, the steps towards decarbonisation to counteract global warming have been actively adopted world-wide. In this respect, hydrogen is regarded as an important candidate of 'clean energy' to replace fossil fuel [4]. However, hydrogen-related degradation of metals designed for hydrogen storage and transport becomes a serious limitation to developing hydrogen as renewable energy [5]. In addition to directly using hydrogen as fuel, HE also limits the application of light-weight high-strength steels in automotive industry for reducing car weight so as to improve the energy efficiency of transportation [6]. Furthermore, with respect to the design and construction of new wind turbines, lifetimes are determined by the bearing components which have been found to be susceptible to hydrogen-accelerated rolling contact fatigue due to contact with hydrogen-bearing lubricants [7]. In the nuclear industry, hydrogen is one of the corrosion causes in pressurised water reactors whose repair comes at significant economic loss [8]. Even in petroleum industry, the design of refining pressure vessels must

specifically take HE effect into account by incorporating extra-thick walls (up to 350 mm), the use of which significantly increases the pipelines weight and hence increases material and transportation cost [9]. This selection of current hydrogen-induced problems demonstrates that HE is not only a concern in term of engineering safety but also limits the applicability of many metallurgical advances in renewable technologies developed to combat climate change.

This work starts by introducing the HE phenomenon in Chapter 2, particularly its influence on the mechanical properties of materials. It then discusses the origin of HE from the fundamental aspects of hydrogen-metal interaction to the proposed mechanisms by which it can cause materials to fail. The strategic approaches previously implemented to mitigate HE are reviewed. The critical need for experimental evidence to underpin the theoretical investigations into the mechanisms by which the introduction of a distribution of fine carbides into metal microstructure can act as hydrogen traps for HE resistant purposes is highlighted. Here, atom probe tomography (APT) is emphasised due to its very high 3D spatial resolution for the characterisation of fine features in microstructure combined with its capability to map hydrogen. At the end of Chapter 2, the current technical challenges of using APT to provide the required atomic-scale hydrogen distribution are revisited. Based on that discussion, the framework of this study is established, which addresses the development of cryogenic sample transfer technique to retain hydrogen in the atom probe specimen.

In Chapter 3, the bearing steel incorporating microstructural features designed for hydrogen trapping investigated in this study is introduced. The experimental characterisation techniques and analysing methods used are discussed in detail. Chapter 4 presents the results of atom probe characterisation of as-received material. The main focus of this initial study is to define the nature of the studied carbides and the determination of

their composition. In Chapter 5, the initial results from reference hydrogen-charging experiments are interpreted with respect of previous work in this area published in the literature using standard post-charging sample transfer methods to the atom probe, as well as the effect of hydrogen charging is shown. Chapter 6 presents the results of proof-of-concept experiments regarding the necessity for cryogenic treatment to the charged sample to immobilise the hydrogen atoms for APT analysis. It also presents an in-depth analysis of the APT data, including advanced algorithms to discern the hydrogen-trapping mechanism in the studied material. Chapter 7 addresses finding alternative solution for the cryogenic sample transfer treatment requiring less specialised equipment and APT instrument modification requirements and that is potentially applicable to any commercial atom probe. In Chapter 8, examples of research enabled by the developed cryo-transfer technique, developed in the previous chapter, with regard to the analysis hydrogen uptake in material are demonstrated. Finally, summary, conclusions, and suggestions of future work are provided in the last chapter.

2. Literature Review

2.1 Hydrogen embrittlement

In the literature regarding HE, the majority of published works only report the consequences of the embrittling effect as observed from mechanical tests. However, there are some studies dedicated to discerning the most appropriate mechanisms by which the occurrence of HE can be properly explained. These works regarding mechanisms have proposed several possible candidates so far, and most of which have their own experimental support [1, 10, 11]. However, it is known that underlying operation of these mechanisms will depend on the studied materials, e.g. nickel alloys or steels, or even where the hydrogen occurs in the microstructure, e.g. lattice or grain boundary. Hence ascribing a single mechanism to explain HE phenomena that is applicable to all metals is known to be inappropriate [12]. This review attempts to correlate the proposed mechanisms with current understanding of the hydrogen-metal interaction and highlights the key role of experimental evidence in the understanding to these interactions.

Prior to the discussion of hydrogen-metal interactions, it is pertinent to start from a macroscopic perspective by reviewing the information provided by tensile and fatigue testings which are the most fundamental and arguably the most insightful techniques to elucidate HE. These techniques have revealed many essential characteristics of HE which considerably helps researchers and engineers understanding this phenomenon. Note that while this study is mostly interested in its influence on steel, other metals will also be discussed when exemplification of relevant hydrogen effect is required.

2.1.1 Hydrogen influences in mechanical properties

It is widely accepted that the presence of hydrogen reduces metal ductility (elongation or reduction-of-area) and strength (peak stress) [1, 13-16]. Under tensile testing, the hydrogen-loaded metals generally result in earlier fracture than the case with absence of hydrogen, and the extent of this early fracture can be more quantitatively measured in fatigue test by the reduction of cycle-to-fracture or fatigue life [14, 17]. HE also manifests itself as accelerated crack propagation in the hydrogen-loaded sample in comparison to hydrogen-free case [1, 18], and this increase of crack growth rate can result in a transition from ductile failure mode to brittle intergranular failure mode in some materials [19]. Therefore, these macroscopic findings from these mechanical testing experiments provide certainty as to the role of hydrogen to embrittle metal structures.

The extent of HE, in terms of toughness loss, has been related to the hydrogen content in tested samples. Examined materials has been observed to increasingly lose toughness increasing hydrogen content up until reaching the solubility limit of the samples of hydrogen [20-23]. After hydrogen charging, if the hydrogen is then fully liberated from undeformed samples, the mechanical properties of the original uncharged material are restored [2]. This phenomenon indicates that the presence of hydrogen is responsible to the consequent embrittling. However, it is worth noting that up until the point of fracture the hydrogen has no effect on the nature of the elastic deformation [21, 22], so the influence of hydrogen on the materials is not observable until their plastic deformation.

In addition, the effect of HE has been found to be more severe in high-strength martensitic steels, whereas low- or medium-strength ferritic steels are found to be less prone to HE in comparison [1, 18]. This phenomenon implies that the problem is microstructure-specific. Also, it has found that the extent by which HE affects material

properties is sensitive to the strain rate of the mechanical test, whereby a more prominent effect is observed at low strain rate as compared to the cases tested at high strain rate [1, 14, 24, 25]. Furthermore, susceptibility to HE is often greatest around room temperature, gradually decreasing with decreasing temperature [1, 16]. Together these observations imply that the embrittling process has a kinetic factor which is generally accounted as the diffusion of hydrogen through the microstructure.

2.1.2 Surface entry of hydrogen

It is discussed above how hydrogen can affect the performances of metals in regards of their mechanical properties. Consequently, it is necessary to know how hydrogen uptake is conducted at metal surface. When metals exposed to hydrogen-bearing environment, hydrogen gas molecules ($H_2(g)$) can adsorb onto the surface, then dissociate into adsorbed hydrogen atoms (H_{ads}) and finally be absorbed into the metal if energetically favourable [26]. The absorbed hydrogen atoms (H_{abs}) also can leave the material by recombination with another hydrogen atom at the surface to form a gas molecule and desorbs from the surface. These processes are expressed as

$$\frac{1}{2}H_2(g) \leftrightarrow H_{ads} \leftrightarrow H_{abs} \tag{1}$$

According to Sievert's law [27], the final absorbed hydrogen concentration (C_H) in metal, which is from the last term in the chain reaction (1), can be associated to the hydrogen pressure hence its fugacity (f_H) from the first term ([28] for the fugacity/pressure association). The factor of ½ then gives the square root relation of these two terms as

$$C_H = S\sqrt{f_H} \tag{2}$$

where S is the constant obtained from the reactions of the surface solution and molecule dissociation. Eq(2) implies that hydrogen uptake can be facilitated by increasing external hydrogen pressure [29]. Therefore, in laboratory tests for introducing hydrogen into bulk metal, high-pressure gas charging cell is typically considered to exaggerate hydrogen concentrations and hence the embrittling effect to enable observation. However, this approach requires use of a high-pressure hydrogen chamber which generally requires the implementation a sophisticated pipeline architecture to both facilitate pressurisation as well as addressing safety concern due to the combustibility of hydrogen [30-32]. Hence these constraints can make hydrogen gas charging less adaptable to most laboratories.

In a laboratory setting, hydrogen liquid charging (or hydrogen electrolytic loading) is generally considered more practical due to less demanding experimental requirements in comparison to the gas charging method [26]. Liquid charging utilises the electrolysis of water to create a hydrogen-rich environment at the cathode to which the potential is applied. The metal sample to be charged is attached to this cathode. At the anode, an aggressive oxygen environment is expected; hence an inert but conducting material such as gold or platinum is typically used to resist the corrosive oxidation [14, 26]. Instead of using pure water which has low conductivity hence slow reaction rate of electrolysis, the electrolytic experiment typically adds electrolyte in the solution, which can either be acid or alkaline. Considering both acid and alkaline charging solutions, the respective cathode reactions are

$$H_3O^+ + e^- \rightarrow H_{ads} + H_2O \text{ (in acid solution)} \quad (3)$$

$$\text{or } H_2O + e^- \rightarrow H_{ads} + OH^- \text{ (in alkaline solution)} \quad (4)$$

At high charging potential, the hydrogen evolution at the sample surface is aggressive and hence increases the probability of hydrogen recombination, which sometimes can be observed visually by the formation of bubbles in the experiment [33].

In the case of gas charging, it is possible to directly quantify the amount of hydrogen introduced to the metal according to Sievert's law by considering its charging fugacity. However, the quantification of the hydrogen content in the material resulting from liquid charging, which is governed by the rate of the hydrogen evolution reaction, is more difficult to assess. Accordingly, Liu et al. deduced a relationship between the hydrogen fugacity from the hydrogen evolution in liquid charging (f_H') and the applied potential (V_a) so that f_H' can be implemented in Sievert's law in eq(2) [34]:

$$f_H{}' = A\ exp\ [\frac{(V_a - V_R)F}{\gamma RT}] \tag{5}$$

where F, R, and T are the Faraday and gas constants, and absolute temperature, respectively, A and γ are the constants determined by the hydrogen desorption mechanism specific to the charging solution, and V_R is the reference potential which is a fixed value specific to the reference electrode [35]. This relation thus allows an estimate the hydrogen fugacity with control of the polarisation of liquid-charging experiment. From this equation, it is also apparent that the hydrogen fugacity can be advantageously altered across a wide range of values via the adjustment of charging potential. However, liquid charging is disadvantageous in respect that it can only facilitate a limited range of charging temperatures around ambient level in most laboratories due to the use of water [34, 36-38]. Also, the chemical environment in liquid charging is more corrosive to metals being charged in comparison to those treated in gas charging cell. This induced corrosion during the charging experiment is highly undesirable [39]. Hence these disadvantages must also be considered when selecting a hydrogen-charging method in laboratory.

2.1.3 Hydrogen in metals

Having addressed the manner of hydrogen uptake from the metal surface, it is now pertinent to discuss hydrogen-metal interactions within the bulk. Hydrogen-metal interaction is multi-facetted given that hydrogen not only interacts with lattice but also nearly all microstructural imperfections. Hydrogen solute in metal is sometimes regarded as a proton as a result of sharing its outer-shell electron like metallic bonded; however, theoretical study has shown that it is energetically more stable for the hydrogen in metal to keep an electron and remain as a neutral atom [40]. This suggests that the hydrogen solute in metal should be able to omit quantum effect and be regarded as classical particles. Moreover, it has been shown that at the typical temperature range that most steels experience in service (around room temperature), the results of the properties modelled by either classical or quantum calculations are very similar [41]. Hence, in this study, quantum level effects which can potentially relates to properties such as diffusion are not considered.

Hydrogen is generally endothermic when dissolving in metal and hence has low solubility at the level of part per million in atomic ratio, except in members of VB Group of elements or Pd which allow hydride formation [42]. This very low solubility highlights the fact that HE occurrence in metal must only require such small amounts of hydrogen to effectively trigger. Due to the uniquely small size of hydrogen atom, as a solute in metal it occupies interstitial sites in the lattice. For example in steels, hydrogen resides at tetrahedral and octahedral interstitial sites, respectively, in body centred cubic (BCC) and face centred cubic (FCC) lattices [43]. Due to interstitial occupancy and the low elastic movement required of the lattice hydrogen atoms in metal matrix, hydrogen diffusivity is generally high in metal. For example, pure α-iron has about 10^{-8} m^2/s at room temperature [44]. However in other steels, hydrogen diffusivity can greatly decrease for up to 10 orders

of magnitude at room temperature from the level of α-iron [23]. This difference has been ascribed to the increased number of lattice imperfections, such as solute-induced lattice distortions, vacancies, grain boundaries, dislocations, or inclusions which act as 'hydrogen traps' and provide energy sinks in which diffusing hydrogen can reside, as illustrated in the energy schematic Figure 1 [45, 46].

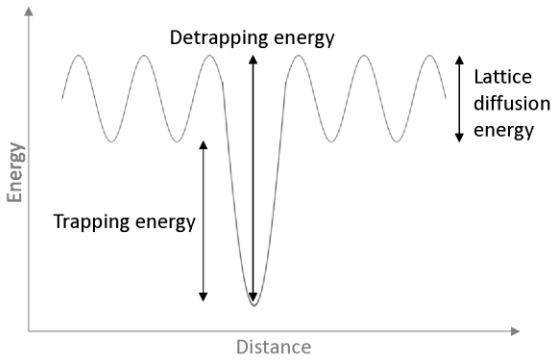

Figure 1 – A schematic energy profile of hydrogen in metal lattice with the presence of a hydrogen trap allowing the diffusing hydrogen being sequestered by an energy sink

The energy sink for trapping hydrogen in Figure 1 is typically specified with its trapping and detrapping energies which are the energies released and required, respectively, when hydrogen atom jumps into and out of the microstructural trap. These two energy terms are sometimes interchangeable in literature when the lattice diffusion energy is small enough to be negligible such as in ferrite matrix. Considering the hydrogen trapping process as a homogeneous thermally-activated reaction, the reaction rate can be described by Kissinger's equation [47]:

$$\frac{dx}{dt} = A(1-x)exp\,[\frac{-E_T}{RT}] \tag{6}$$

where x is the fraction of the hydrogen trapped by the microstructural trap in metal with respect to global hydrogen content, t is time, A is the reaction constant, R is gas constant, T is the absolute temperature, and E_T is the trapping energy. Thermal Desorption Analysis

(TDA), allows the hydrogen desorption rate of a hydrogen-containing sample being analysed to be measured as a function of time at a constant heating rate (θ).Hence, TDA can enable hydrogen trapping energy to be experimentally determined by the temperature at a reaction peak of hydrogen desorption (T_{peak}) with the following relation, under the assumption that the hydrogen desorption from a certain microstructural feature presents as a Gaussian peak in hydrogen desorption spectrum [48]:

$$E_T = -R\left[\frac{\partial \ln(\theta/T_{peak}^2)}{\partial(1/T_{peak})}\right] \tag{7}$$

In the case containing non-Gaussian peaks, as an example shown in Figure 2, the experimental peaks are modelled as the sum of the smaller Gaussian simulated peaks, and then the obtained trapping energy will be associated to microstructural features, typically based on microscopic observations [49]. Through the application of this TDA method, a wide range of the trapping energies of many common hydrogen traps in metal microstructure have been experimentally determined as listed in Table 1.

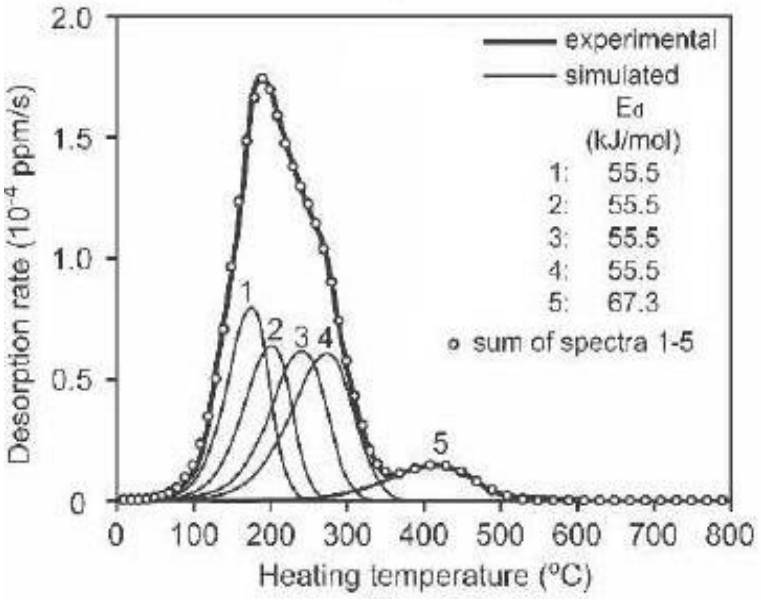

Figure 2 – Example of TDA data in a TiC-containing ferritic steel and the deconvolution of the peak [49]

Trap type	Trapping energy (kJ/mol)	Reference
Vacancy	24-29	[50]
Grain boundary	17	[48]
	30	[51]
Dislocation strain field	27	[48]
Dislocation core	60	[52]
Microvoid	35	[48]
	48	[53]
Cementite incoherent interface	11	[54]
MnS incoherent interface	72	[53]
Iron oxide incoherent interface	47	[55]
TiC/ferrite semi-coherent interface	42	[56]
	56	[49]
	87	[57]
TiC interior	100	[49]
V_4C_3 (site not specified)	33-35	[58]
	52-58	[59]
Mo_2C (site not specified)	11	[60]
	25-30	[61]
NbC (site not specified)	63-68	[62]

Table 1 – Common trapping sites and their trapping energies in ferritic matrix measured by thermal desorption analysis except the dislocation core was by diffusion method instead.

In late 70s, Pressouyre and Bernstein first applied the use of hydrogen trapping to HE mitigation. They verified the concept that only the diffusible (or non-trapped) hydrogen in metal participates the embrittling process rather than the trapped hydrogen [63-66]. Since these pioneering works, a research field investigating hydrogen trapping to mitigate HE has essentially been initiated. However, it is known in more recent reaches that not all hydrogen traps are benign to the mechanical properties of the material [3]. Hence when designing the microstructure for HE resistance, a comprehensive consideration of the influence that hydrogen traps will have on the overall mechanical properties is first required. The benefits of hydrogen traps are rooted from either their intrinsic interactions with hydrogen or their roles during material deformation with the presence of hydrogen. The following discussion is dedicated to establishing this understanding by consideration of several common hydrogen traps. This will provide the foundation of later discussion about HE mechanisms as well as the designing criteria for microstructure to generate HE resistance.

2.1.3.1 Vacancies

Hydrogen can actively interact with vacancies in metals. Vacancies are known to be energetically favourable for the accommodation of single or even multiple hydrogen atoms [50, 67-71]. Apart from being accommodated by vacancies during diffusion, hydrogen can also reduce the formation energy of vacancies in many metal systems [67, 72-74]. For a specific range of hydrogen pressure, high numbers of vacancies can even be directly generated in metal [75-79]. Accordingly, Nagumo accounted hydrogen-vacancy mutual stabilisation as the origin of HE based on his observation by TDA [10]. He found that plastic deformation with accelerated crack growth in a hydrogen-charged martensitic steel induces a significant increase in the number of a strong hydrogen traps. This is demonstrated by the increased area under the graph and the establishment of a second-high temperature peak between 500 and 700 K shown in Figure 3 which is ascribed to strain-induced vacancies. Based on this empirical observation, one can understand that that vacancy has negative effect to the resistance of the metal against HE.

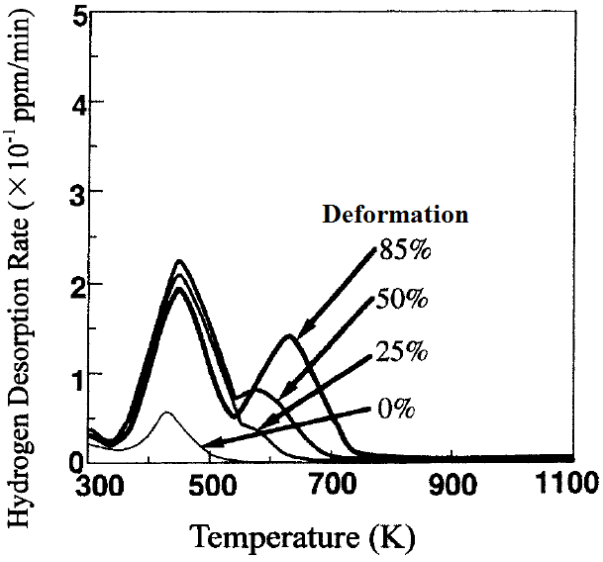

Figure 3 –Hydrogen desorption as a function of temperature for the samples at different deformation extent in a martensitic steel. The deformation is defined by the reduction of cross sectional area [10]

2.1.3.2 Dislocations

Theoretical investigation has shown that hydrogen solute can segregate to dislocation cores which provide elastically relaxed sites for interstitial solutes as shown in Figure 4 [72, 73]. This hydrogen segregation can induce a screening effect which reduces the energy required for dislocation glide and hence facilitates material strain [43, 72, 73]. This concept accounts well for the kinetic response of HE extent to strain-rate and temperature in mechanical testing (Section 2.1.1). At low strain rate or high temperature, hydrogen diffusion can maintain dislocation glide and continuously affecting dislocation gliding stress at the core. In contrast, at high strain rate or low temperature, the high-velocity dislocations decouple with the relatively slow-diffusing hydrogen and so require the same dislocation-gliding stress as the cases in hydrogen-free condition. This hydrogen-enhanced dislocation dynamics was critically verified by Robertson's observation on the change of dislocation velocity during the deformation of a stainless steel in the environment with and without hydrogen under the monitor of in-situ transmission electron microscope (TEM) [80]. His work directly showed that the presence of hydrogen increases the dislocation velocity in the steel at a fixed stress and confirmed that the presence of hydrogen favours the dislocation activity.

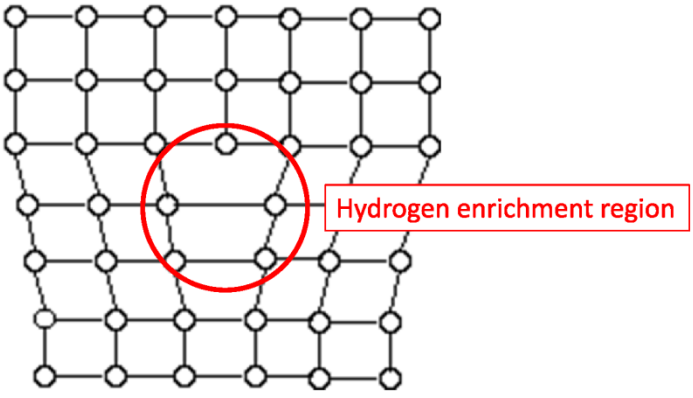

Figure 4 – Schematic of where hydrogen segregation occurs in an edge dislocation.

On the other hand, since hydrogen segregates at the dislocation core and can follow its movement at low strain rate, the dislocation can be regarded as actually transporting hydrogen [81-86]. This phenomenon can induce the redistribution of hydrogen during deformation [81], and in particular can increase the susceptibility to HE at the dislocation-accumulated region in metal microstructure such grain boundaries [84, 87-90].

2.1.3.3 Grain boundaries

The presence of hydrogen was found to induce many metals, including FCC nickel and BCC iron, transitions of fracture mode from ductile transgranular to brittle intergranular [87-89, 91] (see Appendix for fracture modes). These phenomena prompted speculation that hydrogen may directly weaken the bonding strength of grain boundaries (GB) and then result in intergranular crack propagation [92, 93]. Theoretical calculation has shown that GB in BCC metals can attract hydrogen whereas those in FCC metals cannot [43, 94]. However, many studies suggest that grain boundary failure is more prone to locally increased hydrogen content transported by the enhanced dislocation activity and whereas direct debonding by hydrogen is less responsible for this failure [95-98]. Hence, the exact mechanism by which grain boundaries contribute to HE is still elusive apart from its hydrogen trapping nature.

2.1.3.4 Microstructural inclusions

Inclusions such as carbides are very important to metal for strengthening purposes [99]. Among all inclusions in steels, transition metal carbides such as TiC, VC, or NbC have attracted considerable interest due to their great strengthening contribution of up to 300 MPa [100]. In addition, these types of carbide have been empirically found to have efficacy in HE resistance [3, 58, 101], hence their interaction with hydrogen is of interest. In theory, it is known that inclusions in metals can allow hydrogen to reside at

inclusion/matrix interfaces because the presence of hydrogen passivates their non-saturated bonds at the interfaces [43, 102-104]. In contrast, some studies have indicated that the interior of inclusion compounds is less effective for trapping due to their impenetrability for hydrogen atoms resulting from their stable structure with fully-occupied interstitial sites by non-metallic solutes and incorporation of fully saturated covalent bonds [43, 102-104]. However, Di Stephano et al. found that for certain circumstances in which the vacancies in these transition metal carbides are connected, the interior trapping site of transition metal carbide for hydrogen atom is still achievable [104]. Despite the fact that these theoretical studies have provided significant understanding about hydrogen-inclusion interactions, many of the insights are difficult to experimentally verify. This limitation of hydrogen characterisation techniques impede progress to further refine such models and hence developing a deeper understanding of the trapping mechanism which could consequently be exploited in designs to mitigate HE. This task to develop characterisation capabilities will be addressed in later Section 2.2.3 with more details.

2.1.4 Proposed mechanisms for hydrogen embrittlement

Based on the garnered insights into hydrogen-metal interactions, the developed models describing HE based upon these understandings can now be discussed.

2.1.4.1 Brittle-hydride formation

In transition metals such as Ti, Zr, or V [1, 11, 19], it is widely accepted that the embrittling consequence of ductile-to-brittle transition by hydrogen is due to the formation of metal-hydride in the microstructures which are more brittle than the original phase and facilitates the crack propagation during deformation. As illustrated in Figure 5, the crack propagates via the iterative processes of diffusible hydrogen concentrating at the stress-intense area at the crack tip, this leads to the formation of more brittle-hydride phase

embrittling this region, and finally the hydride being cleaved with the crack tip meeting the virgin matrix initiating another cycle [72, 73, 105]. In other materials such as Fe [42], although the formation of its hydride is theoretically difficult, Song and Curtin predicted that the ductile-to-brittle transition in ferrite is due to the crack tip hydride which suppresses the dislocation activity based on the thermodynamics of hydride phase formation. Hence crack tip blunting results in cleavage along low-yield lattice planes [106, 107]. However, Robertson et al.'s later observations via in-situ environmental TEM do not support their prediction for the crack extension path, which means this mechanism of HE in iron remains controversial [11].

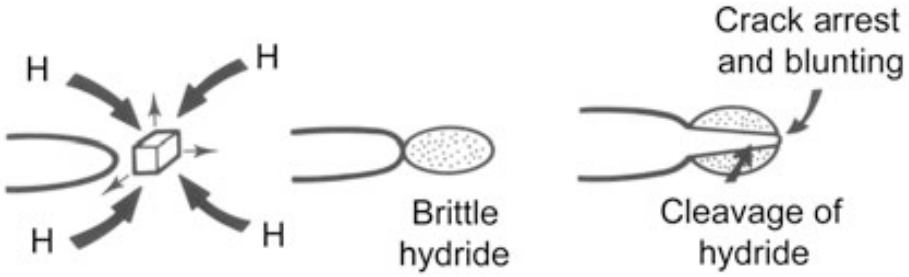

Figure 5 –Schematic of the crack tip growth in the mechanism considering brittle-hydride formation [1].

2.1.4.2 Hydrogen-enhanced decohesion (HEDE)

This mechanism which was first developed in the 1970s by Oriani and co-workers operates similarly to the process of the brittle-hydride formation at crack tip, however cleavage is not due to hydride failure but because the hydrogen concentration at the crack tip locally reduces the atomic cohesion energy [108-110]. It has been argued that macroscopic observations that purport to show sharper crack tips within hydrogen-charged sample with respect to hydrogen-free case support this theory [111]. However, apart from this, the decrease in atomic cohesion energy within the metal lattice still lacks suitable experimental confirmation. Hence, the validity of this mechanism for transgranular fracture (Appendix) is uncertain. At grain boundaries, this mechanism seems more applicable given

that the hydrogen segregation does reduce the cohesion energy of GB in theory [43, 94, 112]. However, some other studies also evidently show that the hydrogen-induced GB failure can result by other mechanism introduced in the following content due to excess hydrogen being transported to GB and hence locally increasing the susceptibility of GB to HE [87, 89, 98, 113], so whether HEDE underpins hydrogen-induced GB failure is still in debate.

2.1.4.3 Hydrogen-enhanced local plasticity (HELP)

In some materials, particularly low-strength ferritic steels, ductile features such as dimples in transgranular fracture surface (Appendix) in the charged samples have been observed. An *a posteriori* interpretation of this phenomenon was inferred by Beachem [114]. As shown in Figure 6, hydrogen-enhanced local plasticity (HELP) proposes that the hydrogen concentration at the crack tip, due to the stress concentration (the grey area), facilitates local dislocation activity by screening the elastic field around dislocation cores and reducing the energetic requirements for glide. The enhanced dislocation motion increases the probability of the formation and rapid growth of defects such as voids. Ultimately, the void growth can lead to micro-void coalescence (MVC) which reduced the stress required for crack tip propagation [115]. The enhancement of dislocation activity underpins this mechanism and has been critically verified by Robertson et al via environmental TEM, as discussed earlier in this section [80]. Recently, state-of-the-art micro-mechanics tests have shown the increased defect density at the crack tip front within a ferritic sample when it exposed to hydrogen in the environmental SEM, providing further direct support for the HELP model of HE [116, 117]. Furthermore, although the HELP mechanism has previously been excluded as a viable explanation for intergranular fracture, advanced fractographic studies have found high-density dislocations at hydrogen-induced crack vicinity which arguably could result from the hydrogen-enhanced dislocation activity

[87, 113]. Despite that HELP depiction of crack growth does not contain the exact procedure of the void formation at the crack tip front, which is a critical factor for crack propagation, this mechanism still became the most accepted mechanism due to Robertson's decisive evidence and has been extensively associated to many dislocation-related failures due to the presence of hydrogen.

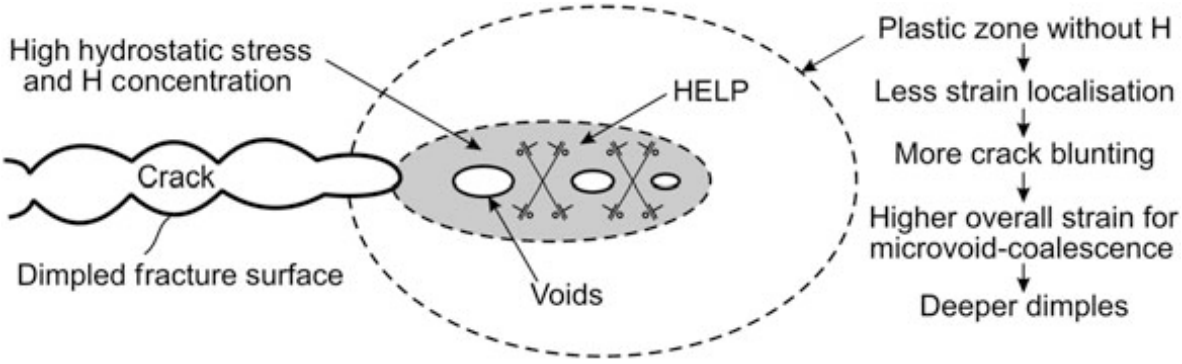

Figure 6 – Schematic of HELP mechanism [1]

2.1.4.4 Adsorption-induced dislocation emission (AIDE)

Similar to HELP, adsorption-induced dislocation emission (AIDE) mechanism was proposed by Lynch based on the observation of dimpled fracture surface in low-strength steels [1] together with the consensus that the metal surface has higher affinity to hydrogen than the lattice in the bulk [46, 118]. At the crack tip front, in contrast to the HELP assumption that the 'pre-existing' solute hydrogen facilitates the dislocation activity, AIDE regards the surface hydrogen absorbing from the environment as activating dislocation motion, shown in the broken-line region and highlighted by the insert in Figure 7. AIDE then follows the same MVC process as HELP to facilitate accelerated crack growth. Hence only the dislocations originating from the hydrogen-rich surface are excited, resulting in the enhanced dislocation emission from the crack tip, as indicated by the solid lines shown in Figure 7. AIDE associates the surface of the metal to the supply of hydrogen and is in direct disagreement with the key role of lattice hydrogen solute as predicted in HELP. Lynch

further provided evidence for this mechanism in the form of observations of crack growth which were accelerated in the presence of hydrogen but then decreased when surface hydrogen supply was interrupted from the experiment environment [119]. However, this mechanism is generally regarded as an amended model of HELP, which still based on the experimental observations of the activated dislocation activity by Robertson [80] and cannot refute the fact that lattice can accommodate hydrogen, despite being in more dilute level than surface, and influence dislocation activation to some extent.

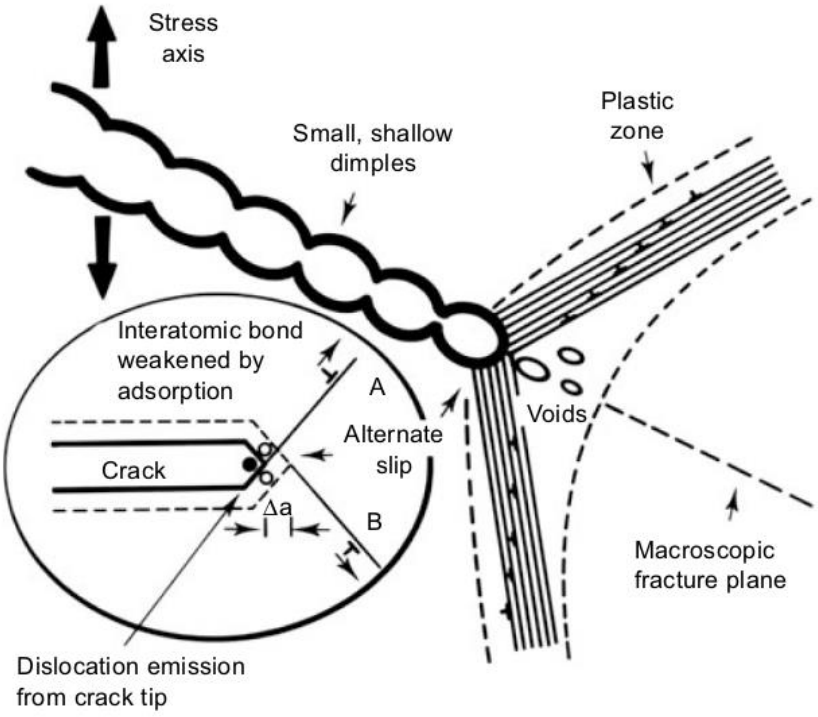

Figure 7 – Schematic of AIDE mechanism which depicts the formation of dimpled fracture surface with the coalescence of the voids at the crack tip front facilitated by the hydrogen-enhanced dislocation activity at the fracture surface [1]

2.1.4.5 Hydrogen-enhanced strain-induced vacancy (HESIV)

Based on the hydrogen-vacancy interaction described in Section 2.1.3.1, Nagumo proposed that the origin of HE should be attributed to their unique mutual stabilisation which results in hydrogen-enhanced strain-induced vacancies (HESIV) [23]. As illustrated in Figure 8, HESIV regards that the presence of hydrogen increases the number of vacancy

and renders formation of voids more probable, in turn these voids eventually agglomerate, accounting for the observation of dimpled fracture surfaces. It would seem reasonable to consider HESIV as a complementary explanation for the void formation in HELP or AIDE and vice versa for void agglomeration which is better predicted by HELP or AIDE. Indeed, both theoretical [120] experiment [69] investigations show that the presence of hydrogen can be associated to an increase in vacancy numbers. However, a recent theoretical consideration has shown that the hydrogen interaction energy with vacancy is not sufficient to suppress its annihilation when incident upon a mobile dislocation [68]. Hence the process of vacancy growth into voids, which is critical to the initiation of HE in many proposed mechanisms, remains inconclusive to date.

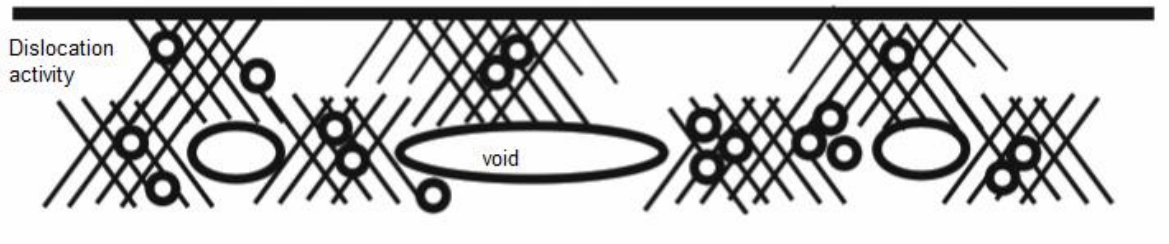

Figure 8 – Schematic of HESIV mechanism [23]

2.1.5 Summary

Based on the discussion so far, one could conclude when comparing the theoretical assertions above, insightful experimental evidence is a limiting factor to assessing the extent of their respective validities with respect to understanding to HE or hydrogen-metal interactions. Experimental studies focusing on the mechanisms driving HE are relatively scarce with respect to the large number of HE-related works that have been published. For example, Robertson's hydrogen-enhanced dislocation experiment provides strong evidence for theoretical speculation about hydrogen-dislocation interaction being conclusively [11]. Beyond that, this work also opens up possible explanations to other known phenomenon

such as hydrogen-induced grain boundary failure, such that it no longer can only ascribed to HEDE but can result from the facilitated transport of hydrogen by dislocations. Another example is that Pressouyre and Bernstein both theoretically predicted and experimentally verified the correlation between HE extent and the content of trapped hydrogen in the examination of ductility reduction of carbide trap containing ferritic steels [63-66]. Their study has become an essential reference in HE mitigation research for a large number of subsequent works. Recently, Bhadeshia reviewed the approaches and evidence based on Pressouyre and Bernstein's hydrogen-trapping strategy for HE mitigation [3]. This review systemically describes the ongoing research focussed around the development of HE mitigation. This work together with more recent findings is discussed in the following section.

2.2 Mitigation of hydrogen embrittlement

The extent of HE is related to material hydrogen content, specifically the concentration of diffusible hydrogen [63-66]. Hence, the fundamental concept upon which HE mitigation is to reduce this diffusible hydrogen content in metals. Common strategies include removing pre-existing hydrogen, inhibiting hydrogen surface ingress, and innocuously immobilising the microstructural hydrogen at engineered sites in the microstructure.

2.2.1 Hydrogen liberation and surface protection

Hydrogen can pre-exist in materials from the solute of feedstock or the production stage involving the use of hydrogen or hydrogenous compounds such as pickling, electroplating, or heat treatment within hydrogen-contaminated atmosphere [7]. In order to reduce the hydrogen uptake during production, using a vacuum or inert-gas treatment in the molten stage of metal production is suggested for degassing of otherwise dissolved hydrogen [121].

Alternatively, an outgassing procedure at a suitable temperature (typically at 150-230°C depending on the hydrogen tenacity in the materials) without inducing side transformations in the material towards the final stage of the production is generally considered [122]. This procedure can take hours, even days, of treatment time which must also consider sample geometry and size. However, this method is only able to remove the pre-existing hydrogen but has no effect to the hydrogen ingress from service environment.

Surface coating is a straight-forward and essential strategy against HE, which allows preventing or limiting hydrogen ingress in the material and can be applied in various manners [3]. Cadmium, Zn-Ni, nitrides such as TiN or Si_3N_4, and oxides such as TiO_2 and Al_2O_3 and even 'Black oxide' magnetite (Fe_3O_4) have been reported as effective in reducing hydrogen ingress [3]. However, some coating techniques which require post-degassing of hydrogen may significantly increase production complexity and cost [123]. Also, coating for inhibiting hydrogen ingress relies much on its quality and must take into account factors such as the in-service abrasion [124] as well as deformation [125].

2.2.2 Designing hydrogen-trapping microstructure

2.2.2.1 Considerations

As described in Section 2.1.3, Pressouyre and Bernstein found that metals will be less prone to HE if less diffusible hydrogen presents in microstructure [63-66]. In order to reduce the content of diffusible hydrogen, in addition to surface protection, hydrogen traps can thus be introduced into the metal by incorporating specific features into microstructure to provide intrinsic resilience to hydrogen. However, hydrogen trapping is rarely the only concern in the design of metal microstructure, other properties such as strengthening, fatigue resistance, as well as phase stability also must be taken into account [3]. Further the overall efficacy of a given microstructure to HE mitigation is normally too complicated to

simulate and hence is only able to be experimentally determined. Among the traps listed in Table 1 in Section 2.1.3, the features such as MnS particles are not well-suited for HE-resistant microstructure due to its particular susceptibility for crack initiation at matrix/particle interface with the presence of hydrogen [126, 127]. Other examples such as vacancies and dislocations are known to facilitate the defect formation and hydrogen transport as described in Section 2.1.3.1, and hence potentially increase microstructure susceptibility to HE. Accordingly, these microstructural features are generally excluded in the HE-resistant design despite of their hydrogen trapping abilities.

The hydrogen trap that remains elusive in terms of understanding its role in HE mitigation efficacy is the grain boundary. Given that GBs in BCC steels in principle trap hydrogen [43, 94], some experimental results have shown that increasing GB fraction per unit volume decreases the HE susceptibility [128-131]. What makes the role of GBs more elusive is that, rather than just trap hydrogen, GBs in some systems have been found to provide fast diffusion paths for hydrogen to which the deterioration by HE was ascribed [132, 133]. In general, given grain refinement is generally regarded improving metal ductility, fine grain size is still adopted in many designs for HE mitigation [129, 131, 134].

Apart from having a beneficial effect (or at least non-detrimental on desired material properties, the HE-resistant microstructure also needs to account the hydrogen trapping energy as discussed in 2.1.3. Given that components suffering from hydrogen attack are generally service near room temperature, the trapping energy to retain hydrogen for a sufficiently long time with respect to typical metal component service at room temperature is computed as 50-60 kJ/mol based on Kissinger equation shown in eq(6) [33]. This value of trapping energy has been cited in multiple papers as a standard of whether the trapped hydrogen would be expected to re-enter the microstructure during the service. Namely this value is used to define the *reversibility* of hydrogen trap [135-137]. However, not all HE-

threatened components experience room-temperature environment in service, such as steels and nick-based alloys in pressurised water fission reactors. Furthermore, not all applications have similar lengths of service time [8]. Hence, the reversibility of hydrogen trap actually should be considered application-specific by taking the temperature and temporal terms in eq(6) of the Kissinger's equation into account. Namely, under the consideration of the component service life as the time that hydrogen retention should last, the ratio of trapping energy (E_T) to temperature (T) should be defined as the metric of hydrogen trap reversibility for the studied application instead of an absolute value of E_T which might be in the risk of over-simplification [33].

In addition to the definition of reversibility, there also exists lack of understanding in the literature explaining the data variation of the TDA measurement. As shown in Table 1, many traps, such as TiC particles, have been reported to exhibit a wide range of trapping energies. This is because the TDA measurement lacks microscopic insight, which is unable to directly associate the measured trapping energy to a specific trapping site. Instead, it relies to some extent on the subjective interpretation of the operator. In addition, the extensively used Kissinger's model by considering hydrogen trapping as a homogenous reaction may not be fully applicable to describe the real microscopic level behaviour of hydrogen trapping, such as the case of TiC which involves trapping contributions from both the interface and interior of the particle [49]. Kirchheim recently addressed this gap in understanding and hence developed a new model taking into account the condition of individual trap having multiple trapping energies [138]. However, the sophisticated calculations from this work have not yet been extensively adopted in the literature to date.

As described in Section 2.1.3.4, carbides generally trap hydrogen at their interface [43, 104]. However, their hydrogen trapping efficacy depends on their morphology. In pearlitic steels which incorporate lamellar cementites across the span of the grains, it is found that

the lamellar orientation only impedes hydrogen permeation when the ingress direction is normal to the lamellar cementite precipitates [139, 140]. This directional effect is undesirable in the consideration of HE resistant design given the direction of approach of environmental hydrogen ingress is typically in random manner. Accordingly, a dispersed distribution of carbide particles, such as transition metal carbides TiC, NbC, or V_4C_3, have instead been generally considered. Several studies have shown increased resilience to HE with the distribution of dispersed carbides in microstructures [56, 58, 59, 61-63]. In order to obtain the optimised HE-resistant microstructure, these dispersed carbide traps are being discussed in the following section with respect to their hydrogen trapping efficacy.

2.2.2.2 Transition metal carbide trap of hydrogen

It is empirically known that the incorporation of transition metal carbides (TMC) into the microstructure can significantly reduce the susceptibility of steels to HE [56, 58, 59, 61-63]. From the perspective of microstructural engineering, one may pose the following questions in order to guide the design a highly HE-resistant steel:

1. What carbide type/structure optimises hydrogen trapping/HE resistance?
2. What number density of carbides is needed to inhibit the embrittlement?
3. What direct evidence can verify the association of the proposed hydrogen trapping sites with reduced susceptibility?

Regarding the first question, the thermodynamically stable structures of common TMCs in a ferrite matrix are summarised in Table 2, where the TMC's stoichiometry is presented in the generalised form of M to X ratio, which respectively represent metal and non-metal (such as carbon or nitrogen) constituent elements. Due to the nature of substitutional and interstitial occupancies of metal and non-metal elements, the stable structure of the precipitates can be predicted with the knowledge of this M/X ratio [141]. For example, the ratio of 1 to 1.33 has FCC structure, whereas a ratio of 2 to 2.33 implies an HCP structure.

Experimentally, FCC type carbides such as NbC or V_4C_3 have exhibited better hydrogen-trapping performance, and hence HE resistance, than the HCP type such as Mo_2C [56, 59, 61, 142].

Precipitate type	M/X ratio	Precipitate structure	M
MX	1	FCC	Ti, Nb, V, Mo
M_4X_3	1.33	FCC	Ti, V, Nb
M_2X	2	HCP	Mo, W, Fe
M_7C_3	2.33	HCP	Cr, Mo, W, Fe
$M_{23}C_6$	3.83	FCC	Cr, Mo, W, Fe
M_6C	6	FCC	Cr, Mo, W, Nb, Fe

Table 2 – Stoichiometry of carbides and their stable structures in ferrite [141], where M is the constituent metal element as substitutional solute and X is interstitial solute such as carbon or nitrogen in the carbide.

In terms of the required carbide number density to mitigate the embrittling effect during component service, this variable very much depends on the expected amount of hydrogen ingress within the service. Specifically, one needs to consider the service lifetime and the hydrogen uptake conditions to determine the hydrogen ingress [3, 7]. These conditions have previously been considered by modelling in several investigations [137, 143, 144]. From the point-of-view of material processing, the introduction of finely dispersed carbide into ferritic matrix can be achieved by a metallurgical method, 'interphase precipitation', which is an eutectoid reaction allowing fine TMC (10 to 20 nm) to be precipitated during $\gamma \rightarrow \alpha$ transformation at 600-700°C along the γ/α boundary as shown in Figure 9 [100, 145-149]. Figure 9 also shows that the carbide number density is highly tailorable with the adjustment of heat treatment condition [147, 149]. Hence the microstructural design of HE-resistant steels that will accommodate the required amount of hydrogen is practically feasible.

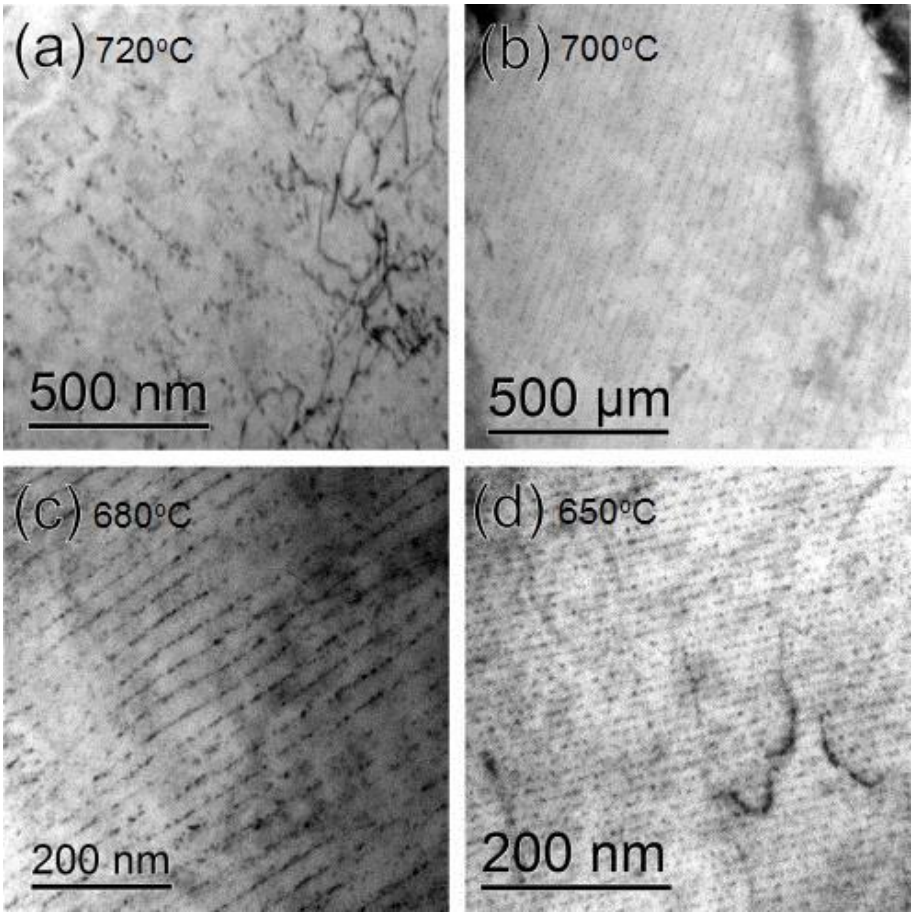

Figure 9 – Finely dispersed nano-sized (Ti,Mo)C interphase precipitate with various densities from the noted temperatures of heat treatment between 650 and 720°C [147]

Regarding the third question, the verification of hydrogen trapping behaviour in fine TMCs is often conducted from a theoretical perspective. Kawakami and Matsumiya investigated the hydrogen trapping sites in TiC and V_4C_3 precipitates, respectively, and concluded that hydrogen will be trapped at the precipitate/ferrite interface in TiC and the carbon vacancies inside the V_4C_3 carbide [103]. De Stefano et al. further accounted for the effect of co-occupancy of hydrogen atoms to a TiC trap as well as the result of incorporating connected network carbon vacancies [104]. They found that in the case of hydrogen atoms co-occupancy, the trap binding energy is significantly offset in comparison to that of an individual hydrogen due to the repulsion energy between the two hydrogen atoms. They also found that when the carbide incorporates a network of connected carbon

vacancies incident with the particle interface, the interface energy barrier is reduced and hence facilitates hydrogen penetration to its interior to occupy deeper carbon-vacancy traps. Considering carbon vacancies in TMC, calculations undertaken by Yu et al. indicate that TMCs from the VB Group such as V_4C_3 tend to have more carbon vacancies than those corresponding to metals from the IVB group such as TiC [150]. The combination of the prediction of Yu et al. and the results of De Stefano et al and Kawakami and Matsumiya suggests V_4C_3 type carbides should trap hydrogen at the interior carbon vacancy of the carbide whereas TiC will trap at its interface. However, these statements require experimental verification by techniques that can analyse the fine carbides and map the hydrogen they contain. Experimental techniques currently capable of hydrogen mapping are therefore revisited in the following section.

2.2.3 Characterisation of hydrogen trapping

Mapping the hydrogen in specific microstructure is difficult due to its low mass, the low concentrations in which it occurs in the systems of interest, and its high diffusivity in metal samples as summarised by Koyama et al. [151]. The uniquely low mass of hydrogen is accompanied with its comparatively very small electron cloud. This electron cloud represents a very small electron and X-ray cross section which do not allow appreciable interaction with incident of electron-beam (e-beam). As a result, using transmission electron microscopy (TEM), only the hydrogen in hydrides having periodic structures such as Pd-H, have been successfully identified [152, 153]. In non-hydride formers, such as Fe, electron energy loss spectrometry (EELS) was undertaken by Tatsumi et al. to map hydrogen in ferrite lattice, however it was found to be inconclusive [154]. Their EELS result in Figure 10(e) shows little differentiation between the before and after hydrogen-charging cases. Figure 10(d), which is the signal map of hydrogen-charged sample

normalised by the hydrogen-free case in the same sample, indicates that the technique is not currently able to give high resolution for the hydrogen mapping. Therefore, it is evident that e-beam is currently not suitable to directly characterise hydrogen solute in metals susceptible to HE such as Fe or Ni. Furthermore, as mentioned in Section 2.1.3, hydrogen has low concentration and high diffusivity in common HE-susceptible metals, which respectively makes its signal in the metals insignificant and hard to retain after charging before the analysis.

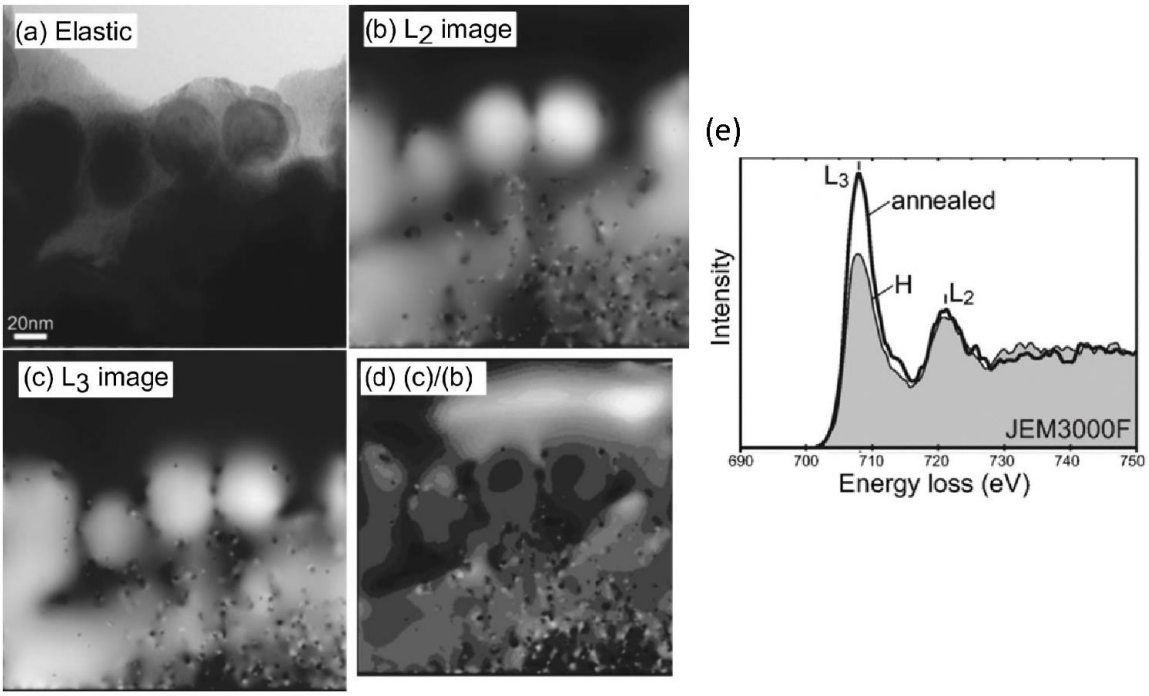

Figure 10 – (a) Elastic-electron map of steel microstructure. (b) and (c) are the inelastic electron maps from respective peaks shown in (e). (d) is the relative intensity map of (c) with respect to (d). And (e) is the EELS spectra with and without hydrogen loading.

In addition to e-beam, neutron-based characterisations have been successfully demonstrated in the investigation of its hydrogen interaction with carbide materials [155, 156]. The state-of-the-art neutron-imaging technique, small-angle neutron scattering (SANS), allowing direct visualisation of the spatial location hydrogen which has been successfully demonstrated for the observation of trapped hydrogen in blister within an iron

specimen [157]. Proton [158, 159] and radioactive ^{3}He have also been utilised in attempts to observe the distribution hydrogen close to the sample surface by depth profiling [160]. However, these techniques have only limited spatial resolution, down to the micrometre scale, which is restricted by the limits of the spatial sensitivity of their detectors [161].

Alternatively, one can coat a layer of material such as Ag or Pd that interacts strongly with and hence enables the tracking the hydrogen location, via the resulting changes observable in either optical or electrical properties, e.g. hydrogen microprint technique (HMT) [162-164] and scanning kelvin probe (SKP) [165, 166]. However, the spatial resolutions of these techniques are limited to the micrometre level by the sensitivity of the coating to hydrogen and so they are also not well-suited for the analysis nano-scaled carbide study [151]. Secondary ion mass spectroscopy (SIMS) is a technique using bombardment of ions to yield atoms from the surface of a specimen, in the form of secondary ions. The collect the signals enables the mass-to-charge ratio of these secondary ions to be measured so that the constituent elements of the material, including hydrogen, can be unambiguously detected [167-169]. However, the spatial resolution of this technique is limited by the precision of ion beam, whereby although the current technique allows sub-micron information to be resolved but is not routinely readily nanometre-scale [151].

Atom Probe Tomography (APT) is regarded as having a unique combination of very high 3D spatial resolution and great mass-resolving power [151]. This technique uses field-evaporation phenomenon to remove and analyse individual atoms from the apex of a needle-shaped specimen, resulting in atom-by-atom 3D map of the original material, where each atom has been chemically identified via time-of-flight spectroscopy [170]. As early as 1984, Spitznagel et al. demonstrated the ability of 1D atom probe (a forerunner to APT) to detect trapped hydrogen at TiC interface [171]. Many subsequent works also successfully observed hydrogen within a material microstructure with the use of this technique [36, 167,

172-177]. In particular, Takahashi et al. delivered the first unambiguous 3D atomic scale imaging of hydrogen trapped by carbide as shown in Figure 11 with the use of a custom-adapted atom probe instrument [178]. In their work, the TiC trapping site was qualitatively defined as the interface by visual inspection of the APT data. Their pioneering work successfully provided the foundations for a research field to analyse hydrogen in metals, specifically those requiring high spatial resolution characterisation.

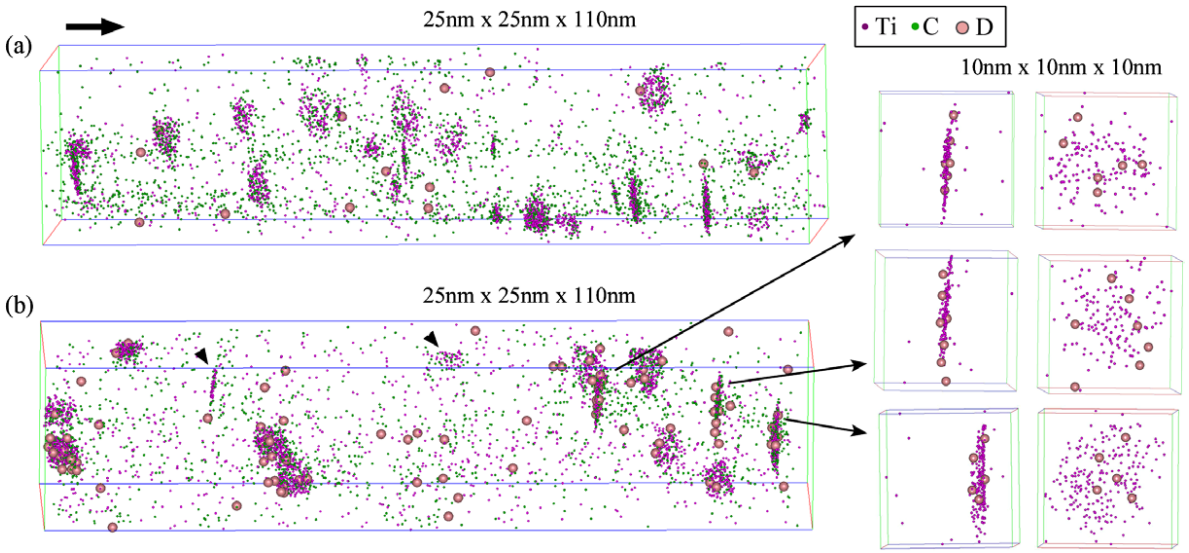

Figure 11 – The first 3-D APT observation showing isotopic hydrogen (red dots) being trapped in the TiC particles in ferritic matrix [178]

So far in this thesis, strategic approaches for HE mitigation have been introduced in general. It has been discussed how the introduction of benign hydrogen traps such as finely-dispersed carbides in the metal microstructure can enhance the intrinsic resistance of materials to HE. The optimisation of hydrogen trapping microstructure against HE requires a thorough understanding of the carbide trapping phenomenon, which has been mostly investigated by theoretical approaches. However, without robust experimental evidence, this understanding remains restricted. Atom probe tomography has been demonstrated to have promising capabilities in terms of hydrogen detectability and the required spatial resolution to provide the needed insights into fine-scale carbides. Hence, using APT to

study hydrogen trapping by the fine carbide could underpin critical experiments in HE and its mitigation for both scientific and industrial communities to advance their understanding. Hence, previous works regarding the technical challenges and the experimental requirements are reviewed in the following section.

2.2.4 Carbide hydrogen-trapping characterisation in atom probe

Despite the success of Takahashi et al., applying APT to the characterisation of hydrogen trapping in carbide steel remains a challenging task which must address some important factors discussed in this section, i.e. the interference of hydrogen artefact in vacuum chamber, quantification of carbide-trapping site, carbide characterisation, and the hydrogen position retaining strategy in the specimen after ex-situ hydrogen loading.

2.2.4.1 Hydrogen artefact in vacuum chamber

Hydrogen is known to be the primary residual gas in ultra-high vacuum (UHV) environments, which contributes 70% of the gas pressure. It cannot be removed completely by any current means [179, 180] given that the hydrogen originates from ambient atmosphere through the vacuum chamber wall which is usually constructed from stainless steel penetrable for hydrogen [181]. Likewise in APT, this background hydrogen is inevitably detected during data acquisition as an artefact, however obscures the artificially loaded hydrogen signal [182]. Sundell et al. and Kolli have attempted to minimise this artefact signal by calibration instrumental analysis conditions but failed to reduce it to below the level of hydrogen solubility in ferrite (10^{-4} at. %) [182, 183]. This means that it is difficult to distinguish whether a detected hydrogen signal is from the artificial loading process or the artefact from the analysis chamber in atom probe data. This fact makes the APT research introducing hydrogen in its natural isotopic abundance into the materials ambiguous in the experiments for hydrogen quantification in material microstructure [184-

186]. To separate the loaded signal from background artefact, loading deuterium as a substitute of hydrogen is generally considered [187, 188]. Deuterium has only 0.015% natural abundancy and can be resolved in the APT mass-to-charge-state ratio spectrum (2 Da) with respect to hydrogen signal which consists of protium (1 Da). Whilst the mass difference of protium with deuterium has been a raised as concern when using it as a substitute in diffusion-related studies, theoretical investigations however indicate that this isotope effect in ferritic steel is insignificant [189, 190]. Accordingly, deuteration is a reasonable requirement for assuring the fidelity of hydrogen signal in many vacuum techniques, not just restricted to APT [191].

2.2.4.2 Determining carbide type

The chemical constitution, or more specifically the constituent ratio of metal to non-metal elements (M/X ratio), is a critical metric to inform whether a carbide is of FCC or HCP type. Determining carbide chemistry is essential for associating the measured hydrogen trapping properties to the specific carbide of interest. However, the accuracy of carbon concentration measurements in steels has been known to be limited in APT analysis, due to detector efficiency effects such as ‘dead time’. The dead time is the minimum time required between a region on the face of the detector registering the detection of an ion and being able to resolve the next [170]. This dead-time is approximately 3 nano-second in commonly used atom probe instrument, LEAP 3000X HR [192]. This limitation is exasperated by the fact that the field evaporation of carbon in steels is known for its strong tendency to result in ‘pile-up’ signals. This refers to the situation whereby two or more ions received by the detector during the APT experiment are spatially and temporally close together, which may not allow the respective signals to be resolved within the dead time [170]. Consequently, this carbon detection loss can limit the accuracy of carbide chemistry determination. To address this detrimental effect, multiple researchers have investigated the

sensitivity of this effect to the atom probe experimental parameters [192-196]. Studies have found that this compositional error can be minimised by the application of appropriate experimental parameters, such as voltage pulse fraction, laser energy, and specimen temperature [192, 193]. As shown in the example of an APT steel analysis in Figure 12, after a careful series of experiments to calibrate of instrumental parameters the carbon and iron contents are both found to match the respective nominal values at 60 K of sample stage temperature.

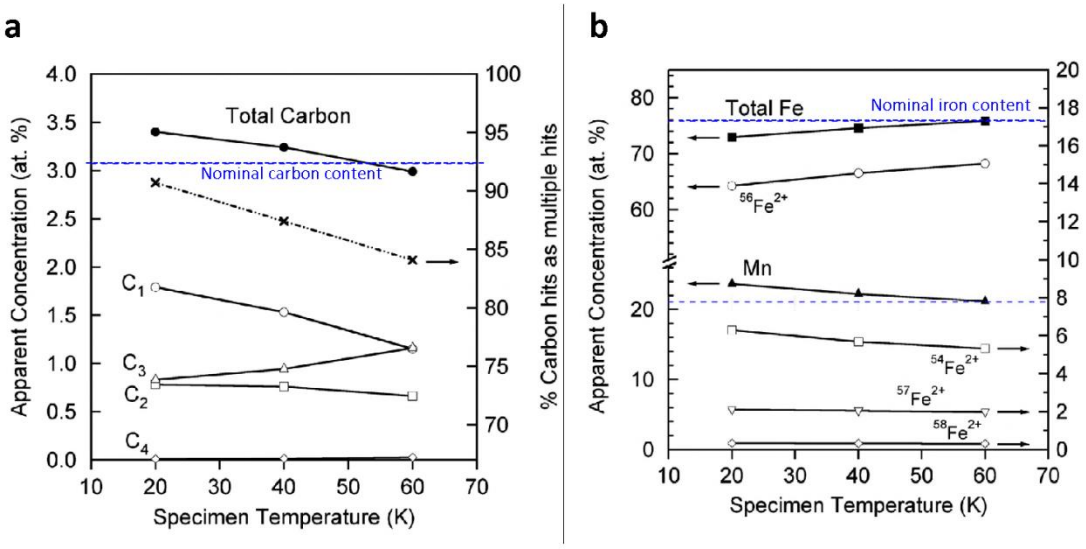

Figure 12 – The measured contents of (a) carbon and (b) iron as a function of atom-probe specimen stage temperatures [192]. The data show the contents are closest to the nominal numbers with the input of 60K.

2.2.4.3 Retaining loaded hydrogen in the APT specimen

The atom probe experiment requires an ultra-sharp needle-geometry specimen, with tip diameter less than 100 nm, to allow the field evaporation phenomenon as described in Section 3.2.1.1. This required specimen small dimensions however can allow the loaded hydrogen to escape from the material due to the shorter diffusion distance as compared to other techniques using bulk specimen. In addition, the UHV environment of APT during sample transfer (see Section 3.2.4 for details) also facilitates desorption of the loaded

hydrogen. Both of these issues can be verified by TDA experiments which examined the effect of sample size as well as degassing environment to the measured hydrogen content [197]. As shown in Figure 13 (a), the detected hydrogen content decreases with the decreasing sample thickness, whereas in Figure 13 (b) the hydrogen content in measured in the vacuum-degassed sample is generally lower than the corresponding sample in the Ar-degassing environment. As such, a custom technique to retain the loaded hydrogen in atom probe specimen is essential to allow the detection of comparable hydrogen signal with respect to other techniques.

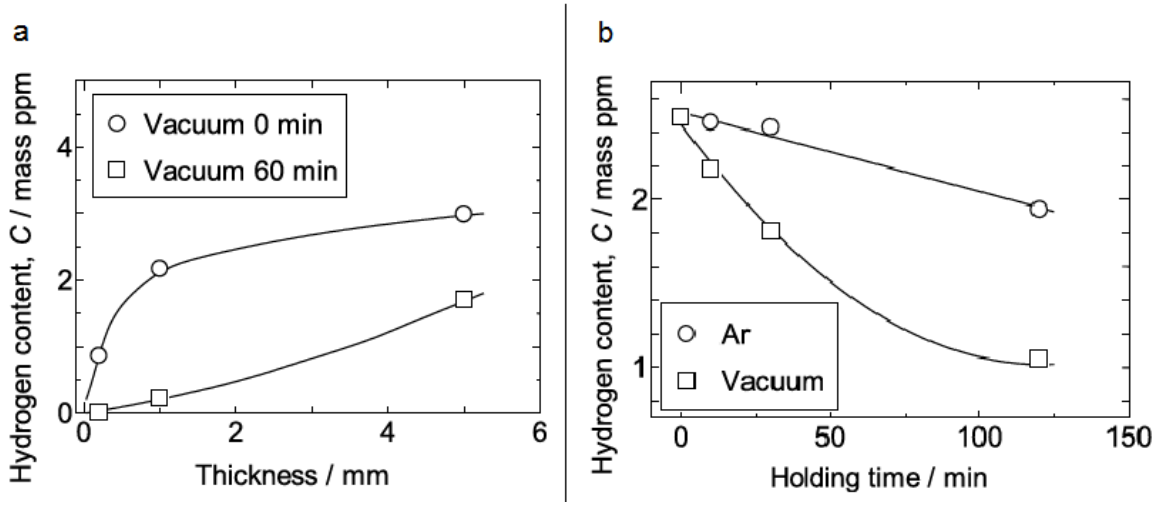

Figure 13 – (a) Effect of sample size on hydrogen content with two degassing time in vacuum. (b) Effect of degassing environment to hydrogen content. Pure iron samples are used in both tests.

In literature, the previous studies incorporating standard sample-transfer method whilst successfully detecting hydrogen after its loading generally use strong hydrogen-retaining strategies that utilise features such as oxide [172] or crystallised hydride-forming metal such as nickel [198], vanadium, palladium, or niobium [30, 167, 173-177]. The only successful unambiguous characterisations of hydrogen trapping by small precipitates in a ferritic matrix were undertaken by Takahashi et al. using a custom cryogenic sample-transfer chain [178, 199]. This cold chain is likely a key component to allow the loaded hydrogen to be immobilised and hence retained, to some extent, in the microstructural in

traps. This is in comparison to the work of Haley et al. which implemented room-temperature transfer after the hydrogen charging and did not observe trapped but only detrapped hydrogen atoms in the APT reconstruction of the material [36].

Cryogenic sample-transfer technique (cryo-transfer) has been previously developed for the microscopic characterisation of biological specimen, typically from liquid environment which require a rapid cryogenic treatment to retain its structure for examination [200]. Using atom probe, Panitz and co-workers demonstrated the first cryo-transfer experiment which enabled the observation of vitreous ice forming from the water layer during cryo-transfer in a prototype atom probe variant-instrument known as the Imaging Atom Probe [201-203]. To date, the use of cryo-transfer has been expanded to more research fields including hydrogen in metal. Some of the most recent studies have successfully integrated cryo-transfer into hydrogen characterisation techniques such as TDA [204] and SIMS [205] to observe weakly trapped hydrogen in steel which was previously not measurable using the corresponding techniques with conventional specimen transfer methods. These results provide further confirmation that cryo-transfer is an essential factor in term of hydrogen characterisation.

2.3 Summary

In this review, the characteristic consequences of hydrogen embrittlement have been introduced. Current understanding of HE and the proposed mechanisms underpinning this phenomenon were discussed, with a particular emphasis on the properties of hydrogen and its interactions with microstructural features such as vacancy and dislocations. However, the key to continue advancing our understanding to hydrogen embrittlement is actually further experimental evidence to underpin the proposed models of either embrittlement or hydrogen-metal interaction.

Based on the understanding of hydrogen embrittlement so far, the strategic approaches for the mitigation such as minimising pre-existing hydrogen and hydrogen in-service ingress, and most importantly, introducing hydrogen trap have previously been investigated. In the case of high-strength steels, the latter is found to be most applicable with the use of finely-dispersed transition metal carbides to act as hydrogen traps. However, the discussion above has also note that current understanding of the origin of the hydrogen-trapping property of these carbides is poor, including their exact trapping energy or mechanism, i.e. what are their exact trapping sites. Hence, a specific experiment providing insights into proposed trapping models are required. APT has been shown to meet the requirements of such experiments; however technical challenges exist such as hydrogen artefact in the instrument and hydrogen loss during sample transfer. Building upon this current state of the field, this study aims to establish a feasible experimental protocol for the study of microstructural hydrogen trapping in steels via the use of APT.

3. Material and Experimental Method

3.1 Proposed material

This study investigates a ferritic steel by Tata Steel Europe subjected to hot rolling at 980 ºC and then coiling at 650 ºC. The nominal composition is presented in Table 3.

Element	Mn	Mo	V	C	Nb	Al	Si	N	Fe
Wt.%	1.56	0.51	0.25	0.096	0.056	0.05	0.026	0.004	Bal.
At.%	1.59	0.3	0.27	0.45	0.034	0.1	0.05	0.02	Bal.

Table 3 – Nominal composition of studied ferritic steel

The mechanical testing and microstructural characterisation of the initial material was conducted at Prof. W. Mark Rainforth's laboratory at the University of Sheffield. The material demonstrated 902 MPa of yield strength, 964 MPa of tensile strength, and 18.2% elongation. Using scanning electron microscope (SEM) and an energy-dispersive-spectrometer (EDS) equipped transmission electron microscope (TEM), the material microstructure was examined and is shown in Figure 14. SEM observation (Figure 14(a)) shows a ferritic microstructure with a measured grain size of 3.2 μm, as obtained by the intercept method [206]. TEM was used to identify the carbide morphology as shown in Figure 14(b), which can be seen to have stringer and sphere shapes and sizes in the range of 10-20 nm. The EDS result in Figure 14(c) indicates the constituent elements of the carbides as V, Mo, C, and Nb. The observed copper signal is not regarded due to contribution from the sample holder.

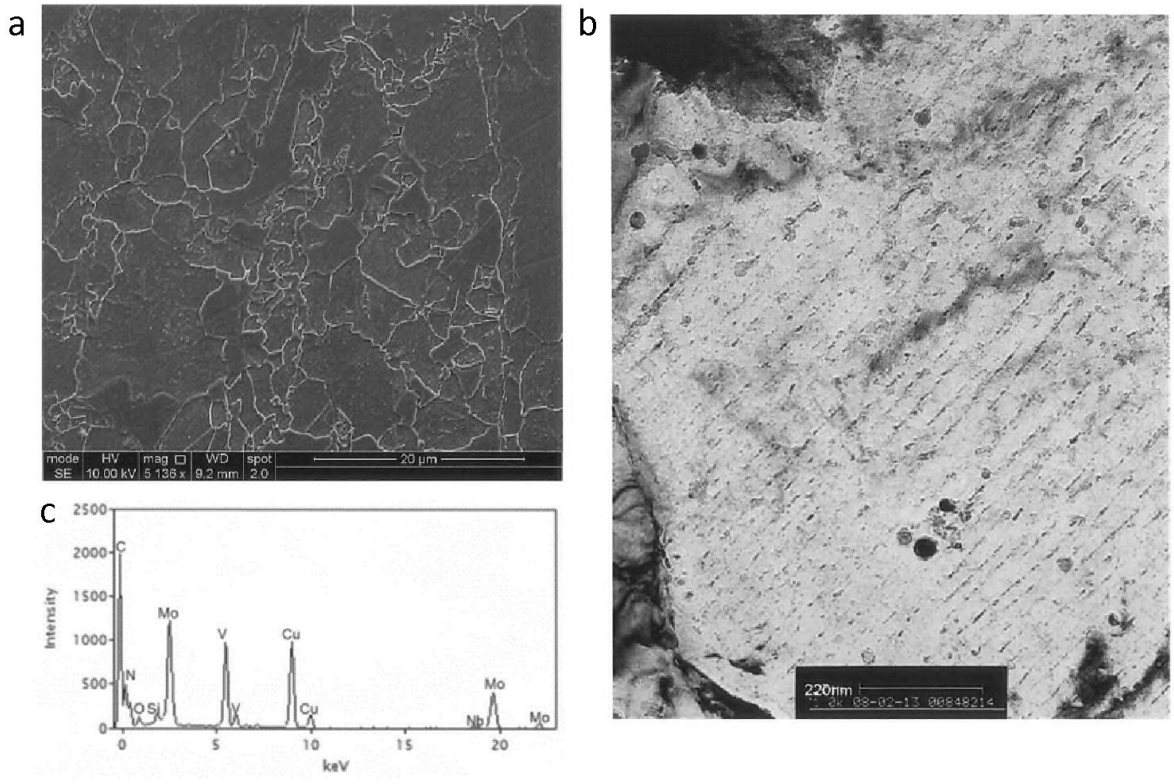

Figure 14 - Microstructure of the as-received material. (a) SEM image shows ferritic matrix with a grain size measured as 3.2 µm by the intercept method. (b) TEM image shows the finely-dispersed carbides with the size of 10-20 nm. (c) EDS analysis of the carbides shows the constituent elements of the carbide, including V, Mo, C, Nb. Courtesy of University of Sheffield.

3.2 Atom Probe Tomography (APT)

3.2.1 Principles

3.2.1.1 Field evaporation

When an electric potential (V) is applied to a very sharp needle-shaped specimen placed in a vacuum chamber, an intense electric field (F) can be generated at the apex of the tip. The strength of the electric field is proportional to the applied voltage and inversely proportional to the radius of the tip (R) [170]:

$$F = \frac{V}{k_f R} \tag{8}$$

where k_f is the field factor with a value between 2 and 4 accounting for the reduction of the actual field from the theoretical value due to the geometry of the tip and the local electrostatic environment [207]. When an electric field is applied to the sharp tip, the atoms at the tip surface can become polarised. As shown in Figure 15, the energy state (green curve) of an atom at the surface subject to the effect of an intense electric field can be significantly deformed to the red curve which shows a reduced energy barrier (Q_n) for the atom to be ionised and leave the specimen. This phenomenon is called field evaporation. The field evaporated ions are subsequently projected by the highly divergent electric field onto a position-sensitive digital detector. By applying a combination of a DC voltage and either voltage pulses or ultrafast laser pulses, time-controlled field evaporation of individual atoms from the surface can be achieved, which becomes the foundation of the APT technique [170].

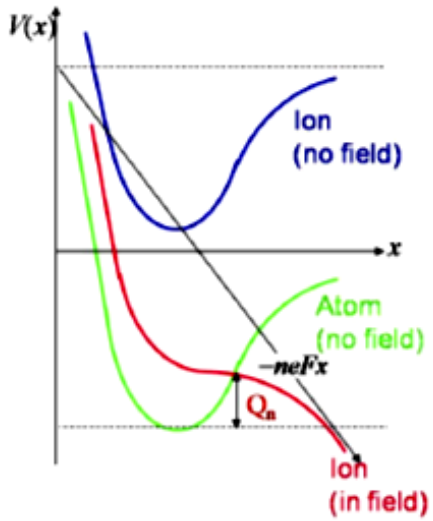

Figure 15 - Energy diagram of a surface atom (green) and its corresponding ion with (red)/without (blue) the application of an electric field at a tip surface. The energy barrier for the atom to be ionised is reduced to Q_n in the presence of the electric field [170].

3.2.1.2 Time-of-flight

In the APT experiment, the chemical identity of a detected ion is determined by time-of-flight (TOF) measurement. TOF can be determined with the knowledge of the time when

the ion leaves the tip, which is assumed to be the time at which a specific voltage or laser pulse is applied to the specimen and the time at which the ion strikes the detector and is registered as an event. Consider an ion with mass (m) evaporated at a charge state (n) by a high voltage (V) and travelling between the specimen and detector across a flight distance (L) with TOF (t_f). Assuming that the potential energy acquired from the electric field ($E_{field} = neV$) is fully transformed to kinetic energy of the ion ($E_{ion} = \frac{1}{2}mv^2$, where v is the ion velocity which is assumed to be L/t_f) an expression can be derived such that [170]

$$M = \frac{m}{n} = 2eV(\frac{t_f}{L})^2 \quad (9)$$

where M is the mass-to-charge-state ratio of the ion. This enables the chemical identification of the ion to be experimentally determined by the measurement of TOF at certain applied voltages in an instrument with a fixed ion flight distance.

3.2.2 Instrument

A simplified schematic of a local electrode atom probe instrument configuration is shown in Figure 16. This instrument design consists of (from the left side of Figure 16):

A. Cryogenerator for inhibiting the noise originated from the migrated atoms at the sample shank
B. DC high-voltage supply to sample stage to generate the standing electric field
C. Local-electrode to provide superposition of voltage pulses enabling time-controlled field evaporation ions, and also confine the distribution of electric field locally
D. Time- and position-sensitive ion detector composed of microchannel plate (details in [208]) and multiple delay-line detectors (DLD)

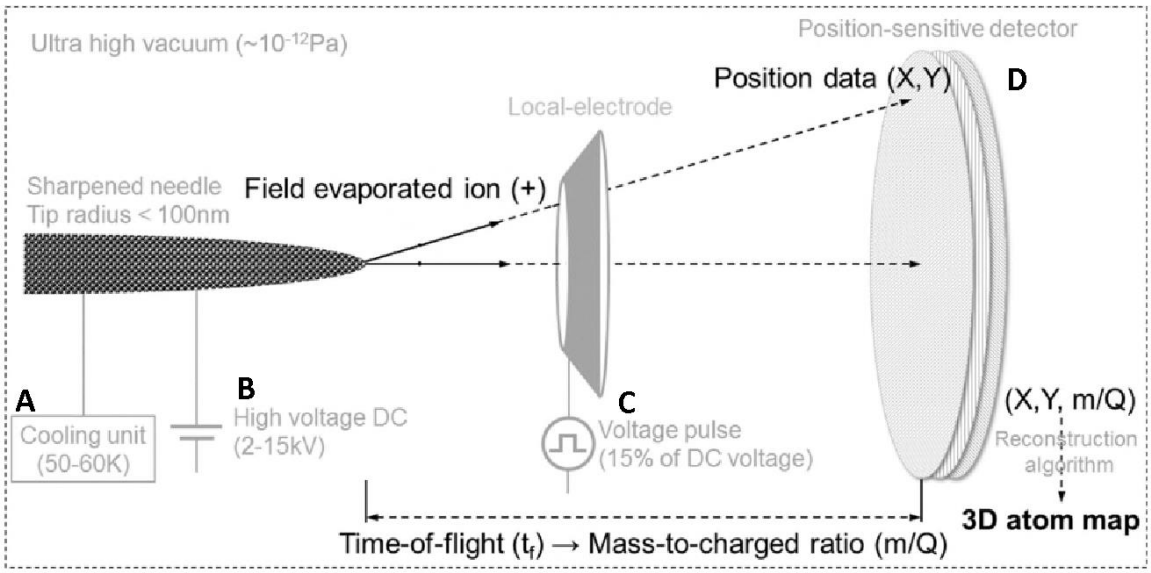

Figure 16 – Schematic of the configuration of a commercial local electrode atom probe. Note here that only the components most relevant to this study are presented for succinctness. Schematic is not to scale.

In the present study, the datasets in Chapter 6 were obtained using a LEAP 4000X HR (ETH Zürich, Switzerland), whereas other datasets used a LEAP 3000X HR (Oxford). All APT data was saved in the RHIT file format (details as [209]) which records the time-of-flight and detector-coordinate information of each detected ion, and then processed in CAMECA IVAS software (Version 3.6.14).

3.2.3 Electropolishing sample preparation

A very sharp needle-shaped sample, typically with an end radius less than 100-nm is required to facilitate the generation of sufficient electric field at the sample surface for field evaporation in an APT experiment. In the first step of sample preparation, the bulk material was cut into 1 x 1 x 15 mm matchstick bars prior to sharpening. Then a standard two-stage electropolishing was applied to sharpen these matchsticks into APT samples [209]. As shown in Figure 17(a), the first stage was conducted in a layer of polishing electrolyte of 25% perchloric acid in acetic acid on the top of an inert liquid. The connections of the

polishing sample and a gold counter-electrode are to the positive and negative potentials of a 15-25V DC source, respectively. This configuration is set-up to locally remove material from the middle of the matchstick bar. Upon application of the potential, the electropolishing sample was moved up and down to ensure thinning uniformity of the polished area. This step forms a neck at the centre of the polished area. The process finishes when this neck yields and the matchstick separates into two needles (Figure 17(b)). Subsequently, both needle samples were rinsed in the order of distilled water, ethanol, and isopropanol and then crimped in small copper tubes for handling.

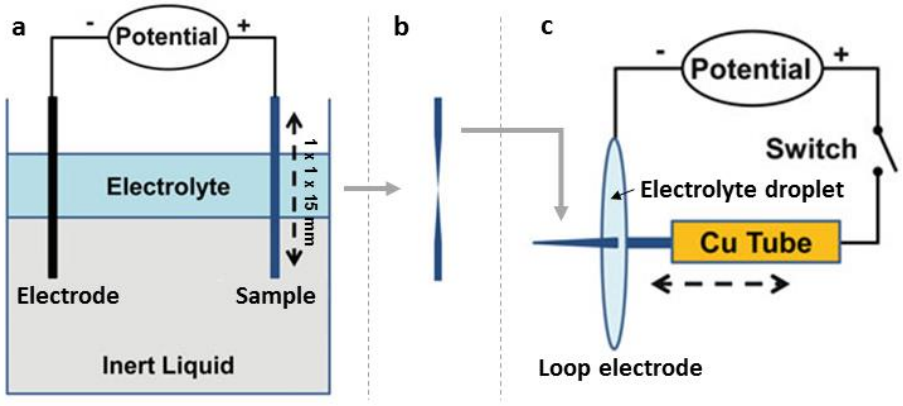

Figure 17 - Schematics of the two-stage electropolishing to produce APT samples. Replotted from [209]

As shown in Figure 17(c), second stage polishing was conducted with the sample and a gold metal loop connected to positive and negative potentials of a 5-30 V DC source, respectively. The loop contained a droplet of the electropolishing electrolyte of 2% perchloric acid in 2-butoxy ethanol. With the aid of an optical microscope of 10x magnification, the sharpening process consisted of iterating the steps of placing the needle through the droplet without applying potential and then applying voltage as it is withdrawn from the electrolyte. The applied voltage was decreased as a fine tip radius was progressively obtained. At the point that 10x optical microscope was not sufficient to resolve the tip sharpness, and a separate 125x optical microscope was used instead. When

the apex of the tip could no longer be in focus in the view of this microscope, then the sharpening was regarded as complete.

3.2.4 Sample loading

The sharpened needles were first loaded into a four-needle sample carrier 'puck', and this puck was loaded into a 'carousel' as shown in Figure 18(a) and (b). The carousel carries up to six pucks. Alternatively, a cryo-transfer process which involves a customised puck and carousel will be introduced in more detail in later Section 3.5.2.

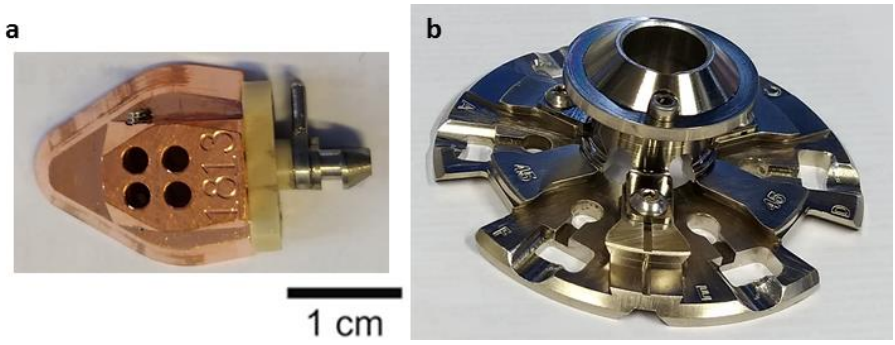

Figure 18 – (a) a four-needle sample puck and (b) a carousel to carry up to six pucks in LEAP chambers.

Subsequently, the carousel was loaded into the loading chamber of the atom probe (loadlock). The puck containing the sample was introduced to the analysis chamber using the following procedure: rapidly pumping to a pressure below 10^{-5} Pa in the loadlock; then moving the specimen to the buffer chamber and reducing pressure to 10^{-6} Pa; finally, the specimen was loaded into the analysis chamber and pumping pressure levels down to approximately 10^{-9} Pa. For the as-received reference sample discussed in Chapter 4, the buffer chamber step typically pumped down overnight so as to remove contamination prior to the atom probe experiments and reach appropriate vacuum levels. In the case of a hydrogen-charged sample (Section 5.2), the room-temperature transfer procedure (RT-transfer) consists of 18 minutes pumping in loadlock and a subsequent 2 minutes for

passing through the buffer chamber so as to reduce the time between the leaving hydrogen-charging environment and reaching the cryo-stage in the analysis chamber. Other custom procedures with sophisticated requirements will be discussed in detail in Section 3.5.

3.2.5 Experimental parameters

To tackle the challenge of accurately measuring carbide chemistry discussed in Section 2.2.4.2, a calibration method previously established in the literature regarding sample temperature and pulse fraction (PF%) was conducted. Pulse fraction refers to the fraction of voltage applied to the specimen in a pulsed manner to that of the constant standing potential. The aim of the calibration was to optimise the accuracy of compositional measurements by identifying any systematic variations introduced by changing these parameters [192, 193]. The apparent composition of the sample presented here is defined by the criteria described in Section 3.2.6. The concentration for each element was measured as a function of the sample-stage temperatures of 44K, 60K, and 76.4K at 15% of pulse fraction as shown in Figure 19(a). 60K gives the overall measured concentration closest to the nominal value for this alloy. The concentrations measured as a function of varying PF% at 60K between 5% and 25% are shown in Figure 19(b). The condition that produced results in closest agreement with the nominal composition was obtained at 15%. These results concerning selection of the best experimental parameters generally agree with the literature's findings [192, 193]. 60K and 15% of PF% are therefore selected in this study. In addition, among the existing carbon quantification studies [192-196], pulse frequency has not yet been found to have any significant effect to the result of content measurement by atom probe. Accordingly, the most common 200k Hz among the literatures is used in this study.

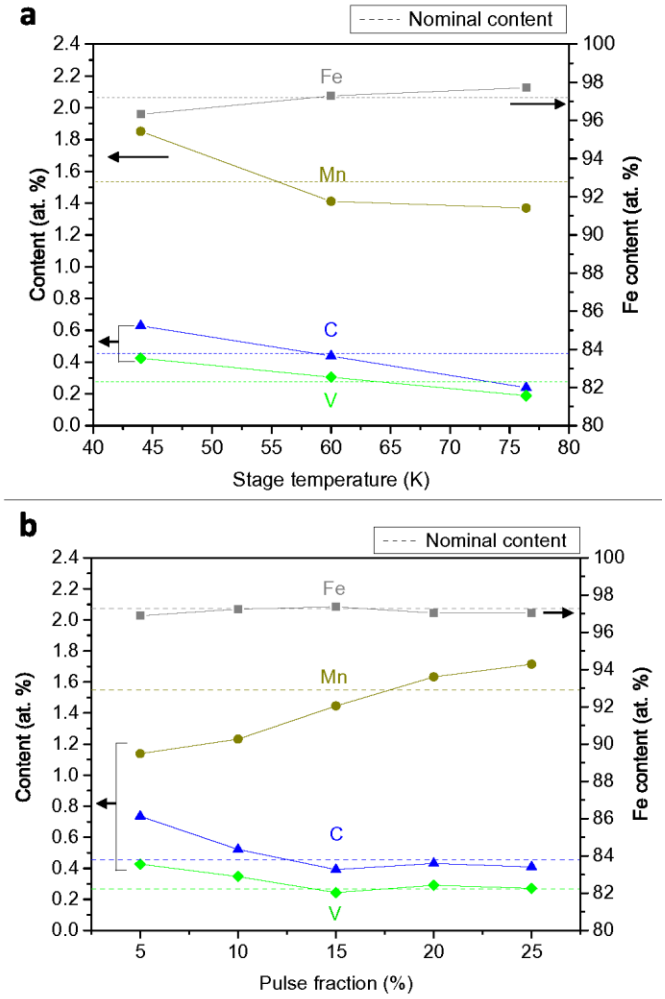

Figure 19 – (a) The measured concentrations of elements at stage temperature of 44K, 60K, and 76.4K based on statistics of 5, 3.3, and 2.5 million ions, respectively. (b) The measured concentrations as a function of pulse fraction each based on statistics of 3 million ions.

3.2.6 Mass spectra peak labelling

'Peak labelling' or 'ranging' was conducted to assign the identities of peaks in the atom probe mass spectra to the detection of specific ions in the experiment. To this end, the 'weights' algorithm developed by Haley et al. was used to aid this process [210]. An example of mass spectra ranging from the APT analysis of an as-received reference sample containing 3.4 million ions is shown in Figure 20. The ranging of the reference data was finalised by deconvolving the contributions to the peak at 24 Da, which represents a mass-to-charge-state ratio overlap between C_2^+ and C_4^{2+}. Deconvolution of contributions to such

overlapping peaks can be achieved by the analysis of adjacent non-overlapping peaks, comparing these to isotopes of known natural abundances. The contribution of background hydrogen was omitted from the analysis [180, 211]. A general background was obtained by IVAS and was used to subtract the raw signals to obtain the corrected composition.

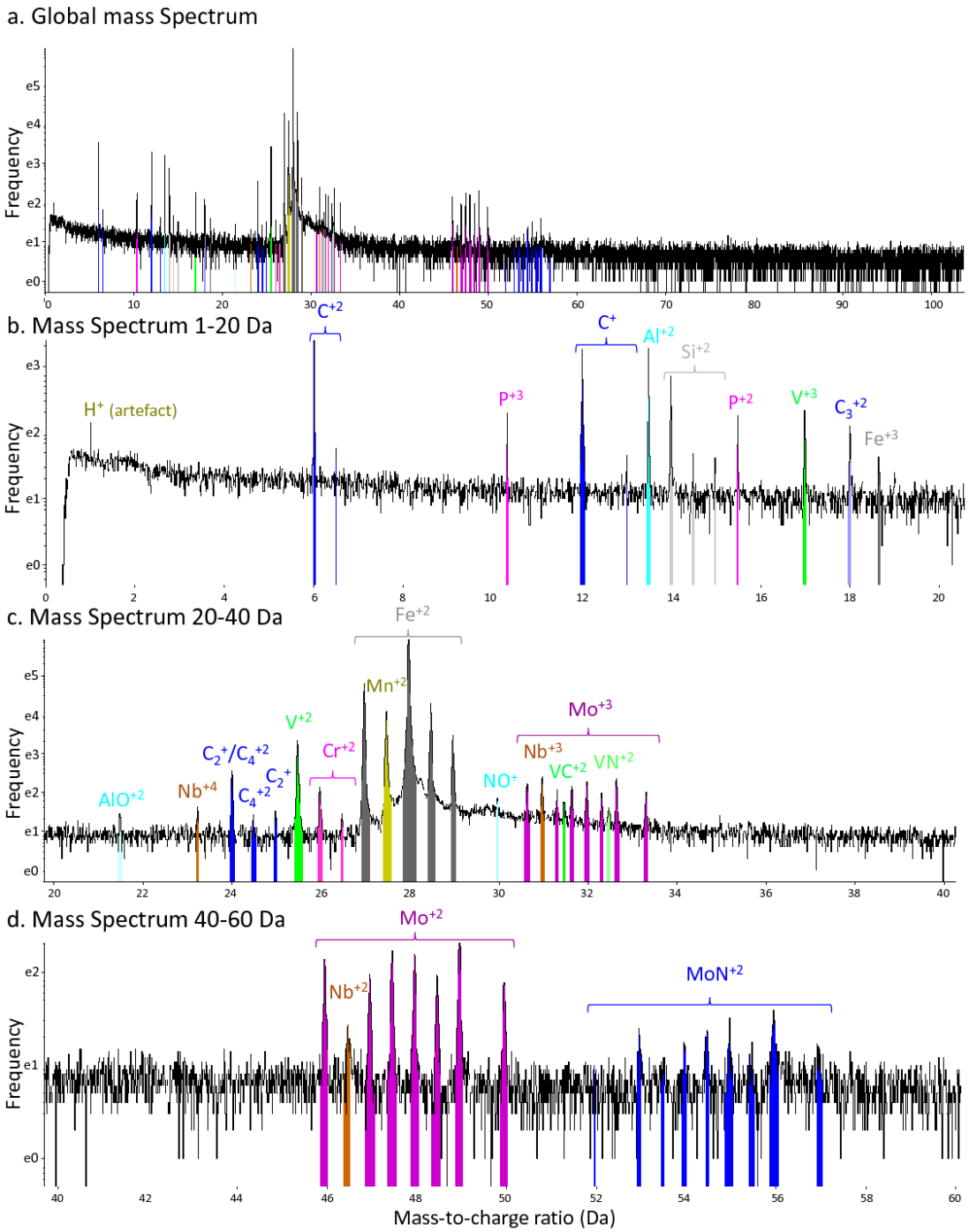

Figure 20 – Global and segmented APT mass spectrum (frequency axis in log scale) showing ranged ions for as-received reference sample of the ferritic steel described in Section 3.1 (R14_25949)

3.2.7 3D reconstruction

APT is a technique whereby the ions projected from a needle-specimen tip are collected by a position-sensitive detector. Hence each ion is assigned detector coordinates from where it struck the detector. The protocol to project ions back to real space coordinates in the specimen is known as 'reconstruction'. A detailed treatment of standard reconstruction algorithms can be found in [212]. The reconstruction protocol is based upon a reverse projection geometry that assumes the APT specimen takes the form of a perfect hemispherical cap on a cone. It also assumes that the radius of this hemisphere is known at the time that each atom is field evaporated. A basic schematic is shown in Figure 21. For the N^{th} detected ion in the sequence of field evaporation that strikes the detector at coordinates, X_D, Y_D is approximated to have taken a straight flight path from point T on the sample surface. Due to effects from the electrostatic environment, this straight flight path does not follow a line of trajectory originating from the theoretical centre of the hemispherical cap (O) but instead originates from a projection point (P) further into the specimen. The projection point is located along the depth axis of the specimen at a distance ξR from the apex, where R is the radius of the tip and ξ describes the extent of compression by the field distribution and is called image compression factor or ICF. L is the specimen to detector flight path length of the atom probe instrument. The distances, D and d, represent the distance between the position of the atom on the surface and the in-depth axis of the specimen and the distance between its resulting detector coordinate and the centre of the detector, respectively. The angle θ is the launch angle with a projection centre in the centre of the hemispherical cap, whereas θ' is the launch angle actually observed in the experiment due to the compressed ion trajectory.

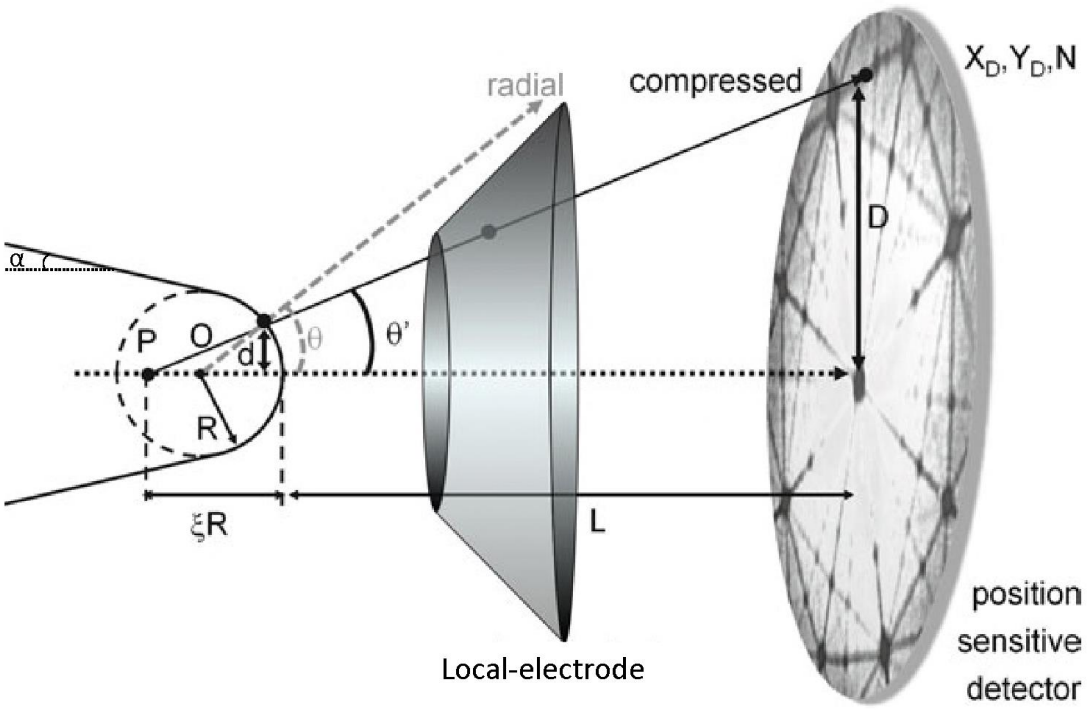

Figure 21 - Schematic of point project model used in APT data reconstruction algorithm [170]

3.2.7.1 Image compression factor

In some certain cases, ICF can be determined by examination of crystallographic poles in detector space. A desorption map can be generated in the form of 2D frequency distribution of coordinates where ions struck the detector. Often this reveals a pattern of local regions of higher or lower density of ion hits. This pattern is representative of the crystallography of the material, with these regions representing poles, i.e. quasi-stereographic projections of specific crystallographic directions onto the detector. The regions of high/low density of hits on the detector originate from aberrations in the trajectory of the ions due to the surface arrangements of protruding atoms on the surface of the specimen in the vicinity of the crystallographic orientations.

However, the presence of poles in raw desorption map are typically not obvious, and in particular they can be obscured by the contribution of secondary phases in the material as shown in Figure 22(a). Accordingly, a filtering protocol was applied to improve the clarity

of the poles in the desorption map [213]. This filtering is based on the fact that after an ion is evaporated from the vicinity of a pole, the probability that an ion from the same pole being evaporated on the subsequent pulse is greater than the likelihood of two atoms from a region between the poles being evaporated by consecutive pulses. Hence the filtering algorithm selects only detected events corresponding to two successive pulses to filter out most of the non-preferential evaporation areas. An example of filtered map is shown in Figure 22(b) which allows the identification of regions preferentially evaporated on consecutive pulses, i.e. poles. A simulated desorption map can be created by using a MATLAB programme of Dr. Daniel Haley, as shown in Figure 22(c), to enable indexing of the major poles observed in the filtered experimental map, in this case [110] and [200].

For small angle, the ICF can be determined by the ratio of θ and θ', which can be determined by $\theta_{crystal}$ and $\theta_{observed}$, the theoretical angle between two crystallographic directions and the angle between the directions observed from the desorption map in experimental data [214]. $\theta_{observed}$ can be determined by eq(10)

$$\theta_{observed} = \tan^{-1} \frac{D_{observed}}{L_{virtual}} \tag{10}$$

where $L_{virtual}$ is the virtual distance of L in reflectron-equipped atom probe, and for the purpose of that this calculation can be considered equivalent to the schematised model in Figure 21. The value of $L_{virtual}$ is 42 mm in the LEAP3000X HR used in this study [215]. $D_{observed}$ is the distance between the centres of two major poles on the desorption map for example between the [110] and [200] in Figure 22(b). In this instance, the observed angle is calculated as 0.54 rads. The theoretical crystal angle between [110] and [200] is 45° (0.758 rads). Finally, an initial ICF in this case was determined as 1.45.

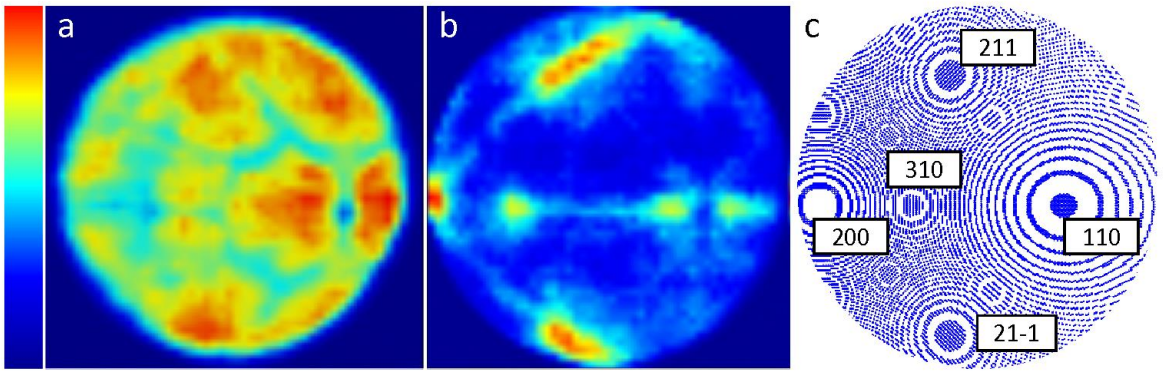

Figure 22 – Desorption map for determining crystallographic poles in APT data from a sample of the ferritic steel described in Section 3.1, (a) raw desorption map (all detected hits), (b) filtered map with the method of [213] showing only events where ions are detected on 2 successive pulses, (c) simulated detector map of body-centred-cubic crystal rotated to correspond to the experimental map in (b).

3.2.7.2 Initial radius and spatial distribution map

Spatial distribution maps (SDM) allow examination of the atom-distribution frequency to specific crystallographic planes in APT data [216]. An SDM plots a frequency distribution of atomic offsets by examining the local distribution around each atom in the region of interest in the reconstruction. An initial reconstruction was generated. By examining this closely, crystallographic planes, are often observable in the vicinity of specific crystallographic poles. Herein, data originating in the reconstruction from cylindrical sub-volumes along the identified [110] and [200] poles, respectively, as shown in the desorption map of Figure 22(b), was selected for correction of initial radius and ICF [215]. Initially, the default values of initial radius and ICF for the specific example introduced in Section 3.2.7.1 were 36.33 nm and 1.65, respectively. Then the reconstruction centred around the [110] pole was examined, and a more accurate ICF value of 1.45 was determined, as outlined in the last section. At this stage, the initial radius was adjusted to match the theoretical plane spacing between (110) in this ferritic alloy, which is 0.202 nm [99]. Then the reconstruction was moved to the region centred around the [200] pole for examining the theoretical angle between (100) and (200) which should be 45°. Here ICF

was adjusted until 45° was obtained [99]. Subsequently, the reconstruction region was moved back to around [110] pole for adjusting the initial radius to obtain 0.202 nm plane spacing again, and the region required to move back to [200] for ICF adjustment by matching the 45° between the planes. After few iterations, the optimised initial radius and ICF were determined as 35.5 nm and 1.35, respectively, resulting in the final SDMs shown in Figure 23(a) and (b).

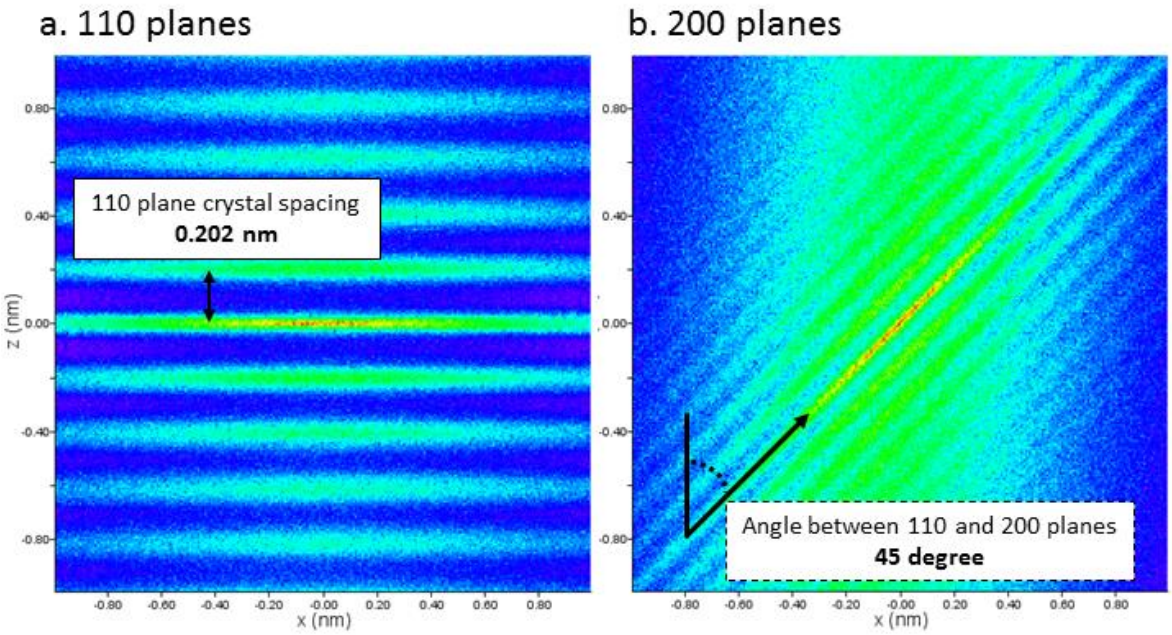

Figure 23 – x-z SDMs of (a) 110- and (b) 200-pole region from an optimised reconstruction, where the theoretical plane spacing of bcc iron, 0.202 nm, and the theoretical angle of 110 and 200, 45°, were able to be obtained in (a) and (b), respectively.

3.2.7.3 Reconstruction error

Not all datasets are sufficiently large enough to provide statistics to enable crystallographic poles to be identified and hence for an ICF to be determined. Therefore, calibrating reconstructions can often be difficult. However, with a comparison between uncalibrated and calibrated data, the dimensional error induced by the default reconstruction can be estimated and accounted for the uncalibrated datasets. In the case of datafile R34_05028 where the data is sufficient to undertake the calibration described in

Sections 3.2.7.1 and 3.2.7.2, the default IVAS settings (R = 36.33 nm and ICF = 1.65) gave a reconstructed volume of 101 x 98 x 111 nm, whereas the corrected inputs (R = 35.5 nm and ICF = 1.35) gave the volume as 82 x 80 x 152 nm. Accordingly, lateral 22% to 23% and in-depth 27% of spatial error are obtained in this dataset to show the importance of reconstruction calibration and the extent of distortion which can be expected in an uncalibrated tone.

3.2.7.4 Trajectory aberration and matrix correction

Given that APT is a technique collecting information from field-evaporated ions, any uncertainty induced during the evaporation can cause aberration in the perceived trajectory of the ions. These effects can originate from a complex combination of inhomogeneous field, distribution, surface diffusion, and most significantly, the difference between the evaporation fields of multiple phases within a material [170]. As shown in Figure 24, materials containing precipitates that require lower and higher field than the matrix to be evaporated will result in areas of higher and lower density at the detector, respectively. A low-density region at the detector in the experiment of the material containing high-field precipitates will consequently correspond to an aberrant low-density region in the reconstruction. This is known as a local-magnification effect due to a local change in the surface of the specimen in turn due to preferential retention of the high-field precipitate, which is seen in the ferritic material containing carbide precipitate such as the one used in this study [170]. It results in deviated ion-projections from both the precipitate and matrix as plotted in the right of Figure 24. However, the reconstruction algorithm assumes that the specimen tip is at all times a perfect hemisphere. This results in spatially blurred precipitates in the reconstruction (i.e. incorporation of matrix atoms into the reconstructed precipitate). This leads to inaccurate measurement of precipitate composition due to the matrix contamination. However, further data processing in the form of ‘matrix correction’

can be applied to remove this contribution and obtain a more accurate assessment of precipitates [217], which involves an initial measurement of matrix composition, and then a subtraction of the matrix composition from the measured precipitate composition. This correction was applied to all measurement for the interested V-Mo-Nb carbide precipitate in this study.

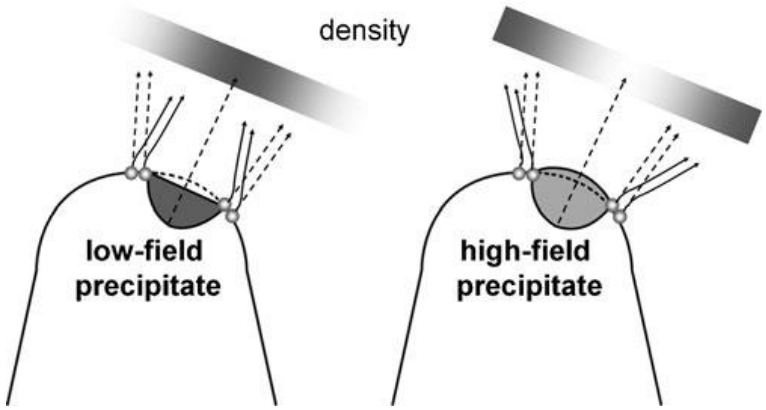

Figure 24 – Schematics of the difference of ion trajectories and resulting event density on the detectors by the trajectory aberrations induced when analysing specimens containing low- and high-field precipitates, respectively [170].

3.2.8 Precipitate analysis

3.2.8.1 Random comparator

Before investigating any compositional segregation or precipitation within APT data, a comparison between real data its corresponding randomised comparator is necessary to quantify the statistical significance of solute clustering [170]. The randomisation herein was executed by randomly relabelling the ion identities in the original data.

3.2.8.2 Isoconcentration surface

Isoconcentration or isodensity surfaces, both generally known as ‘isosurfaces’, refer to an interface defined by a certain local property, chemical concentration or atomic density, respectively, to isolate regions of the 3D dataset having the specified value of this property. It is effective in identifying and spatially visualising compositional changes such as

precipitation by defining a 3D atomic map. An example is shown in Figure 25(a). An isosurface is produced by first partitioning the entire dataset into voxels with a certain uniform size, then the content within each voxel is individually characterised. An isosurface is formed by connecting adjacent voxel with the user-defined elemental density of concentration. Further processing can be applied to enhance continuity [218] and smooth the joining together of the final isosurfaces. In this study, two representative parameters, i.e. voxel size and the value of isoconcentration (isovalue), were selected to evaluate their effects to the define isosurface, whereas further discussion in other parameters such as delocalisation value is beyond the scope of this study. The voxel size affects the statistics in each voxel and the spatial resolution of the resulting isosurfaces, whereas the increase of isovalue generally reduces the numbers of defined isosurfaces and leaves only the isosurfaces having higher isoconcentration/isodensity in the analysis.

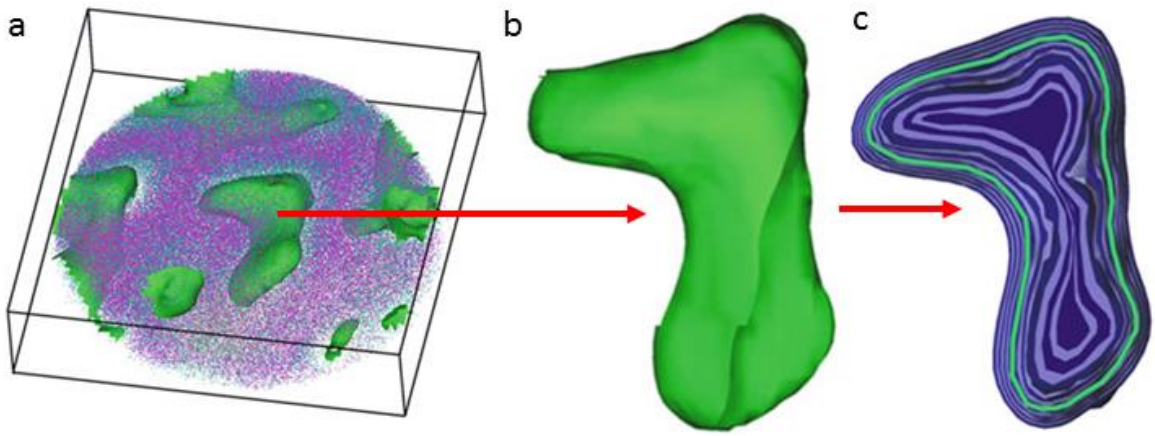

Figure 25 – (a) Example of isosurface (green) in an APT map. (b) Close view of an isosurface in (a). (c) The 2D schematic of the proxigram defining the (b) isosurface shown by the green curve [170].

Once isosurfaces are generated, as shown in Figure 25, a proximity histogram or 'proxigram' can be obtained by computing the composition within the individual regions (the purple bands in Figure 25 (c)) at a varying distance along a direction normal to the isosurfaces, which is in the form of 1D concentration profile [219]. Proxigrams allow for

measurement of the properties of the microstructural features defined by the isosurfaces, such as cluster composition. Often such measurements can be optimised by only examining data in the core of the isosurface sufficiently far from the interface to limit contributions from the matrix effects (as described in Section 3.2.7.4). However, if the actual precipitate size is not sufficiently large, this core volume away from the interface is not available for the composition measurement. Moreover, if the defined isosurfaces falsely join multiple clusters together, then the central volume being measured in proxigram would also contain matrix contributions and thus would not be provide the correct chemistry.

3.2.8.3 Nearest Neighbour distribution

Nearest Neighbour (NN) distributions enable the investigation of the average local atomic neighbourhood surrounding each type of element in the data. NN distributions generate a histogram of distances between a specific type(s) of atom and its atomic nearest neighbour of this same types (or a different type) [170]. Alternatively, a kNN distribution can be generated by measuring distance between an atom and its k^{th} nearest neighbour. Interpretation of these distributions is enabled by comparison with a random comparator. For example, atomic clustering can be identified if the experimentally-measured distribution highlights shorter NN distances than that of the randomised data. This NN distribution analysis was applied to all results in this study to identify the clustering of elements of interest.

3.2.8.4 Maximum separation of solutes

Solute clusters can be identified and analysed in APT data by use of a clustering algorithm. The *maximum separation* method defines any two solute ions separated by less than a defined distance (d_{max}) as belonging to same cluster [220]. The defining procedure for carbides first requires specifying the solutes which are V, Mo, Nb, and carbon monomer

(C), dimer (C_2), and trimer (C_3) in this study according to the TEM EDS data (Section 3.1). Next d_{max} needs to be defined, joining up pairs of clustered solutes into discrete networks of connected atoms and thereby defining the clusters. If too large d_{max} is applied atoms from the matrix may be included in the clusters or else two discrete clusters may be erroneously identified as a larger single cluster. Conversely, if using too small d_{max}, the actual clusters may be incorrectly separated into multiple smaller clusters by the algorithm. In addition, there is a statistical probability that some solute ions randomly distributed in the matrix can be identified as clusters if they are coincidently close together. These clusters are typically small and thus a minimum cluster solute number (N_{min}) is applied to the results of maximum separation algorithm to remove such random clusters below certain size.

Williams et al. demonstrated a method to determine d_{max} and N_{min} in a relatively objective manner [217]. They defined an objective function $(N_{real} - N_{rand}) / N_{real}$ to quantify the confidence against 'real clusters' defined by given parameters in the analysis of an experimentally derived APT dataset as compared to its random comparator of the same overall composition, where N_{real} and N_{rand} are the numbers of defined clusters obtained from the real data and its random comparator, respectively. An example of using this objective approach to determine d_{max} and N_{min} is shown in Figure 26, with the selected threshold confidence value of 0.99 displayed as the red line. For a N_{min} of 5 (solid line), any d_{max} between 0.5 and 0.7 nm can give a 99% confidence of generating 'real clusters'. At this point, the authors suggest that a higher d_{max} within this range should be used rather than a lower one given high d_{max} can avoid unnecessary separation of the defined clusters.

In practice, this method was performed utilising an in-house d_{max}-sweeping program written by Dr. Daniel Haley which automatically generates data randomisation (for the random comparator) and then iteratively applies the maximum separation method using d_{max} values ranging from 0.1 to 3 nm to both the real and randomised datasets. These yields

both N_{real} and N_{rand} sweepings then was applied to the datasets to obtain the corresponding values by the objective function approach. This method however still requires a reasonable N_{min} being selected before assigning d_{max}. In this study, the selection of N_{min} was guided by the size of the largest cluster as defined in the random comparator by a pre-assigned d_{max} as demonstrated in Section 4.2.2.1. The final d_{max} was found by following the objective-function method with the selected N_{min}.

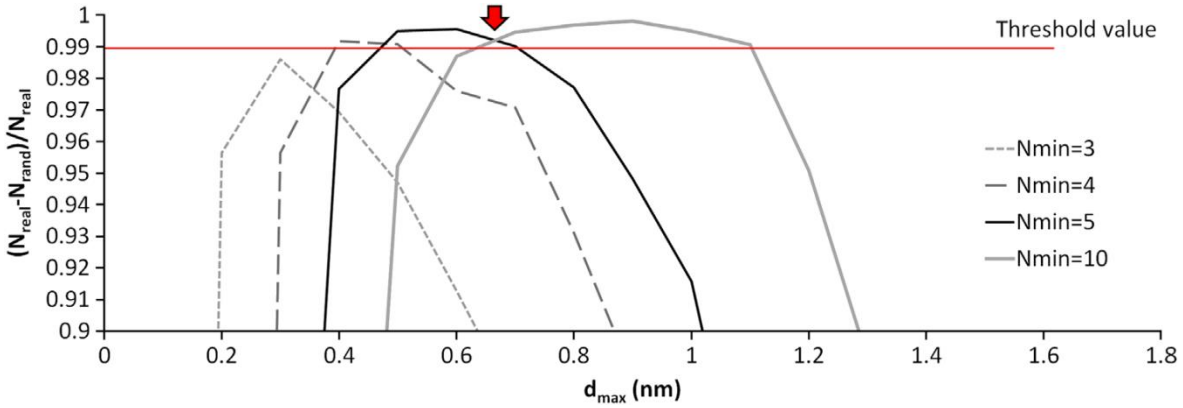

Figure 26 – Using objective function proposed by Williams et al. to determine optimised values of the parameters d_{max} and N_{min} defined in [217]

After initially defining the clusters, they only consist of the specified solute ions. Next an envelope distance or inclusion distance (L) is applied to examine the local neighbourhood around each clustered solute ion, which now serves to incorporate the matrix ions within this distance into the cluster. The size of L is bounded by a value of half d_{max}. A larger than this value may result in double counting the contribution of single matrix atoms between two adjacent clusters separated by d_{max}. Figure 27(a) shows the effect of increasing L on the resulting cluster definition. This corresponds to the radius of grey circles around the green carbide solutes. Increasing L results in not only filling up the interior of the clusters with matrix ions. But when it becomes too large it also erroneously including a shell of non-relevant matrix ions at the cluster surface, as the right end of Figure 27(a) shows.

In order to remove these ions that have erroneously incorporated into the cluster, an erosion step, defined by the distance, $d_{erosion}$, is applied to the matrix atoms which were not defined in clusters in the envelope stage. This removes from the cluster analysis all matrix ions surrounding the non-clustered matrix ions within this erosion distance, bounded by L so as not too over-erode into the cluster interior. The effect of increasing $d_{erosion}$ is shown in Figure 27(b), which corresponds to the progressive removal of surface matrix ions. Given this effect of $d_{erosion}$, this parameter was thus utilised to study the constitution of cluster surface along the increment of $d_{erosion}$.

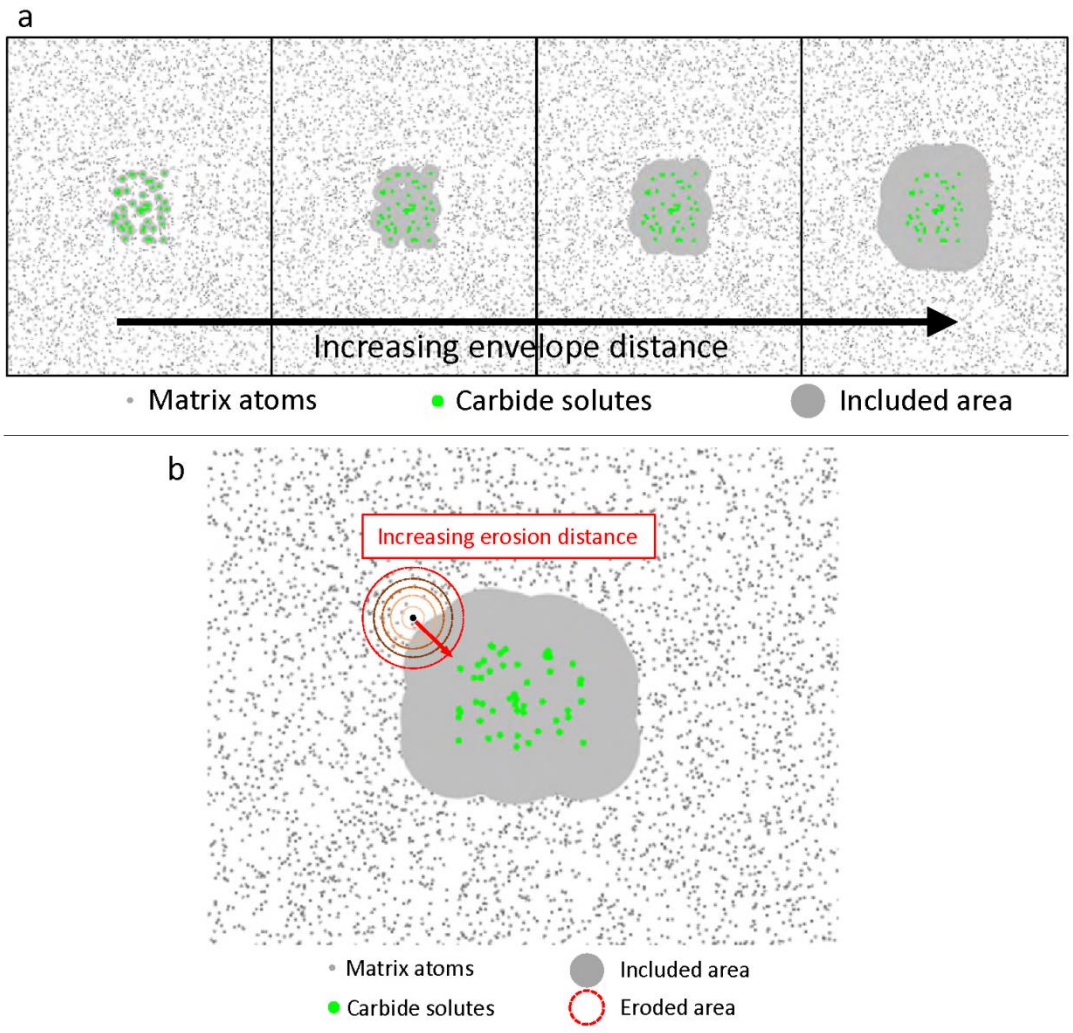

Figure 27 – Schematics of (a) envelope distance (L) as the radius of grey circle and effect of increasing it, and (b) erosion distance ($d_{erosion}$) as red circles, which aims to remove the excess area enclosed by the application of L. By sweeping the two parameters, the interior and surface chemistry of the clusters can be accounted. Diagrams is presented in 2D for simplicity.

Lastly, once having the defined the number of clusters in the dataset using both isosurface and cluster-analysis methods, the corresponding carbide number densities of the proposed material are able to be obtained against the volume of calibrated reconstruction.

3.2.8.5 Axial profile along analysis direction

For investigating deuterium distribution in deuterium-containing data, a line-profile analysis along the z axis (analysis direction) was undertaken, to remove the effects of lateral aberration as described in Section 3.2.7.4. Although IVAS allows line profile of any selected region of interest (ROI), collecting the chemical profile of many carbides in a large dataset is time-consuming and involving arbitrary errors when specifying individual ROIs. This therefore requires an automated method which can ultimately provide a superimposed result combining all 1D chemical profiles measured across the selected carbides [215, 221]. Deuterium-containing data was processed with following procedure: The carbides were first identified by an isosurface method with 9.5% isovalue of V (Section 3.2.8.2) to obtain isolated carbide data. Then, a cluster analysis algorithm was utilised to define the centre coordinates and dimensional information of each isolated carbide, respectively. Subsequently, for each cluster with radius of gyration (r_g) normal to the analysis direction (z-axis), a $2r_g$ x $2r_g$ x $5r_g$ cuboid was placed at the centre to collect the chemical profile of the cluster as shown in Figure 28. In the final step, all the profiles from the analysed carbides were normalised in z-direction and then superimposed into to create a global profile, which shows a combined elemental trend regarding all considered clusters.

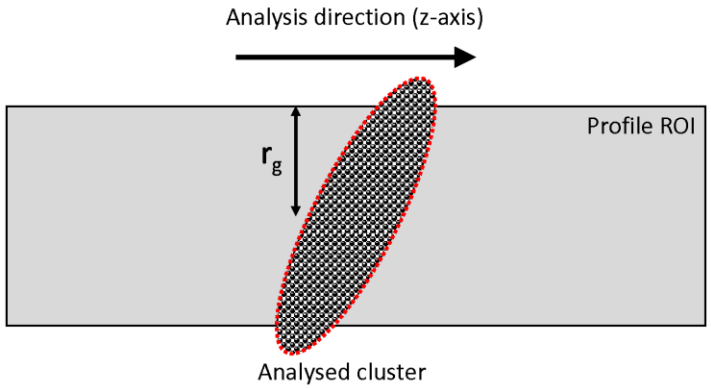

Figure 28 - Schematic of automatically obtaining line profile in an individual carbide. For a cluster having radius of gyration (r_g) normal to the analysis direction, a $2r_g$ x $2r_g$ x $5r_g$ ROI at the centre was used to take the z-axis porfile [215]

3.3 Hydrogen liquid charging

The highest potential that has been attempted in the literature using the same charging solution as here was 1.7V [34]. Herein it was further increased to 2.2V considering the uncertainties in equipment accuracies to guarantee the hydrogen traps in the sample were fully saturated. The charging fugacity in these experiments was speculated by extrapolating the literature data as shown in Figure 29, corresponding to over 10^4 atmospheres.

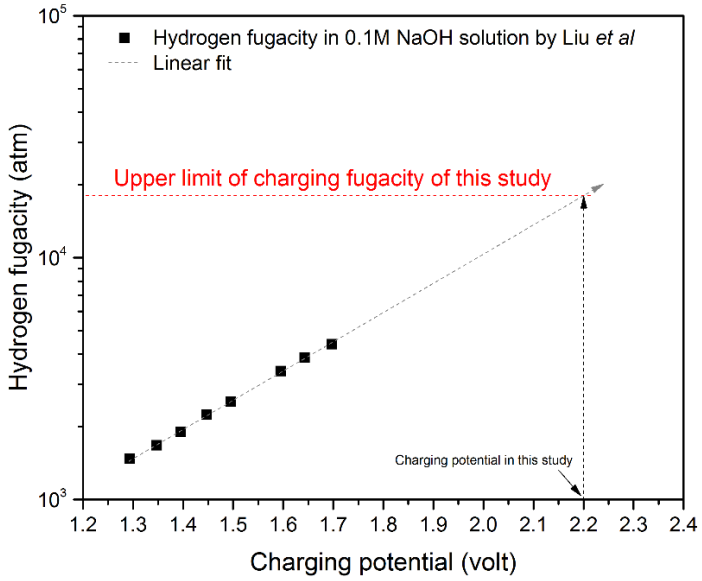

Figure 29 - Hydrogen fugacity at corresponding charging potentials based on permeation testing results of a low-alloying steel charging in 0.1M NaOH aqueous solution in high-potential regime by Liu *et al* [34] and the extrapolated fugacity at the charging potential used in this study.

The liquid charging cell used in this study to introduce deuterium into the samples is illustrated and pictured in Figure 30(a). It incorporates a cathode sample holder and a gold electrode and is a simplified version of the traditional three-electrode configuration without the use of a reference electrode [36]. The entire experimental setup is shown in (b), which includes the charging cell, the ammeter/power-supply (Keithley 487 pico-ammeter/DC voltage), and a digital camera (RS Pro USB Microscope) for monitoring the charging procedure. The sample holder was held in a feedthrough by friction fit and was adjustable in height. After electropolishing the needle-shaped sample was dipped into the solution to about 0.5 mm depth as shown in (c). The scale reference of (c) was obtained by inserting a TEM grid with known dimension in the same view as shown in (d), and then the dimension per pixel of the TEM grid image was obtained and used to estimate the scale in tip image.

Contact area of the tip dipping in the solution (A) was calculated for estimating the current density by assuming the area as cone shape, hereby $A = \pi LR$, where L is the dipping depth and R is the tip radius at the liquid surface. A contact area measurement of 4×10^{-2} mm^2 was obtained in the case of the tip in Figure 30(d), which is much smaller than that of the gold anode, which is approximately 40 mm^2. Because of this orders-of-magnitude difference of contact area, the cathode interface is assumed to take most of the applied charging potential.

Regarding the charging time, the corrosion induced during contact to the reactive liquids used is a concern for preserving the integrity of material properties, therefore it is necessary to minimise this exposure, as is suggested in the literature [33]. In this study, the time for the charging reaction to become sufficiently stabilised was defined as the minimum charging time.

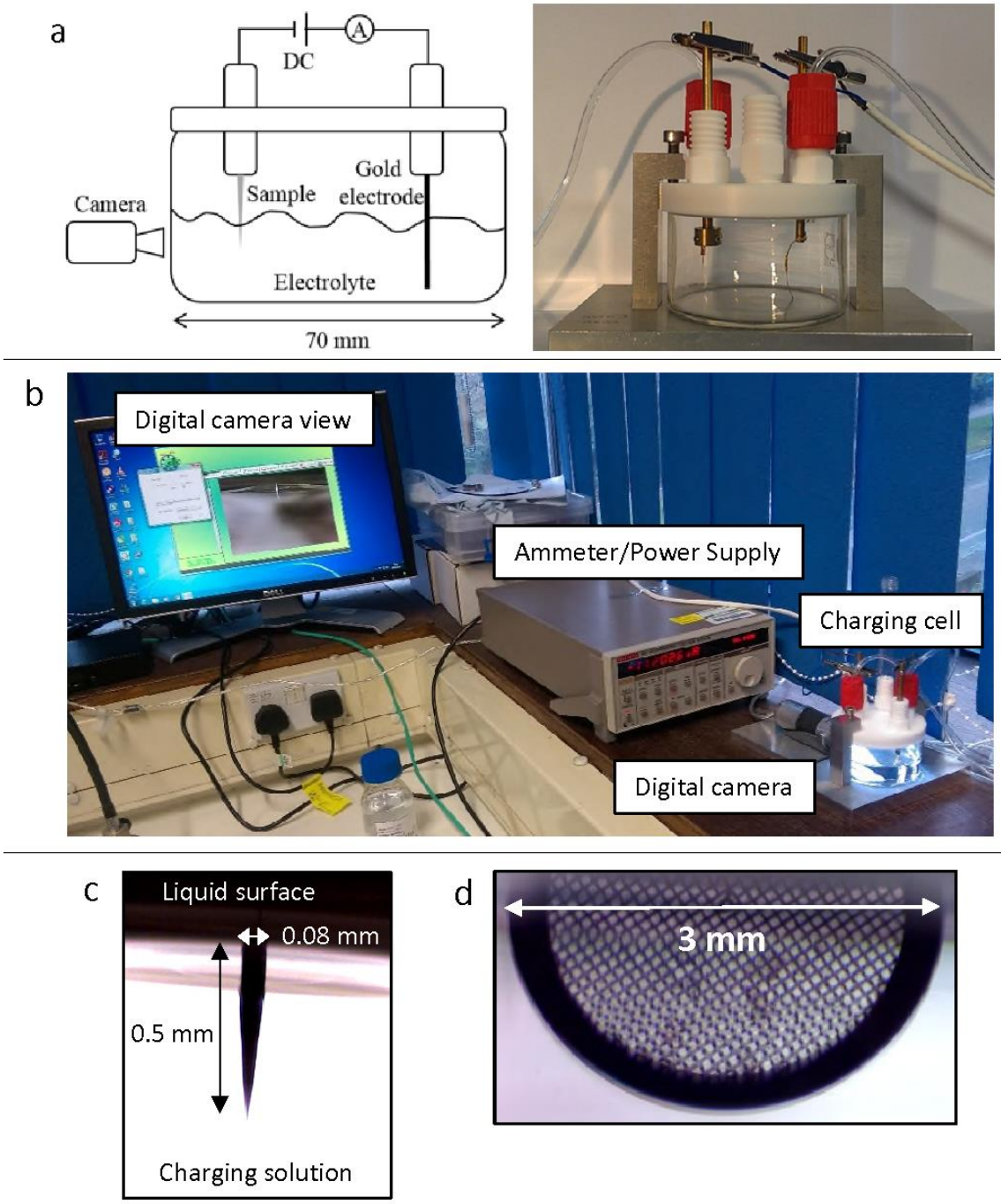

Figure 30 - Configuration of hydrogen electrolytic charging: (a) schematic and (b) picture of the charging cell, (c) overview of charging configuration with power supply/ammeter and observation camera (d) close view of a tip to be charged, (e) a reference TEM grid to obtain tip size.

As shown in Figure 31(a), a significant amount of hydrogen bubbles was observed directly after the application of the charging potential. After 30 seconds, hydrogen bubbles had faded, and this stage corresponded to the emerging plateau in the plot of current density as

a function of charging time shown in Figure 31(b). Thus, the time for stabilisation was defined as 30 seconds which became the standard charging time used in this study. After charging, the sample was immediately removed from the cell and cleaned with compressed air to remove residual charging solution. Finally, the samples were mounted to a four-needle puck and then either loaded into the LEAP 3000X HR or subjected to other treatments described in Sections 3.4 and 3.5. The entire cleaning and mounting period was about 2 minutes in typical experimental procedures.

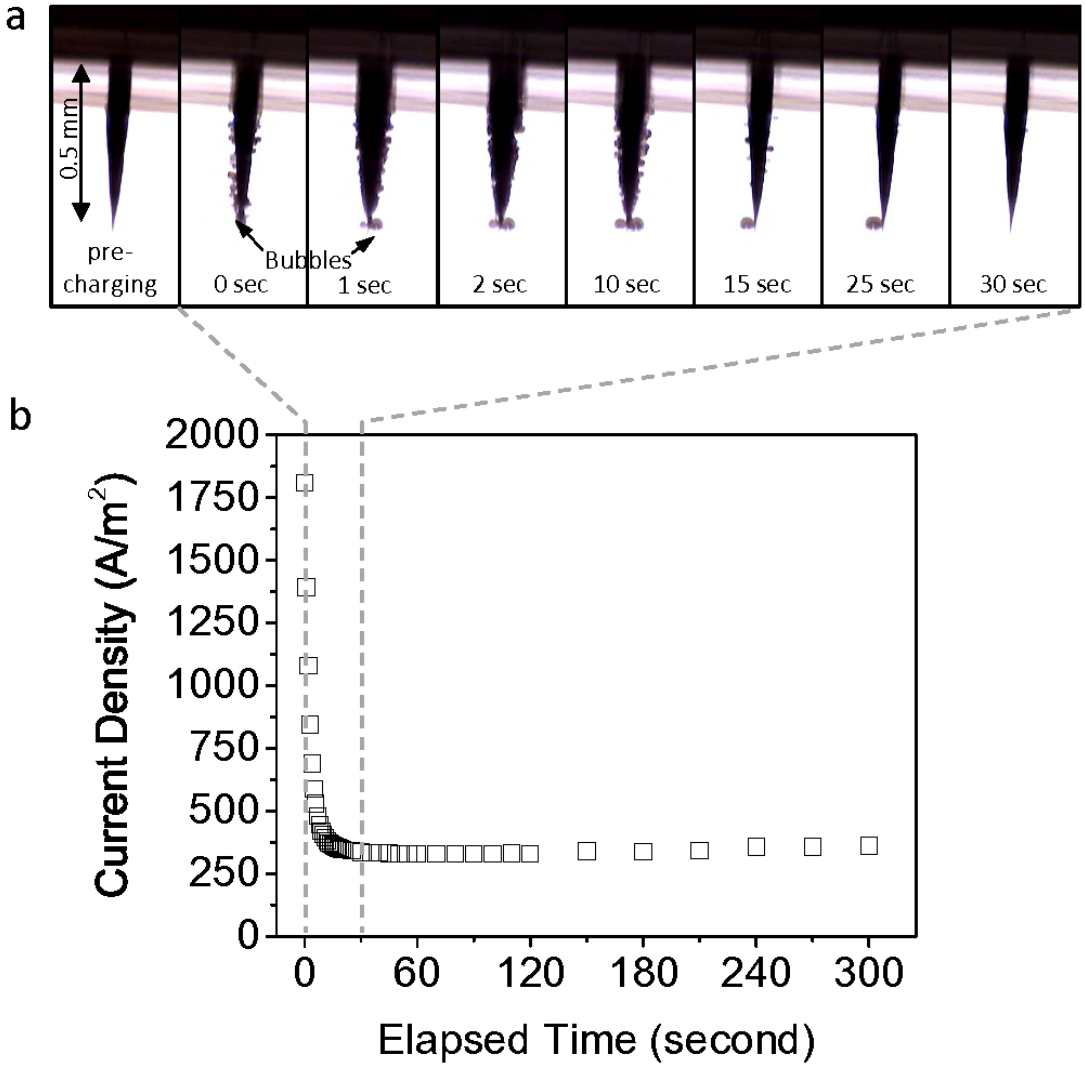

Figure 31 – (a) Recording of hydrogen charging as time elapsed. Significant bubbles were observed immediately after switching on and then disappeared gradually after 30 second of charging. (b) The current density obtained from the measured current the estimated tip dimension as a function of the elapsed time in charging experiment.

3.3.1 TEM observation of liquid-charging effect

To investigate the effect of charging-induced corrosion on needle samples, a 200keV TEM (JEOL JEM-2100 with LaB_6 gun) was used to observe pre- and post-charging samples. Operation of the TEM was assisted by Dr. Andrew London. After electro-polishing preparation of APT needle samples described in Section 3.2.3, TEM samples were further thinned by the second stage electropolishing as described in Section 3.2.3 from APT samples. This took place until all samples were less than 1 mm in diameter in order to reduce the magnetic field effects during TEM operation. The samples were mounted into 1 mm brass tubes and then loaded into a TEM tomographic holder (Fischione 2050) as shown in Figure 32(a). This holder has a sample shield shown in Figure 32(b) allowing the needle sample to be withdrawn for protection during transfers.

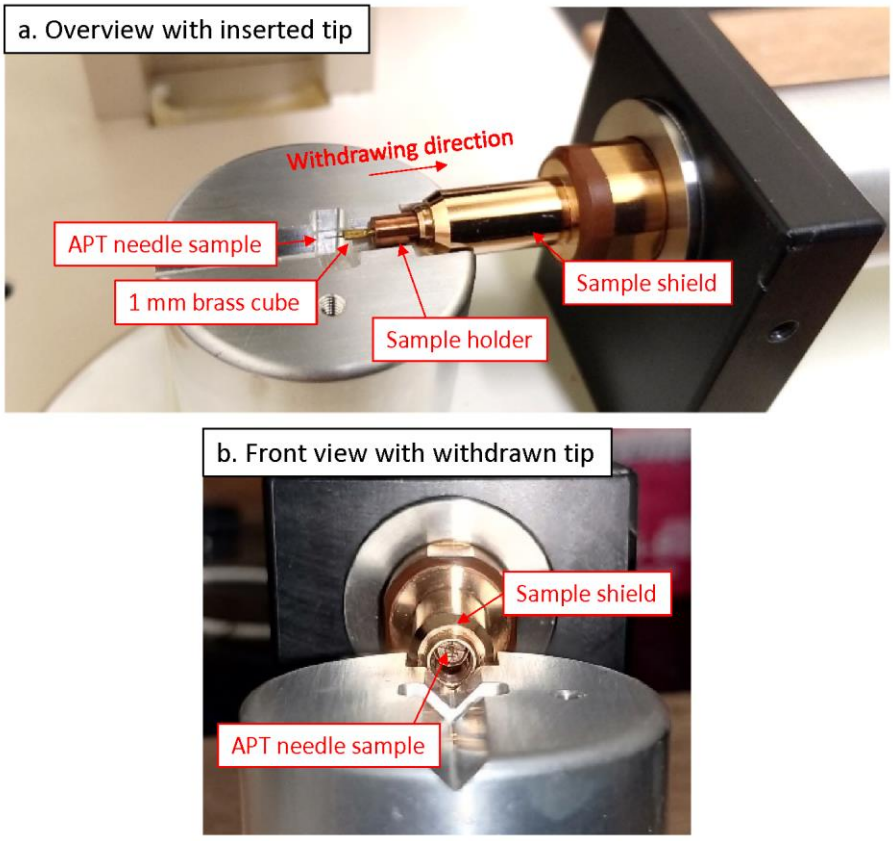

Figure 32 - APT sample was loaded to a TEM tomographic holder (a) in inserted mode and (b) in withdrawn mode

TEM operation requires ultra-sharp needle samples (less than 100 nm in diameter) to allow the electron beam to transmit through the tip under observation. After standard alignment, the tips were observed in bright field which required some rotation with the sample stage of JEM-2100 to identify the precipitates clearly. After rotation angles were marked, the samples were removed for the hydrogen-charging process (Section 3.3) for 5 minutes, and subsequently returned to TEM to conduct post-charging observation at the same angle.

3.4 Vacuum Cryo-Transfer

As discussed in Section 2.2.4.3, to retain the charged hydrogen in traps before APT analysis, Vacuum Cryo-Transfer (VCT) cold-chain at ETH Zürich was adapted in some experiments to the sample loading process in LEAP 4000X HR [222]. The VCT process consists of sample cooling and transferring procedures which are shown schematically in Figure 33 accompanied with photos of the critical auxiliaries in Figure 34. After the liquid charging and sample-puck loading procedure was carried out as described in Section 3.3 (steps A and B in Figure 33), the puck was loaded into a commercial Leica VCT-100 shuttle (step C). Next the VCT shuttle was attached to the docking port of a commercial Baltec 'BAF' sample-cooling chamber (step D) as shown in Figure 34(a) in order to rapidly evacuate the VCT shuttle chamber. The sample then was cooled inside the BAF on a cryogenic stage at -174°C (100 K) connecting to a flowing LN_2 as well as a heater to allow fine temperature control as shown in Figure 34(b). After 20 minutes of stabilisation, the sample was removed from the cooling stage using the VCT custom thermally-insulated arm shown in Figure 34(b). The VCT shuttle was then detached and connected to the docking port of the modified LEAP4000X HR as shown in Figure 34(d) (step E).

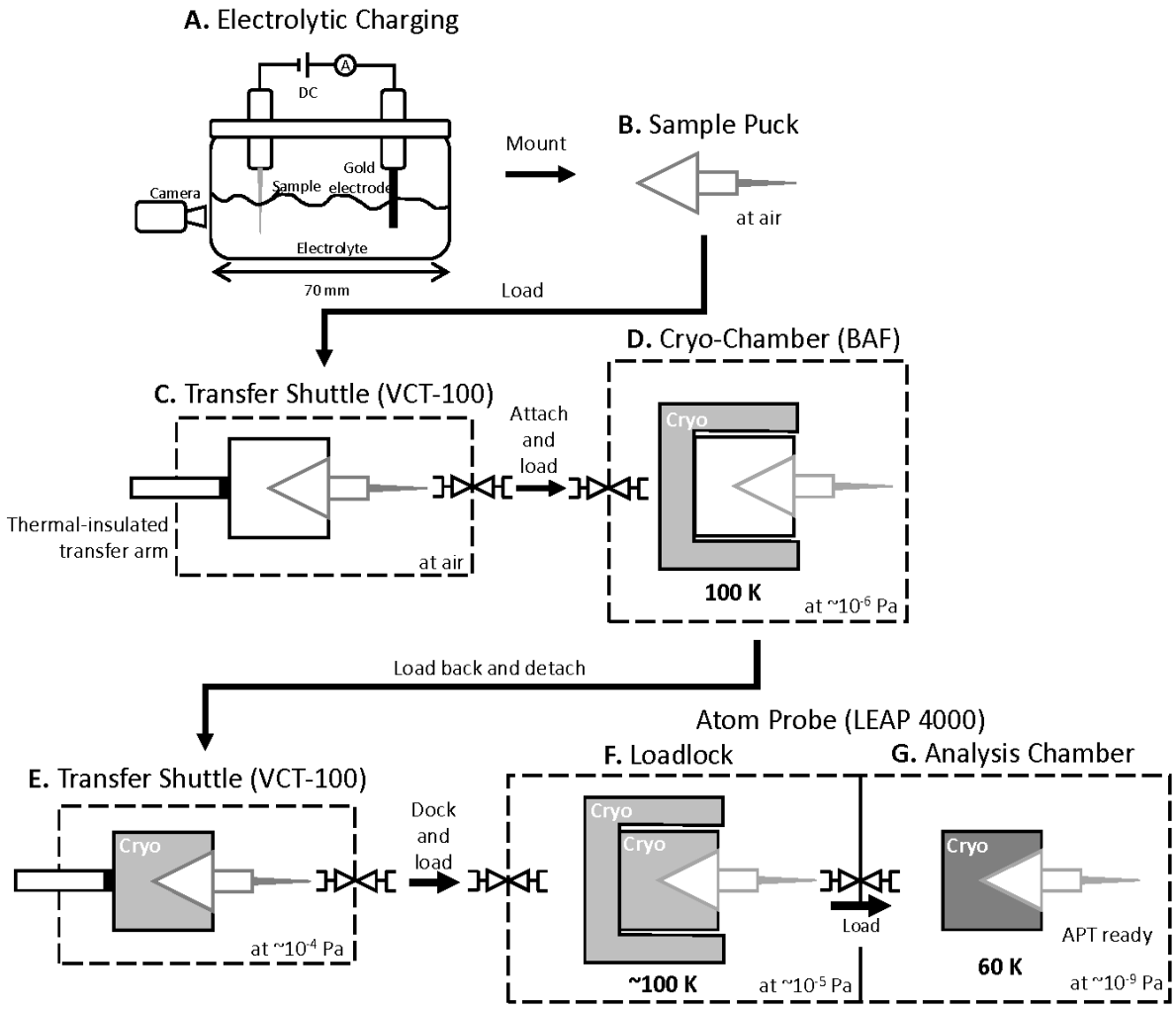

Figure 33 – Experimental procedure of vacuum cryo-transfer (VCT) with the uses of a cryo-chamber, transfer shuttle, and a docking system in a modified LEAP 4000

During the stabilisation, a custom cryo-finger pre-cools a custom cryo-carousel in the modified loadlock of the LEAP4000X HR for later carriage of the cryo-sample as shown in Figure 34(c). This figure also shows the cold trap connecting the docking port and the loadlock, which limits ingress of any contaminants from the VCT shuttle into the LEAP vacuum system. The cryo-sample puck then was loaded into the atom probe loadlock where a pre-cooled cryo-carousel was able to retain the cryogenic state of sample until the loading into the buffer chamber (step F). Finally, the sample was loaded to the LEAP sample stage at 60K in the analysis chamber to conduct the APT experiment (step G).

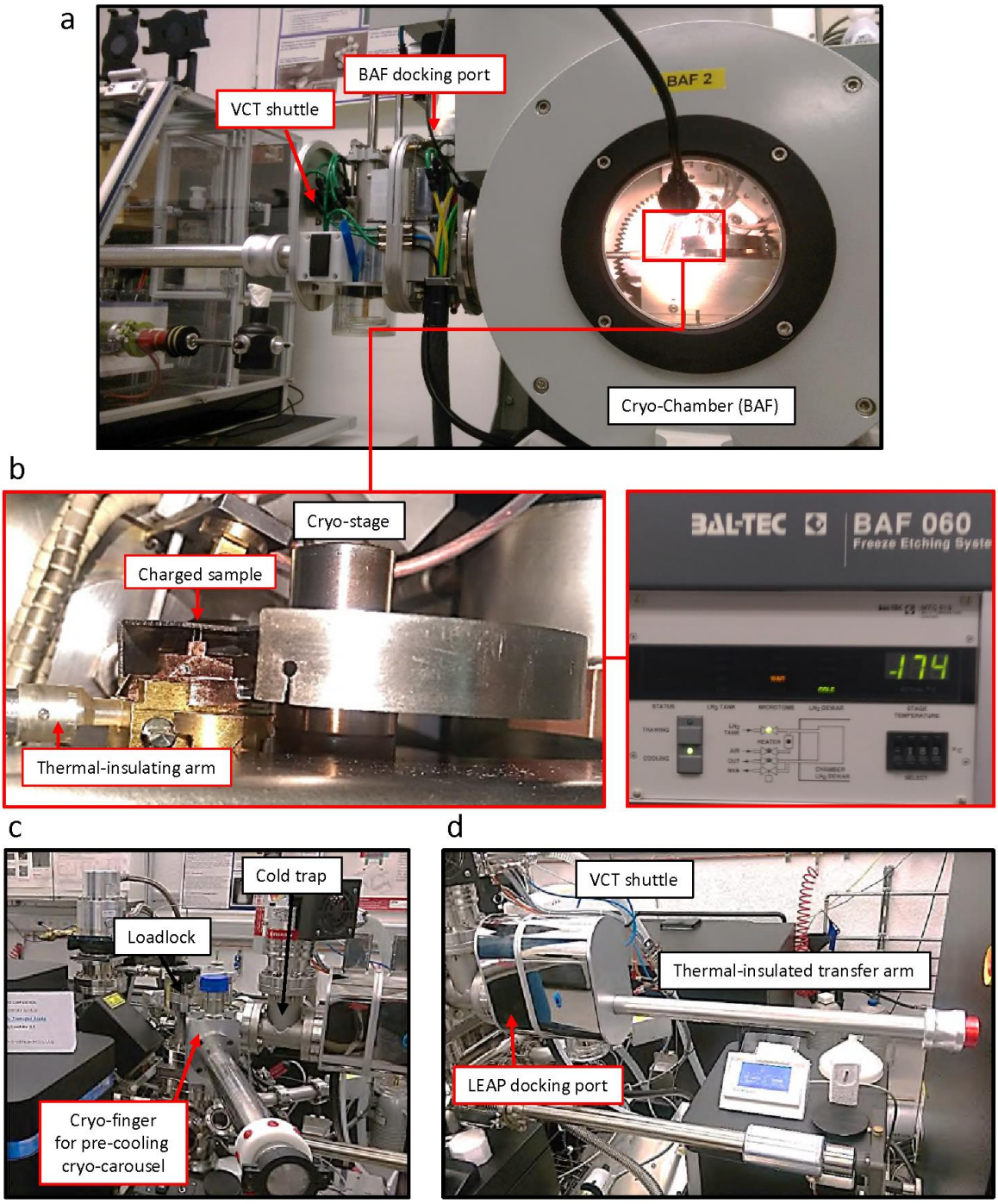

Figure 34 – Pictures of VCT apparatus at ETH Zürich, (a) VCT shuttle docking at cryo-chamber, (b) cooling stage with a sample puck with charged sample and the temperature control panel, (c) the modified loadlock equipped with a cryo-finger, (d) VCT shuttle docking at the port of the modified LEAP4000X HR

3.5 Simplifying the cryo-transfer method

3.5.1 Core concepts

As an alternative to cooling the sample using in an additional vacuum chamber stage as described in Section 3.4, the cooling procedure can in principle be simplified to immersing the charged samples in a LN_2 tank after the liquid charging. However, this approach has the problem that when removing cryogenic objects from LN_2 into an ambient environment, the environmental moisture rapidly condenses on their surface forming significant ice contamination. Limiting this contamination is crucial to atom probe needle samples given their stringent requirement in sharpness (Section 3.2.1.1). This ice formation can be as quick as 23 µm per second [223], which implies the acceleration of the transfer for avoiding ice formation is impractical, namely this ice contamination is nearly inevitable in normal operation of transferring cryogenic sample. An ice-removing strategy is therefore required to enable atom probe experiment.

According to the water phase diagram shown in Figure 35(a), the sublimation of the ice at cryogenic temperature (freeze-drying) can be conducted with sufficiently small amount of heating (shown by the blue arrow) that still allows the sample to remain in a cryogenic state. Given that an atom probe instrument comprises multiple vacuum chambers (Section 3.2.2), this freeze-drying for removing ice contamination can be conducted in one of these chambers and integrated into the sample-loading process. If this heating for sublimation is sufficiently minor with respect to that required for hydrogen detrapping, then trapped hydrogen should still be able to be observed in the APT analysis. The conditions for the freeze-drying process are indicated by the blue arrows of Figure 35(b) alongside reference data of water vapour pressure in UHV environment [224]. This graph allows the initial sublimation temperature ($T_{sublimation}$) at the atom-probe chamber vacuum pressure to be

estimated, in this case about 150 K. The blue dotted arrow in Figure 35(b) also shows the expected pressure increase during the freeze-drying process. When the ice is mostly removed, the pressure in the continuously pumping chamber is thus expected to decrease and reveal the end of the freeze-drying process. This process can be continuously monitored in the LEAP 3000X HR chambers which are all equipped with fast-response cold cathode gauges.

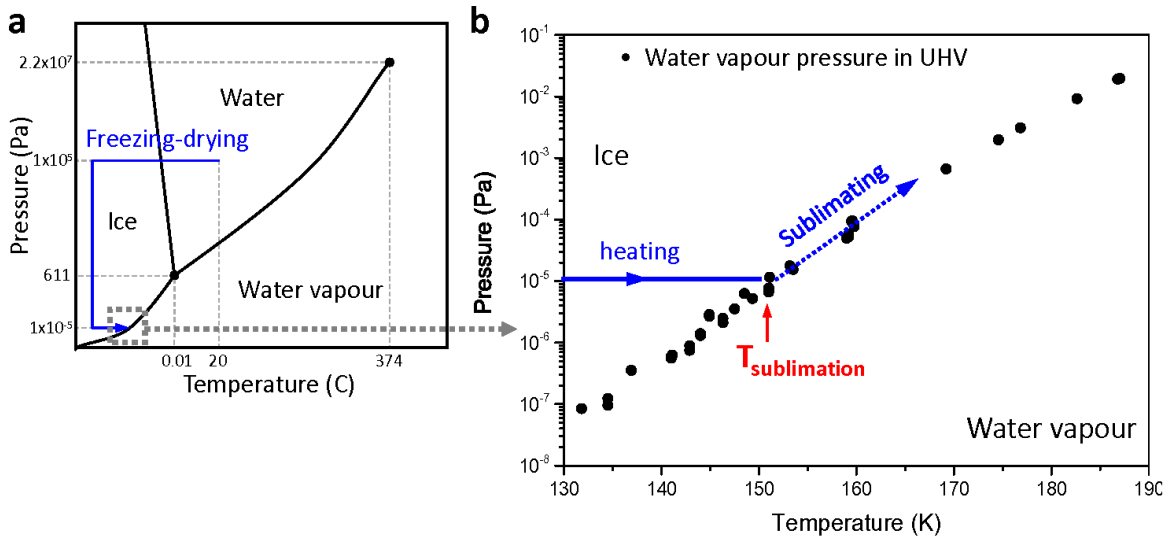

Figure 35 - (a) Water phase diagram with a schematic of freeze-drying procedure. (b) Water vapour pressure at high-vacuum pressure and cryogenic temperature reported in [224], and a sketch of sublimation process performed in this study.

Since the hydrogen detrapping correlates to the thermal state of the sample [138], it is crucial to understand the evolution of the sample temperature after the freeze-drying process. In order to minimise the instrumental requirement in this study as opposed to others requiring modified atom probe systems [178, 199, 222], two methods for temperature measurement without using any additional equipment are proposed in Section 3.5.4. Finally, a method to reduce the amount of ice contamination is also described in Section 3.5.5.

3.5.2 LN_2 immersion and Air Cryo-Transfer

The method directly removing the sample from the LN_2 immersion is referred as Air Cryo-Transfer (ACT) in this study, and a schematic of this concept is shown in Figure 36(a). The critical components incorporated in the ACT include the custom cryo-puck, cryo-block, and block-hat. In order to minimise the heat introduced from the room-temperature transfer arm in the transfer process at the buffer chamber, the external-contact element of a normal specimen puck was replaced with a thermally-insulated counterpart as shown in Figure 36(b). This cryo-puck is an alternative solution to the thermal-insulating transfer arm of the VCT apparatus (shown in Figure 34(b)). The cryo-block shown in Figure 36(c) is a normal LEAP carousel (Figure 18(b) in Section 3.2.4) combined with a custom aluminium piece for increasing the entire thermal mass and hence prolonging the time in cryogenic state. The cryo-block pairs with a block-hat also shown in Figure 36(c), which minimises contact with environmental moisture as the cryo-block is removed from the LN_2. The combined cryo-block and block-hat shown in Figure 36(d) has two thread screws to allow lifting the block-hat alone or the entire assembly. As the assembly is moved into the loadlock, the design of the thermal insulators shown in Figure 36(e) at the bottom of cryo-block allows minimum amount of heat transfer from the LEAP 3000X HR.

In the ACT procedure, first the cryo-block and block hat are pre-cooled in LN_2. Then the cryo-puck holding the hydrogen-charged sample (charging details as Section 3.3) is immersed into LN_2 within 2 minute which is required to load the charged sample into APT puck holder. Next the puck is loaded into the cryo-block using tweezers, and subsequently the cryo-block assembly is combined in LN_2. The cryo-bock assembly is removed from LN_2 after 10 minute and transferred to the LEAP loadlock. Finally, the block-hat is removed immediately and the loadlock is evacuated.

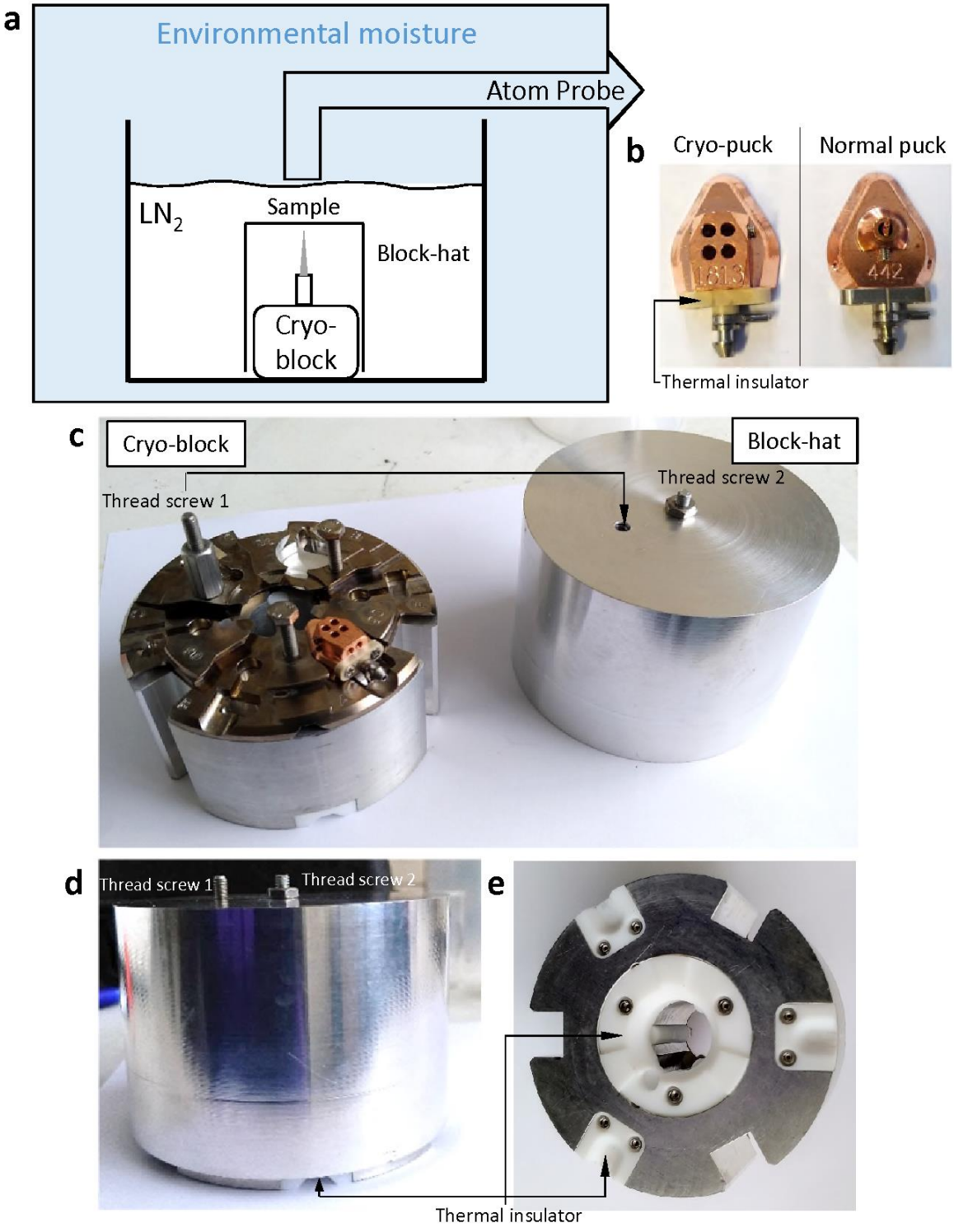

Figure 36 – (a) The configuration of plunge freezing, and ACT method used in this study. The required accessories, (b) cryo-puck and (c) cryo-block, in this method. (d) The combined cryo-block and block-hat, and the thread screw to facilitate the loading and removal process. (e) The thermal-insulating parts at the bottom of the cryo-block to minimise the sample being heated up by the loadlock at room temperature. Courtesy of Dr. David Larson, CAMECA.Inc

3.5.3 Sublimating ice contamination

Once the loadlock pressure reached 10^{-5} Pa, the cryo-puck with the charged sample was moved to the buffer chamber and immediately to the sample stage in the analysis chamber. At this point, the post-cooling state of the specimen can be observed using the built-in optical camera in the LEAP used for aligning the tips with the local electrode. As shown in Figure 37(a), the ACT sample was typically covered with significant amount of ice. When this occurred, the sample puck was removed from the sample stage at 60 K and transferred back to the buffer chamber for the freeze-drying cleaning described in Section 3.5.1. The pressure log of two typical cleanings are shown in Figure 37(b), where the pressure increase corresponding to the beginning of the sublimation and the decrease of the pressure corresponding to the stage that the ice contaminant was mostly consumed and was no longer able to supply sufficient water vapour for continuous increase of pressure. Finally, the recovery of pressure meaning the ice contaminant has been fully removed. The consistency of the trials in respect to the required sublimation time is also shown in the figure. This consistency is attributed to the nearly unchangeable heat transfer from the transfer arm at room temperature of the buffer chamber via the passive thermal insulator of the cryo-puck as shown in the first photo in Figure 37(c). In addition to the pressure changes, the sublimation process can also be observed directly via the view port of the buffer chamber. As shown in Figure 37(c), the progress of ice contamination removal (white coverage in the figure) was clear with elapsed time. Once the cleaning was complete, the samples were reloaded to the sample stage at 60 K in the analysis chamber.

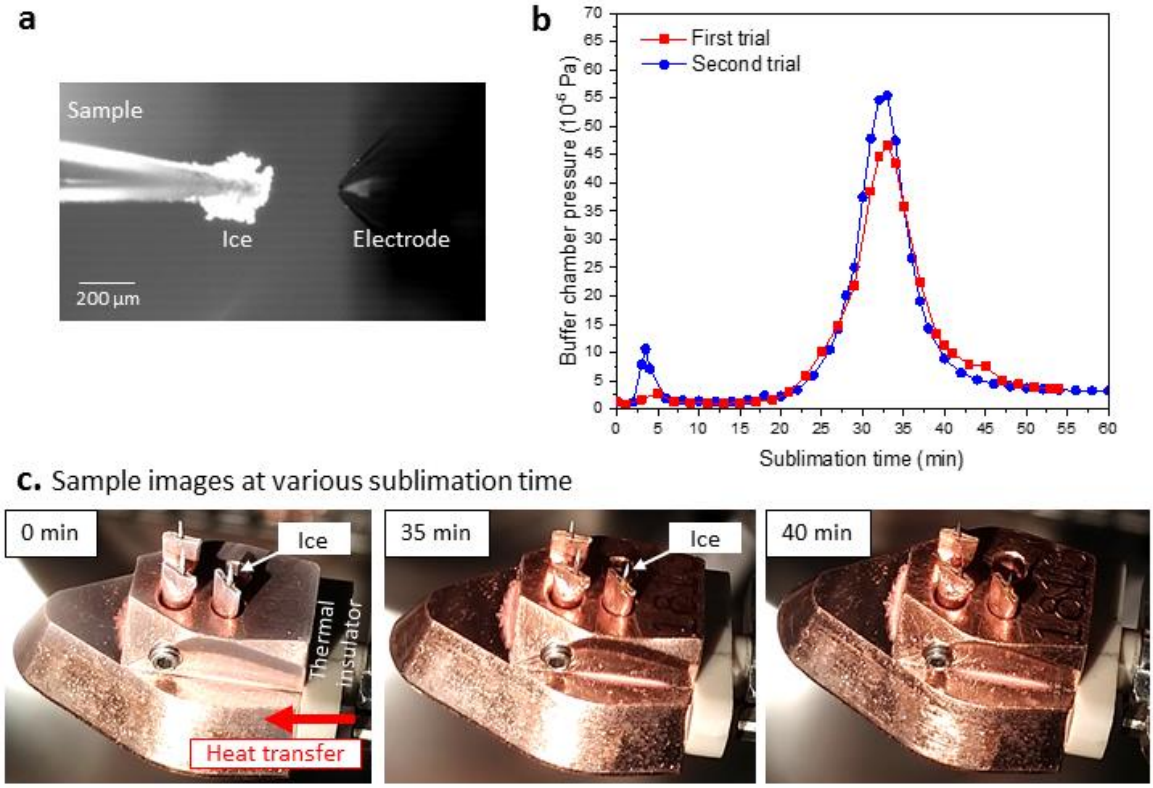

Figure 37 – (a) An ice-contaminated tip not able to conduct APT experiment. (b) The pressure logs of sublimation cleaning of two ice-contaminated samples in the buffer chamber, which shows the starts and ends of the cleaning process. (c) Photo of a cryo-puck being held by the transfer arm in buffer chamber, which obtains heat from the arm via a Teflon piece.

At this point in the process, the full thermal history of the cryo-transfer samples can be plotted as in Figure 38. The steps represented in this figure are: After hydrogen charging and being loaded to the cryo-puck (step A and B), the samples were moved into LN_2 at 77 K (step C). Then the samples left the LN_2 to the LEAP loadlock for approximate 20 minutes of vacuum transfer (step D) and was passively heated to a certain temperature ($T_{as\text{-}loaded}$) during the evacuation. Subsequently, the sample arrived the sample stage at 60 K in the analysis chamber (step E). After being moved back to the buffer chamber for the sublimation process (step F) for 40 minutes and reaching a peak temperature, the sample returned to the LEAP sample stage at 60 K. The critical stage affecting the hydrogen trapping was assumed to be the heating step F which is further investigated in the following section for the quantification of this heating process.

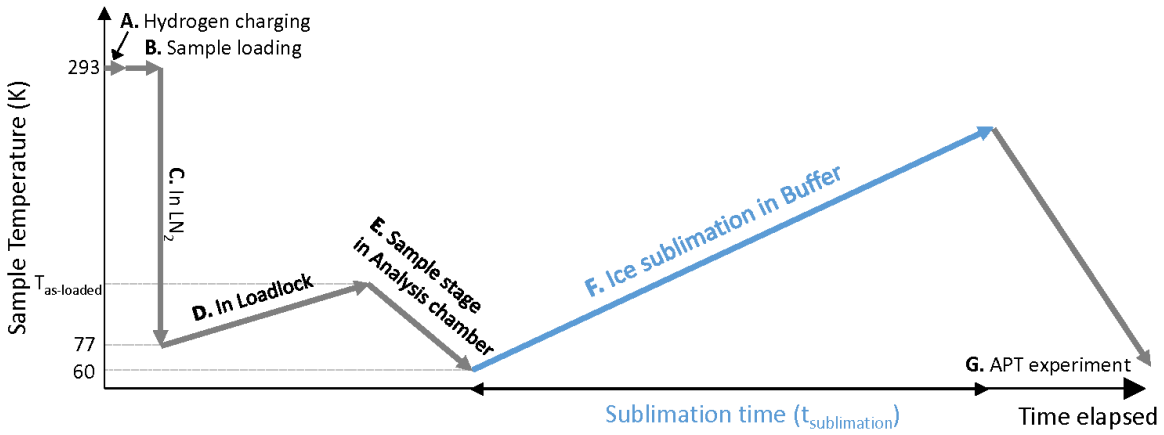

Figure 38 – The thermal history of the sample in the simplified cryo-transfer experiment.

3.5.4 Determining the temperature of the sublimated sample

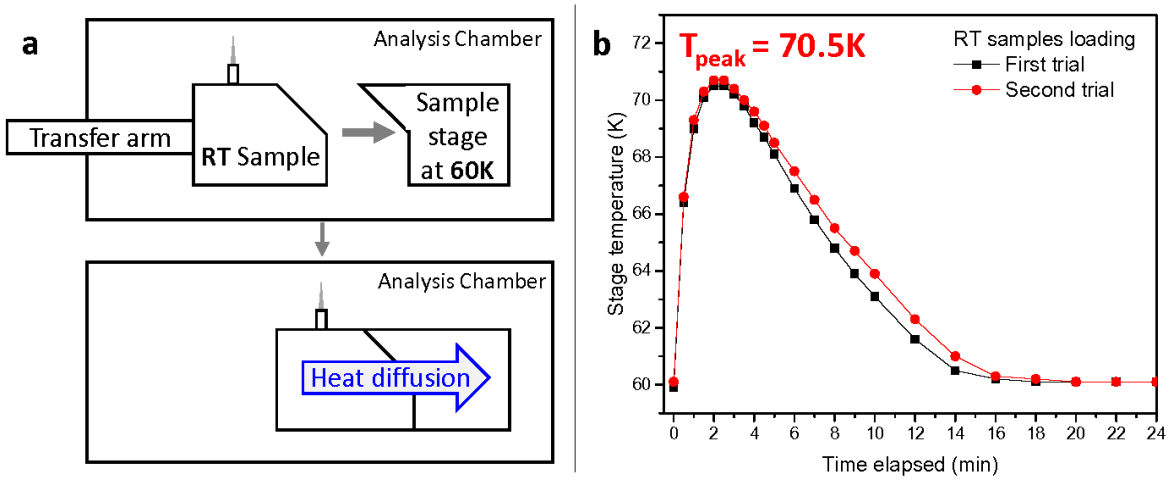

Figure 39 – (a) Schematics of the heat diffusion regime in APT sample loading process. (b) The measured peak temperature in two room temperature sample loading processes.

As shown in Figure 39(a), given that the loading of the sample at any temperature to the sample stage of analysis chamber at a fixed temperature follows the same mechanism of heat diffusion, the sample temperature can be estimated by the linear thermal response of the stage temperature. The instantaneous measurement of the stage temperature is provided by the LEAP built-in thermal couple to the stage [225, 226]. In Figure 39(b), two independent trials of room temperature sample loadings to the stage at 60 K (T_{stage}) show

consistent thermal responses with the same stage peak temperatures at 70.5 K. This peak temperature (T_{peak}) can be linearly correlated to the initial temperature of the sample. The relationship can be defined in eq(11):

$$T_{sample} - T_{peak} = R\,(T_{peak} - T_{stage}) \tag{11}$$

where T_{sample} and R are the loaded sample temperature and the heat transfer coefficient, respectively. With the measurements of room temperature sample loading (T_{peak} = 70.5 K and T_{sample} = 293 K) illustrated as Figure 40(a), R was determined as 21.19 which then allows the calculation for other unknown T_{sample} (Figure 40(b)).

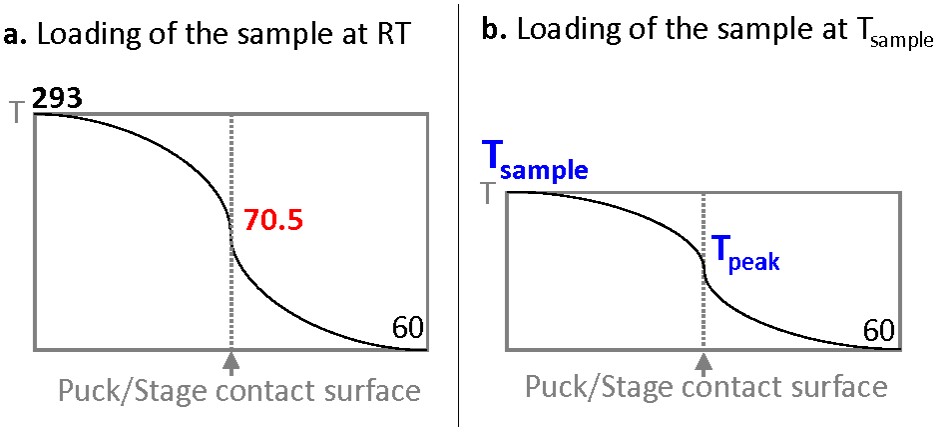

Figure 40 – Sketches of the heat diffusion of Figure 39(a) in (a) the room temperature sample loading and (b) a loading of sample at a certain temperature (T_{sample}) with a measured peak temperature (T_{peak})

An alternative method to using the linear thermal response of the stage is to measure the pressure of the buffer chamber during the sublimation process, as this can also be correlated to the sublimated sample temperature. As shown in Figure 41(a), the data in the highlighted region corresponding to the pressure of early sublimation can be correlated to data in the literature corresponding to water vapour pressure as a function of temperature, which is shown in the highlighted region in Figure 41(b). This gives the corresponding temperature range of the sublimation process as highlighted on the temperature axis [224]. With the

known sublimation times and measured temperatures from both methods, the heating rates in the buffer chamber can be obtained and compared so as to estimate the sample temperature for any specific sublimation time.

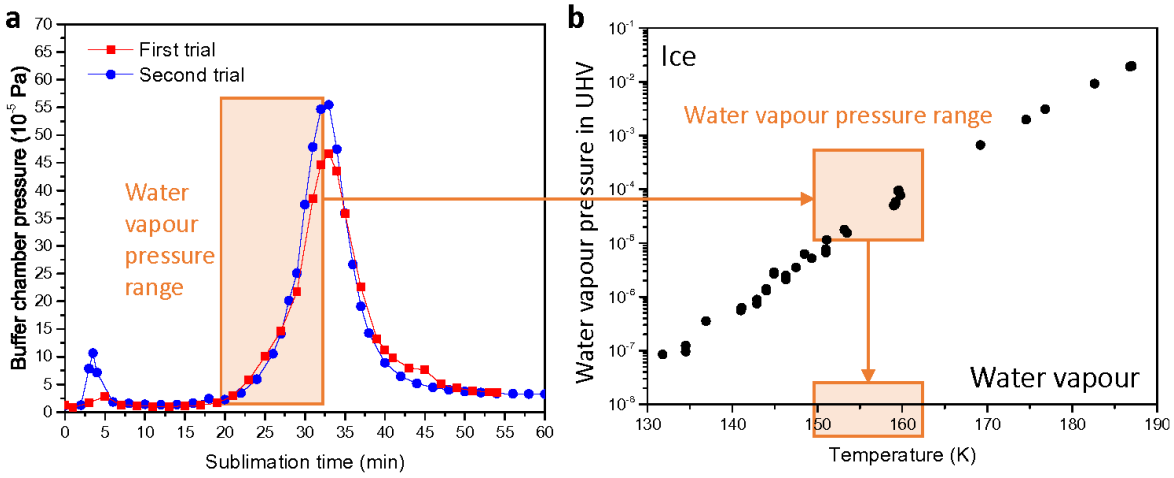

Figure 41 – (a) The pressure measured in the buffer chamber can be correlated to (b) the water vapour pressure measured in the literature [224], which allows the temperature range of sublimation to be extracted.

3.5.5 Dry Cryo-Transfer

As illustrated in Figure 42(a), the Dry Cryo-Transfer (DCT) method uses a custom-made glove box, which is directly connected to the LEAP 3000X HR loadlock. The sample can be manipulated inside the glove box, to isolate the surrounding of the LN_2 tank carrying the cryogenic block assembly and thus limit moisture exposure when removing it from the LN_2. With the presence of LN_2 in the box, the moisture should progressively condense at the LN_2 surface [223], hence reducing the humidity in the box. In particular, the use of the block-hat allows minimum contact with the condensed moisture shown in Figure 42(a), therefore the ice contamination should be significantly reduced in comparison to the ACT method. Accordingly, the reduced ice contamination should require a shorter sublimation period as described in Section 3.5.3, which corresponds to lower final sample temperature compared to the ACT method.

In practice, the DCT was conducted in a 400 mm^3 acrylic box made by 5-mm thick sheets with one side connected to the loadlock by a 500-liter plastic bag plastic bag with a glove as shown in Figure 42(b). A hygrometer (RH318, Omega) was placed in the box to allow instantaneous monitoring of the progressive reduction of humidity due to the condensation. All connections were sealed by tape, and the sealed box had a vent port in case the space was over-pressurised by the vaporised nitrogen. 800g silica gel was placed in the box to reduce the moisture content. Detailed DCT procedure is described in Appendix.

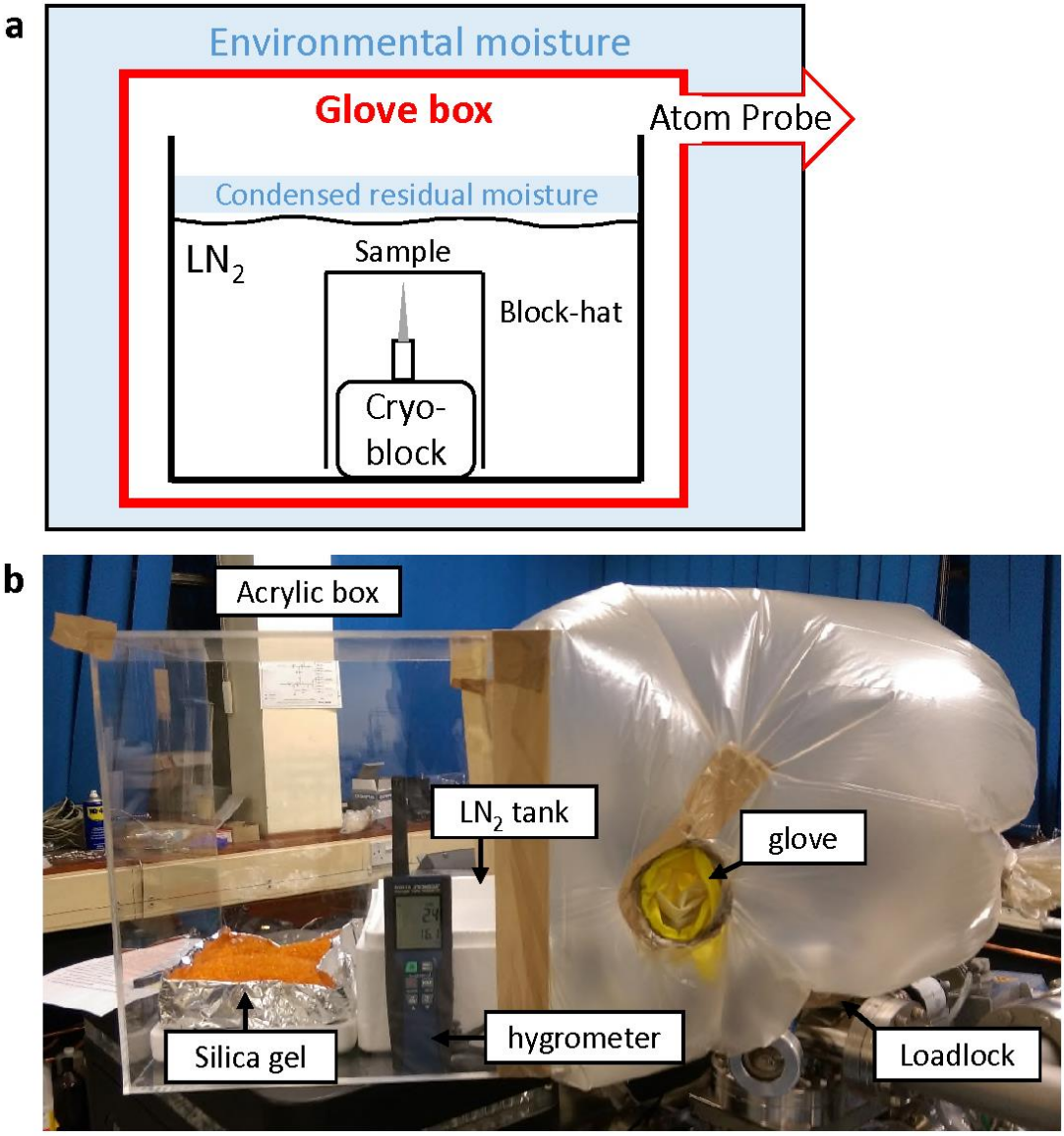

Figure 42 – (a) The configuration of dry cryo-transfer (DCT) which has a glove box for limiting the supply of environmental moisture in addition to ACT. (b) The picture of DCT configuration.

Lastly, to confirm the moisture condensation at the LN_2 surface, the humidity measurements at the vicinities of the LN_2 surfaces for both cases of open and isolated environments were conducted and sketched as Figure 43(a) and (b), respectively.

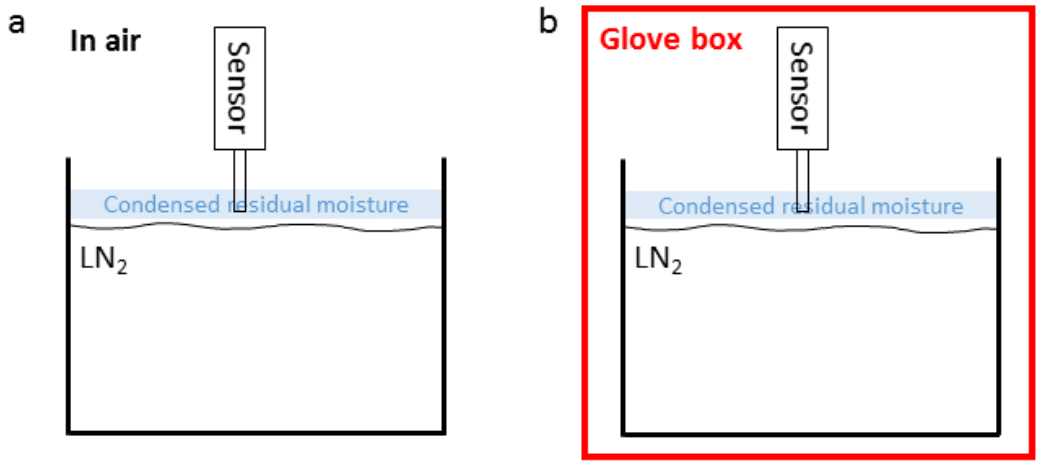

Figure 43 - Schematics of humidity measurement (a) in air and (b) in an isolated box

4. Atom Probe Tomography Characterisation

4.1 Measured Composition

Given that APT is underpinned by the principle of detecting the respective chemical identities of individual atoms (Sections 3.2.1.1 and 3.2.1.2), the technique should be well-suited to the measurement of chemical composition of the material (Section 3.1) to compare with nominal bulk content. Accordingly, the as-received sample was analysed in the LEAP 3000X HR (corresponding to datafile R14_25949) under standard sample-loading procedure (Section 3.2.4) and using instrumental parameters calibrated against the nominal apparent content (Section 3.2.5).

After the data was collected, mass spectrum peak-labelling, background correction, and decomposition of complex-ions were carried out as described in Section 3.2.6. The measured content of as-received sample is shown in Table 4. Notably, the carbon content in this table considered the decomposition of carbon species using the method of Takahashi et al. which accounts for the relative contribution of C_2^+ and C_4^{2+} at the overlapping 24 Da peak based on their isotopic peaks at 25 Da ($^{12}C^{13}C^+$) and 24.5 Da ($^{12}C_3{}^{13}C^{2+}$), respectively [193]. As shown in Section 3.2.6, artefact hydrogen peak (see Section 2.2.4.1 for details) was also detected between 1.004 and 1.011 Da, however this has not been included in the composition measurement. The obtained result is in good agreement with the nominal composition in Table 3 with the exception of P and Cr, which could be the result of contamination picked up during manufacturing process. There is also a 12% deficit of Mn which could be due to its segregation elsewhere in the microstructure, out with the field of view of the analysis. The Mn segregation can instead be verified by using other techniques such as SEM/EDS having relatively larger field-of-view.

Mn	Mo	V	Nb	C	Al	Si	N	O	P	Cr	Fe
1.396	0.317	0.300	0.034	0.459	0.116	0.059	0.03	0.005	0.019	0.016	Bal.

Table 4 – Composition of uncharged sample in atomic percent

As stated in Section 2.2.2.2, the carbide composition correlates with the structural identity of carbide and hence is intrinsically associated to hydrogen-trapping behaviour of the carbide [103, 104]. So quantitatively determining the carbide composition is what more critical than measuring apparent content in this study. Despite the described efforts to carefully calibrate atom probe instrumental parameters for the analysis (Section 3.2.5), in fact one can question that whether this calibration is as applicable when considering local carbide composition. The carbides contain far higher carbon contents than the matrix, and evaporated carbon ions are known to be more susceptible to ion-pile-up-induced signal loss at the detector (Section 2.2.4.2), leading to larger standard deviations on compositional measurements. For best accuracy of carbide composition measurement, one could investigate the local ion pile-up effects by extracting only the carbide region to generate reconstruction and then re-calibrate the instrumental parameters with respect to its content, as previously demonstrated by Takahashi et al. and Thuvander et al. [193, 194]. However, the fine scale of the carbides in the present study (~10 nm) limits the applicability of these methods of utilising focused-ion-beam (FIB) preparation to lift out specific carbide features. Indeed, one could chemically remove the matrix for extracting carbide particles and then measure the apparent content of the remaining carbide particles using inductively coupled plasma technique (ICP) [227]. However, this has not been attempted within the limited timescale of this study which primarily focuses on the development of experimental technique for mapping hydrogen via APT.

Alternatively, in the analysis of the APT data, if one can isolate and extract the multiple hit events (Section 2.2.4.2) localised on the detector due to the nanoscale carbides and then

quantify the local loss of carbon signal, then a more precise quantification of carbide composition should be achievable. However, this extraction of local event multiplicity is not available in the commercial IVAS and requires the development of a custom programme. Furthermore, the extent of the carbon signal loss due to ion pile-up is not only related to the applied instrumental factors but also the type of carbides. This has been demonstrated by Thuvander et al. based on the inconsistent accuracy of carbon quantification in the measurements of various carbides [194]. Namely, when considering the effects of ion pile-up, one may ultimately have to consider more sophisticated factors such as inter-atomic bonding states between carbide solutes. This is still an ongoing research topic [170] and hence using atom probe to exactly quantify the carbide composition remains challenging. To this end, the highest deviation reported in the literature of measured carbide composition from the nominal stoichiometric composition, i.e. 20% deficit [194], is considered and used as the compensation to estimate the upper bound of carbon content.

4.2 Carbide composition

This section regards the extraction and content determination of the studied carbides in datafile R14_25949 of an as-received sample by two frequently used methods in atom probe measurement, i.e. isosurface and maximum separation (Sections 3.2.8.2 and 3.2.8.4).

4.2.1 Isosurface method

4.2.1.1 Randomised data

When investigating a distribution of solute clusters in an APT data set, increasing the isovalue with respect to solute concentration or density (Section 3.2.8.2) elevates the isosurface threshold and hence generally reduces the number of regions in the data meeting

this definition. Systematically increasing the isovalue applied to the random comparator system (Section 3.2.8.1) complementary to the studied data allows an inspection of the isovalue up to which randomly occurring clusters are no longer statistically likely to be detected. Hence this isovalue then can be utilised as the minimum threshold in the analysis of the real dataset to avoid the inclusion of these random clusters in the resulting statistics.

Figure 44 shows that the number of isosurfaces in the random comparator decreases with the increase of isovalue (in atomic percent) with isovalues starting from 0% and greater than 0.5 at.% of vanadium (a carbide solute element as shown in Section 3.1). The number of isosurfaces fully disappears by 2 at.%, and therefore this vanadium isovalue is determined as the minimum threshold value in the analysis of actual data to avoid false-positive isosurfaces. The smaller number of isosurfaces at isovalues below 0.5% is due to the joining up of smaller features to form larger ones, reducing the apparent number of isosurfaces.

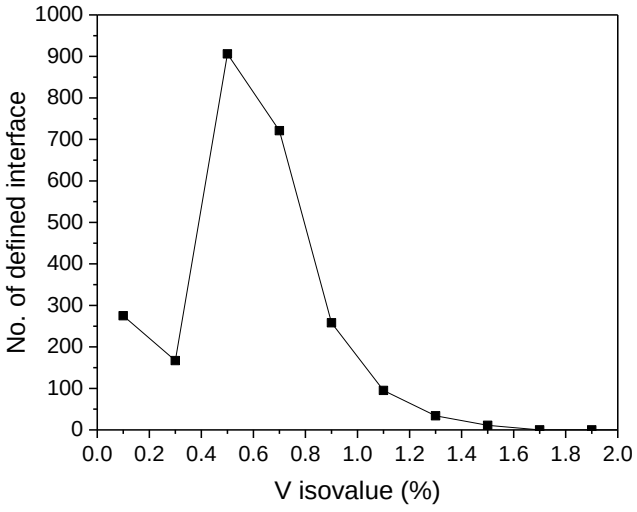

Figure 44 –The number of randomly occurring clusters as a function of isovalue of vanadium (at. %) in a randomised data. No isosurface can be defined at 2% onward which then is determined as the threshold of isovalue for avoiding artefact isosurface in following analysis.

4.2.1.2 Isovalue effect

In order to optimise the measurement of carbide compositions by means of the isosurface method, the influence of the choice of isovalue on the results must first be understood. With the application of a high isovalue, precipitates having relatively small sizes would not be certain to be considered as clusters. This is not necessarily because their content does not meet the isosurface definition but could be due to the effect of trajectory-aberration contributions from the matrix (Section 3.2.7.4) which dilutes their apparent contents. Overlooking these relatively small precipitates would affect the accuracy of carbide composition measurement in average, so applying a low isovalue to best account for these fine clusters is considered here.

As shown in Figure 45(a), when applying vanadium isovalues of 2%, 5%, and 10% to the atom probe reconstruction of the as-received sample data, the number of distinct (isosurface number) was reduced from 56 to 28 to 7, respectively. Proxigrams (Section 3.2.8.2) defined by these isosurfaces were then obtained as shown in Figure 45 where only vanadium (b) and iron (c) species are shown for clarity. On the positive side of the proxigrams of Figure 45(b) representing the carbide interior, the plateaus are not sufficiently clear to enable an obvious measurement of V content in the carbides (Section 3.2.8.2). In addition, Fe proxigrams in Figure 45(c) also do not show the expected iron-free zones based on the assumption that iron is not one of the elements incorporated by the carbides. Accordingly, matrix correction (Section 3.2.7.4) must be considered in this method. These results show the difficulty of using isosurface proxigrams to directly measure the content of these relatively small carbides. Furthermore, the 2% isosurface in Figure 45(a) was found to contain a joint surface erroneously connecting two carbides as highlighted in pink. This connection includes part of matrix and results in the sudden apparent increase in the Fe content in the interior of the carbide in Figure 45(c).

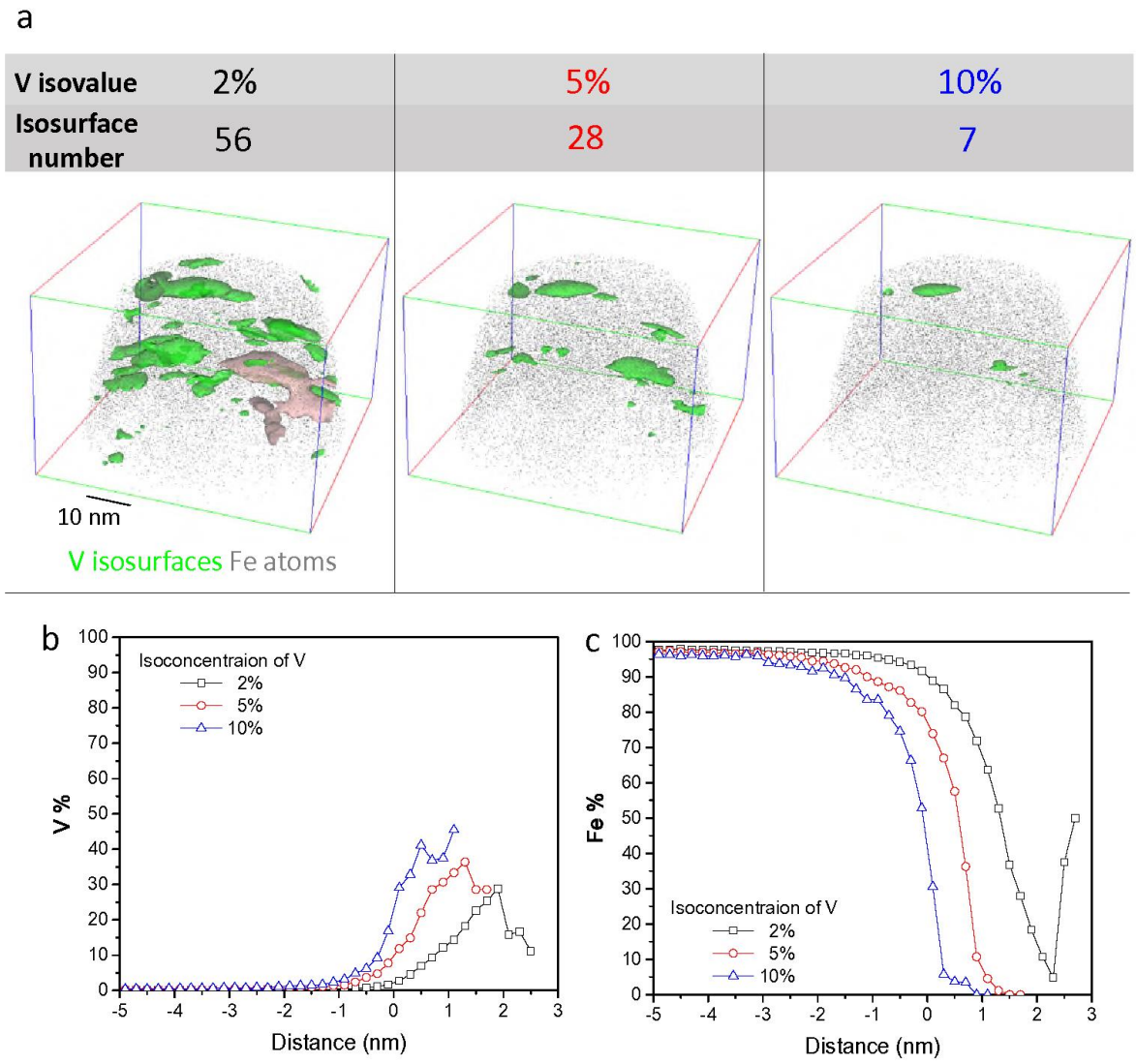

Figure 45 –(a) Numbers of defined isosurfaces with the application of 2%, 5%, and 10% V isovalue, respectively, visualised in green. A joint isosurface in the 2% data is highlighted in pink. (b) and (c) are the proxigrams of V and Fe, respectively, with the application of selected V isovalues using a 0.2 nm bin size.

The matrix content to be subtracted for the correction was determined by averaging the proxigram composition across the plateau area between -8 to -10 nm from the isosurfaces in the proxigrams. The corrected results are shown in Figure 46(a), where the plateaus observed in both 5 at.% and 10 at.% datasets in good agreement with each other. The 5 at.% dataset contains more distinct carbides than the 10 at.% data yet returns a similar plateau value, which suggests the 5% carbides do not have significantly different composition with the 10% carbides. The 2% dataset in Figure 46(a) again shows the effect

of the erroneously joined surfaces, corresponding to the drop of V content at the isosurface centre. However, before this point it reaches the same V content as 5% and 10% datasets. These results suggest that with the consideration of matrix correction, the carbide composition measurements can be consistent.

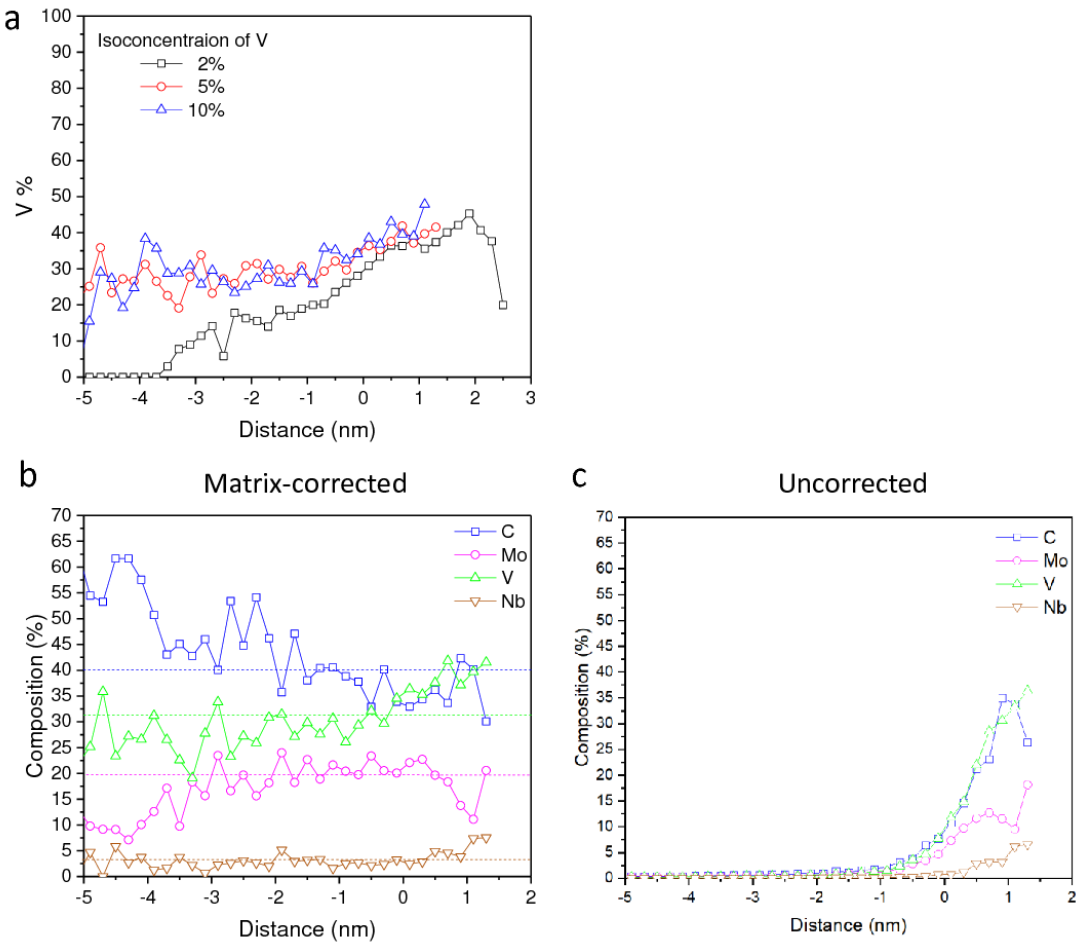

Figure 46 – (a) The V proxigrams averaged across all isosurfaces and applied with matrix correction for carbide defined by 2%, 5%, and 10% V isovalues, respectively, where an agreement between 5% and 10% data can be seen. (b) The matrix-corrected proxigrams of 5% V isovalue with all carbide solutes, where the carbide composition was determined in Table 5 by averaging the compositions between -3 and 1 nm in the proxigrams. (c) The uncorrected proxigrams of the data in (b), where the carbide composition was difficult to be determined.

In Figure 46(b), 5% dataset is shown as an example of the carbide composition measurement in isosurface method with the carbide elements determined in Section 3.1. The plateaus of the carbide-solute proxigrams were defined as -3 to +1 nm, and the solute contents in the carbides were obtained by averaging the compositions across this range. The

broken lines indicate the averaged compositions of the elements. In Figure 46(c), the uncorrected counterpart of Figure 46(b) is shown to present the difficulty for the determination of carbide content without identifiable plateau. The suspiciously high carbon concentration before -3 nm in Figure 46(b) might be a result of over-correction of the matrix-contamination; however, this issue is difficult to examine without other complementary analysis which is beyond the scope of this study.

4.2.1.3 Voxel-size effect

Apart from the chosen isovalue, the isosurface voxel size may also have an influence on the accuracy of carbide composition measurement (Section 3.2.8.2). This study incorporates two voxel sizes, 1 and 2 nm, which thus correspond to the difference of 2 and 8 times, respectively, in the spatial resolution of voxelised data and the atomic statistics per voxel. The previous section has shown results with the application of a 1 nm voxel. In this section, the V isovalues same as 1 nm voxel analysis are applied (i.e. 2% 5%, and 10%). As shown in Figure 47(a), the 2 nm analyses behave similarly to those from the 1 nm dataset in terms of numbers of isosurfaces decreasing with increasing the isovalue. The previously observed joint isosurface is also seen in the 2 at.% data (in pink). The proxigrams of the 5 at.% isosurfaces from the two voxelisations are compared in Figure 47(b) and (c), showing however insignificant differences. After applying the matrix correction in the same manner as the 1 nm analysis, the carbide composition was determined.

The carbide compositions from 1 and 2 nm voxel sizes are summarised in Table 5. The reported metal-to-carbon ratio is based on the assumption regarding V, Mo, and Nb as substitution atoms with respect to each other [141], which can be associated to the structure of carbide as discussed in Section 2.2.2.2. The difference between the obtained elemental concentrations comparing the two voxelisations is limited. Furthermore, their respective M/C ratios are 1.34 and 1.5 for 1 and 2 nm datasets which both suggest an FCC structure

(Section 2.2.2.2). In addition, taking 20% carbon deficit into account (Section 2.2.4.2), the M/C ratios become 1.13 and 1.25, corresponding to either MC or M_4C_3 type, respectively suggesting an FCC structure, so the change of voxel size does not affect the answer to the overarching question pursued in this section.

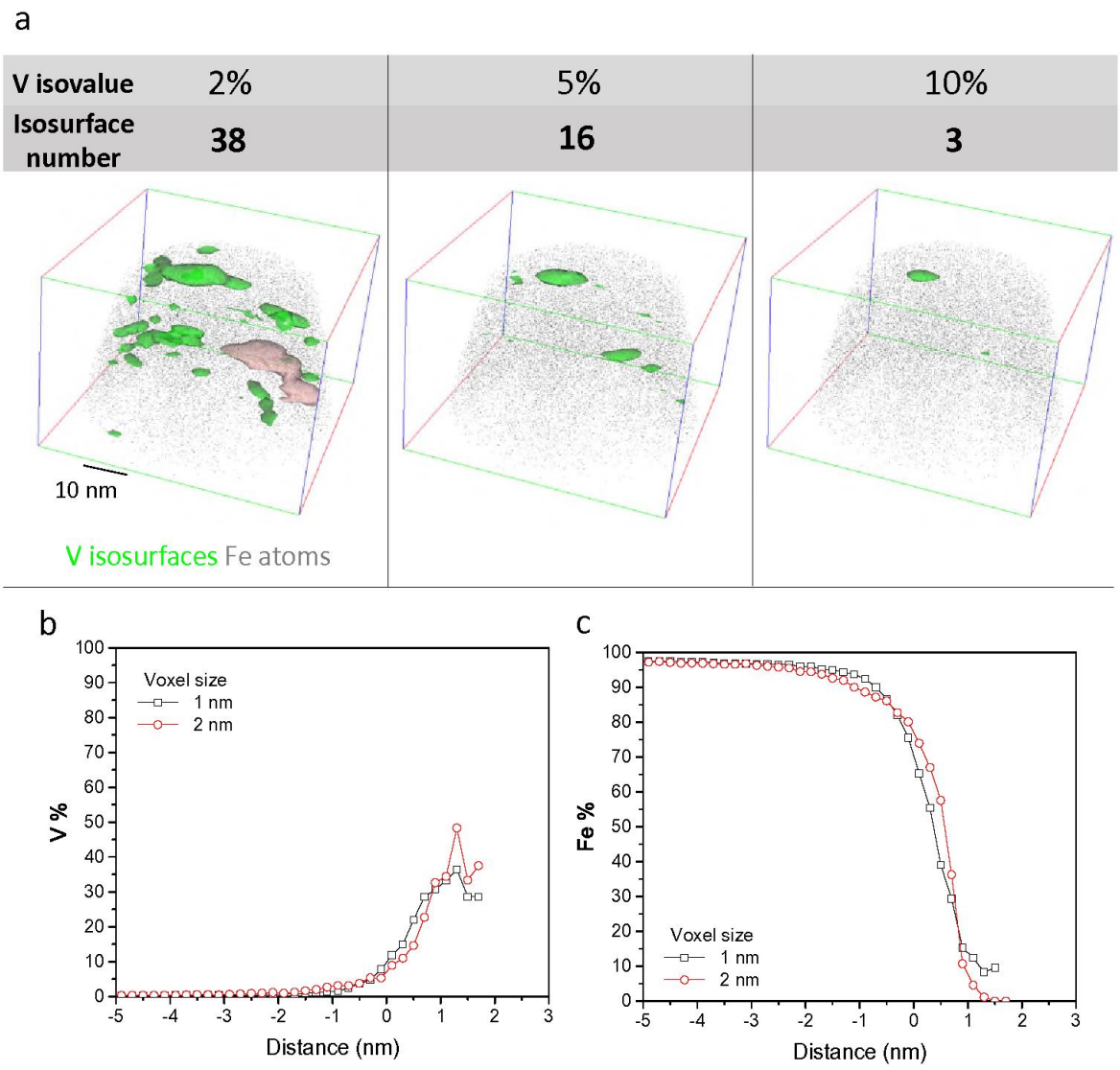

Figure 47 – (a) Numbers of defined isosurfaces with the applications of 2%, 5%, and 10% V isovalue and their visualised isosurfaces in green with the application of 2-nm voxel size. (b) and (c) are the comparison of V and Fe proxigrams between 1- and 2-nm voxel sizes.

Voxel size	C	V	Mo	Nb	Other	Metal-to-carbon ratio
1 nm	**40%**	**32%**	**19%**	**3%**	Bal.	1.35
2 nm	**38%**	**33%**	**21%**	**3%**	Bal.	1.5

Table 5 –Carbide composition (at. %) measured in the plateaus between -3 and +1 nm of matrix corrected proxigrams of 5% V isosurface from two voxel-size datasets.

4.2.2 Maximum separation method

To obtain the carbide composition, alternatively maximum separation cluster identification algorithm method (Section 3.2.8.4) was also applied to the same APT reconstruction of the as-received material (datafile R14_25949). Similar to the isosurface method, one should first consider minimising contributions from randomly occurring solute clusters in the matrix by carefully comparing the real experimental data with randomised data. The cluster parameter selection utilised herein was based on the framework developed by Williams et al. [217].

4.2.2.1 Determining d_{max} and N_{min}

In order to objectively decide on values for d_{max} and N_{min} as described in Section 3.2.8.4, a range of d_{max} values, 0.1 nm to 3.0 nm, were swept in steps of 0.02 nm. For each d_{max} value the resulting number of detected clusters was investigated as a function of varying N_{min} between 5 and 100. The results are shown in Figure 48(a) and (b) for randomised and real data, respectively. The datasets with $N_{min} < 5$ are not shown for clarity because of their large divergence from other datasets. Based on the randomised and real datasets, the products of objective function (see Section 3.2.8.4 for definition) were computed and plotted as Figure 48(c). To more clearly visualise the region of interest, a close-up of the area plotting objective function values between 0.8 and 1.0 of is presented in Figure 48(d).

In Figure 48(a) regarding the cluster number in randomised data, the peak number of clusters was found at d_{max} = 1 nm for N_{min} = 5, and this peak progressively shifts toward larger dmax values with increasing N_{min}. The resulting clusters corresponding to d_{max} = 1 and N_{min} = 5 were examined in IVAS and are visualised in Figure 49(1). The anomalously high number of clusters is confirmed in randomised data with the application of these maximum separation parameters. However, according to Figure 48(b), the application of

this condition in real data does not give as many clusters as in randomised data. This outweighing cluster number in randomised data with respect to the real data thus resulted in the negative product of objective function which corresponds to the dip shown in Figure 48(c). This high number of clusters being defined in randomised data is due to the relatively high solute content of this material which allows the solute atoms still being close enough after randomly shuffling and hence still meeting the criterion of maximum separation with the application of these specific conditions. This phenomenon demonstrates the limitation of this objective function method at certain maximum separation conditions when applied to high-solute-content materials. These d_{max} corresponding with negative values of the objective function are not applicable for guiding the cluster-defining-parameters selection.

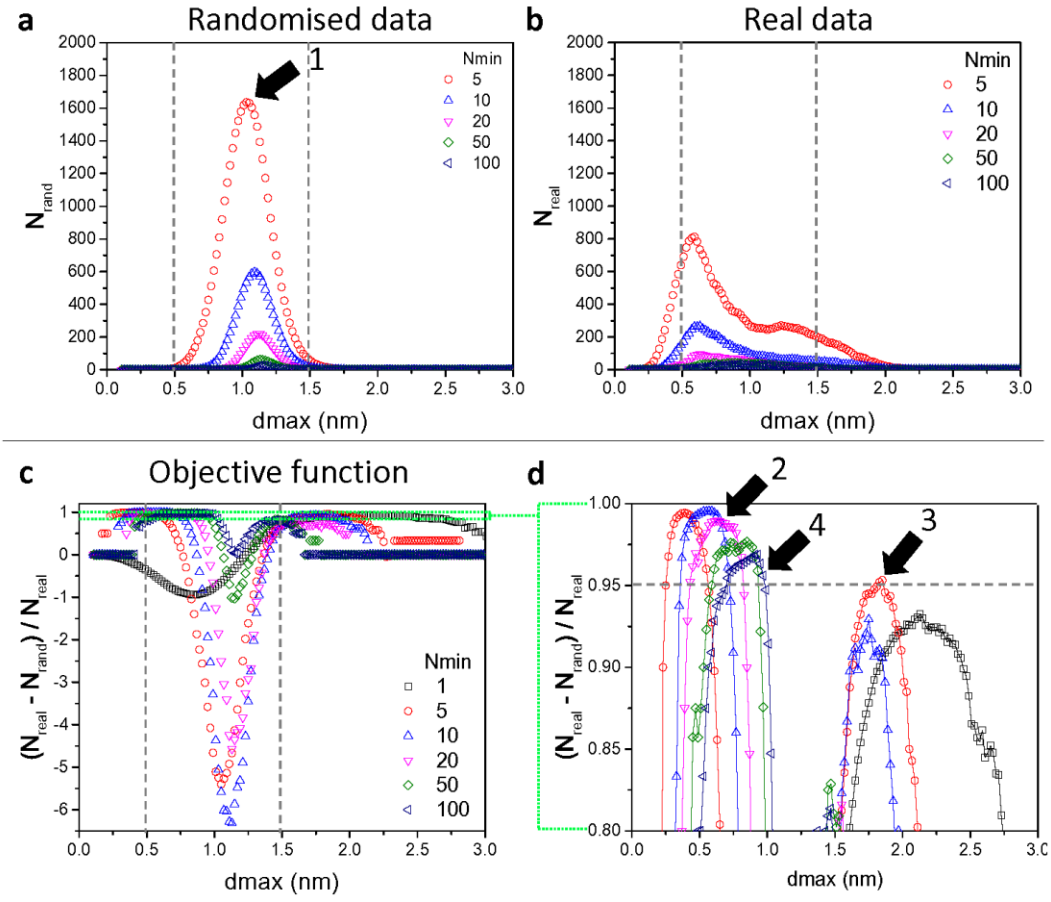

Figure 48 –The numbers of defined cluster as a function of d_{max} in (a) randomised data (N_{rand}) and (b) real data (N_{real}) with the application of selected N_{min} 1, 5, 20, 50, 100. (c) is the objective function $(N_{real} - N_{rand})/N_{real}$) with regard to the data in (a) and (b). (d) is the magnification of the objective function value at 0.8 to 1.0.

95% of the confidence in respect of 'real clusters' is selected herein, as highlighted by the grey broken line shown in Figure 48(d). Three conditions in Figure 48(d) meeting this confidence requirement were selected and utilised in the maximum separation algorithm to visually inspect the corresponding clusters, i.e. (d_{max}, N_{min}) = (0.6 nm, 20), (1.7 nm, 5), and (1 nm, 100) as shown in Figure 49 (2) to (4) which correspond to the parameter values indicated by arrows (2) to (4) in Figure 48(d), respectively. Figure 49(2) shows that with the use of a relatively small d_{max} (i.e. 0.6 nm), some clusters are incorrectly defined as separate clusters, as indicated by the arrows. According to the carbide morphology observed in TEM (Section 3.1), these groups discrete clusters are each most likely a single cluster but disjointed by the cluster algorithm due to the application of a too small d_{max} value. Hence this small d_{max} is not suitable to accurately extract carbide clusters. On the other hand, the application of large d_{max} (i.e. 1.7 nm) was applied as shown in Figure 49(3). The large d_{max} allows the linkage of several solute clusters into a single large carbide as shown by the red cluster in this figure. This condition also deviates significantly from the TEM observation.

Figure 49(4) shows a result applying the intermediate d_{max} (i.e. 1.0 nm) which allows the discrete clusters in Figure 49(2) to be correctly joined up into single clusters as indicated by the arrows. The obtained carbide size and morphology resulting from application of this choice of parameters generally agree with the carbide size and morphology in TEM observation. In addition, the number of defined cluster is 27 in this condition which is reasonable with respect to the isosurface number obtained in Section 4.2.1.2. Accordingly, this condition (i.e. d_{max} = 1 nm, N_{min} = 100) is determined to be used for the carbide extraction in this study.

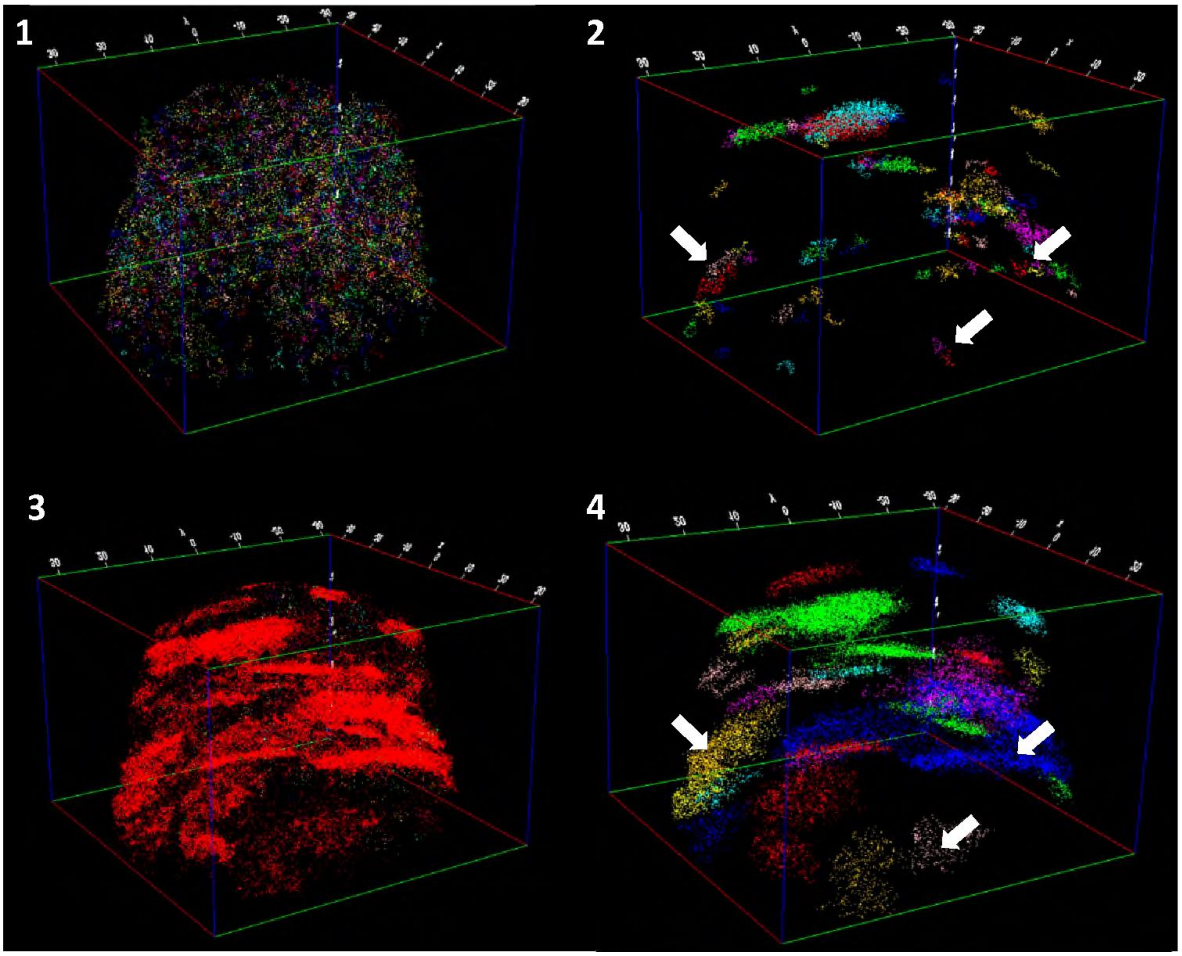

Figure 49 –Visualisation of the clusters defined by maximum separation using various (d_{max}, N_{min}) conditions: (1) (1 nm, 5) in the randomised data, where each colour indicates an individual cluster. (2) (0.6 nm, 20) in the real data (so as follow), where discrete clusters can be found as the arrows pointed. (3) (1.7 nm, 5), where a large cluster is shown due to the use of large d_{max}; (4) (1nm, 100), where the separate clusters in figure 2 are now combined into the clusters having comparable sizes to those observed in TEM (Section 3.1).

4.2.2.2 Carbide composition

Given the other two variables in maximum separation method, i.e. inclusion and erosion distances (L and $d_{erosion}$), have no readily available method for optimisation [217], the condition that L = 0.5 d_{max} (as discussed in Section 3.2.8.4) and no $d_{erosion}$ was applied to obtain the carbide composition herein. Further, matrix correction (Section 3.2.7.4) was applied to the extracted carbides with the matrix content being determined IVAS Cluster Analysis datasheet. Finally, the carbide-solute contents of each cluster were plotted against their cluster size (number of cluster ions) as shown in Figure 50. The apparent carbide-

solute contents were determined by globally averaging the data, i.e. the individual solute element divided by total ion number of the clusters. And the results are summarised in Table 6. The measurement generally agrees with Table 5 from isosurface method, and the resulting M/C ratio of 1.47 (1.18 if taking carbon loss discussed in Section 2.2.4.2 into account) is likely corresponding to M_4C_3 which indicates the FCC structure (Section 2.2.2.2). Considering the carbon signal loss again, the ratio becomes 1.23 which does not change the conclusion that these carbides have an FCC crystal structure.

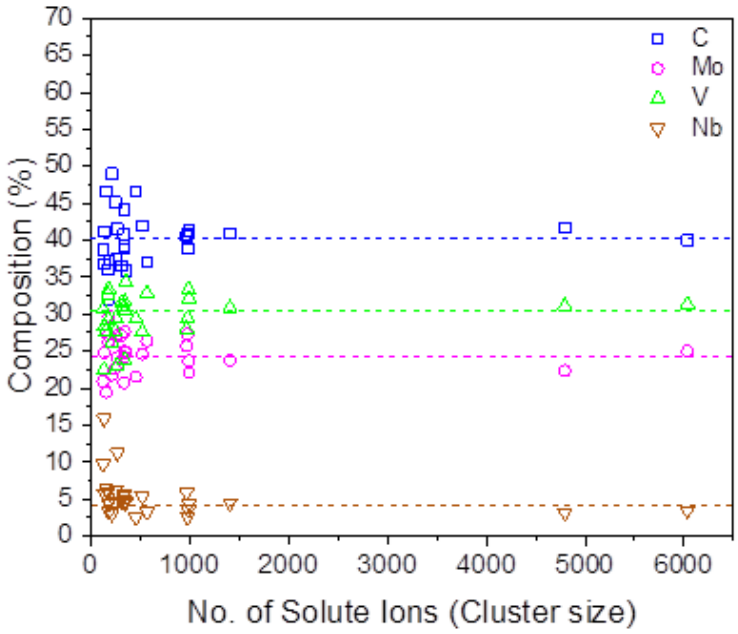

Figure 50 – Composition of each carbide solute against carbide size (total carbide count).

C	V	Mo	Nb	Metal-to-carbon ratio
40%	**31%**	**24%**	**4%**	1.47

Table 6 – Composition of the extracted carbide from maximum separation method with the application of matrix correction.

4.3 Carbide number density

As described in Section 2.2.2.2, carbide trap number density will determine how much interference to the diffusion of hydrogen atoms can be achieved within in the microstructure and hence this can be closely associated with the final efficacy of HE

mitigation. Therefore, properly determining the carbide number density of a material and using this to the inform the hydrogen-adsorption models is of importance to the practical aspect of the engineering design of material microstructure [143].

The calculation of carbide number density relates to the number of carbides. This can be determined in all APT data with the application of the carbide identification techniques as determined in Section 3.2.8.4 given the use of same material across this study. Additionally, the calculation relates to the analysis volume in which the carbides are observed. However, this volume can be different for the same experimental dataset after the application of different reconstruction condition (Section 3.2.7). To precisely determine the volume, reconstruction calibration was applied only to datafile R34_05028 where other datasets were limited by the data statistics as discussed in Section 3.2.7.3. Then the carbide number density was computed as shown in Table 7. To inspect the effect of the calibration to the measurement of carbide number density, the uncalibrated volume was also obtained and used for carbide density computation. Furthermore, another dataset (R14_25949) unable to be calibrated was processed in a similar fashion to account the variance across datasets.

Data	Reconstructed dimensions in x-y-z (nm)	Data volume* (10^{-22} m^3)	Carbide number	Number density (10^{23} m^{-3})
Calibrated R34_05028	82-80-143	7.37	125	**1.7**
Uncalibrated R34_05028	101-98-107	8.31	105	**1.26**
Uncalibrated R14_25949	69-68-47	1.73	27	**1.56**

Table 7 –The calibrated and uncalibrated data of reconstruction volumes, the carbide numbers of being extracted with the carbide definition in Section 4.2.2, and their resulting carbide number densities.*Assuming cylindrical shape of reconstruction.

The difference of the carbide number densities between the calibrated and uncalibrated as well as another uncalibrated dataset can be seen in the last column of Table 7, which is less than an order of magnitude. This implies that the effect of reconstruction precision is actually minor in the scale of carbide number density. In addition, these numbers are close

to the other atom probe measurements for carbide number density by Yen [228] and Mukherjee et al. [229], who reported 2.5 x 10^{23} and 8 x 10^{23} m^{-3}, respectively in the steels using same precipitate nucleation technique of interphase precipitate. Particularly in Yen's work, the atom probe measurement was compared with the TEM one and found in good agreement with each other. This shows the atom probe measurement for carbide number density is referable in general.

4.4 Summary

In this chapter, the material is characterised with emphasis on apparent carbide composition and number density. The concern about systematic losses in the detection of carbon during the APT experiment, particularly when analysing carbides has been examined. The carbide composition within the APT data was then measured through the application of both isosurface and maximum separation methods, respectively. Both methods require optimising input parameters to the algorithms so as to accurately define the carbide clusters and minimise subjective influence contributing to algorithm artefacts. A secondary matrix correction was applied with to the defined carbide clusters then resulting in the measurement of the carbide composition. The difference of the obtained carbide composition between the optimised cluster analysis methods is small.

5. Hydrogen Liquid Charging

5.1 Charging-induced corrosion

As discussed in Section 2.1.2, given exposure to the reactive environment during hydrogen liquid charging, corrosion may significantly affect the structure and viability of any atom probe sample exposed. Enabled by correlative TEM techniques (Section 3.3.1), the same needle-shaped specimen was observed via TEM in an uncharged state and then again after 5 minutes charging under the conditions stated in Section 3.3, as shown in Figure 51(a) and (b), respectively. In these figures, a grain boundary is observed which is then used as a geometric reference to produce the superimposed image of Figure 51(c) from (a) and (b). This shows a significant change in the specimen geometry. A loss of 260 nm of material from the original apex can be seen in Figure 51(c). The corroded tip then was analysed in APT after the standard APT loading procedure (Section 3.2.4) which resulted in the desorption of the charged hydrogen before analysis, and resulted in the reconstruction shown in Figure 51(d), where the reference grain boundary can be observed due to segregation of carbon to the boundary.

These results confirm that the charging process affects the tip geometry. However, although material was removed, the specimen geometry still met the stringent requirements for a successful atom probe experiment. This considerable charging-induced corrosion thus requires the strategic minimisation of liquid-charging time as described in Section 3.3. However, this effect has not been further quantified within the scope of this study.

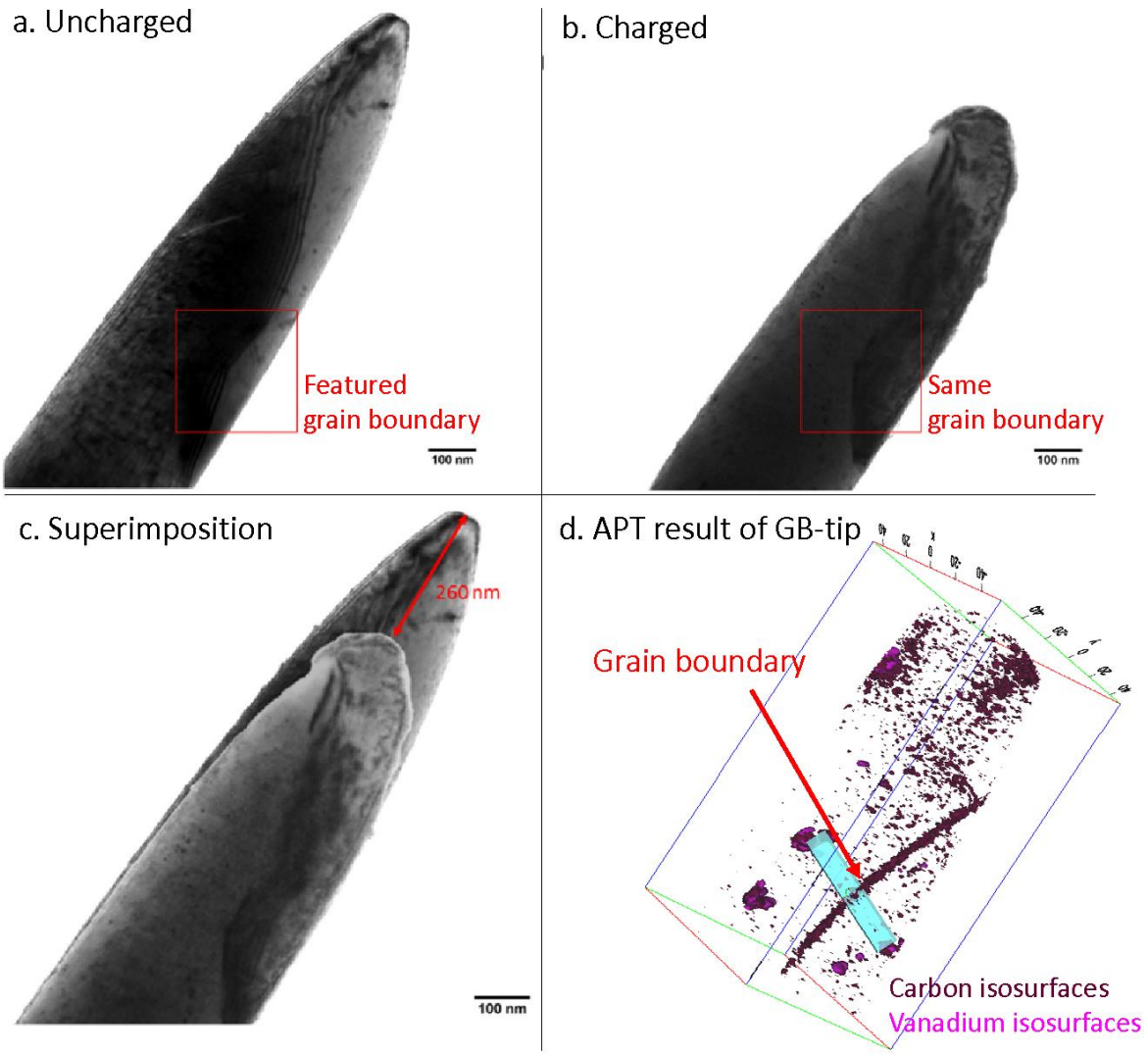

Figure 51 - TEM observation of (a) an uncharged tip containing a grain boundary, (b) the same tip after 5 min charging at 2.2V in 0.1M NaOD solution with same grain boundary being identified, (c) superimposition of (a) and (b) showing that approximate 260-nm material was removed after charging, (d) APT result of the charged tip showing that despite damage the charged tip is still viable.

5.2 Room temperature transferred hydrogen-charged sample

This section assesses the efficacy of the liquid charging followed by room-temperature (RT) transfer to the atom probe and the potential for detrapping of loaded hydrogen. In order to distinguish the signal of loaded hydrogen from the background hydrogen (Section 2.2.4.1), deuterium was used as a proxy for hydrogen, charged into the sample with the use of deuterated medium which is described in detail in Section 3.3. The deuterium-charged

sample then was transferred swiftly into the LEAP 3000X HR cryogenic sample-stage (Section 3.2.2) of the analysis chamber within 20 minutes and was analysed at the APT instrumental conditions stated in Section 3.2.5.

The resulting mass spectrum from the datafile R14_26056 (incorporating 5 million ions after discarding the initial surface layer) is shown in Figure 52. In comparison to the mass spectrum of the uncharged sample shown in Section 3.2.6, a significant 2 Da peak can be observed, which is identified as a deuterium signal, given that a hydrogen(^{1}H)-charging experiment result in Section 6.1 showed that a 2 Da peak due to $^{1}H_{2}^{+}$ was not predominant. After labelling of hydrogen and deuterium peaks (Section 3.2.6), the data was reconstructed and analysed using a NN distribution algorithm (Section 3.2.8.3) to investigate clustering of vanadium and deuterium atoms, as shown in Figure 53(a) and (b), respectively. In Figure 53(a), the vanadium clustering is clear with a higher frequency of shorter pair distances in the real experimental data as compared to its counterpart in the randomised case, which is as expected due to the existence of the carbides. The NN analysis with respect to the deuterium distribution was then was applied to the same data, which gives the result shown in Figure 53(b). No difference is apparent between the deuterium pair distances from the real and randomised distributions can be observed. This suggests that the deuterium atoms are not clustered and implies no significant spatial correlation to the carbides. This result was confirmed by directly inspecting the data reconstruction with respect to vanadium, deuterium, and background hydrogen signals as shown in Figure 53(c), where only vanadium but no hydrogen and deuterium segregations can be observed. The cluster-like area in the left of Figure 53(c) is regarded as an artefact given its correspondence with a high atomic density region, as the red isosurface shown in Figure 53(d), where all ions including hydrogen and deuterium have higher density than in other areas. If the deuterium

atoms were trapped in the carbides, association between the locations of carbide (i.e. vanadium) and deuterium should be observed. However, this is not the case observed here.

This observation of deuterium spatially uncorrelated with the carbide positions could be a result of deuterium detrapping from the carbide during the RT transfer process, which has been observed in the work of Haley et al. using RT APT transfer after deuterium loading of a trap-containing austenitic steel [36]. These results also show a deuterium peak in the mass spectrum however no spatial correlation to any microstructural feature in the resulting atom maps was observed. Their calculations suggest that only 2 seconds are required for deuterium to desorb from atom probe tip sample. However, this contradicts their observation of detected deuterium after 40 minutes of transfer time in vacuum. Hence, they proposed the existence of a deuterium desorption barrier at specimen/environment interface for retaining the detrapped deuterium within the sample, which agrees with the present finding. To limit the observed detrapping effect of deuterium, they proposed lowering the transfer temperature to immobilise the trapped deuterium during this process.

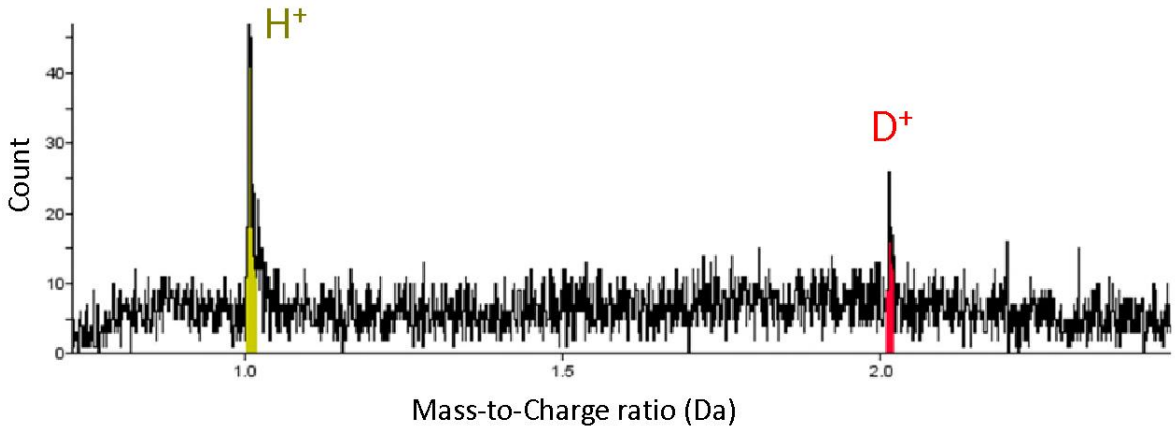

Figure 52 – Mass spectrum results from a liquid charging being followed by room-temperature transfer process to the LEAP 3000X HR. 20 ppm of D was collected in a total of 5M ions.

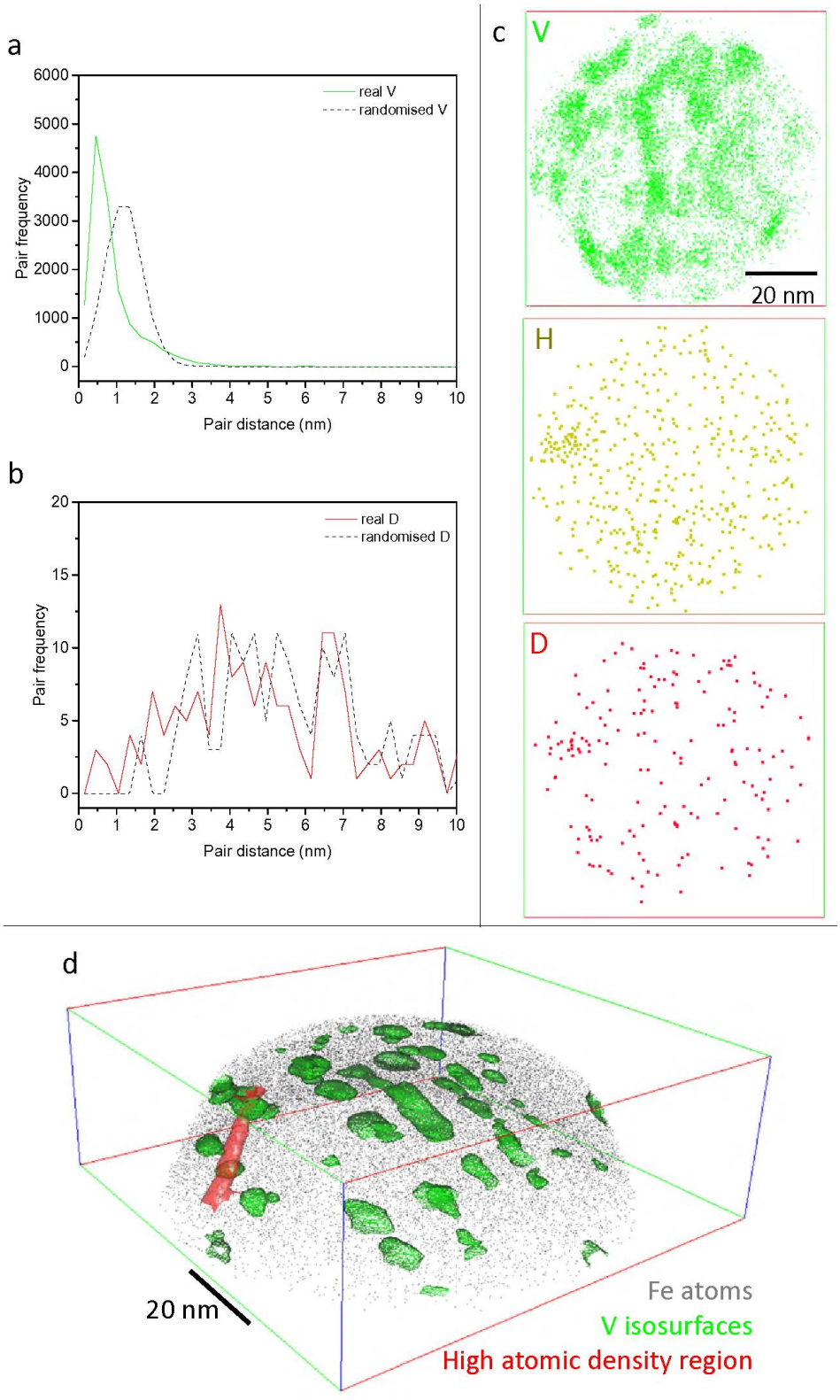

Figure 53 – (a) and (b) are the nearest neighbour analyses of V and D, respectively, which show the apparent cluster in V ions but not in D. (c) shows the top-down (x-y plane) views of the entire dataset of V, H, and D in the reconstructed data. (d) shows a high atomic density area (red) in the dataset as well as the vanadium isosurfaces (green) which have no spatial correlation with the red area.

6. Vacuum Cryo-Transfer

In the previous chapter, liquid charging (Section 3.3) has been confirmed as an effective method for hydrogen/deuterium introduction to the specimen. However, concerns regarding hydrogen detrapping during the RT sample transfer process were highlighted. In this chapter, work to integrate an existing vacuum cryo-transfer (VCT) chain into the sample loading process after hydrogen liquid charging is investigated. The hydrogen-bearing samples after VCT process then were tested in a LEAP 4000X HR in ETH Zürich with the same experimental instrument settings, described in Section 3.2.5, as other experiments in this study.

6.1 Hydrogen charged sample

In the atom probe experiment, background hydrogen (Section 2.2.4.1) can be detected in the forms of H^+, H_2^+, and occasionally H_3^+ resulting in 1, 2, and 3 Da peaks, respectively [182]. To verify that the 2 Da peak in the mass spectrum of Figure 52 was from D^+ rather than H_2^+, a hydrogen-loaded sample, subjected to the charging method stated in Section 3.3 but using 0.1M NaOH-H_2O solution, was examined via APT analysis after the VCT. If a 2 Da peak was detected in this experiment, then the 2 Da in the previous mass spectra could incorporate significant contributions from the $^1H_2^+$ signal of background hydrogen rather than being predominantly the result of the sample deuteration procedure.

The resulting mass spectrum (from dataset R34_05068, incorporating 1.6 million collected ions after removing the surface layer) is shown in Figure 54(a) and exhibits no detectable 2 Da peak. Incorporating the uncharged spectrum shown in Section 3.2.6, these results suggest that $^1H_2^+$ is not the preferential type of hydrogen evaporation regardless of the source and amount of hydrogen. Hence this provides significant confidence that the

detected 2 Da signal in the deuterium-charged samples originates from the deuterium introduced into the microstructure.

A NN distribution analysis (Section 3.2.8.3) was applied to the hydrogen-charged data and the result is shown in Figure 54(b). This indicates clustering of loaded hydrogen. The spatial correlation of hydrogen atoms with the carbides, which indicates the hydrogen-trapping phenomenon, was confirmed by the atom map shown in Figure 55 where the locations of hydrogen atoms (dark yellow large dots) are associated with the carbides represented by vanadium (small green dots) in the maps of figure (b) and (c).

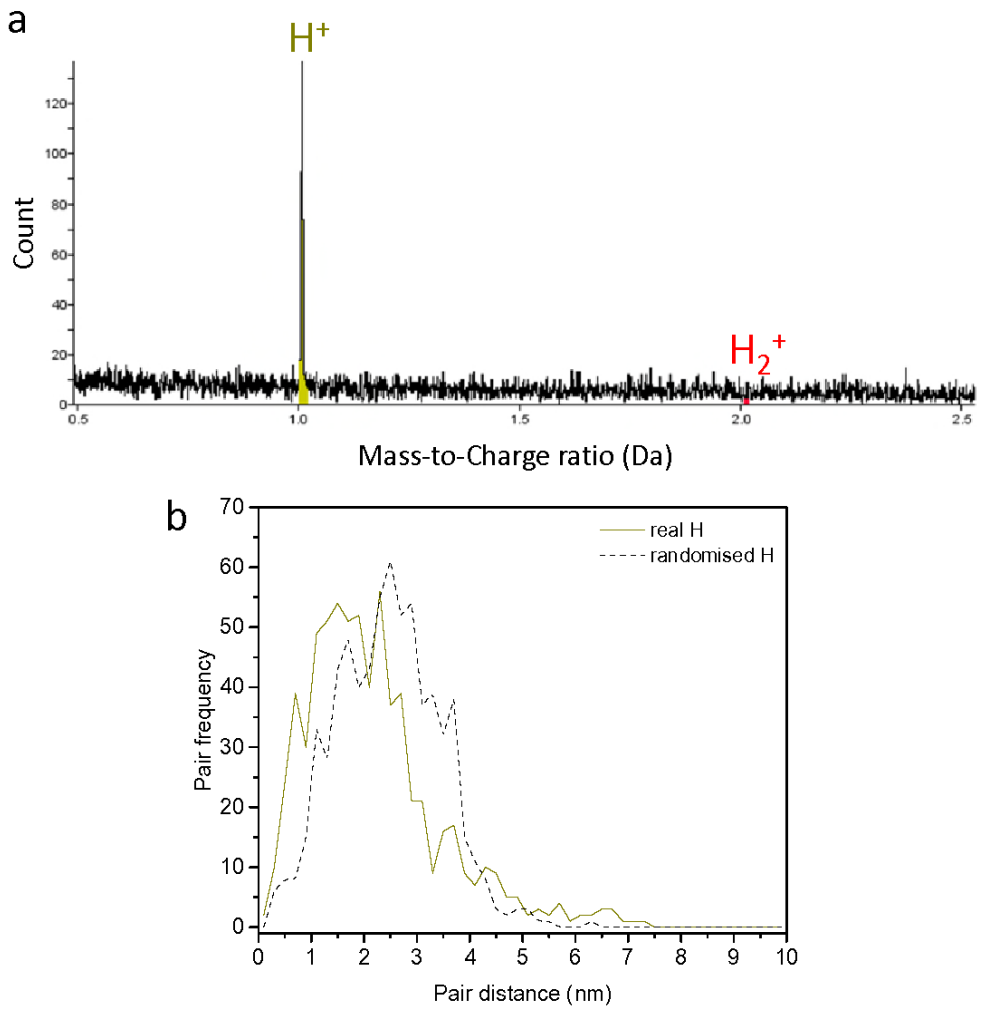

Figure 54 – (a) The mass spectrum of a sample charged in NaOH in H_2O and then using VCT to APT to retain the loaded hydrogen, verifying the 2 Da peak in the previous deuterated result of Figure 52 was only from deuterium. (b) The NN distribution of H in the data shows the clustering of loaded hydrogen.

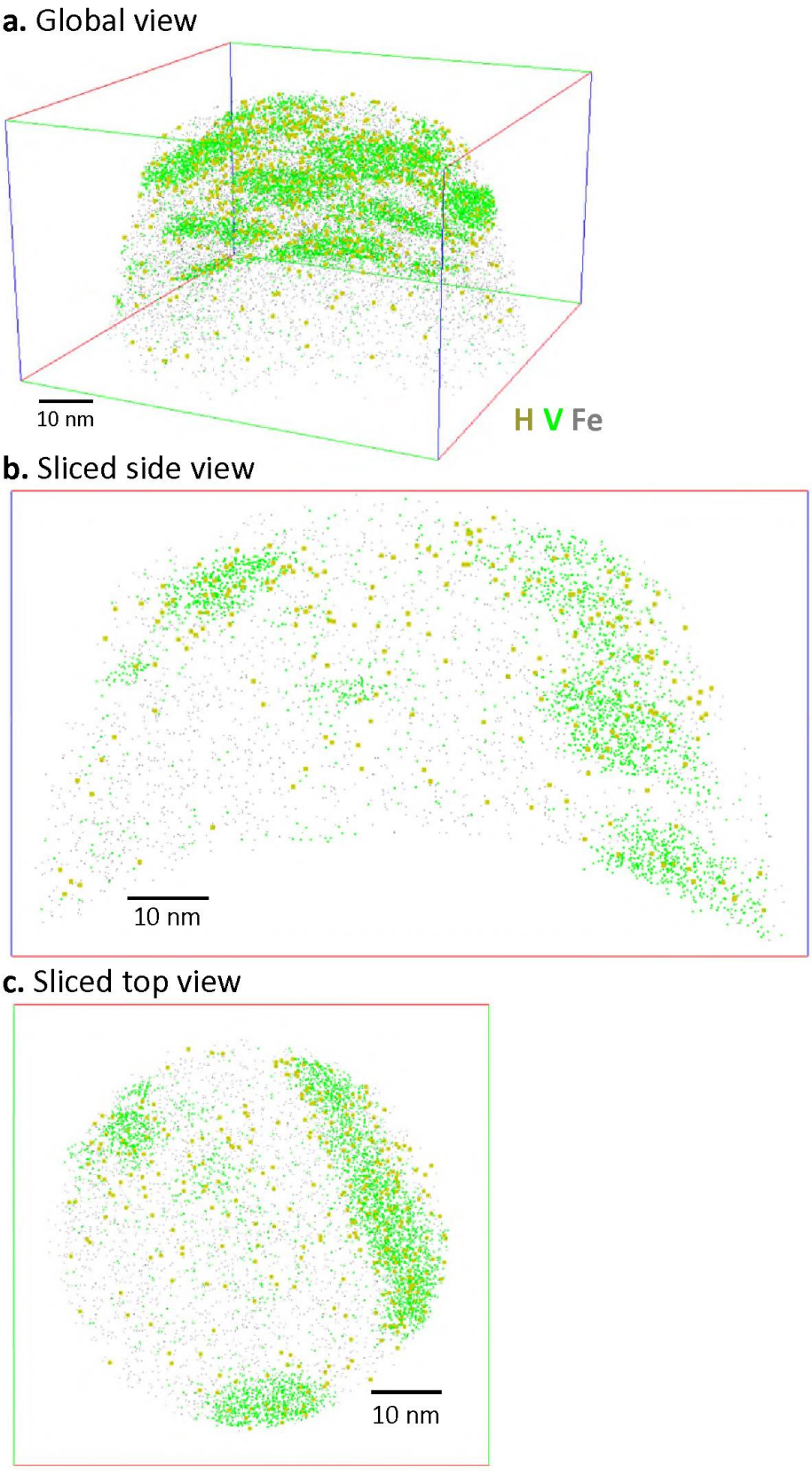

Figure 55 – The trapped hydrogen (dark yellow dots) in the carbides (vanadium shown in green dots) in (a) global view, (b) side-viewed 10-nm thick slice, and (c) top-viewed 10-nm thick slice.

The result in Figure 55 shows that trapped protium atoms are observable if their positions are properly retained by using VCT. However, there is no readily applicable technique to separate the protium signal in the 1 Da peak from the vacuum environment or artificial charging, hence environmental hydrogen can contribute to the 1 Da peak and undermine the quantification of the trapped hydrogen. Therefore, the sample deuteration described in Section 2.2.4.1 for separating the charged hydrogen from the background is still necessary in quantitative analysis of trapped hydrogen and the results combining this with VCT will be presented in the following section.

6.2 Deuterium charged sample

To separate background hydrogen introduced by the analysis environment from that introduced by artificial loading, the deuterium-charged specimen was examined in the LEAP 4000X HR using VCT for sample loading. The resulting data (R34_05028 incorporating 20 million collected ions after removing surface layer) along with the mass spectrum is shown in Figure 56(a). A significant peak at 2 Da corresponding to deuterium is readily observed in this mass spectrum. This deuterium peak corresponds to 76 ppm of global concentration, which is higher than the RT-transfer result in Figure 52. However, care must be taken when making comparisons between datasets. This result suggests more deuterium atoms were retained in the sample during APT analysis with the use of VCT. In addition, a 1 Da signal was still collected, despite the sample deuteration, which should be primarily contributed by hydrogen originating from the analysis chamber. This shows the significance of this background hydrogen signal and confirms that one cannot characterise any 1 Da signal without a robust method to inhibit the hydrogen penetration from the ambient analysis environment [180].

The deuterium NN distribution (Section 3.2.8.3) was examined in Figure 56(b), which clearly indicates the presence of deuterium clustering. Deuterium locations were then examined visually in the 3D atom map. The global 3D reconstruction, along with sliced sub-volumes of this data, are shown in Figure 57 where only deuterium and vanadium (representing the carbides) are shown in red and green for clarity, respectively. The sub-volumes represent slices in the x-y and y-z planes, respectively, in Figure 57(b) and (c), where the clear association between deuterium and carbide positions can be seen. This association provides direct evidence of the carbide trapping of deuterium/hydrogen. To further quantify the deuterium content in the carbide traps, the cluster extraction method discussed in Section 4.2.2 (without regarding deuterium as a cluster solute) was applied to both VCT and RT-transfer data reconstructions. The resulting data is shown in Table 8 which reports the deuterium content respectively: the global reconstruction; the matrix; and the carbide clusters. Table 8 shows that the deuterium signal from the VCT sample is significantly higher than the RT-transferred sample in all regions and hence demonstrates that the VCT method is effective to inhibit deuterium detrapping and enable the observation of deuterium trapped in specific microstructural features.

The in-trap data shown in Table 8 suggests that the VCT process is better suited to inhibiting hydrogen detrapping from the carbide than the RT transfer. In addition, the deuterium content in the RT-transferred sample (15 atppm.) is much higher than the ferrite solubility (~1 atppm.) stated in Section 2.1.3 [36]. This phenomenon could either support the model of Haley et al. which suggests that the sample-surface barrier retains the charged and then detrapped deuterium, or else it could mean that the hydrogen solubility in the studied steel solution is intrinsically higher than the pure ferrite [44]. Unfortunately, these assumptions cannot be verified without further evidence with regard to other kinetic factors such as desorbing time. Furthermore, the deuterium signal in the matrix of the VCT sample

is also higher than the RT-transferred case. This matrix deuterium content could result from the deuterium that was detrapped during the 2-minute sample-loading procedure at room temperature described in Section 3.4, however this also requires more investigation that considers the hydrogen detrapping kinetics and is currently unable to be fully understood within the evidence provided in this study. Future studies could obtain more insight about the possible hydrogen-detrapping/desorption scenario by intentionally extending the time during transfer to the atom probe that the specimen is held at room temperature to investigate the resulting measured hydrogen concentrations in both the matrix and traps.

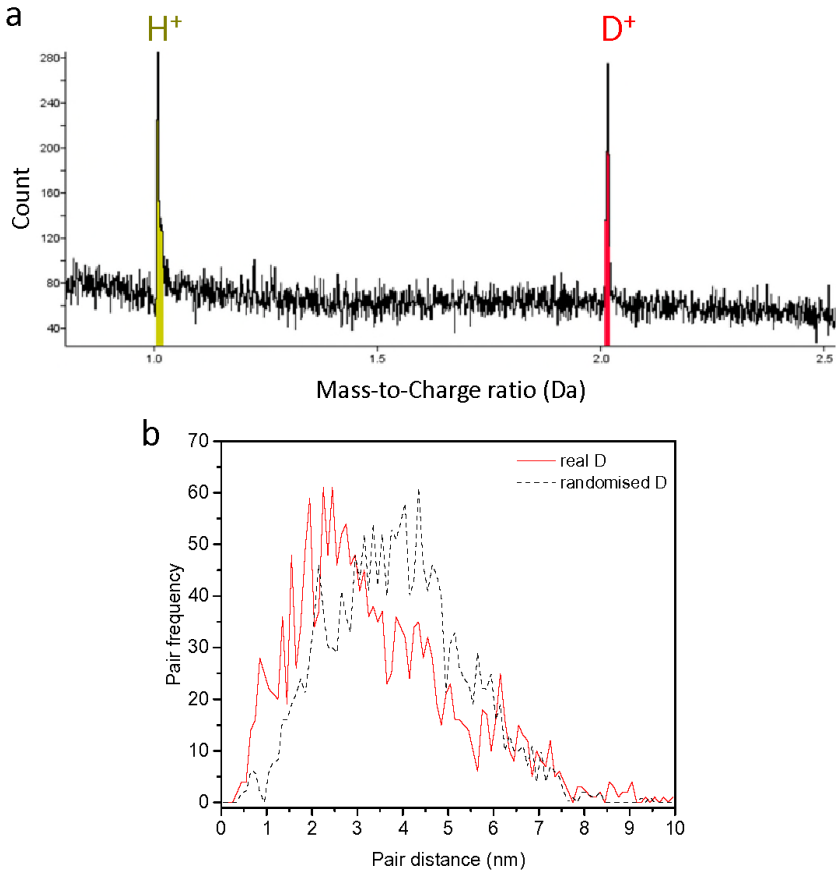

Figure 56 –(a) Mass spectrum of the D-charged sample using VCT to retain deuterium. 76 ppm of global D content was measured. (b) NN distributions of deuterium which shows a small pair distance as compared to a randomsied reference hence incidcates the clustering of D in the data.

Methods	Global	Matrix	In-cluster
Liquid charging then RT-transfer	20	15	77
Liquid charging then VCT	**76**	**68**	**860**

Table 8 – The D contents (in at. ppm) measured in RT-transfer and VCT APT experiments

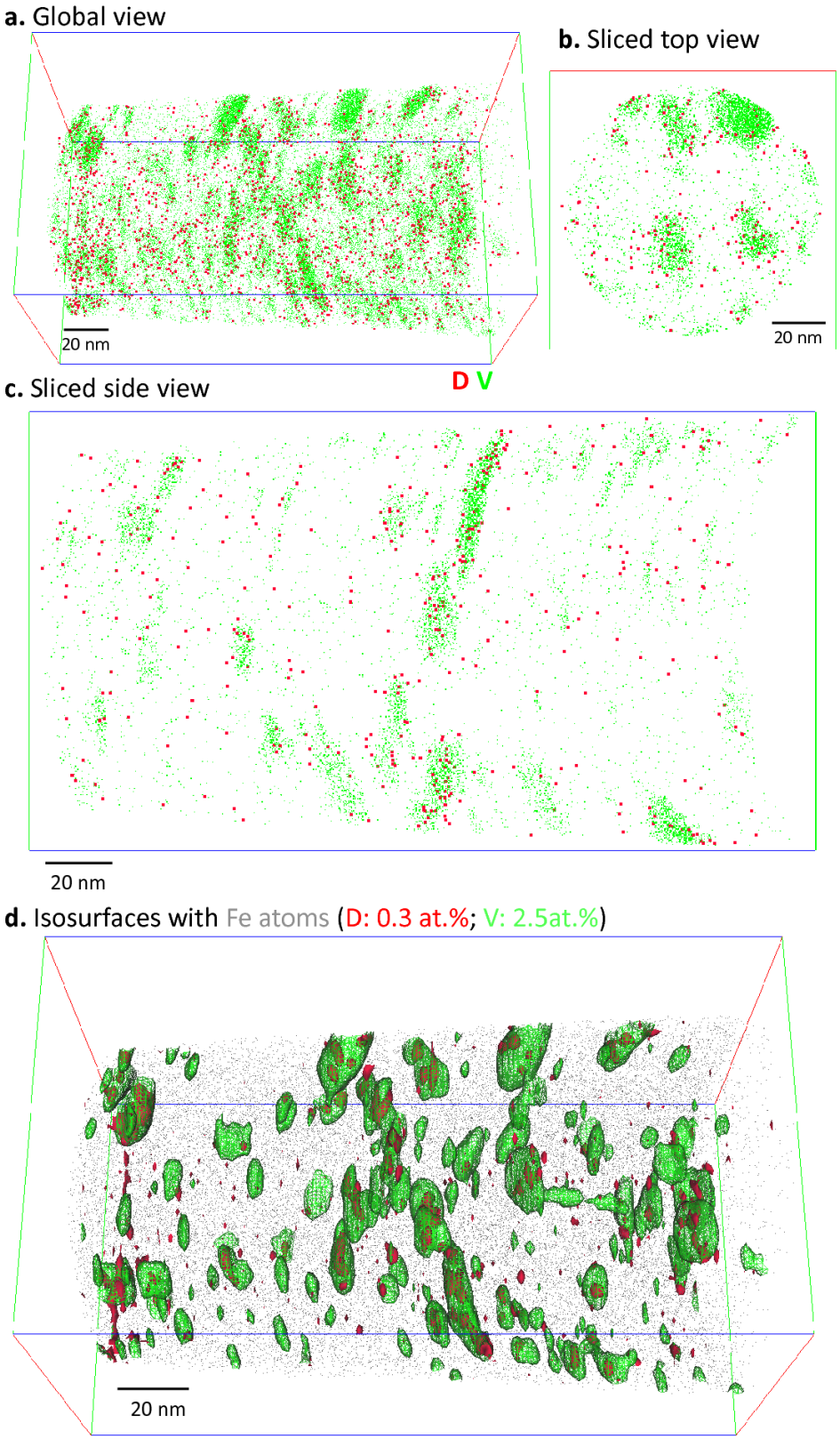

Figure 57 –Trapped deuterium (red dots) in a sample using VCT to retain the charged deuterium: (a) global view, (b) top-viewing 10-nm plane slice, (c) side-viewing 10-nm y-z plane slice, and (d) isosurfaces of D (0.3 at.%) and V (2.5 at.%), where significant spatial correlation between deuterium and the carbides (shown by green dots of vanadium) can be observed.

6.3 Carbide hydrogen trapping site

As discussed in Section 2.2.2.2, understanding the exact mechanism by which the fine-scale carbides traps hydrogen would facilitate optimisation of the hydrogen-trapping/HE-mitigation microstructure. However, whilst prior literature works have demonstrated direct observation of carbide hydrogen trapping [178, 199], a quantitative method to characterise hydrogen trapping sites is still lacking. In this section, three analytical approaches are proposed and applied to the VCT deuterium-trapping data (R34_05028) to investigate the location of trapped hydrogen in the carbides with respect to carbide interior and its interface with the matrix.

6.3.1 Axial concentration profile along analysis direction

The APT data exhibiting deuterium trapping was first processed with the use of 9.5 at.% V isosurfaces to extract 32 carbides. Subsequent cluster analysis was undertaken to determine the respective coordinates of these carbides. Then the axial 1D concentration profile algorithm, described in Section 3.2.8.5 was applied with to extract individual element profiles, the dimensional normalisation of carbide clusters, as well as the superimposition of the obtained profiles across all of the carbides as shown in the schematic Figure 58(a). The resulting profile is shown in Figure 58(b) where the top and bottom carbide-matrix interfaces can be inferred at approximately 25% and 75% of the normalised distance, respectively. The top profile in Figure 58(b) is the distribution of deuterium around the collected carbides, which shows most of deuterium atoms are located in the carbide interior rather than at the interfaces. This result statistically shows that the studied carbides trap hydrogen/deuterium in their interior. This result has been theoretically

proposed, under a mechanism by which hydrogen is associated to the presence of carbon vacancies in carbide bulk [103, 104].

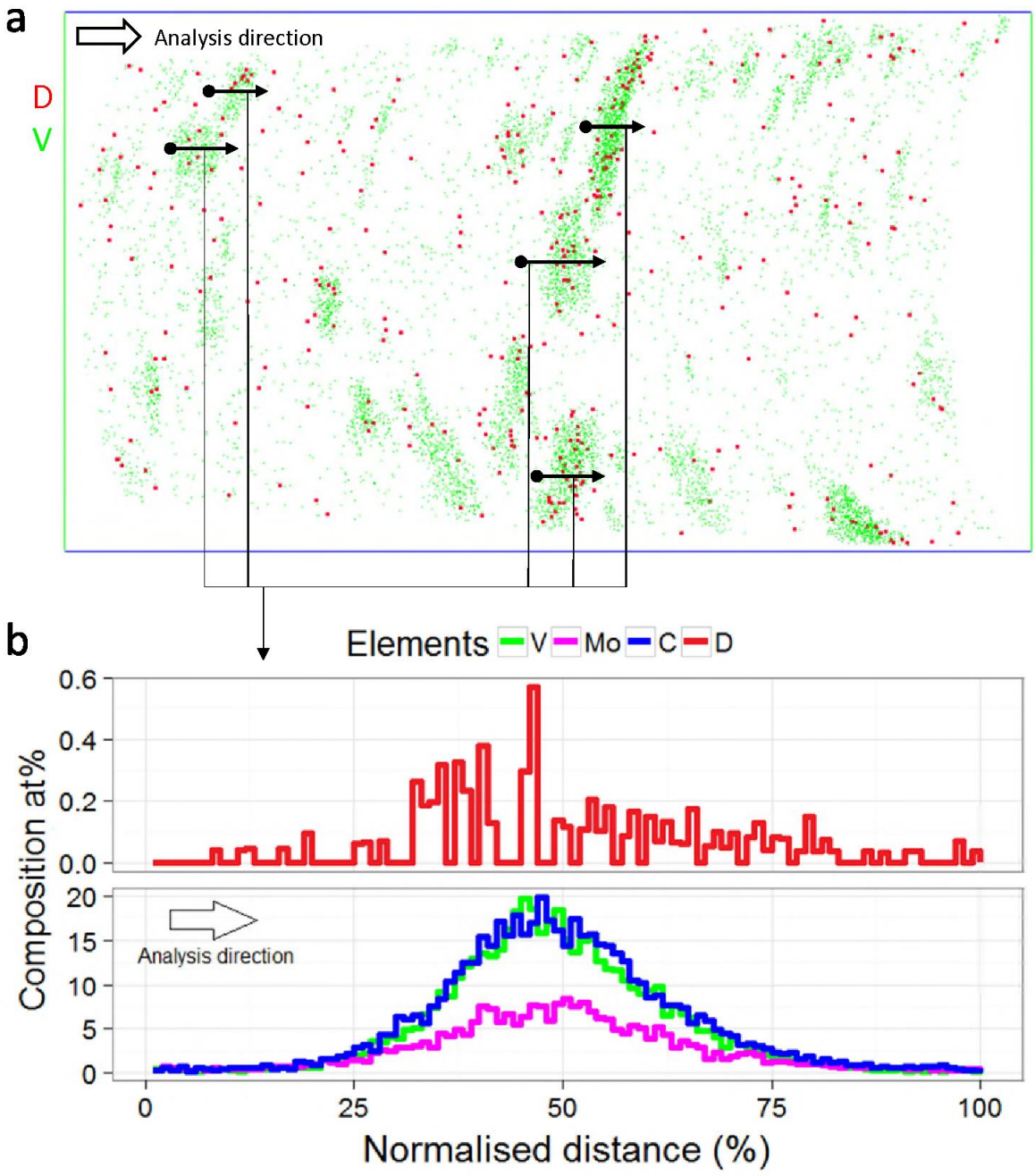

Figure 58 –(a) Schematic of the data processing that collects the individual profiles of carbide solute elements as well as deuterium along the analysis direction and superimposes them to obtain (b). (b) The resulting axial profile which shows the carbide interfaces at 25% and 75% and can be used to determine the deuterium atoms in carbide traps D. Most of these are seen to locate at the interior of carbides instead of the interfaces.

6.3.2 Cluster surface analysis

As stated in Section 3.2.8.4, adjusting the erosion distances ($d_{erosion}$) in the maximum separation method allows investigation of the composition at the cluster surfaces. Schematic representations of hydrogen-trapping in the interior and at the interface of carbide are shown in Figure 59(a) and (b), respectively, with regard to the effect of increasing the erosion clustering parameter. In the case of interior trapping of the hydrogen shown in Figure 59(a), with the increase of $d_{erosion}$, the majority of trapped deuterium will not be removed during the erosion process and hence this will gradually refine the deuterium content measurement with respect to the global cluster composition. In comparison, in interface trapping regime in Figure 59(b), the increase of $d_{erosion}$ will initially remove the excess matrix atoms from the surface and see the refinement of the measured deuterium content. However, further increase will eventually disproportionally remove the trapped deuterium atoms at the interfaces and result in the decrease of the measured deuterium content with the application of relatively large $d_{erosion}$.

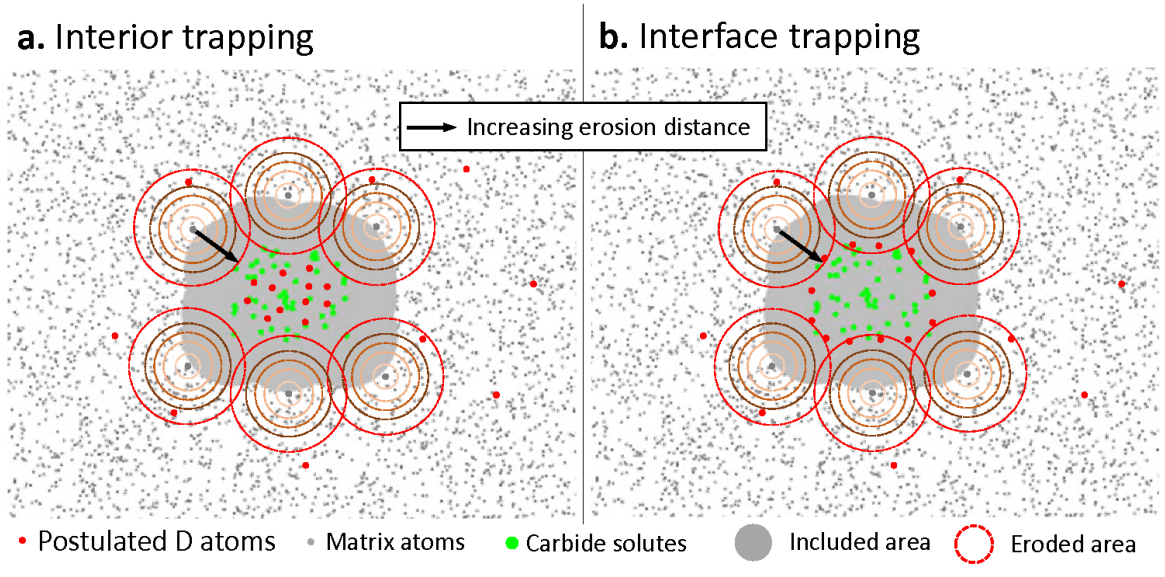

Figure 59 –Schematics of (a) interior and (b) interface hydrogen-trapping of carbide with respect to the effect of increasing erosion distance.

The carbide clusters in the deuterium-trapping data (R34_05028) were first extracted by maximum separation method (Section 3.2.8.4) with varied $d_{erosion}$ from 0 to 0.5 nm (restricted by L, see Section 3.2.8.4) whereas other parameters remained fixed d_{max}, N_{min}, and L (1 nm, 100, and 0.5 nm as determined in Section 4.2.2.1). The apparent counts of deuterium and the total extracted ions from the cluster extractions were plotted as a function of $d_{erosion}$ as shown in Figure 60(a). The figure shows both the decrease in deuterium and total ion counts as a result of removing by the application of the enveloping step in the clustering algorithm. Considering the deuterium content with respect to the total residual ions, namely the red data divided by the black data in (a), the refinement of deuterium content against the increase of $d_{erosion}$ can be seen in Figure 60(b). The carbide interface trapping regime would result in an increase then decrease deuterium content as a function of $d_{erosion}$. However, the observed continuous increase of deuterium content in Figure 60(b) supports the interior trapping regime shown in Figure 59(a).

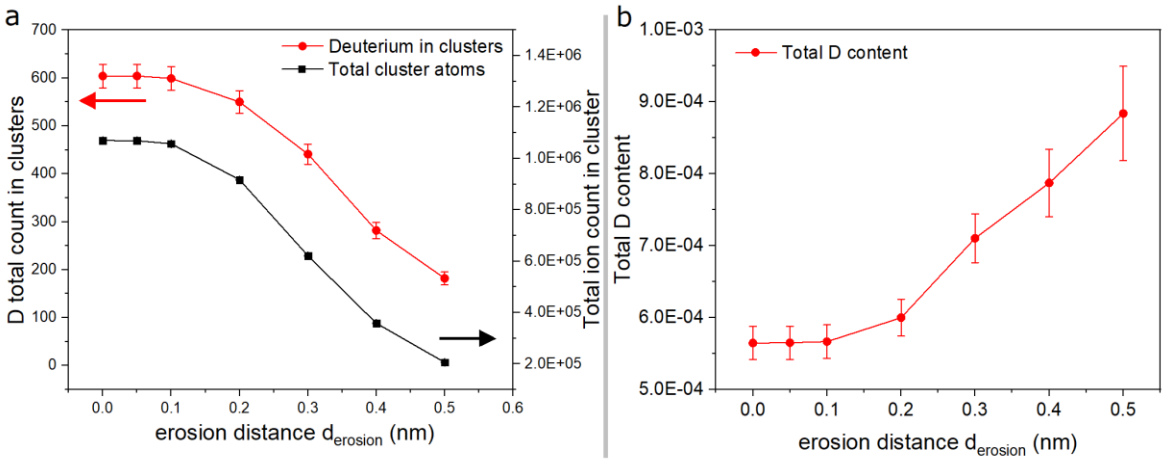

Figure 60 - Total D and Fe counts (top and middle, respectively) within determined clusters against erosion distance. The plateau below 0.1 nm of erosion distance is due to the used erosion being less than the mean distance between the atoms in the APT data, which can be examined by the erosion of Fe. Parameters of d_{max} and L were 1 and 0.5 nm, respectively, and N_{min} was 100. The errors in (a) were estimated based on dilute condition ($\sigma \approx \sqrt{count}$), whereas in (b) the errors were accounted via the propagation of the ones in (a).

6.3.3 In-cluster deuterium linear fitting

For the determination of the interior or interfacial nature of hydrogen-trapping, the total number of deuterium atoms detected in a carbide (n_D) should show linear relation with carbide volume, represented by the total number of atoms in the cluster ($n_{cluster}$) in the case where they are trapped in the interior of the carbide. In comparison, trapping at the interface implies an n_D value that changes with the surface area of the carbide, and hence is proportional to $n_{cluster}^{2/3}$. The cluster extraction method (described in Section 3.2.8.4 with the parameters determined in Section 4.2.2) was applied to the deuterium-trapping data (R34_05028) to obtain n_D which was plotted against both $n_{cluster}$ and $n_{cluster}^{2/3}$. A linear fit was then applied to each set of data, noting that only clusters which were observed to contain deuterium were considered so as to avoid a pinning effect at $n_D = 0$. The resulting linear fittings are shown in Figure 61(a) and (b) respectively. However, the fit R-squares values of 0.93 and 0.91 respectively do not show a clear difference. This result is thus not statistically conclusive to indicate either interior- or interface-trapping of hydrogen.

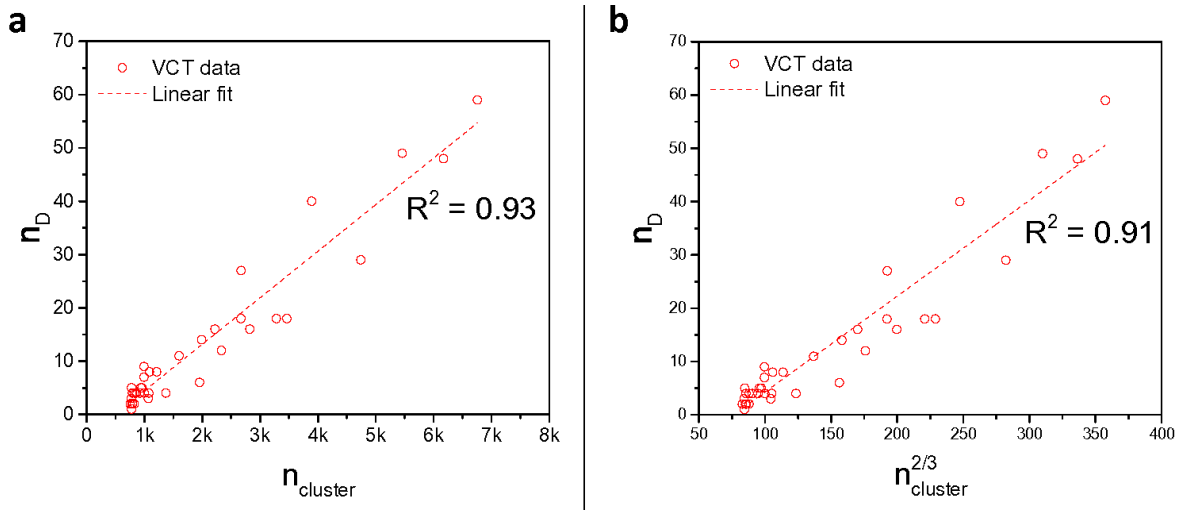

Figure 61 –The linear fitting results of the in-trap deuterium number (n_D) against the number of total ion in each cluster, which is assumed to be proportional to cluster volume (V), and same number to the power of 2/3, which is assumed to be proportional to cluster surface area ($V^{2/3}$).

This inconclusive result could be due to the proposed geometrical model assuming the clusters are spherical in shape and over-simplifying the correlation between the interface surface area and carbide volume. It is possible to extract dimensional information on the carbides from cluster analysis. The reported dimension of any cluster is however measured from the reconstruction of the atom probe data, which should always interpret with caution due to trajectory aberrations that can distort carbide geometry (Section 3.2.7.4). Thus, one could potentially improve the model by considering the actual shape of carbide, which is platelet according to the TEM data in Section 3.1, with more sophisticated factors of cluster geometry, and then generating a computational simulation regarding the deuterium distribution in new geometric model to compare with the new fitting results.

6.3.4 Discussion

Multiple approaches, i.e. axial profile, cluster surface, and in-cluster deuterium fitting, were applied for determining the hydrogen trapping site of the studied V-Mo-Nb carbide in this chapter. A general conclusion can be made in favour of interior trapping rather than interface trapping. This observation is consistent with multiple macroscopic SANS analyses which show hydrogen being trapped at the interior of VC and NbC [155, 156] whereas contradicts the APT observations of Takahashi et al. in TiC and VC carbides, which suggest interface hydrogen trapping in both cases [178, 199]. This inconsistency can be resolved by the following discussion with regards of both experimental and theoretical approaches.

In the early experimental work of Wei and Tsuzaki, they used TDA to macroscopically investigate carbide hydrogen trapping with respect to carbide aging stage, namely carbide interface coherency, as well as annealing process for the penetration of charged hydrogen to the interior trapping site [49]. In the ferrite matrix incorporating incoherent TiC precipitates,

they found no hydrogen trapping after room temperature liquid charging but detected the trapped hydrogen in the samples that were annealed at high temperature after room temperature liquid charging. Whereas their results from the samples with coherent TiC precipitates show trapped hydrogen after room temperature liquid charging. They regard these phenomena with the presence of trapping sites at coherent TiC interface as well as the presence of a high energy barrier at incoherent TiC interface that does not trap hydrogen at room temperature and only allows hydrogen penetration at high temperature toward interior strong traps, as shown in Figure 62 (a) and (b), respectively. Although their evidence about hydrogen trapping sites is indirectly inferred from TDA analysis, their work confirmed that the hydrogen trapping behaviour is subject to the coherency of carbide/matrix interface as well as the hydrogen charging condition. Later, direct investigation of carbide hydrogen trapping via macroscopic SANS with room temperature liquid charging concluded the interior trappings of semi-coherent VC [155] and NbC [156] in BCC steels after room temperature liquid charging. Whereas Takahashi et al. applied APT with mildly heated (200℃) gas charging to directly observe the interface trappings in semi-coherent TiC and VC from their observation of APT [178, 199]. These inconsistencies in the conclusion about trapping site was theoretically discussed in the following works.

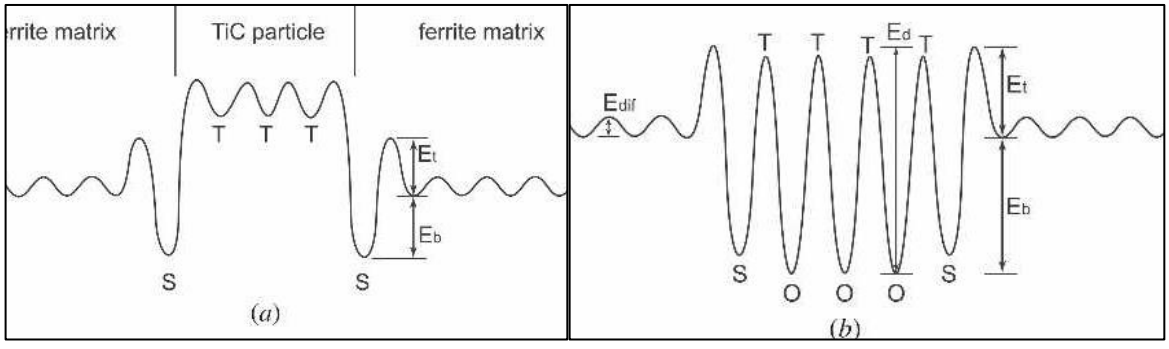

Figure 62 - Schematics of the hydrogen trapping energy profiles of (a) coherent TiC with interface trapping sites and (b) incoherent TiC having high energy barrier at the interface [49]

Via ab initio calculation, Kawakami and Matsumiya considered the relativity of hydrogen trapping strengths of interface and interior trapping sites in coherent FCC-type (rocksalt-structured) carbides [103], specifically TiC and V_4C_3 as representatives of IVb and Vb groups, respectively, as shown in Figure 63. They found that both carbides have strongest hydrogen trapping sites of carbon vacancy at the interior carbon vacancy sites (as shown in Figure 63(a)) and can perform mild trapping by the coherent strain at the vicinity of their interfaces and right at the interface as the broken and solid lines shown in Figure 63(b), respectively. This model suggests that a high energy barrier exists at the TiC interface and impedes hydrogen penetration into these vacancy sites at room temperature, which agrees with Wei and Tsuzaki's observation, whereas the barrier at V_4C_3 interface (thick broken line) is significantly lower than the case in TiC and is easier for hydrogen to penetrate and reach the strongest interior carbon vacancy trapping site.

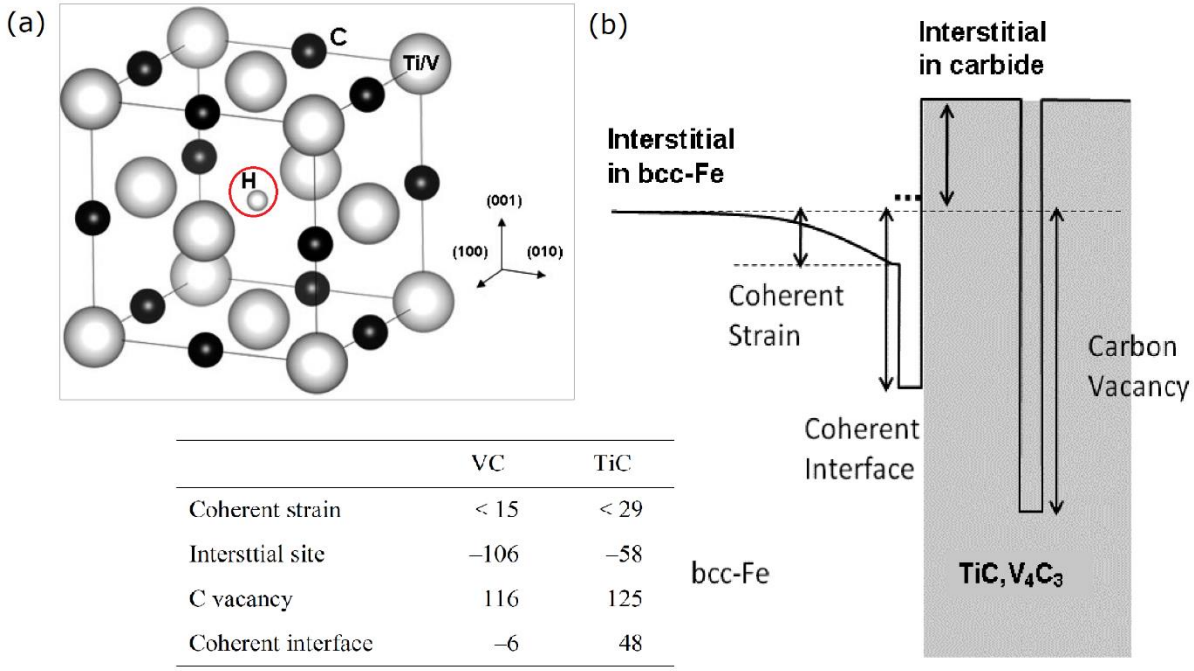

	VC	TiC
Coherent strain	< 15	< 29
Intersttial site	–106	–58
C vacancy	116	125
Coherent interface	–6	48

Figure 63 – Schematics of (a) the carbide unit cell and its carbon vacancy hydrogen trapping site and (b) the hydrogen trapping energy profiles of interface and interior trapping sites and their corresponding quantities of trapping energy in TiC (solid line) and V_4C_3 (broken line) precipitates [103]. The energy unit is kJ/mol.

Later in Di Stefano et al.'s work, the effect of continuously connected carbon vacancies (CCV) in these FCC-structured precipitates to hydrogen trapping and hydrogen penetration was additionally accounted [104]. They quantitatively depicted the energy profile experienced by penetrating hydrogen atom with and without the presence of CCV as shown in Figure 64, where the solid and broken lines correspond to the cases of single isolated carbon vacancy (ICV) and CCV, respectively. The trapping energies of the carbon vacancy at interface, the ICV and CCV inside the carbide are denoted as E_{INT}, E_{ICV}, and E_{CCV}, respectively. The relatively large values of E_{ICV} and E_{CCV} show these features are strong traps for the hydrogen atoms in both temporal and thermal respects. E_{B1} and E_{B2} are the respective energy barriers for hydrogen atoms to reach ICV and CCV sites. In the CCV case, the energy required for hydrogen reaching the interior is much lower than the case of ICV. Di Stefano et al.'s calculation suggests that the hydrogen trapping mechanism is sensitive to the quantity and distribution of interior carbon vacancies as well as the condition for multiple hydrogen atoms simultaneously occupying one of the connected vacancies. Their calculation shows that the escape energy for one of the trapped hydrogen atoms in a single sink that is occupied by two hydrogen atoms is significantly lower than the case of alone hydrogen in an energy sink. This is illustrated as the red broken line shown in Figure 64, where E_{2H} corresponds to the escape energy for one of the two trapped hydrogen atoms and is much smaller than its counterpart of E_{CCV}. This effect is likely to occur in high hydrogen concentration charging regime where excessive hydrogen is present such as in the case of liquid charging. It could facilitate hydrogen moving toward the interior of carbide as the traps can be easily occupied by the aggressive hydrogen atoms so the escape energy for the coming second hydrogen atoms in the trap are much decreased, as the red broken line shown in Figure 64. Consequently, it is reasonable to observe interior

hydrogen trapping if the hydrogen atoms moved inward through this mechanism during liquid charging which introduce excessive amount of hydrogen.

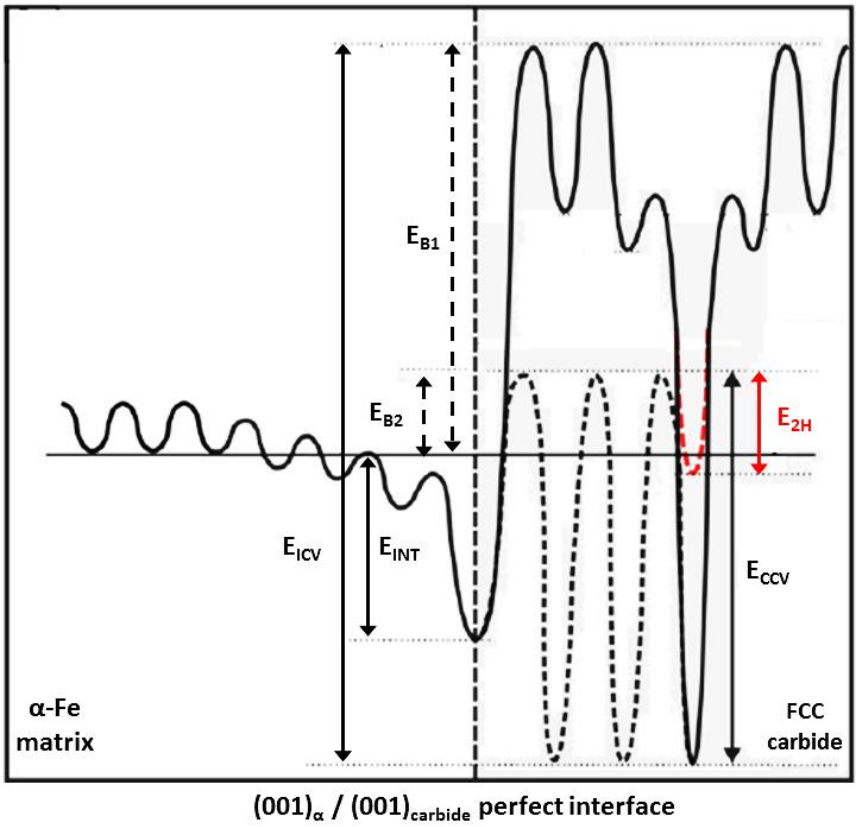

Figure 64 –The energy profile experienced by hydrogen around the carbide trap, which depicts both cases of single isolated carbon vacancy and multiple continuous vacancies inside the carbide [104]

Given the interior trapping requires the presence of CCV, the formation of CCV network in the transition metal carbides of TiC and VC is thus important and has been discussed in Yu et al.'s theoretical studies [150, 230]. They regarded the phase stability of various FCC transition metal carbide phases of Group IVb and Vb metals and concluded that the group Vb carbides such as VC and NbC are more likely to form a stacking-faulted phase incorporating a carbon-depleted layer with respect to the IVb carbides such as TiC. The presence of this layer could meet the requirement of CCV therefore allows the hydrogen penetration towards the interior of the carbide, as suggested by Di Stefano et al.'s model, hence the observation of interior trapping in Vb carbides in this work. In

comparison, the theoretical low tendency of TiC to form the stacking-faulted phase could be the reason that interior trapping is difficult to be experimentally observed in TiC given the absence of CCV and the high barrier to reach the ICV of Di Stefano et al.'s model.

With the understanding of these theoretical models, the experimental findings via APT and SANS can be explained as below. Whilst TiC does not allow interior hydrogen trapping given its high interface energy barrier, the contradictory findings of Takahashi et al. about the interface trapping of semi-coherent carbide of VC can result from their gaseous hydrogen charging method, which is the main difference with other studies. Their mild introduction of hydrogen only allowed the charged hydrogen being trapped at interface strain as depicted in Figure 63 without excessive hydrogen that can facilitate its penetration into the interior strong carbon vacancy trapping sites as shown in Figure 64. Whereas the present study and other SANS analyses used liquid charging that allowed excessive hydrogen for hydrogen penetration. In summary, hydrogen trapping mechanisms can be related to three factors: the coherency of carbide/matrix interface which can be adjusted via sample aging; the local structure of carbide, particularly the density of carbon vacancies and their connection which is related to carbide type (IVb or Vb group); as well as the experimental hydrogen charging method which determines the extent of excessive hydrogen within microstructure and its penetrability toward the carbide inside.

6.4 Summary

In this chapter, the efficacy of VCT in inhibiting hydrogen detrapping is demonstrated. With the use of VCT, both protium and deuterium trapping were detectable. However, even though in the analysis of the as-received material the hydrogen introduced by the analysis environment was not correlated to the carbides and the hydrogen-charged material was, the source of protium detected in the carbides must still be considered as ambiguous and the

use of deuterium for the characterisation of hydrogen trapping in APT is mandatory. In the observation of trapped deuterium, quantitative analyses were applied to determine the hydrogen trapping sites, which indicated that the hydrogen is located within the interior of the carbides studied, not the interface with the matrix. This hydrogen-trapping regime then was associated with the charging method and the thermodynamic characteristics of the studied carbide, particularly focussing on those of carbon vacancies. With the method developed in this study, more insight about hydrogen trapping mechanisms in carbide can be gained by applying this method to the other materials with similar constitution but at different aging stages.

7. Simplified APT Cryo-Transfer Protocol

In the last chapter, cryo-transfer was demonstrated as a necessary procedure to retain the charged hydrogen in traps during sample loading in order to characterise the filled traps during an atom probe experiment. However, the cryo-chain used in the last chapter (details as Section 3.4) not only requires specialised instrumentation such as the BAF and the transfer shuttle, but also significant and expensive modifications to the commercial atom probe, which reduces the applicability to other research laboratories with conventional APT instruments. This chapter presents results from the development of the simplified cryo-transfer method described in Section 3.5, which critically remove the instrument modifications requirement for hydrogen-trapping characterisation in atom probe technique.

7.1 Sublimation cleaning of the specimen surface

As described in Section 3.5.2, to load the hydrogen-charged and LN_2-cooled sample into the LEAP, the sample was removed from LN_2 and exposed to the ambient environment which contains moisture which in turn condenses on the cryogenic-cooled sample surface. This air cryo-transfer (ACT) process resulted in a layer of ice which undermines the geometric requirements of the atom probe sample. To regain the sharpness required, a sublimation-based process described in Section 3.5.3 was conducted in the LEAP buffer chamber.

Two trials of ACT were conducted, and the corresponding sublimation pressure logs are shown in Figure 37(b) in Section 3.5.3 highlighting the ongoing sublimation process from 20 to 50 minutes after the samples were removed from the analysis chamber cryogenic sample-stage. Images of the same specimen in their pre- and post-cleaning states are shown

in Figure 65, respectively, confirming the effectiveness of the sublimation treatment for removing the ice contamination around 100-200 µm in thickness.

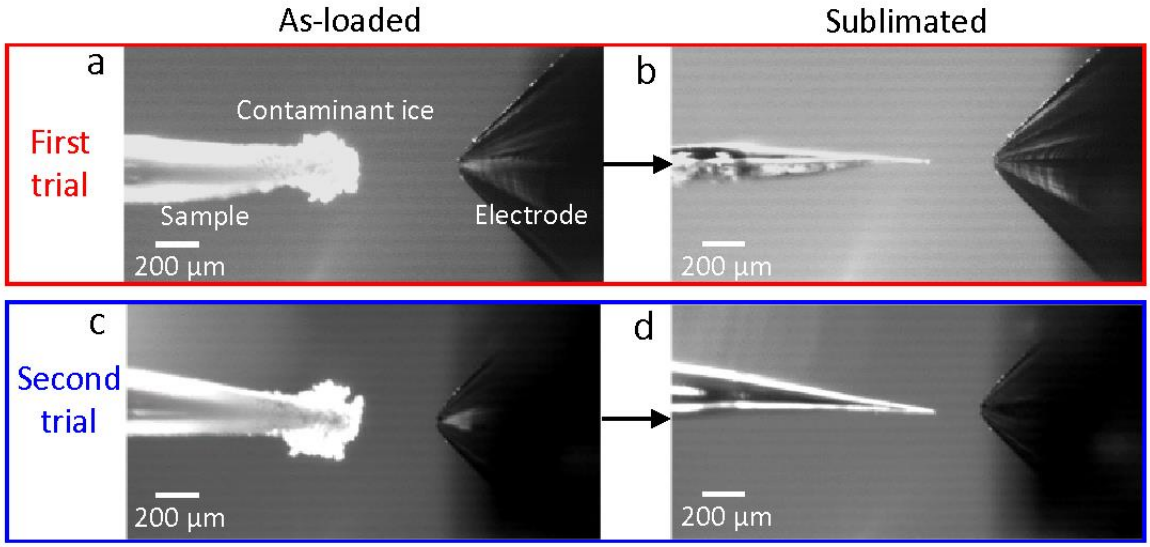

Figure 65 – Two tips showing the result of sublimation cleaning for ice contamination in different trials. (a) and (c) are the status prior to sublimation, which are significantly contaminated. (b) and (d) show the tips after 55 and 90 min of sublimation, respectively. The 55 min is the minimum time needed to clean the tips based on the tip images.

7.2 Sample temperature measurement

According to the water phase diagram shown in Figure 35 in Section 3.5.1, the ice-cleaning sublimation inevitably induces sample heat-up. This heating is undesirable particularly in the present study which aims to remain the sample temperature as low as possible for the immobilisation of charged hydrogen. As discussed in Section 2.2.4.3, hydrogen desorption is susceptible to thermal interference, even at cryogenic temperatures [204]. Accordingly, the ability to trace sample temperature is critical for associating the observed microstructural hydrogen distribution and quantity to the thermal history of the specimen before reaching the APT analysis stage.

The measurements based upon monitoring the thermal linear response of the analysis stage, described in Section 3.5.4, are shown in Figure 66. As illustrated in the top schematic,

besides the point specified by the red broken line corresponding to the time that the sample arrived the cryo-stage with 62.7K peak temperature, the green, magenta, and blue broken lines correspond to the sublimation time of 30, 63, and 90 minutes in the buffer chamber before being transferred back to the sample-stage where peak temperatures of 63.4K, 66.5K, and 68.1K were measured, respectively. Substituting the value of these peak stage temperatures into eq(11) in Section 3.5.4 enabled the peak sample temperatures to be determined as 117K, 135K, 204K, and 240K, respectively. The result of 117K indicates the effectiveness of the cryo-block (described in Section 3.5.2) for maintaining cryogenic status of the sample from 77K of LN_2. Regarding the sublimation time of the samples and their corresponding temperatures, the heating during the sublimation process can be plotted as the blue linear fit in Figure 67 which can be expressed as

$$T_{sample}(K) = 2.01\, t_{sub} + 67.76 \tag{12}$$

where T_{sample} is the sample temperature in Kelvin, t_{sub} in minute is the sublimation/heating time, namely the elapsed time in the buffer chamber. Given the consistency of the sublimation procedure shown in Figure 37(b) in Section 3.5.3, this relationship can enable an estimate of the sample temperature for any given sublimation time.

Alternatively, as described in Section 3.5.4, prior literature provides a table to associate the pressure and temperature during ice sublimation in a UHV environment [224]. The results obtained from this table are plotted as the orange data shown in Figure 67. The fitting of the data then gives another prediction of the sample hearing during the sublimation process, which can be expressed as

$$T_{sample}(K) = 1.22\, t_{sub} + 130.61 \tag{13}$$

The deviation of eqs (12) and (13) from each other might be due to either the limited data statistics or the applicability of the previous assumption about the stage method (Section 3.5.4). Provided more measurement involving in the literature [224] to acquire both pressure and sample temperature, the pressure method associated to the literature is regarded as less certain than the stage method proposed in this study. Accordingly, eq(12) from the stage method is used to determine the sample temperature in this study.

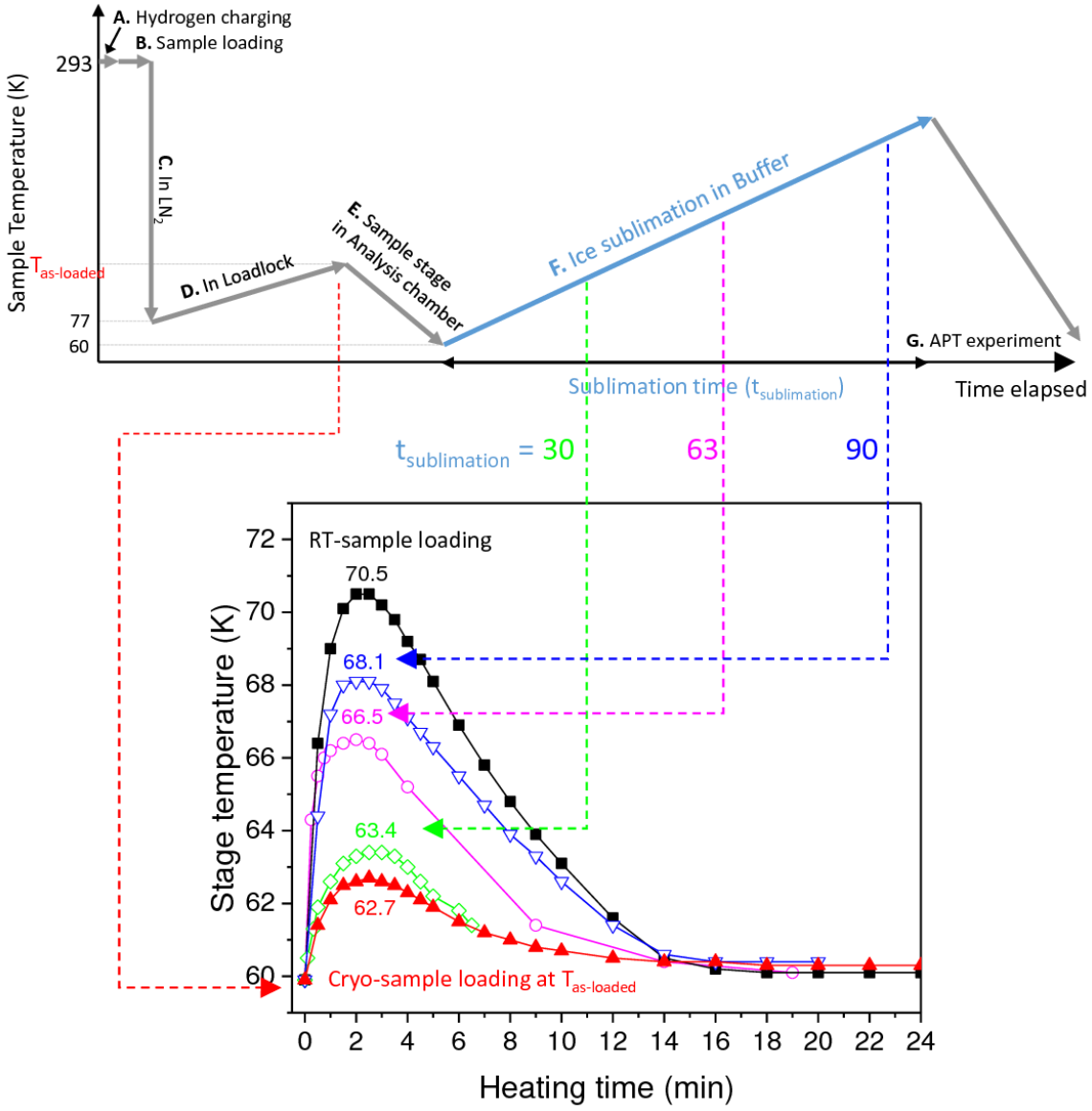

Figure 66 – Sample thermal history diagram from the simplified cryo-transfer method and the temperature logs of the sample-stage in the analysis chamber correspond to 30, 63, 90 minutes of sublimation time as well as the as-loaded and RT-sample data. The logs give 62.7K, 63.4K, 66.5K, and 68.1K of the peak temperatures in the calculation of eq(11). Then 117K, 135K, 204K, and 240K were correlated to the given sublimation times, respectively.

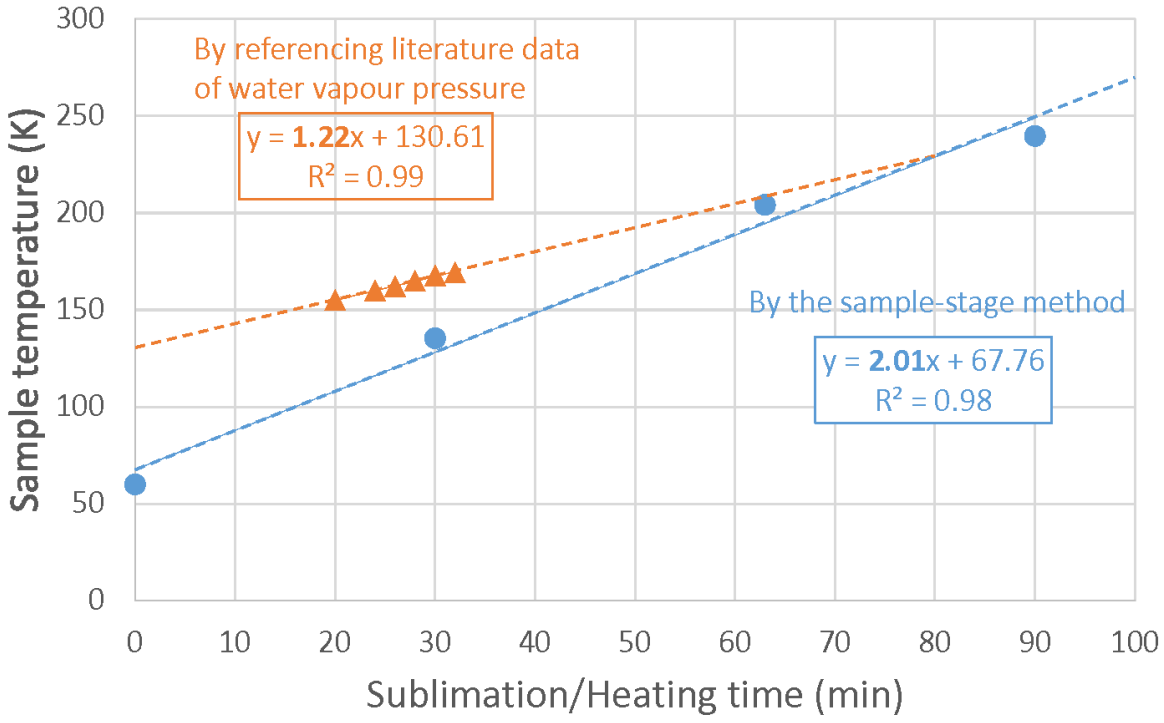

Figure 67 – Blue dots are the sample temperatures determined from Figure 66 and eq(11) and the zero point of the sample-stage temperature, 60K. The blue broken line is the linear fit of the dots, which gives the fitting equation of eq(12). Orange dots are the data referenced from [224] and the broken line is their linear-fitting result which gives eq(13) to describe the heating during the sublimation process.

7.3 Atom probe results from Air Cryo-Transfer

After deuterium charging, the samples were immediately immersed in LN_2. Subsequently, the ACT procedure was used to load the specimen into the atom probe, followed by a sublimation time of 50 minutes in the buffer chamber. This sublimation time corresponds to an estimated peak specimen temperature of 168 K by eq(12). The atom probe mass spectrum acquired from the resulting APT analysis (datafile R14_25556 incorporating 3 million ions after removing surface layer) is shown in Figure 68(a) where significant 2 Da peak corresponding to the charged deuterium can be observed. The data shows 85 atppm. of deuterium content, which is higher than the room-temperature transfer protocol in Section 5.2. In addition, the spatial distribution of the deuterium was examined

by NN analysis (Section 3.2.8.3) as shown in Figure 68(b). The NN distribution suggests the clustering of deuterium however with limited certainty due to the limited data statistics. The spatial correlation between deuterium atoms and carbide traps was examined in the reconstructed atom map as shown in Figure 69. In the 10-nm-thick slices, spatial correlations between deuterium and carbides are visually apparent.

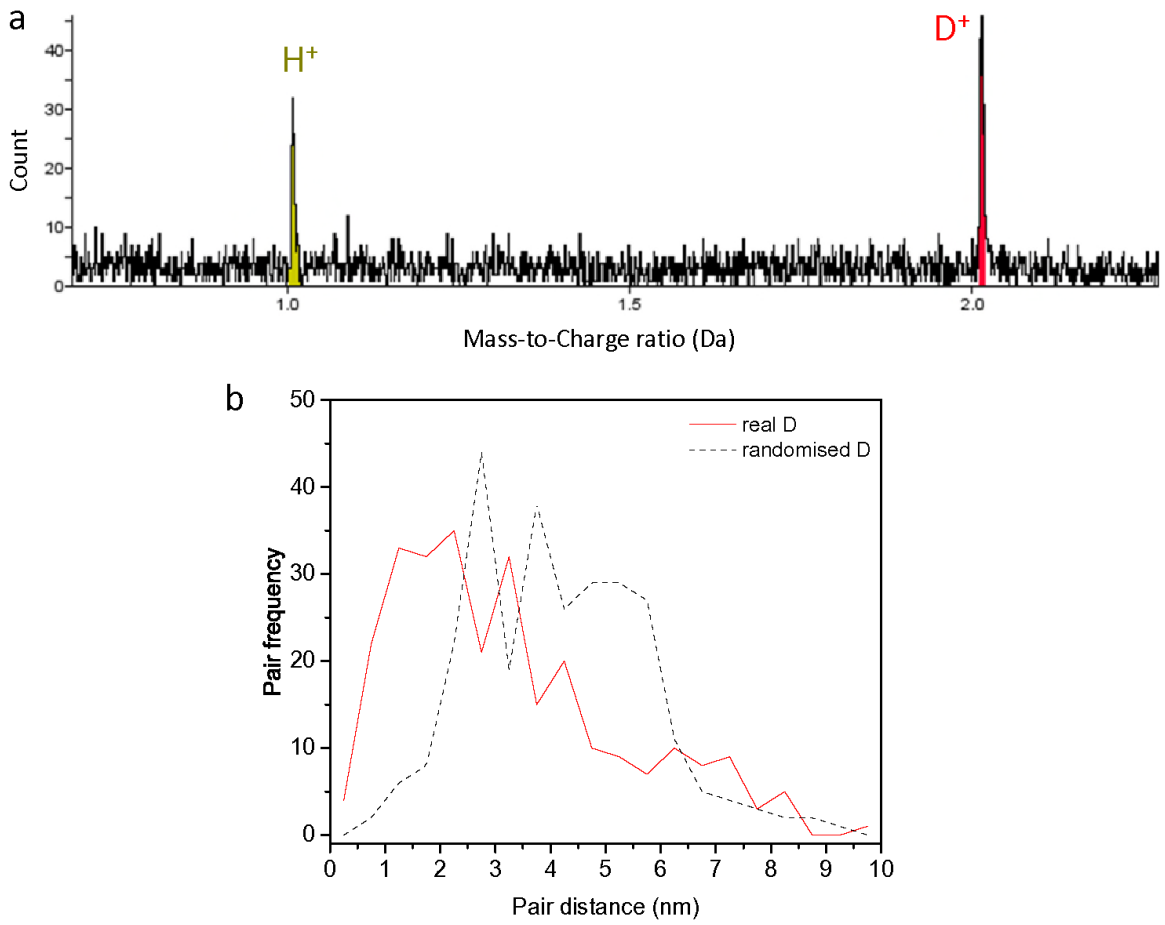

Figure 68 – (a) Mass spectrum of deuterium-charged sample using ACT, where significant 2 Da peak corresponding to the retained D can be observed. (b) The NN distribution of D, indicating possible clustering in the APT data.

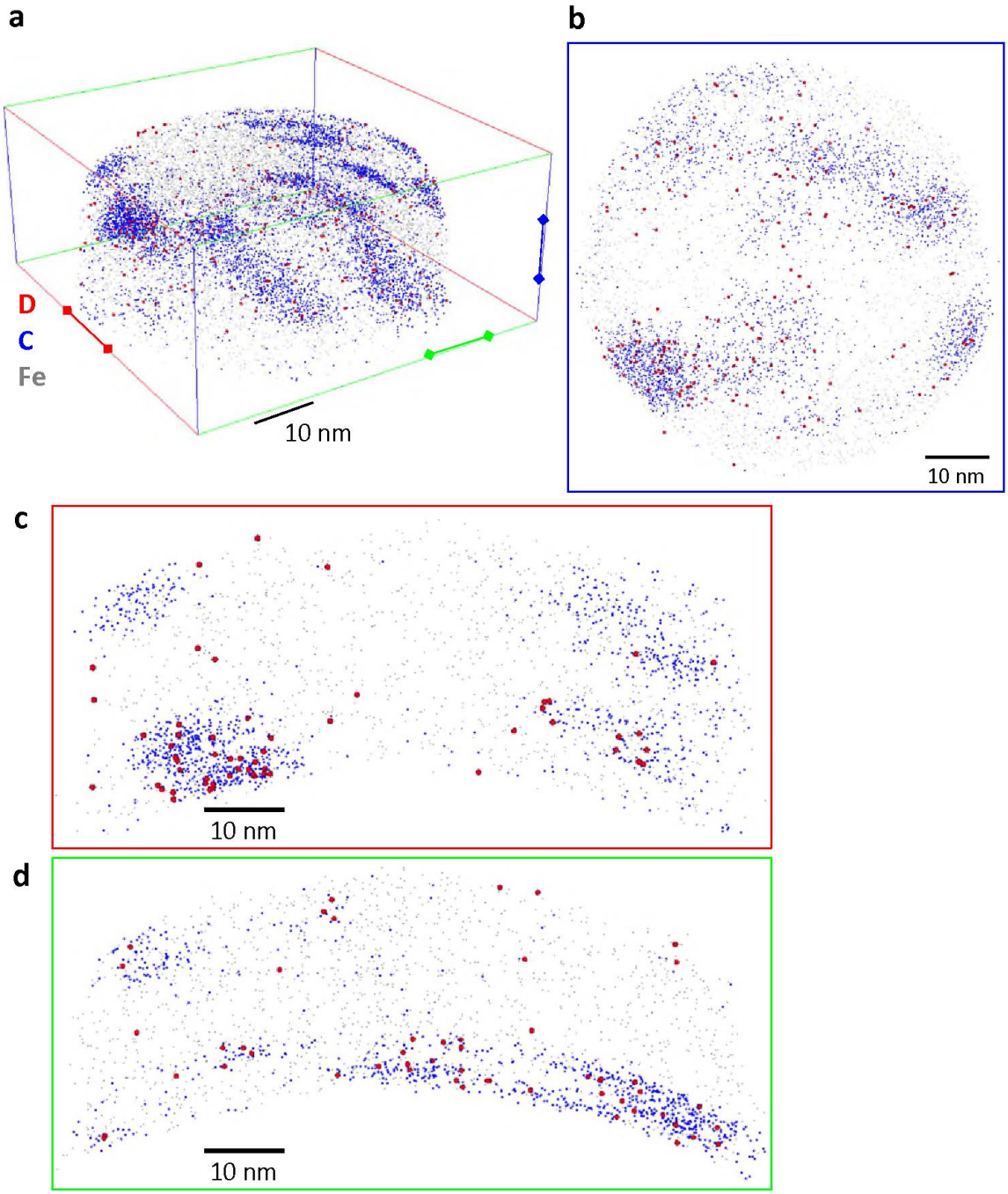

Figure 69 - APT atom map of ACT sample and its slices showing the location of trapped D atoms, which are (a) global map, (b) top-down x-y plane slice, (c) side y-z plane slice, and (d) side x-z plane slice. Each slice is 10-nm in thickness. All maps show only D, C, and 1% of Fe ions for clarity.

7.4 Dry Cryo-Transfer

As described in Section 3.5.5, ice contamination introduced from the ambient air (shown in Figure 65 in Section 7.1) undermines the atom probe sample requirement and

requires an undesirable extended sublimation cleaning process which heats up the sample and hence could result in detrapping of the charged hydrogen. Therefore, if the ambient moisture experienced by the cryogenic sample can be minimised, then the induced contamination should be reduced. Reduced contamination would require less time to sublimate any ice and in-turn reduces the extent of heating of the hydrogen-charged sample, minimising any hydrogen loss/diffusion.

7.4.1 Condensed moisture measurement at LN_2 surface

Moisture condensation measurements at the LN_2 surface were conducted using the configuration described in Section 3.5.5. As shown in Figure 70(a), a series of relative humidity (RH) time-elapsed measurements, including inside the glove box (green triangles) as well as the surfaces of LN_2 in air (blue dots) and inside the box (red squares), were undertaken and compared to the ambient value (black squares) for reference. When the moisture supply was limited by the box whilst the LN_2 was present in the box, the RH in the box environment was found to be lower than the ambient level at all the times during the experiment and decreased further with elapsed time due to the moisture condensation of the LN_2. This result suggests that the isolation provided by the box can effectively limit the moisture supply and hence reduce the environmental RH experienced by the sample. Furthermore, at the beginning of the test time, the LN_2-surface datasets at first increase with time because of the combined effects of establishing moisture condensation and reducing temperature due to the adjacent LN_2 surface, but then progressively decreased due to the descent of the LN_2 surface which allows the moisture levels and temperature to be returned to the conditions that moisture fully condensed at the LN_2 surface. The respective in-air and in-box relative humidities in Figure 70(a) show that in the current configuration moisture condensation at the LN_2 surface is inevitable regardless the use of box isolation. In order to

confirm the relative humidity decrease corresponds to the descent of LN_2 surface, the in-box RH sensor was manually moved back to the LN_2 surface after 20 minutes of the elapsed time during the measurement, which resulted in the regain of RH and a second progressive descent as shown in Figure 70(b). This result confirms the existence of the condensed moisture at the LN_2 surfaces. However, the investigation of the exact thickness of this moisture-condensed layer requires the understandings of both temperature gradient and the moisture supply at the LN_2 surface which requires the development of sophisticated computational models beyond the scope of this work.

With the evidence of this condensed moisture, the block-hat in the configuration shown in Section 3.5.2 is thus necessary for minimising sample contact with this layer. In this arrangement, once the cryogenically cooled sample passes through the layer, the low-humidity atmosphere within the glove-box space other than the LN_2 surface should allow less ice formation on its surface during the transfer as schematised in Figure 42.

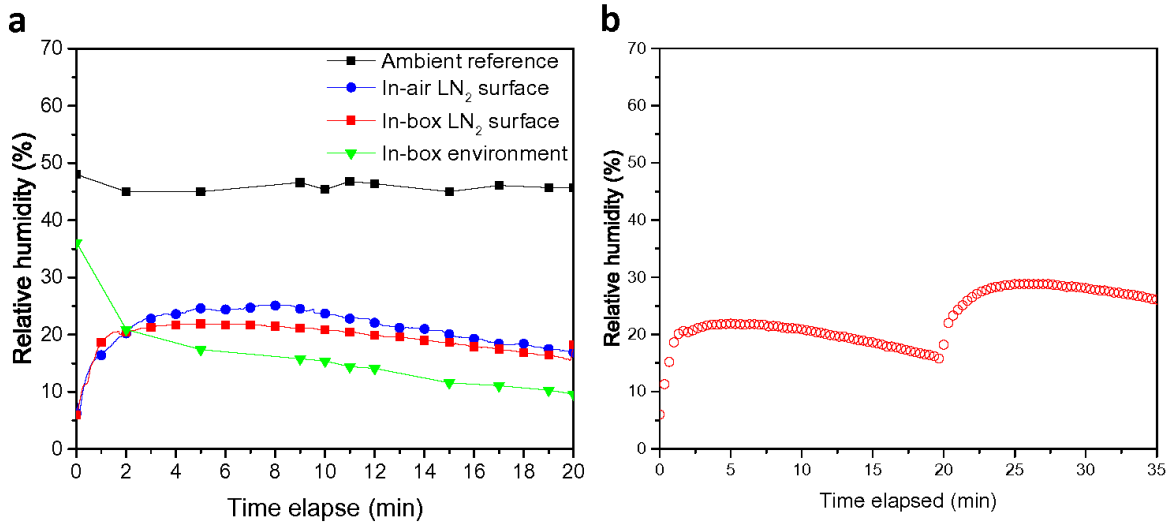

Figure 70 – (a) The measurements of relative humidity in the ambient (black) and in-box (green) environments, and at the vicinity of the LN_2 surface in open space (blue) and the box (red). (b) The change of humidity at in-box LN_2 surface as the sensor repositioning to the vicinity of evaporating LN_2 surface at 20 min of measuring time.

7.4.2 Reduced ice contamination

As shown in Figure 71(a), the DCT allows less ice contamination to be introduced as compared to the specimen that underwent ACT to the atom probe (Figure 65). The DCT tip then was cleaned in the buffer chamber, and the resulting vacuum pressure is plotted as a function of time by the red squares in Figure 71(c). The time for the DCT sample to fully sublimate the ice contamination is clearly less as compared to the ACT (plotted with black circles). This shorter sublimation time then can be correlated to a lower estimated peak sample temperature of 148K according to eq(12). This result confirms the use of dry box can effectively reduce the ice contamination, hence the sublimation time, and the final sample temperature from 168K using ACT to 148K using DCT.

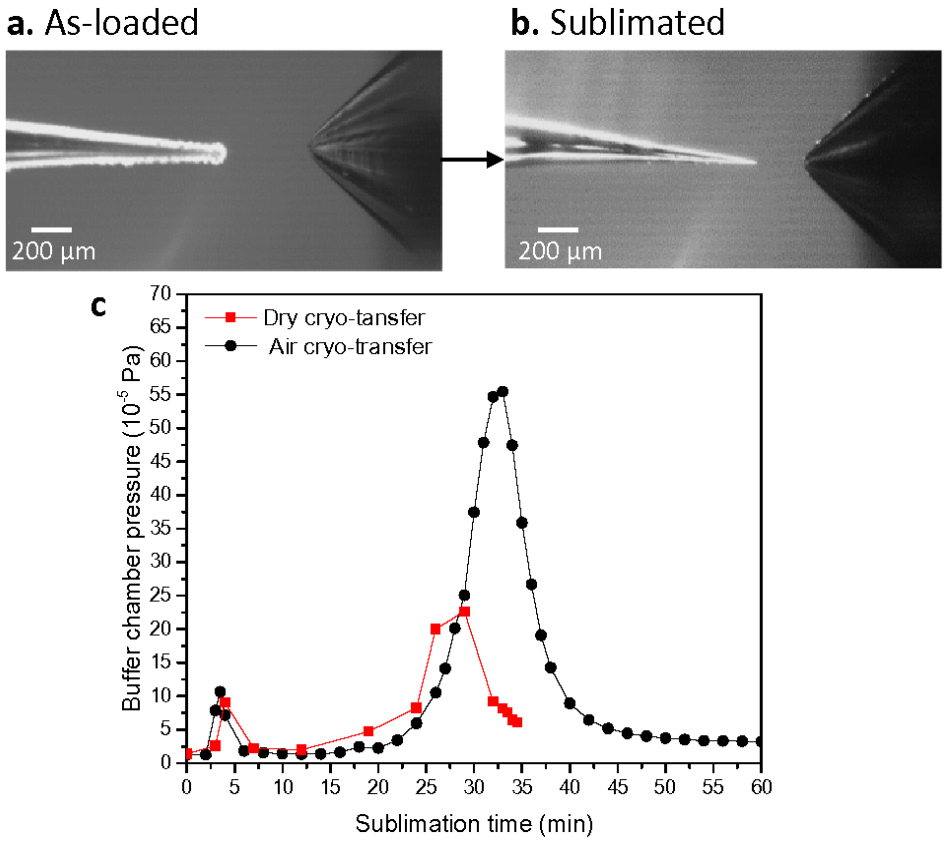

Figure 71 –(a) The reduced ice contamination after the application of DCT, and (b) the sublimated sample. (c) The sublimation pressure log in the buffer chamber which shows a shorter time of sublimation as compared to air cryo-transfer method. This shorter time then can be corresponded to lower sample temperature after sublimation according to eq(12).

7.4.3 Atom probe results from Dry-Cryo Transfer

Two datasets (R14_25335 and R14_25438 incorporating 3 million and 1.7 million ions, respectively) were obtained from two successful trials of the DCT experiment. Both analysed specimens correspond to peak temperature of 148K associated by eq(12) with their sublimation time. The surface layers of both datasets were removed. Figure 72 shows the significant deuterium peaks from the datasets which correspond to 26 and 69 atppm., respectively. This variability will be discussed in further detail below.

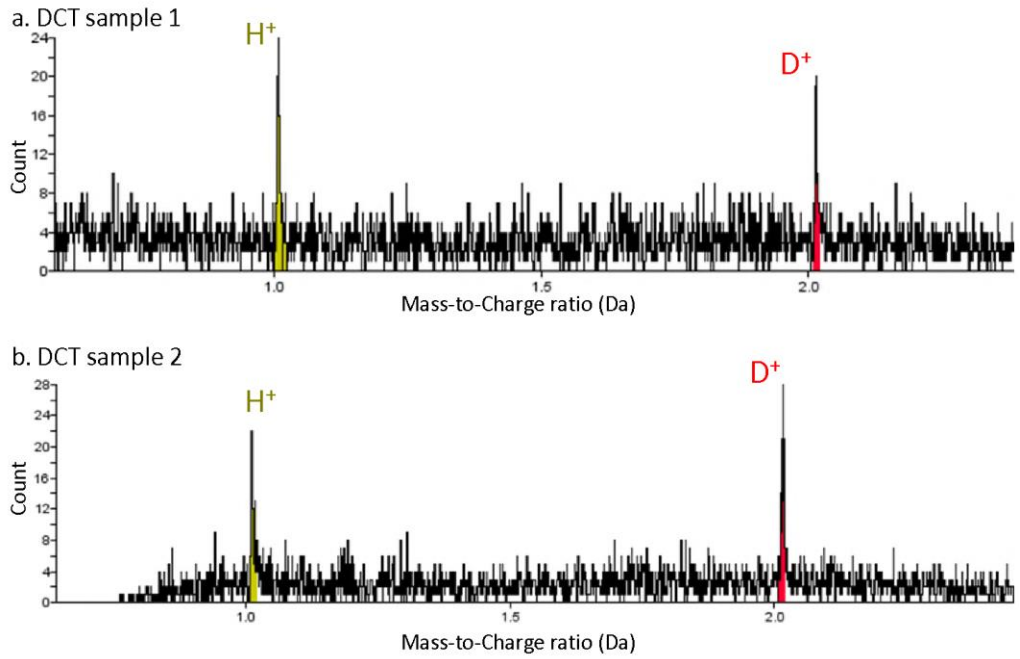

Figure 72 - Global mass spectra of two DCT samples from the datasets (a) R14_25335 and (b) R14_25438.

The spatial correlation between the locations of deuterium atoms and the carbides was examined in the reconstructed atom maps shown in Figure 73. The carbide-associated deuterium can be seen from the sliced sections of the maps of Figure 73(b), (c), (e), and (f). These results indicate that the DCT method is sufficient to reduce the deuterium detrapping during the sample transfer to the atom probe and hence enables the observation of deuterium trapping in the carbides.

DCT sample 1

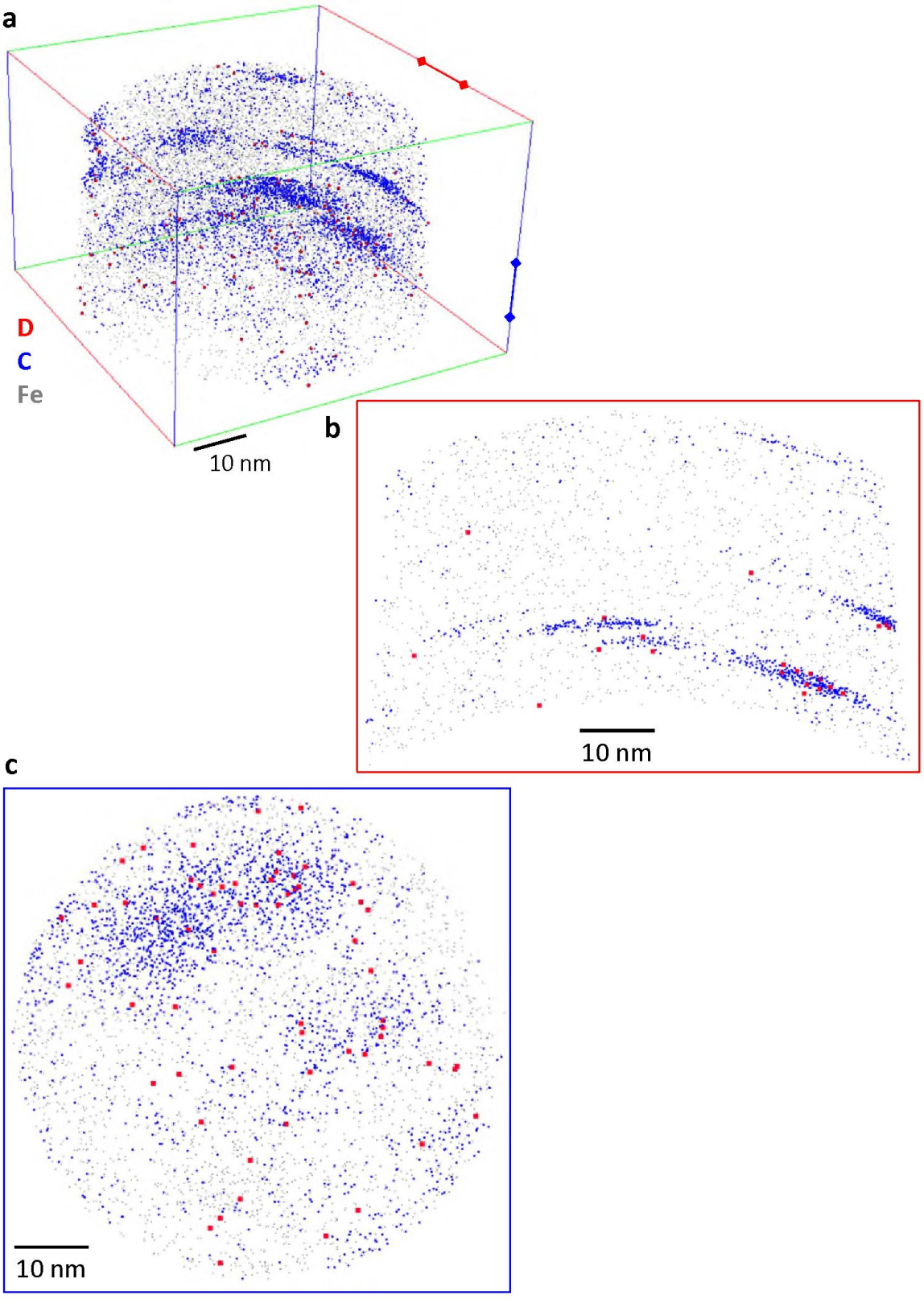

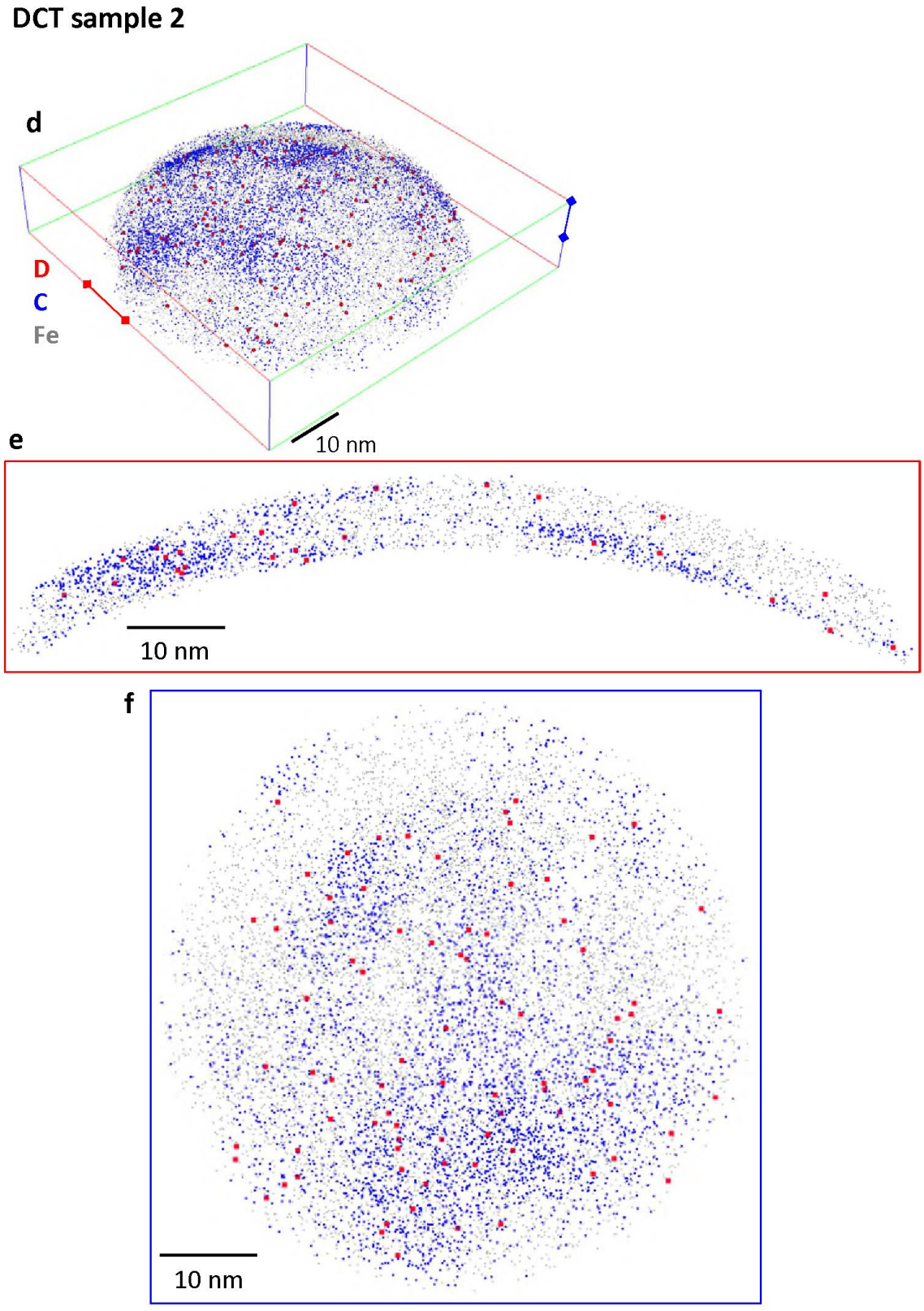

Figure 73 – Resulting APT full atom maps and slices of experiments on two DCT samples (labelled 1 & 2). (a) and (d) are Global maps. (c) and (e) are top-down x-y plane slices, and (b) and (f) are side y-z plane slices, where localised D atoms can be observed more easily than in the global maps. Each slice is 10-nm in thickness. All maps show only D, C, and 1% of Fe ions for clarity.

7.5 Discussion

7.5.1 Deuterium retaining abilities of the transfer methods

To quantitatively assess the sample-transfer methods to the atom probe presented in this work, the clusters from all the discussed deuterium-trapping datasets from Chapter 5 to 7 were extracted by the cluster definition stated in Section 4.2.2. For each APT transfer protocol, the number of detected deuterium atoms in each carbide is plotted as a function of the total number solute atoms incorporated by that carbide as shown in Figure 74. Linear fitting then was applied to each set of data and the value of the slope derived. This slope represents a measure of the number of trapped/retained deuterium per unit carbide ion, namely the deuterium retaining ability. Hence Figure 74, provides a comparison of relative deuterium retaining ability, where the ACT (blue) and VCT (red) experiments appear to demonstrate the best deuterium retention, then DCT (green, combining both datasets obtained), and RT-transfer is the least effective. All methods in which the specimen is cryogenically cooled certainly appear to demonstrate better deuterium retaining abilities than RT-transfer.

7.5.2 Threshold temperature for hydrogen detrapping

Given hydrogen desorption is a thermally-activated process [48, 232, 233], the DCT and ACT processes resulting in different temperatures (estimated to be 148K and 168K, respectively) would be expected to lead to different measured normalised contents of deuterium. This however is contradicted by the result shown in the corresponding slopes of DCT and ACT in Figure 74 which would appear to imply that deuterium has been most effectively retained in the ACT experiment. This could either be attributed to data scatter due to the limited size of the APT datasets or alternatively imply that in this system the

deuterium retaining ability is not sensitive to the range of temperature reached by the sample in these experiments.

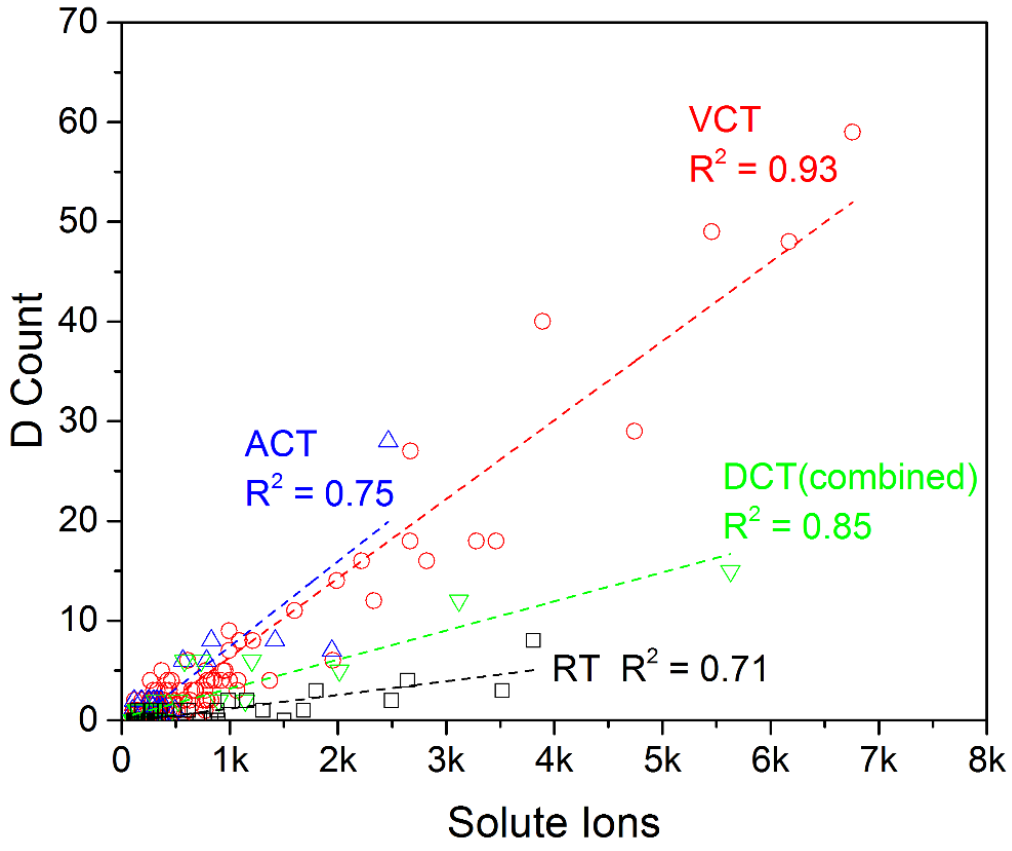

Figure 74 –Comparison of the linear fit slopes of data from all APT transfer methods to investigate the relative ability of retaining charged D. Each spot means the retained D content in a single carbide trap. The linear fits of the spots represent the trends of D retaining ability of respective methods. VCT (red), ACT (blue), and DCT (green) all show better abilities to retain charged D as compared to RT method.

7.5.3 Cluster-size effect to hydrogen trapping

In order to examine the deuterium capacity with regard to the cluster size, the deuterium concentration of individual carbides for all transferring methods are shown in Figure 75. RT-transfer (black squares) once again shows the least retaining power among all the APT specimen transfer methods applied. However, this figure does not show apparent relation between deuterium content and cluster size. This indicates that the deuterium content is not necessarily related to cluster size and the in-cluster deuterium contents, namely there is no

clear relationship between the trapping abilities of small and big clusters. This finding fits well to the interior trapping mechanism suggested in Section 6.3.4, which implies the content of trapped deuterium in carbide should be at a fixed level depending on the number of carbon vacancy networks and contradicts an interface trapping model which should see more effective deuterium contribution from small carbides having high surface/volume ratios with respect to large carbides. This finding also agrees with the observations of Takahashi et al. which actually suggests the deuterium trapping efficiency (deuterium content in each carbide) is independent of carbide sizes if normalising the deuterium counts by the numbers of carbide ions [199].

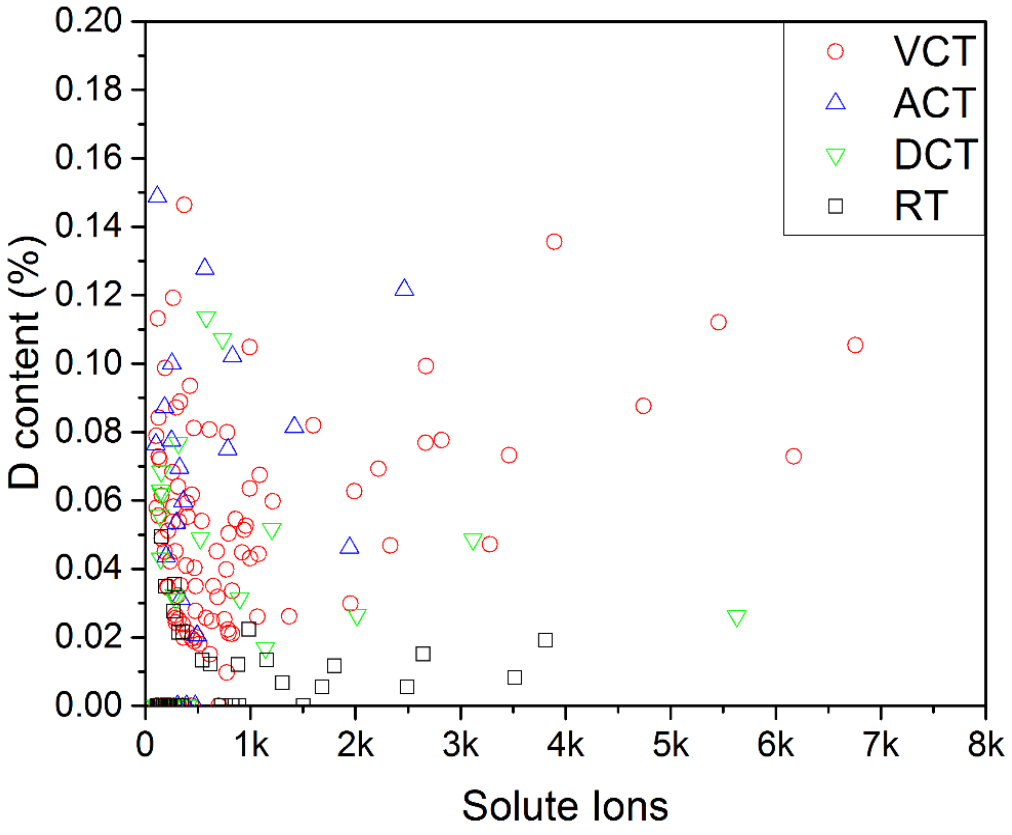

Figure 75 – D content of all collected carbides from all transfer methods. The figure shows all the methods used in this study allow more deuterium being retained in the carbides than RT transfer.

7.6 Summary

In this chapter, instrument modification-free alternatives to the VCT cryo-chain, i.e. ACT and DCT, were developed and their implementations were described in detail. This is of great importance in term of the applicability of the techniques to the atom probe system in other laboratories interested in the characterisation of hydrogen trapping. The critical challenge with respect to the formation of ice contamination on the cryogenic sample surface was addressed by the application of a sublimation cleaning procedure in the atom probe buffer chamber. In the sublimation process, the sample heating was able to be quantified by both the thermal linear response of the atom probe sample cryo-stage in the analysis chamber and also by associating the pressure in the buffer chamber with the literature data for the region of water phase diagram regarding vapour pressure in UHV. In association with the sample temperature, the observed hydrogen trapping confirmed the effectiveness of the proposed methods in respect of atom probe hydrogen-trapping characterisation. Finally, the datasets regarding the APT analysis of hydrogen trapping utilising the different specimen transfer protocols in this thesis were compared. The comparison shows that for the purposes of characterising the bearing steel in this study the proposed sample transfer methods are as applicable as VCT in term of retaining loaded hydrogen. Furthermore, this work investigated the relationship between carbide trapping ability and carbide size, which used to be overlooked in the literature. The ability and the carbide size do not show significant relation dependent, meaning the bigger carbides are not necessarily able to trap higher content but only higher number of deuterium.

8. Investigating Hydrogen Pickup Route using Cryo-APT

8.1 Hydrogen uptake during electropolishing

In a previous study by Karnesky et al. using APT to study hydrogen trapping in metal [198], concerns were raised that in the case of samples pre-charged with deuterium during sample preparation the protium from electro-polishing solution may replace the deuterium. They claimed this protium replacement undermined their pre-deuteration, but when they used deuterated acid for electropolishing preparation protium replacement was avoided. And they believe the additional deuterium source even enhanced the D signals in their proposed microstructural traps. In this section, this protium-deuterium replacement effect in microstructural traps during electropolishing preparation is examined by using fully deuterated acid (2% deuterated perchloric acid in deuterated 2-butoxy ethanol) to polish as-received samples. Then as-polished samples are subsequently cryo-transferred to the atom probe to freeze the hydrogen diffusion directly after electropolishing process, before APT analysis as before.

Three trials with three samples within a single cryo-transfer cycle were attempted with the DCT procedure stated in Section 3.5. Their resulting APT mass spectra are shown in Figure 76, where only one sample containing a small amount of deuterium (43 counts in 500 thousand collected ions) can be seen after removing surface contamination in all datasets. The spatial correlation between the deuterium signals and the carbide clusters then was examined in the data reconstruction. As shown in Figure 77, no visually discernible spatial correlation of the carbides (vanadium atoms shown in green) with deuterium (red) can be seen, neither with hydrogen (dark yellow). This randomly distributed deuterium

could be introduced into the microstructure and retained the by sample surface barrier effect as discussed in Section 5.2.

All the deuterated-electropolishing results showing here do not support Karnesky et al.'s claim about the signal enhancement and replacement at hydrogen trap. This difference may originate from the different types of materials and their difference in trap type, where an austenitic steel and nitride precipitate traps were applied in their study. A program of repeat experiments using matched material may be required in order to further confirm their claims.

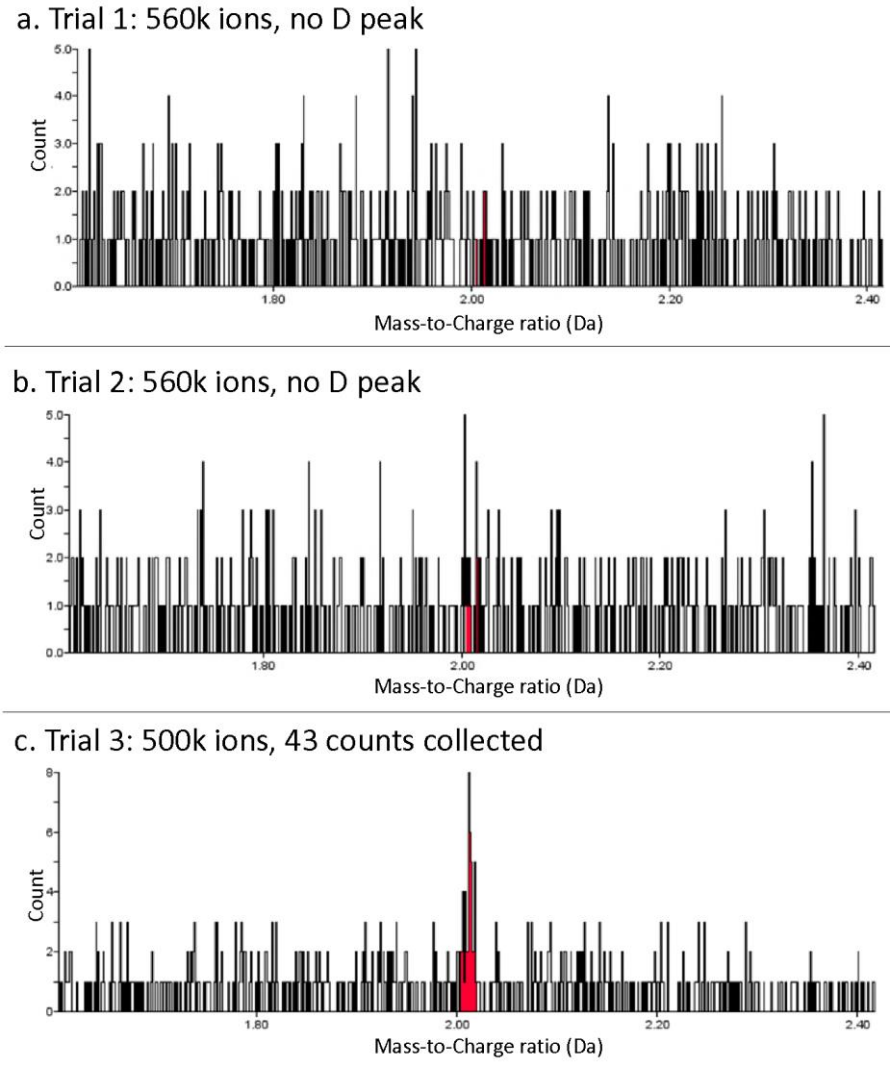

Figure 76 – Mass spectra from three trials of the deuterated-acid-polishing experiments (R14_25638, R14_25641, and R14_25639 in the order of trail number). Only the third data R14_25639 shows 43 counts of deuterium in 500k ion statistics.

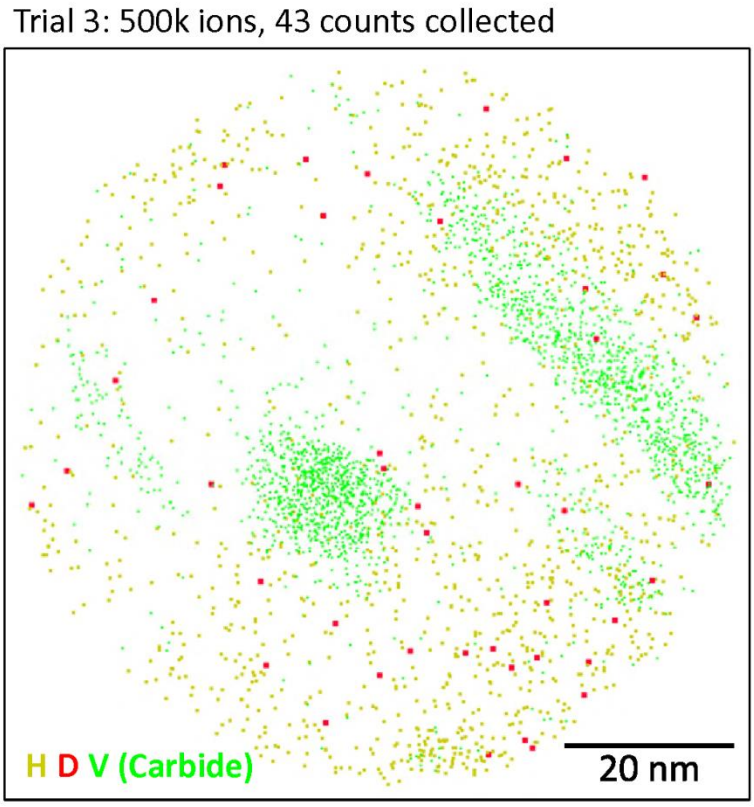

Figure 77 – Top-down overview of the entire dataset of the third trial in Figure 76 having deuterium signal. No spatial correlation is observed between the carbides and detected D.

8.2 Hydrogen uptake source in liquid charging

As discussed in Section 2.1.2, the hydrogen uptake via hydrogen liquid charging is typically assumed as from the dissociation of water molecule. However, when using NaOH solution, the electrolyte is also a potential source of hydrogen that could contribute to hydrogen uptake into the material. Similar concerns regarding the pickup source of hydrogen were raised in a study of Jambon et al. for understanding the effects of corrosive media in a pressurised water reactor attacked by a gaseous mixture of hydrogen and water vapour [234]. By using deuterium as a hydrogen tracer and SIMS which has very good resolution to hydrogen isotopes, the authors successfully demonstrated that the hydrogen pickup originated from water vapour in the gas-vapour mixture. Given APT also has the ability to unambiguously resolve hydrogen isotopes, this isotope-tracer method should be

applicable in atom probe. Accordingly, deuterium as a hydrogen tracer was introduced into various combinations of liquid-charging solutions listed in Table 9 for understanding the hydrogen pickup during liquid-charging. The implications for these trials are also stated in Table 9. The results of first two solutions in Table 9, i.e. NaOD in D_2O and NaOH in H_2O, have been shown in Chapter 6, and the charging experiments (Section 3.3) with the use of the last two solutions were followed through application of the DCT method (Section 3.5.5) to retain trapped deuterium.

Electrolyte	Solvent	Purpose or implication in this study
NaOH	H_2O	Confirm 2 Da peak is not from H_2^+ ion and atom probe applicability for protium-trapping study
NaOD	D_2O	Confirm atom probe applicability for deuterium-trapping study
NaOD	H_2O	If trapped deuterium is observed, then **electrolyte** is the source of hydrogen pickup
NaOH	D_2O	If trapped deuterium is observed, then **water** is the source of hydrogen pickup

Table 9 – Liquid-charging solutions with various combinations of electrolyte and water solvent for investigating the source of hydrogen pickup during charging.

- **NaOD-H2O charging**

Figure 78 shows the APT analysis of the steel charged with 0.1M NaOD-H_2O, and the mass spectrum of Figure 78(a) shows no deuterium signal being detected. This result implies the NaOD in the solution did not actively contribute to any hydrogen/deuterium introduction into the sample. In addition, the hydrogen clustering was confirmed by the NN distribution analysis (Section 3.2.8.3) in Figure 78(b) and the direct observation in the atom-by-atom reconstruction of the data in (c). The spatial correlation between hydrogen (dark yellow) and the carbides (shown by green vanadium atoms) is seen in this dataset whereas the deuterium signal (red) is negligible. This hydrogen trapping observation is consistent with the results from normal-solution charging shown in Section 6.1.

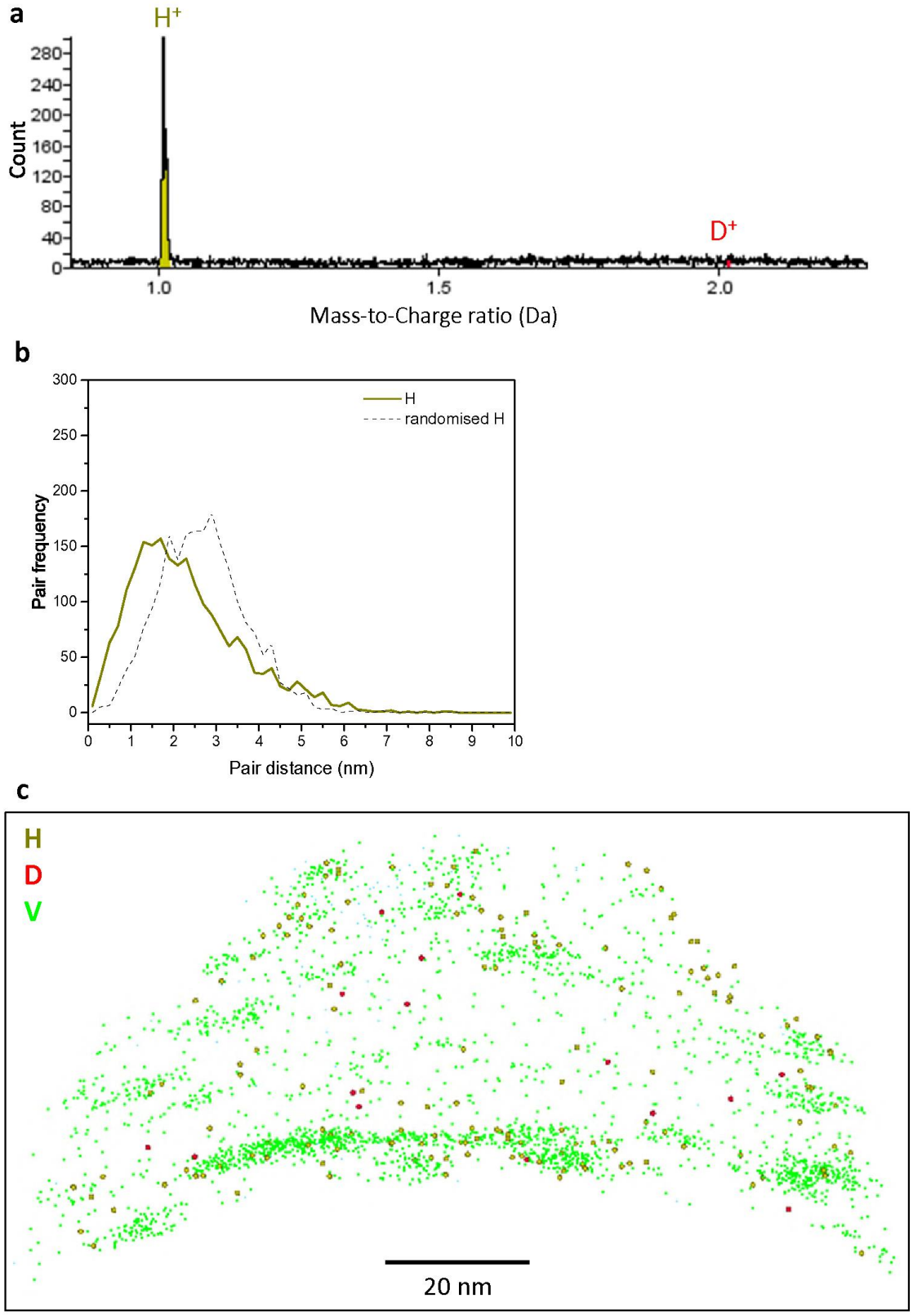

Figure 78 – Datafile R14_26012 with 7.9M ions statistics. (a) Mass spectrum of a NaOD-H_2O-charged sample. No D is observable, confirming the insignificant role of electrolyte in liquid charging. (b) shows the clustering of H atoms by NN distribution and its trapping in the carbides by (c) of y-z 10nm slice.

- **NaOH-D_2O charging**

Figure 79 shows the experimental results of 0.3M NaOH in D_2O charging. The mass spectrum of Figure 79(a) has a significant deuterium peak with respect to the hydrogen one, the latter of which is presumed to come mostly from background hydrogen. This means deuterium from the heavy water is the primary source of hydrogen in this charging solution. Regarding hydrogen clustering, Figure 79(b) NN distribution shows a significant clustering of the collected deuterium signal in analysis. The reconstruction in Figure 79(c) confirms the spatial correlation between deuterium atoms and the carbides, whereas the hydrogen signal is more homogeneously distributed. These results show the effectiveness NaOH-D_2O solution and the active role of the charging solvent to deuterium introduction.

In summary, with the use of isotopic hydrogen tracer, as well as the cryo-transfer method developed in this study, the pickup source of hydrogen as water solvent in electrolytic charging was critically determined by APT. This finding suggests that trapped hydrogen is primarily from the water rather than the electrolyte during electrochemical charging and implies that the use of NaOD in liquid charging may not be necessary. This implication could have useful implications in terms of cost effectiveness when considering using deuterated liquid-charging experimental set-ups, as well as offering an insight into ion migration mechanisms during the charging.

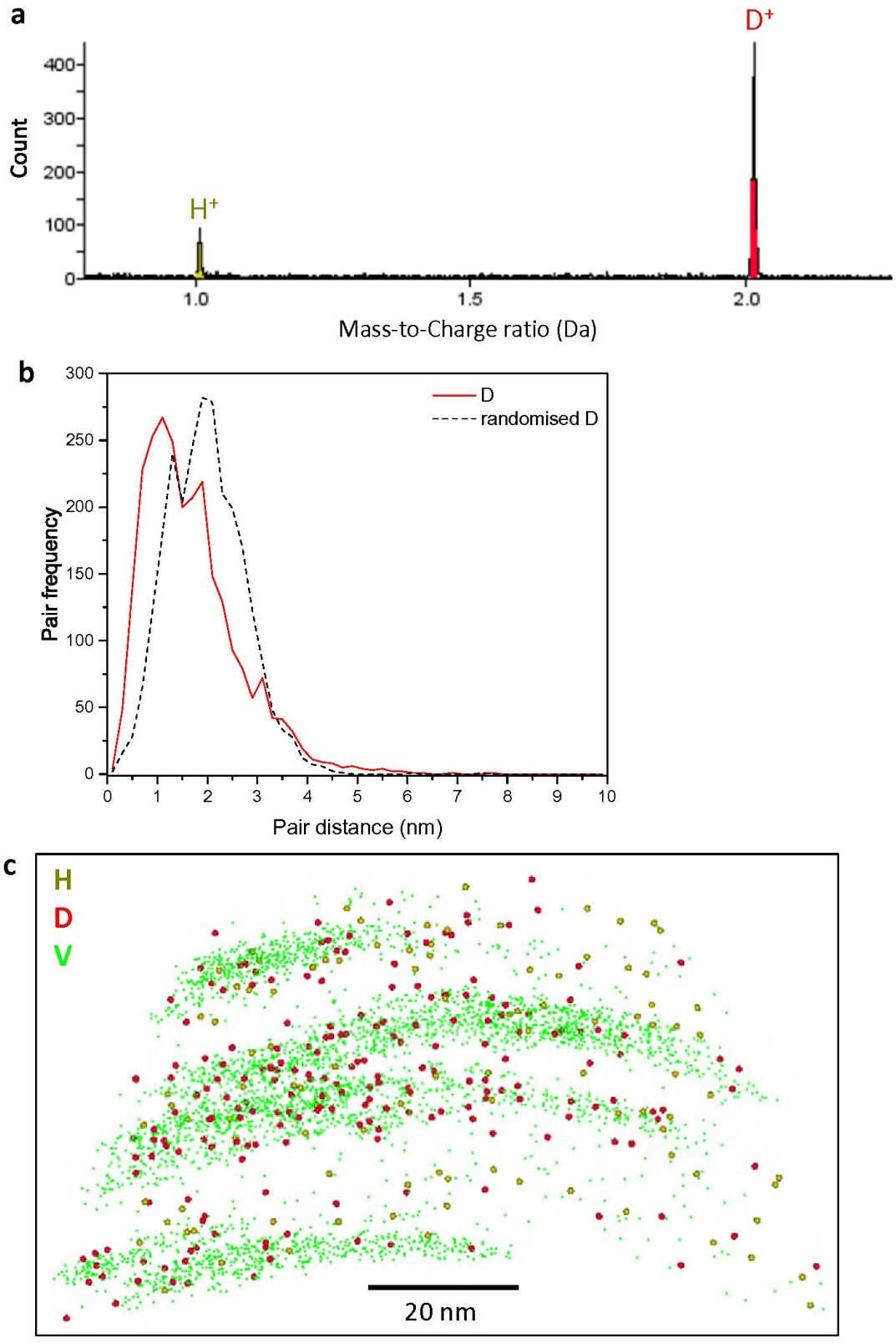

Figure 79 –Datafile R14_25977 with 3.5M ions statistics. (a) Mass spectrum of a NaOH-D_2O-charged sample. Significant D is observed and implies the effectiveness of the solution in liquid charging. (b) shows the clustering of D atoms by NN distribution and being confirmed by the direction observation in the reconstructed data as shown in (c) of a x-z 10nm slice.

9. Conclusions and Future Work

9.1 Conclusions

The literature has shown that APT characterisation of hydrogen trapping in steel provides critical insight for our understanding of the microstructural design of HE resistant steel. However, the experimental requirement of this characterisation technique for introducing hydrogen into needle-shaped APT specimen and subsequent retaining hydrogen in the specimen limits this topic being further studied and means the hydrogen trapping mechanism remains inconclusive. A simplified hydrogen charging method via electrolytic route was previously proposed in the literature. However, this approach was not able to successfully observe trapped hydrogen, possibly due to the room-temperature environment during sample transfer to the atom probe, which results in the introduced hydrogen remaining diffusible and allows hydrogen detrapping. Through the development and incorporation of a custom APT cryogenic sample-transfer chain, this work demonstrates that reducing the sample transfer temperature to cryogenic level enables the direct observation of carbide-trapped hydrogen. In addition, the 3D spatial analysis of the hydrogen enabled by this work, based upon application of an advanced 1D concentration profile algorithm, demonstrated for the first time that the APT can provide sufficient resolution to definitively indicate the trapping mechanism of nanoscale microstructure. In this case, the analysis shows that the trapped hydrogen primarily locates at the interior of carbide rather than matrix/carbide interface within the bearing steel microstructure.

Previous theoretical work raised significant concerns about ability of hydrogen to ingress into the carbide, and hence the interior of the carbide to act as a strong trapping site. However, the result indicating trapping hydrogen in the interior of the nanoscale carbides

investigated in this study agrees with another literature model that predicts the presence of strong hydrogen trap of carbon vacancies at carbide interior. The experiments in this study demonstrate that the theoretically proposed network of carbon vacancies, enabling hydrogen to reach trapping sites within the carbides, could be valid. Further study with the use of the experimental technique developed in this study is believed to be able to provide more insight of the hydrogen trapping mechanism in the design of HE resistant steel and enables the future optimisation of the design.

Given the importance of a cryogenic post-charging environment for the APT observation of hydrogen trapping, this work further developed a simplified cryo-transfer method (ACT) which removes the requirement for customised commercial instruments and modifications to the existing atom probe design. It is hence readily adaptable to other commercial atom probe instruments. The method developed here is based upon the concept of ice sublimation in a low pressure and low temperature environment. It was demonstrated to be effective for removing the ice contamination at the sample surface introduced during the process of transferring the cryogenically-cooled sample. Furthermore, a method was developed to determine the sample temperature after the sublimation process. This uses the thermal response of the sample stage in atom probe instrument and also requires no additional auxiliary instrumentation. It was then validated by analysis of the pressure in the buffer chamber during the sublimation which could be related to the specimen temperature using the low-pressure region of the water phase diagram.

Given the seriousness limitations that ice contamination represents to the APT specimen, a more sophisticated simplified cryo-transfer (DCT) for minimising the contamination by creating an environment with minimum moisture content was developed. The required sublimation time for removing ice contamination was decreased and hence the resulting final specimen temperature before being introduced to the cryo-stage in the atom

probe analysis chamber was decreased from 168K with ACT to 148K with DCT. The resulting difference in measured hydrogen contents within the specimens between the ACT and DCT applications were not large for the studied material. This may be indicative of the strength of the carbides to act as trapping sites. However, further development of the DCT approach may well find important applications for the characterisation of weaker microstructural traps that require the specimen to be held at lower temperature during the sample transfer.

The simplified APT cryo-transfer method then was applied in the determination of the origins of hydrogen pickup during electropolishing and electrolytic charging. The results suggest that the electropolishing process for atom probe specimen preparation does not introduce hydrogen that pre-occupies the carbide traps. Furthermore, they indicate that the trapped hydrogen is primarily contributed by the water solvent of the electrolytic charging solution rather than the electrolyte. These results suggest that the necessary deuteration for atom probe characterisation of hydrogen trapping can be simplified without using deuterated electropolishing acid during sample preparation and deuterated electrolyte during electrolytic charging.

In summary, this work demonstrates an experimental method to verify hydrogen trapping in materials which has been regarded as a key strategy for the mitigation of HE. This technique of microstructural analysis can be combined with the mechanical performance of HE resilience and other microscopies providing complimentary scales of hydrogen characterisation or the information of microstructural features to establish a complete knowledge of HE resistant design.

9.2 Suggestions for Future Work

A series of methods to enable, then ultimately simplify, the experimental protocol for the characterisation of carbide hydrogen trapping in steel are demonstrated in this study. Based on the developed protocols, it is possible to conduct some further experiments to further improve understanding of the hydrogen trapping behaviours in the studied carbide hence advance the design of HE resistant microstructure of carbide steel.

As described below, future research avenues could access significant new insights into hydrogen trapping using the developed experimental protocol but systematically investigating the effects of parameters such as deuterium charging times and final specimen temperature. This is followed by discussion of possible experiments on similar materials that would focus on how trapping strength is affected by issues such as carbide size and chemistry. Such experiments require access to a set of materials where these features are systematically altered through processing routes but would not involve significant adjustment of the presented APT experimental protocol.

Finally, this section addresses longer-term perspective for APT characterisation of hydrogen trapping including the incorporation of focused ion beam (FIB) or cryo-FIB for site-specific analysis of APT as well as using laser-pulsed APT to quantitatively analyse microstructural deuterium. These points are considered to have a broader impact to the hydrogen-material interaction in general however involve significant further work to addresses technical and analytical challenges.

1. Effect of hydrogen charging fugacity

Section 6.3.4 discusses the connected-carbon-vacancy (CCV) hydrogen-trapping model proposed by Di Stefano et al [104], which indicates the double occupancy of hydrogen in CCV trap can result in the reduced hydrogen detrapping energy. This reduced trapping

energy could enable hydrogen penetration into the carbide interior and results in the carbide interior trapping. The double occupancy is associated to excessive supply of microstructural hydrogen, which in this study is attributable to by high-fugacity hydrogen charging. To verify this hypothesis, one can alter the hydrogen charging fugacity (hence amount of hydrogen supply) and investigate its correlation with the observed hydrogen content within the carbide trap. If reducing hydrogen-charging fugacity reduces the content of interior hydrogen, then this hypothesis can be confirmed.

According to eq(5) in Section 2.1.2, hydrogen charging fugacity can be reduced by decreasing the applied charging potential. To this end, a preliminary experiment (R14_25294 incorporating 5 million ions) with reduced charging potential of 1.2V hence reduced hydrogen fugacity, in comparison to 2.2V conventionally applied in the other experiments, was conducted prior to the cryo-transfer (Section 3.5). The charging resulted in the mass spectrum shown in Figure 80 where no deuterium signal can be observed. This could suggest that at this charging fugacity is insufficient to induce excess hydrogen for the double occupancy in the carbide. However, this no detection of deuterium signal contradicts to the RT transfer dataset shown in Section 5.2 which suggests that the deuterium signal should be detected regardless the application of cryo-transfer. So Figure 80 means either the charging was failed, or all the introduced deuterium desorbed before cryo-transfer. The answer is however not available until further investigation being conducted.

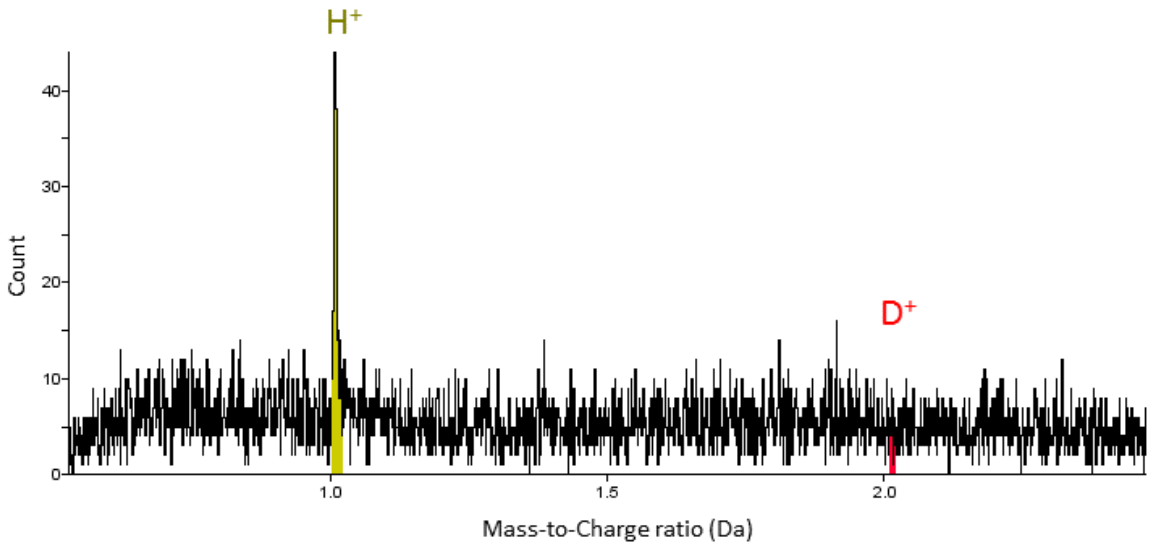

Figure 80 – Mass spectrum of datafile R14_25294 from the sample charged at 1.2V for 10 minutes rather than 2.2V for 0.5 minute as other experiments in this study however shows no D peak.

2. Hydrogen detrapping kinetics

This study has shown that the trapped hydrogen can be observed if cryogenically immobilised, but that hydrogen is detrapped if the sample was left in a suitable condition for a sufficient period of time, such as an extended time at room temperature. In practise, one can leave hydrogen-bearing samples at RT for a systematic set of time prior to cryogenic cooling and before atom probe analysis. Alternatively, one can fix the time-to-cryo and thereby adjust the final temperature of sample-loading environment so the thermal-detrapping character of the trap can be determined. These detrapping characterisations at the microscopic scale can be associated with macroscopic data such as TDA to further elucidate the exact hydrogen detrapping mechanism which has been over-simplified over a long time [3].

If more experiment in the future still shows no correlation between the measured sample temperature and the deuterium retaining extent, this could suggest the hydrogen desorption at APT sample scale in this certain range of temperature has not yet been activated. Then if further increase of sample temperature subsequently results in decrease in

deuterium content in trap with statistical significance, then the temperature activating hydrogen desorption can be determined. This information can then be compared with the hydrogen desorption observed from the macroscopic perspective using relatively large samples and allows more understanding of the sample-dimension dependence of hydrogen desorption. This has only been studied in a limited fashion in a round-robin set of experiments using the TDA technique [197].

3. Effect of precipitation coarsening and chemistry

As discussed in Section 6.3.4, Wei and Tsuzaki suggest the hydrogen trapping behaviour is related to the coherency of carbide/matrix interface hence carbide coarsening stage. One could further verify this with the present experimental protocol by regarding the change of hydrogen trapping site at various precipitation coarsening stages. Also, this study regards the interphase-precipitation carbide trap in ferritic matrix (Section 2.2.2.2). However, hydrogen trapping can be achieved by other types of trap such as oxide, nitride, or grain boundary. Applying this study's techniques in other traps would be able to provide more insight in hydrogen-trap interaction hence improve our understanding of the efficacy of these features to HE mitigation. Before applying the technique in other traps, one can first assess the applicability by comparing the trapping energies of the to-study trap with the trap used in this study, which is FCC V-Mo-Nb carbide presumably associating with FCC V_4C_3 having 33-35 kJ/mol according to [3]. If the trapping strength of the to-study carbide is higher than present one, then sufficient retaining ability of this technique for loaded hydrogen is expected.

4. Incorporation with cryo-FIB

The protocols in this study use electropolishing preparation of APT specimen which allows only random sampling. For site-specific analysis, focused-ion-beam (FIB) technique has been well-developed for APT specimen preparation [170]. FIB has been incorporated

with cryo-transfer ability [235] and is believed having great potential in site-specific application of deuterium-trapped specimen such as hydrogen trapping at grain boundary, which remains unclear of its role in the design of HE resistant microstructure (Section 2.2.2). Although the ion milling process, which could locally heat the sample and thereby affect the deuterium trapping measurement, requires optimisation process to find the best experimental condition, this route could open up a great area of hydrogen trapping study in many microstructural traps.

5. Application of laser-pulsing APT

The key limiting factor in the collection of data statistics in the atom probe experiment of this study is sample yield [209]. All of the studied APT samples herein failed before 10 million ions were acquired with only one exception. Improving sample yield can be achieved by switching from voltage pulsing to laser pulsing in the APT experiment [209]. Apart from the yield consideration, laser APT also allows the study of non-metal materials with the incorporation of FIB-lift-out sample preparation [170]. However, a concern exists that thermal energy supplied by the laser pulse to excite the atoms on the sample apex would locally elevate the specimen temperature and may potentially detrap or even desorb the pre-charged hydrogen within microstructure (Section 2.2.4.3). This localised heating in the sample can be minimised by increasing the precision of laser beam, namely reducing the laser beam size, to just excite the very top atoms rather than the whole tip. This need has been fulfilled in the atom probe instrument equipped with ultra-violet laser [236] which very much reduces the heat-affected area whilst remains more region of sample in cryogenic state than the early LEAP model.

Nevertheless, in laser-pulsing atom probe, $^{1}H_{2}^{+}$ at 2 Da is typically detected as artefact, which obscures the quantification of the charged deuterium ions [237] (Section 2.2.4.1). A preliminary result (R83_01822 incorporating 29 million ions) of the mass spectrum from a

deuterium-charged and RT-transferred sample (Section 5.2) is shown in Figure 81 in respect of this peak-overlap problem at 2 Da. However, the mass spectrum also shows 4 Da peak which is presumably from D_2^+ but not H_4^+ given the absence of 3 Da peak ($^1H_3^+$). To examine the precipitate trapping of the detected deuterium, NN distribution (Section 3.2.8.3) against D_2^+, as compared to the V^+ that is a certainly clustered element, and data reconstruction were carried out as shown in Figure 82. The comparison of D_2^+ and V^+ NN (Figure 82(a) and (b), respectively) indicates no deuterium trapping since no D_2 but only V clustering can be verified. The absence of deuterium trapping can be further confirmed by direct observation in the reconstructed atom maps as the data slices shown in Figure 82(c) and (d) where D_2^+ and V^+ signals are shown in red and green, respectively. Note that this experiment did not apply with any cryo-transfer method (Sections 3.5) and thus the absence of D trapping here can be explained by the deuterium detrapping during the sample transfer procedure. It will be interesting to apply cryo-transfer to confirm whether the observation of deuterium trapping is possible in laser-pulsing atom probe.

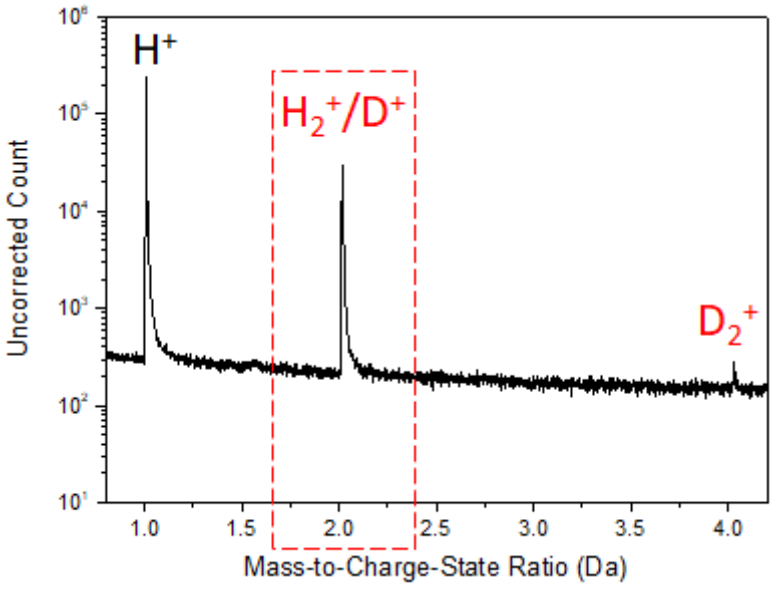

Figure 81 – Mass spectrum of a deuterium-charged sample with RT transfer showing 4 Da peak but no 3 Da peak. (R83_01822)

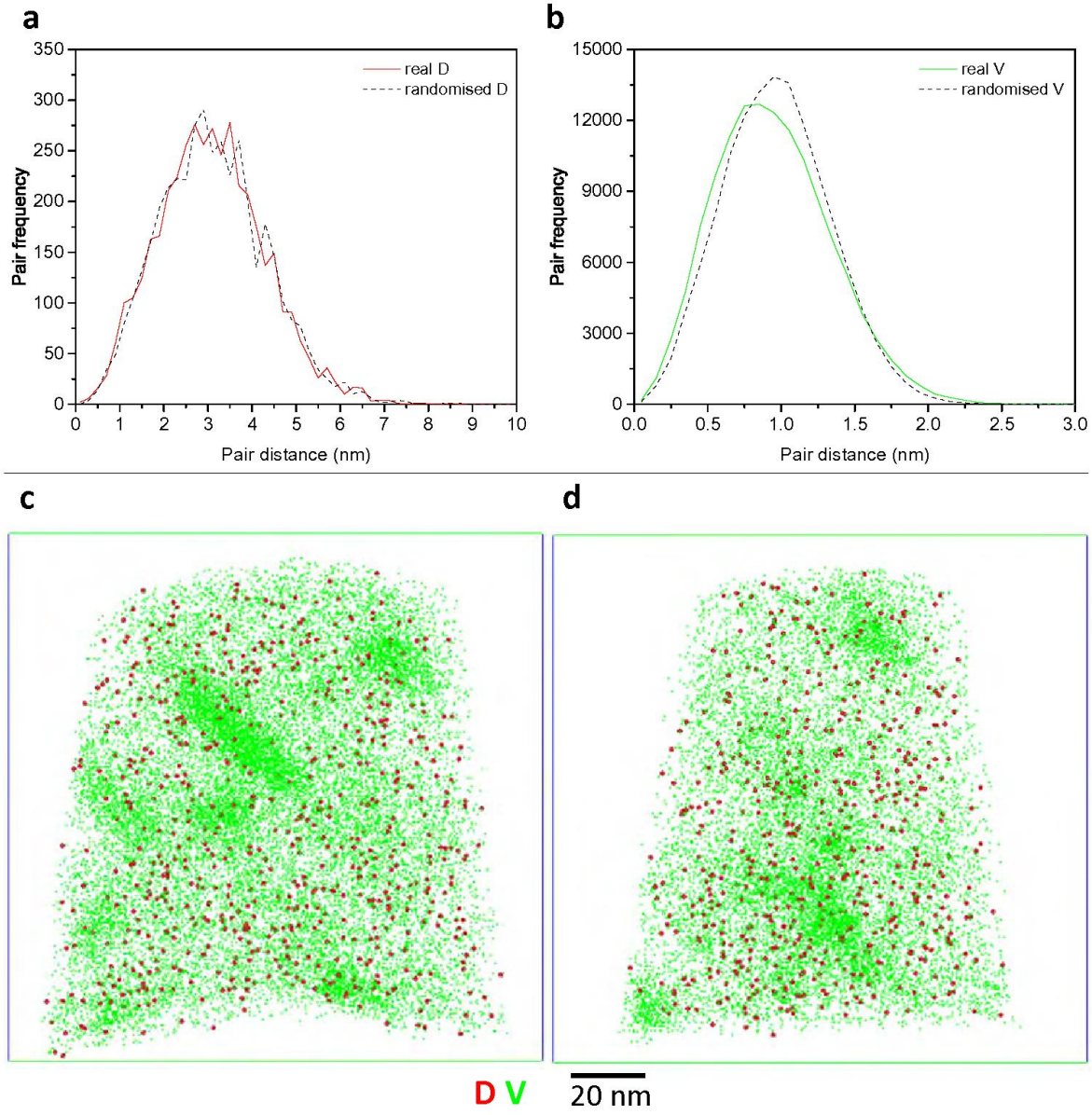

Figure 82 – NN distribution of (a) D_2 ion and (b) V ion which show the clustering of the latter one but not the other. (c) and (d) are two example slices (y-z plane with 20 nm in thickness) from the deuterium-charged dataset (R14_01822) showing no apparent spatial correlation between 4 Da signals and the carbides.

6. Other possibilities

With the capability to analyse hydrogen distribution which provides the implication of hydrogen-materrials interaction, this method can allow more hydrogen-related topics to be studied. For example, the compositional variation at a corroded crack front has been considered corresponding to the mechanism of crack initiation or propagation. With the

application of APT, Meisnar et al. demonstrated that the chemical variation at a stress-corroded crack tip front can be studied at near-atomic scale [239]. Combining their method with the deuterium introduction and retention protocols developed in this work, it is possible to reveal the distribution of deuterium at the crack tip front which could provide critical insight about the role of hydrogen in the debate of stress corrosion mechanism. Likewise, the role of hydrogen in the material oxidation process, which is particularly controversial in pressurised water reactor in nuclear industry [172], can also be revisited with the application of this protocol. Furthermore, APT has also shown its importance in revealing the elemental distribution in biological [240] or geological [241] materials at atomic scale. With the integration of this hydrogen characterisation protocol, APT can be further applied in the studies of how these materials incorporate hydrogen during their formation or the corrosion process in the contact with hydrogen-bearing substances. Due to the ubiquity of hydrogen in this universe, this protocol is believed having great potential to enable many hydrogen-related material questions to be answered.

Bibliography

1. S. Lynch, *Hydrogen embrittlement phenomena and mechanisms.* Corrosion Reviews, (2012). **30** 3-4: p. 105-123.
2. W.H. Johnson, *On Some Remarkable Changes Produced in Iron and Steel by the Action of Hydrogen and Acids.* Proc. R. Soc. Lond. , (1874). **23**: p. 168-179.
3. H.K.D.H. Bhadeshia, *Prevention of Hydrogen Embrittlement in Steels.* ISIJ International, (2016). **56** 1: p. 24-36.
4. N.P. Brandon and Z. Kurban, *Clean energy and the hydrogen economy.* Philosophical Transactions of the Royal Society a-Mathematical Physical and Engineering Sciences, (2017). **375** 2098.
5. T. Michler, et al., *Assessing hydrogen embrittlement in automotive hydrogen tanks*, in *Gaseous Hydrogen Embrittlement of Materials in Energy Technologies*. (2012), Woodhead Publishing. p. 94-125.
6. S.V. Brahimi, et al., *Alloy and composition dependence of hydrogen embrittlement susceptibility in high-strength steel fasteners.* Philosophical Transactions of the Royal Society a-Mathematical Physical and Engineering Sciences, (2017). **375** 2098.
7. M.A. Stopher and P.E.J. Rivera-Diaz-del-Castillo, *Hydrogen embrittlement in bearing steels.* Materials Science and Technology, (2016). **32** 11: p. 1184-1193.
8. G.A. Young Jr, et al., *Hydrogen embrittlement in nuclear power systems*, in *Gaseous Hydrogen Embrittlement of Materials in Energy Technologies*. (2012), Woodhead Publishing. p. 149-176.
9. S. Pillot and L. Coudreuse, *Hydrogen-induced disbonding and embrittlement of steels used in petrochemical refining*, in *Gaseous Hydrogen Embrittlement of Materials in Energy Technologies*. (2012), Woodhead Publishing. p. 51-93.
10. M. Nagumo, *Hydrogen related failure of steels - a new aspect.* Materials Science and Technology, (2004). **20** 8: p. 940-950.
11. I.M. Robertson, et al., *Hydrogen Embrittlement Understood.* Metallurgical and Materials Transactions B-Process Metallurgy and Materials Processing Science, (2015). **46** 3: p. 1085-1103.
12. F.F. Dear and G.C.G. Skinner, *Mechanisms of hydrogen embrittlement in steels: discussion.* Philosophical Transactions of the Royal Society A: Mathematical, Physical and Engineering Sciences, (2017). **375** 2098.
13. M. Koyama, et al., *Overview of hydrogen embrittlement in high-Mn steels.* International Journal of Hydrogen Energy, (2017). **42** 17: p. 12706-12723.
14. Q. Liu and A. Atrens, *A critical review of the influence of hydrogen on the mechanical properties of medium-strength steels.* Corrosion Reviews, (2013). **31** 3-6: p. 85-103.
15. I.M. Bernstein, *The role of hydrogen in the embrittlement of iron and steel.* Materials Science and Engineering a-Structural Materials Properties Microstructure and Processing, (1970). **6** 1: p. 1-19.
16. C. Borchers, et al., *Effect of hydrogen on the mechanical properties of stainless steels.* Advanced Engineering Materials, (2008). **10** 1-2: p. 11-23.
17. Y. Tsuchida, et al., *Effect of hydrogen absorption on strain-induced low-cycle fatigue of low carbon steel.* Fatigue, (2010). **2** 1: p. 555-561.
18. J.P. Hirth, *1980 Institute of Metals Lecture the Metallurgical-Society-of-Aime - Effects of Hydrogen on the Properties of Iron and Steel.* Metallurgical Transactions a-Physical Metallurgy and Materials Science, (1980). **11** 6: p. 861-890.

19. M. Dadfarnia, et al., *Recent advances on hydrogen embrittlement of structural materials.* International Journal of Fracture, (2015). **196** 1-2: p. 223-243.
20. M.Q. Wang, et al., *Effect of hydrogen and stress concentration on the notch tensile strength of AISI 4135 steel.* Materials Science and Engineering a-Structural Materials Properties Microstructure and Processing, (2005). **398** 1-2: p. 37-46.
21. M. Wang, et al., *Effect of hydrogen on the fracture behavior of high strength steel during slow strain rate test.* Corrosion Science, (2007). **49** 11: p. 4081-4097.
22. G. Lovicu, et al., *Hydrogen Embrittlement of Automotive Advanced High-Strength Steels.* Metallurgical and Materials Transactions a-Physical Metallurgy and Materials Science, (2012). **43a** 11: p. 4075-4087.
23. M. Nagumo, *Fundamentals of hydrogen embrittlement*. (2015), New York, NY: Springer Berlin Heidelberg. pages cm.
24. H.J. Maier, et al., *Effects of Hydrogen on Ductile Fracture of a Spheroidized Low-Alloy Steel.* Materials Science and Engineering a-Structural Materials Properties Microstructure and Processing, (1995). **191** 1-2: p. 17-26.
25. T. Depover, et al., *Fractographic analysis of the role of hydrogen diffusion on the hydrogen embrittlement susceptibility of DP steel.* Materials Science and Engineering a-Structural Materials Properties Microstructure and Processing, (2016). **649**: p. 201-208.
26. A. Turnbull, *Hydrogen diffusion and trapping in metals*, in *Gaseous Hydrogen Embrittlement of Materials in Energy Technologies*. (2012), Woodhead Publishing. p. 89-128.
27. A. Helmi, *Sieverts' Law*, in *Encyclopedia of Membranes*, E. Drioli and L. Giorno, Editors. (2015), Springer Berlin Heidelberg: Berlin, Heidelberg. p. 1-2.
28. B. Baranowski, *Thermodynamics of Metal-Hydrogen Systems at High-Pressures.* Berichte Der Bunsen-Gesellschaft Fur Physikalische Chemie, (1972). **76** 8: p. 714-+.
29. C. San Marchi and B. Somerday, *Technical reference for hydrogen capability of materials*, in *Sandia Report*. (2012), Sandia National Laboratories.
30. D. Haley, et al., *Atom Probe Analysis of Ex Situ Gas-Charged Stable Hydrides.* Microscopy and Microanalysis, (2017). **23** 2: p. 307-313.
31. S. Dumpala, et al., *An integrated high temperature environmental cell for atom probe tomography studies of gas-surface reactions: Instrumentation and results.* Ultramicroscopy, (2014). **141**: p. 16-21.
32. K.A. Nibur and B.P. Somerday, *Fracture and fatigue test methods in hydrogen gas*, in *Gaseous Hydrogen Embrittlement of Materials in Energy Technologies*. (2012), Woodhead Publishing. p. 195-236.
33. A. Turnbull, *Perspectives on hydrogen uptake, diffusion and trapping.* International Journal of Hydrogen Energy, (2015). **40** 47: p. 16961-16970.
34. Q. Liu, et al., *Determination of the hydrogen fugacity during electrolytic charging of steel.* Corrosion Science, (2014). **87**: p. 239-258.
35. J.O.M. Bockris and P.K. Subramanyan, *The equivalent pressure of molecular hydrogen in cavities within metals in terms of the overpotential developed during the evolution of hydrogen.* Electrochimica Acta, (1971). **16** 12: p. 2169-2179.
36. D. Haley, et al., *Atom probe tomography observation of hydrogen in high-Mn steel and silver charged via an electrolytic route.* International Journal of Hydrogen Energy, (2014). **39** 23: p. 12221-12229.
37. Y.S. Chen, et al., *Direct observation of individual hydrogen atoms at trapping sites in a ferritic steel.* Science, (2017). **355** 6330: p. 1196-1199.

38. Y.-S. Chen, et al., *Simplifying Observation of Hydrogen Trapping in Atom Probe Tomography.* Microscopy and Microanalysis, (2017).
39. P.W. Chu and E.A. Marquis, *Anodic Hydrogen Evolution and Localized Corrosion during Galvanostatic Polarization of a Peak-Aged Mg-Y-Nd-Zr Alloy.* Journal of the Electrochemical Society, (2016). **163** 8: p. C402-C409.
40. A.T. Paxton and C. Elsasser, *Electronic structure and total energy of interstitial hydrogen in iron: Tight-binding models.* Physical Review B, (2010). **82** 23.
41. M.J. Gillan, *Quantum Simulation of Hydrogen in Metals.* Physical Review Letters, (1987). **58** 6: p. 563-566.
42. F.D. Manchester and ASM International., *Phase diagrams of binary hydrogen alloys*. Monograph series on alloy phase diagrams. (2000), Materials Park, OH: ASM International. xv, 322 p.
43. T. Hickel, et al., *Ab Initio Based Understanding of the Segregation and Diffusion Mechanisms of Hydrogen in Steels.* Jom, (2014). **66** 8: p. 1399-1405.
44. H. Wipf, *Solubility and diffusion of hydrogen in pure metals and alloys.* Physica Scripta, (2001). **T94**: p. 43-51.
45. R.A. Oriani, *Diffusion and Trapping of Hydrogen in Steel.* Acta Metallurgica, (1970). **18** 1: p. 147-&.
46. A. Pundt and R. Kirchheim, *Hydrogen in metals: Microstructural aspects.* Annual Review of Materials Research, (2006). **36**: p. 555-608.
47. H.E. Kissinger, *Reaction Kinetics in Differential Thermal Analysis.* Analytical Chemistry, (1957). **29** 11: p. 1702-1706.
48. W.Y. Choo and J.Y. Lee, *Thermal-Analysis of Trapped Hydrogen in Pure Iron.* Metallurgical Transactions a-Physical Metallurgy and Materials Science, (1982). **13** 1: p. 135-140.
49. F.G. Wei and K. Tsuzaki, *Quantitative analysis on hydrogen trapping of TiC particles in steel.* Metallurgical and Materials Transactions a-Physical Metallurgy and Materials Science, (2006). **37a** 2: p. 331-353.
50. A.T. Paxton, *From quantum mechanics to physical metallurgy of steels.* Materials Science and Technology, (2014). **30** 9: p. 1063-1070.
51. I.M. Bernstein, *Effect of Hydrogen on Deformation of Iron.* Scripta Metallurgica, (1974). **8** 4: p. 343-350.
52. A.J. Kumnick and H.H. Johnson, *Deep Trapping States for Hydrogen in Deformed Iron.* Acta Metallurgica, (1980). **28** 1: p. 33-39.
53. J.L. Lee and J.Y. Lee, *Hydrogen Trapping in Aisi-4340 Steel.* Metal Science, (1983). **17** 9: p. 426-432.
54. G.W. Hong and J.Y. Lee, *The Interaction of Hydrogen and the Cementite Ferrite Interface in Carbon-Steel.* Journal of Materials Science, (1983). **18** 1: p. 271-277.
55. G.W. Hong and J.Y. Lee, *The Interaction of Hydrogen with Iron-Oxide Inclusions in Iron.* Materials Science and Engineering, (1983). **61** 3: p. 219-225.
56. T. Depover and K. Verbeken, *The effect of TiC on the hydrogen induced ductility loss and trapping behavior of Fe-C-Ti alloys.* Corrosion Science, (2016). **112**: p. 308-326.
57. H.G. Lee and J.Y. Lee, *Hydrogen Trapping by Tic Particles in Iron.* Acta Metallurgica, (1984). **32** 1: p. 131-136.
58. H. Asahi, et al., *Hydrogen trapping behavior in vanadium-added steel.* Isij International, (2003). **43** 4: p. 527-533.
59. T. Depover and K. Verbeken, *Evaluation of the effect of V4C3 precipitates on the hydrogen induced mechanical degradation in Fe-C-V alloys.* Materials Science and

Engineering a-Structural Materials Properties Microstructure and Processing, (2016). **675**: p. 299-313.
60. D.M. Li, et al., *Hydrogen trap states in ultrahigh-strength AERMET 100 steel.* Metallurgical and Materials Transactions a-Physical Metallurgy and Materials Science, (2004). **35a** 3: p. 849-864.
61. T. Depover and K. Verbeken, *Evaluation of the role of Mo2C in hydrogen induced ductility loss in Q&T Fe-C-Mo alloys.* International Journal of Hydrogen Energy, (2016). **41** 32: p. 14310-14329.
62. E. Wallaert, et al., *Thermal Desorption Spectroscopy Evaluation of the Hydrogen-Trapping Capacity of NbC and NbN Precipitates.* Metallurgical and Materials Transactions a-Physical Metallurgy and Materials Science, (2014). **45a** 5: p. 2412-2420.
63. G.M. Pressouyre and I.M. Bernstein, *Kinetic Trapping Model for Hydrogen-Induced Cracking.* Acta Metallurgica, (1979). **27** 1: p. 89-100.
64. G.M. Pressouyre, *Trap Theory of Hydrogen Embrittlement.* Acta Metallurgica, (1980). **28** 7: p. 895-911.
65. G.M. Pressouyre and I.M. Bernstein, *An Example of the Effect of Hydrogen Trapping on Hydrogen Embrittlement.* Metallurgical Transactions a-Physical Metallurgy and Materials Science, (1981). **12** 5: p. 835-844.
66. G.M. Pressouyre, *Hydrogen Traps, Repellers, and Obstacles in Steel - Consequences on Hydrogen Diffusion, Solubility, and Embrittlement.* Metallurgical Transactions a-Physical Metallurgy and Materials Science, (1983). **14** 10: p. 2189-2193.
67. R. Nazarov, et al., *First-principles study of the thermodynamics of hydrogen-vacancy interaction in fcc iron.* Physical Review B, (2010). **82** 22.
68. A. Tehranchi, et al., *Hydrogen-vacancy-dislocation interactions in alpha-Fe.* Modelling and Simulation in Materials Science and Engineering, (2017). **25** 2.
69. K. Sato, et al., *Quantitative evaluation of hydrogen atoms trapped at single vacancies in tungsten using positron annihilation lifetime measurements: Experiments and theoretical calculations.* Journal of Nuclear Materials, (2017). **496**: p. 9-17.
70. N.Z. Carr and R.B. McLellan, *The thermodynamic and kinetic behavior of metal-vacancy-hydrogen systems.* Acta Materialia, (2004). **52** 11: p. 3273-3293.
71. H. Zheng, et al., *Electronic structure and binding energies of hydrogen-decorated vacancies in Ni.* Physical Review B, (1997). **55** 7: p. 4174-4181.
72. R. Kirchheim, *Reducing grain boundary, dislocation line and vacancy formation energies by solute segregation II. Experimental evidence and consequences.* Acta Materialia, (2007). **55** 15: p. 5139-5148.
73. R. Kirchheim, *Reducing grain boundary, dislocation line and vacancy formation energies by solute segregation. I. Theoretical background.* Acta Materialia, (2007). **55** 15: p. 5129-5138.
74. R. Nazarov, et al., *Ab initio study of H-vacancy interactions in fcc metals: Implications for the formation of superabundant vacancies.* Physical Review B, (2014). **89** 14.
75. H. Sugimoto and Y. Fukai, *Hydrogen-induced superabundant vacancy formation in bcc Fe: Monte Carlo simulation.* Acta Materialia, (2014). **67**: p. 418-429.
76. Y. Fukai, et al., *Hydrogen-induced superabundant vacancies and diffusion enhancement in some FCC metals.* Diffusions in Materials: Dimat2000, Pts 1 & 2, (2001). **194-1**: p. 1063-1068.

77. H. Sugimoto and Y. Fukai, *Hydrogen-induced superabundant vacancy formation by electrochemical methods in bcc Fe: Monte Carlo simulation.* Scripta Materialia, (2017). **134**: p. 20-23.
78. Y. Fukai, et al., *The phase diagram and superabundant vacancy formation in Fe-H alloys under high hydrogen pressures.* Journal of Alloys and Compounds, (2003). **348** 1-2: p. 105-109.
79. V.S. Mikhalenkov, et al., *Positron-Annihilation Study of Vacancy Defect Nucleation during Deformation of Hydrogen Charged Nickel.* Physica Status Solidi a-Applied Research, (1995). **149** 2: p. K5-K8.
80. I.M. Robertson, *The effect of hydrogen on dislocation dynamics.* Engineering Fracture Mechanics, (2001). **68** 6: p. 671-692.
81. G. Itoh, et al., *Evidence for the transport of impurity hydrogen with gliding dislocations in aluminum.* Scripta Materialia, (1996). **35** 6: p. 695-698.
82. C. Hwang and I.M. Bernstein, *Dislocation Transport of Hydrogen in Iron Single-Crystals.* Acta Metallurgica, (1986). **34** 6: p. 1001-1010.
83. J. Chene and A.M. Brass, *Hydrogen transport by mobile dislocations in nickel base superalloy single crystals.* Scripta Materialia, (1999). **40** 5: p. 537-542.
84. M. Dadfarnia, et al., *Modeling hydrogen transport by dislocations.* Journal of the Mechanics and Physics of Solids, (2015). **78**: p. 511-525.
85. J.K. Tien, et al., *Hydrogen Transport by Dislocations.* Metallurgical Transactions a-Physical Metallurgy and Materials Science, (1976). **7** 6: p. 821-829.
86. M. Hashimoto and R.M. Latanision, *The Role of Dislocations during Transport of Hydrogen in Hydrogen Embrittlement of Iron.* Metallurgical Transactions a-Physical Metallurgy and Materials Science, (1988). **19** 11: p. 2799-2803.
87. S. Wang, et al., *Hydrogen-induced intergranular failure of iron.* Acta Materialia, (2014). **69**: p. 275-282.
88. A. Nagao, et al., *The role of hydrogen in hydrogen embrittlement fracture of lath martensitic steel.* Acta Materialia, (2012). **60** 13-14: p. 5182-5189.
89. M.L. Martin, et al., *Hydrogen-induced intergranular failure in nickel revisited.* Acta Materialia, (2012). **60** 6-7: p. 2739-2745.
90. F. Lecoester, et al., *Hydrogen embrittlement of the Ni-base Alloy 600 correlated with hydrogen transport by dislocations.* Materials Science and Engineering a-Structural Materials Properties Microstructure and Processing, (1999). **262** 1-2: p. 173-183.
91. R. Nishimura and O.M. Alyousif, *A new aspect on intergranular hydrogen embrittlement mechanism of solution annealed types 304, 316 and 310 austenitic stainless steels.* Corrosion Science, (2009). **51** 9: p. 1894-1900.
92. R.M. Latanision and H. Opperhauser, *Intergranular Embrittlement of Nickel by Hydrogen - Effect of Grain-Boundary Segregation.* Metallurgical Transactions, (1974). **5** 2: p. 483-492.
93. C.L. Briant, et al., *Study of Hydrogen Induced Intergranular Cracking in 304 Stainless-Steels.* Jom-Journal of Metals, (1976). **28** 12: p. A65-A65.
94. Y.J.A. Du, et al., *First-principles study on the interaction of H interstitials with grain boundaries in alpha- and gamma-Fe.* Physical Review B, (2011). **84** 14.
95. A. Tehranchi and W.A. Curtin, *Atomistic study of hydrogen embrittlement of grain boundaries in nickel: II. Decohesion.* Modelling and Simulation in Materials Science and Engineering, (2017). **25** 7.

96. A. Tehranchi and W.A. Curtin, *Atomistic study of hydrogen embrittlement of grain boundaries in nickel: I. Fracture.* Journal of the Mechanics and Physics of Solids, (2017). **101**: p. 150-165.
97. M. Koyama, et al., *Characteristics of hydrogen-assisted intergranular fatigue crack growth in interstitial-free steel: role of plastic strain localization.* International Journal of Fracture, (2017). **206** 1: p. 123-130.
98. S. Wang, et al., *Effect of hydrogen environment on the separation of Fe grain boundaries.* Acta Materialia, (2016). **107**: p. 279-288.
99. H.K.D.H. Bhadeshia and R.W.K. Honeycombe, *Steels : microstructure and properties*. 3rd ed. (2006), Oxford: Butterworth Heinemann. xi, 344 p.
100. M.Y. Chen, et al., *Interphase precipitation in vanadium-alloyed steels: Strengthening contribution and morphological variability with austenite to ferrite transformation.* Acta Materialia, (2014). **64**: p. 78-92.
101. A. Nagao, et al., *The effect of nanosized (Ti,Mo)C precipitates on hydrogen embrittlement of tempered lath martensitic steel.* Acta Materialia, (2014). **74**: p. 244-254.
102. K. Kawakami and T. Matsumiya, *Ab-initio Investigation of Hydrogen Trap State by Cementite in bcc-Fe.* Isij International, (2013). **53** 4: p. 709-713.
103. K. Kawakami and T. Matsumiya, *Numerical Analysis of Hydrogen Trap State by TiC and V4C3 in bcc-Fe.* Isij International, (2012). **52** 9: p. 1693-1697.
104. D. Di Stefano, et al., *First-principles investigation of hydrogen interaction with TiC precipitates in alpha-Fe.* Physical Review B, (2016). **93** 18.
105. D.G. Westlake, *A Generalized Model for Hydrogen Embrittlement.* Asm Transactions Quarterly, (1969). **62** 4: p. 1000-&.
106. J. Song and W.A. Curtin, *A nanoscale mechanism of hydrogen embrittlement in metals.* Acta Materialia, (2011). **59** 4: p. 1557-1569.
107. J. Song and W.A. Curtin, *Atomic mechanism and prediction of hydrogen embrittlement in iron.* Nature Materials, (2013). **12** 2: p. 145-151.
108. R.A. Oriani, *Mechanistic Theory of Hydrogen Embrittlement of Steels.* Berichte Der Bunsen-Gesellschaft Fur Physikalische Chemie, (1972). **76** 8: p. 848-&.
109. M.S. Daw and M.I. Baskes, *Semiempirical, Quantum-Mechanical Calculation of Hydrogen Embrittlement in Metals.* Physical Review Letters, (1983). **50** 17: p. 1285-1288.
110. W. Gerberich, *Modeling hydrogen induced damage mechanisms in metals*, in *Gaseous Hydrogen Embrittlement of Materials in Energy Technologies*. (2012), Woodhead Publishing. p. 209-246.
111. H. Vehoff and P. Neumann, *Crack-Propagation and Cleavage Initiation in Fe-2.6-Percent-Si Single-Crystals under Controlled Plastic Crack Tip Opening Rate in Various Gaseous Environments.* Acta Metallurgica, (1980). **28** 3: p. 265-272.
112. Y. Takahashi, et al., *Direct evaluation of grain boundary hydrogen embrittlement: A micro-mechanical approach.* Materials Science and Engineering a-Structural Materials Properties Microstructure and Processing, (2016). **661**: p. 211-216.
113. M.L. Martin, et al., *Interpreting hydrogen-induced fracture surfaces in terms of deformation processes: A new approach.* Acta Materialia, (2011). **59** 9: p. 3680-3687.
114. C.D. Beachem, *New Model for Hydrogen-Assisted Cracking (Hydrogen Embrittlement).* Metallurgical Transactions, (1972). **3** 2: p. 437-+.
115. H.K. Birnbaum and P. Sofronis, *Hydrogen-Enhanced Localized Plasticity - a Mechanism for Hydrogen-Related Fracture.* Materials Science and Engineering a-

Structural Materials Properties Microstructure and Processing, (1994). **176** 1-2: p. 191-202.
116. Y. Deng, et al., *Hydrogen-enhanced cracking revealed by in situ micro-cantilever bending test inside environmental scanning electron microscope.* Philosophical Transactions of the Royal Society a-Mathematical Physical and Engineering Sciences, (2017). **375** 2098.
117. T. Hajilou, et al., *In situ electrochemical microcantilever bending test: A new insight into hydrogen enhanced cracking.* Scripta Materialia, (2017). **132**: p. 17-21.
118. K. Christmann, *Some General-Aspects of Hydrogen Chemisorption on Metal-Surfaces.* Progress in Surface Science, (1995). **48** 1-4: p. 15-26.
119. S.P. Lynch, *Environmentally Assisted Cracking - Overview of Evidence for an Adsorption-Induced Localized-Slip Process.* Acta Metallurgica, (1988). **36** 10: p. 2639-2661.
120. I.H. Katzarov, et al., *Hydrogen embrittlement I. Analysis of hydrogen-enhanced localized plasticity: Effect of hydrogen on the velocity of screw dislocations in α-Fe.* Physical Review Materials, (2017). **1** 3.
121. M. Hallberg, et al., *A new approach to using modelling for on-line prediction of sulphur and hydrogen removal duving ladle refining.* Isij International, (2004). **44** 8: p. 1318-1327.
122. J. Hill, *Hydrogen Bake out, Preheat and Postweld Heat-Treatments Help Solve Corrosion Problems for Oil Industry.* Welding Journal, (1992). **71** 7: p. 51-53.
123. H. Lachmund, et al., *Heavy plate production: demand on hydrogen control.* Ironmaking & Steelmaking, (2000). **27** 5: p. 381-386.
124. D. Figueroa and M.J. Robinson, *The effects of sacrificial coatings on hydrogen embrittlement and re-embrittlement of ultra high strength steels.* Corrosion Science, (2008). **50** 4: p. 1066-1079.
125. A.M. Brass and J. Chene, *Influence of deformation on the hydrogen behavior in iron and nickel base alloys: a review of experimental data.* Materials Science and Engineering a-Structural Materials Properties Microstructure and Processing, (1998). **242** 1-2: p. 210-221.
126. D. Hejazi, et al., *Effect of manganese content and microstructure on the susceptibility of X70 pipeline steel to hydrogen cracking.* Materials Science and Engineering a-Structural Materials Properties Microstructure and Processing, (2012). **551**: p. 40-49.
127. M.J. Zhao, et al., *Hydrogen-induced Modification in the Deformation and Fracture of a Precipitation-hardened Fe-Ni Based Austenitic Alloy.* Journal of Materials Science & Technology, (2014). **30** 11: p. 1155-1159.
128. K. Takasawa, et al., *Effects of grain size and dislocation density on the susceptibility to high-pressure hydrogen environment embrittlement of high-strength low-alloy steels.* International Journal of Hydrogen Energy, (2012). **37** 3: p. 2669-2675.
129. I.J. Park, et al., *The advantage of grain refinement in the hydrogen embrittlement of Fe-18Mn-0.6C twinning-induced plasticity steel.* Corrosion Science, (2015). **93**: p. 63-69.
130. S. Bechtle, et al., *Grain-boundary engineering markedly reduces susceptibility to intergranular hydrogen embrittlement in metallic materials.* Acta Materialia, (2009). **57** 14: p. 4148-4157.

131. Y. Mine, et al., *Effect of ultrafine grain refinement on hydrogen embrittlement of metastable austenitic stainless steel.* International Journal of Hydrogen Energy, (2017). **42** 22: p. 15415-15425.
132. H. Iwaoka, et al., *Hydrogen diffusion in ultrafine-grained palladium: Roles of dislocations and grain boundaries.* Acta Materialia, (2016). **107**: p. 168-177.
133. Y. Mine, et al., *Grain-boundary diffusion and precipitate trapping of hydrogen in ultrafine-grained austenitic stainless steels processed by high-pressure torsion.* Materials Science and Engineering a-Structural Materials Properties Microstructure and Processing, (2011). **528** 28: p. 8100-8105.
134. Y. Bai, et al., *Effect of grain refinement on hydrogen embrittlement behaviors of high-Mn TWIP steel.* Materials Science and Engineering a-Structural Materials Properties Microstructure and Processing, (2016). **651**: p. 935-944.
135. B.A. Szost, et al., *Hydrogen-Trapping Mechanisms in Nanostructured Steels.* Metallurgical and Materials Transactions a-Physical Metallurgy and Materials Science, (2013). **44a** 10: p. 4542-4550.
136. T. Michler and M.P. Balogh, *Hydrogen environment embrittlement of an ODS RAF steel - Role of irreversible hydrogen trap sites.* International Journal of Hydrogen Energy, (2010). **35** 18: p. 9746-9754.
137. M. Dadfarnia, et al., *Hydrogen interaction with multiple traps: Can it be used to mitigate embrittlement?* International Journal of Hydrogen Energy, (2011). **36** 16: p. 10141-10148.
138. R. Kirchheim, *Bulk Diffusion-Controlled Thermal Desorption Spectroscopy with Examples for Hydrogen in Iron.* Metallurgical and Materials Transactions a-Physical Metallurgy and Materials Science, (2016). **47a** 2: p. 672-696.
139. H.L. Lee and S.L.I. Chan, *Hydrogen Embrittlement of Aisi 4130 Steel with an Alternate Ferrite Pearlite Banded Structure.* Materials Science and Engineering a-Structural Materials Properties Microstructure and Processing, (1991). **142** 2: p. 193-201.
140. L. Tau and S.L.I. Chan, *Effects of ferrite/pearlite alignment on the hydrogen permeation in a AISI 4130 steel.* Materials Letters, (1996). **29** 1-3: p. 143-147.
141. D.A. Porter, et al., *Phase transformations in metals and alloys*. 3rd ed. / David A. Porter, Kenneth E. Easterling, and Mohamed Y. Sherif. ed. (2009), Boca Raton, Fla. ; London: CRC.
142. F.G. Wei, et al., *Nano-Precipitates Design with Hydrogen Trapping Character in High Strength Steels.* Effects of Hydrogen on Materials, (2009): p. 448-+.
143. M.A. Stopher, et al., *Modelling hydrogen migration and trapping in steels.* Materials & Design, (2016). **106**: p. 205-215.
144. E.I. Galindo-Nava, et al., *Hydrogen transport in metals: Integration of permeation, thermal desorption and degassing.* Journal of Materials Science & Technology, (2017).
145. R.W.K. Honeycombe, *Transformation from Austenite in Alloy-Steels.* Metallurgical Transactions a-Physical Metallurgy and Materials Science, (1976). **7** 7: p. 915-936.
146. R. Okamoto, et al., *Interphase precipitation in niobium-microalloyed steels.* Acta Materialia, (2010). **58** 14: p. 4783-4790.
147. H.W. Yen, et al., *Interphase precipitation of nanometer-sized carbides in a titanium-molybdenum-bearing low-carbon steel.* Acta Materialia, (2011). **59** 16: p. 6264-6274.

148. S. Mukherjee, et al., *Three-dimensional atom probe microscopy study of interphase precipitation and nanoclusters in thermomechanically treated titanium-molybdenum steels.* Acta Materialia, (2013). **61** 7: p. 2521-2530.
149. Y.J. Zhang, et al., *Effects of transformation temperature on VC interphase precipitation and resultant hardness in low-carbon steels.* Acta Materialia, (2015). **84**: p. 375-384.
150. X.X. Yu, et al., *Ab initio investigations of the phase stability in group IVB and VB transition metal carbides.* Computational Materials Science, (2016). **112**: p. 318-326.
151. M. Koyama, et al., *Recent progress in microstructural hydrogen mapping in steels: quantification, kinetic analysis, and multi-scale characterisation.* Materials Science and Technology, (2017): p. 1-16.
152. A. Baldi, et al., *In situ detection of hydrogen-induced phase transitions in individual palladium nanocrystals.* Nature Materials, (2014). **13** 12: p. 1143-1148.
153. R. Ishikawa, et al., *Direct imaging of hydrogen-atom columns in a crystal by annular bright-field electron microscopy.* Nature Materials, (2011). **10** 4: p. 278-281.
154. K. Tatsumi, et al., *Detection of hydrogen at localized regions by unoccupied electronic states in iron carbides: Towards high spatial resolution mapping of hydrogen distributions.* Journal of Applied Physics, (2007). **101** 2.
155. B. Malard, et al., *Hydrogen trapping by VC precipitates and structural defects in a high strength Fe-Mn-C steel studied by small-angle neutron scattering.* Materials Science and Engineering a-Structural Materials Properties Microstructure and Processing, (2012). **536**: p. 110-116.
156. M. Ohnuma, et al., *Direct observation of hydrogen trapped by NbC in steel using small-angle neutron scattering.* Scripta Materialia, (2008). **58** 2: p. 142-145.
157. A. Griesche, et al., *Three-dimensional imaging of hydrogen blister in iron with neutron tomography.* Acta Materialia, (2014). **78**: p. 14-22.
158. P. Reichart, et al., *3D hydrogen microscopy with sub-ppm detection limit.* Nuclear Instruments & Methods in Physics Research Section B-Beam Interactions with Materials and Atoms, (2004). **219**: p. 980-987.
159. K. Peeper, et al., *3D-microscopy of hydrogen in tungsten.* Journal of Nuclear Materials, (2013). **438**: p. S887-S890.
160. I.G. Hughes, et al., *Depth profiling of deuterium using nuclear reaction analysis.* Nuclear Instruments and Methods in Physics Research Section B: Beam Interactions with Materials and Atoms, (1993). **79** 1: p. 487-489.
161. N. Kardjilov, et al., *Neutron imaging in materials science.* Materials Today, (2011). **14** 6: p. 248-256.
162. K. Ichitani, et al., *Recent development in hydrogen microprint technique and its application to hydrogen embrittlement.* Isij International, (2003). **43** 4: p. 496-504.
163. T. Ohmisawa, et al., *Detection of hydrogen trap distribution in steel using a microprint technique.* Journal of Alloys and Compounds, (2003). **356**: p. 290-294.
164. K.K. Ichitani, M., *Visualization of hydrogen diffusion in steels by high sensitivity hydrogen microprint technique.* Science and Technology of Advanced Materials, (2003). **4**: p. 545-551.
165. M. Rohwerder and F. Turcu, *High-resolution Kelvin probe microscopy in corrosion science: Scanning Kelvin probe force microscopy (SKPFM) versus classical scanning Kelvin probe (SKP).* Electrochimica Acta, (2007). **53** 2: p. 290-299.

166. S. Evers, et al., *Hydrogen detection in metals: a review and introduction of a Kelvin probe approach.* Science and Technology of Advanced Materials, (2013). **14** 1.
167. P. Kesten, et al., *H- and D distribution in metallic multilayers studied by 3-dimensional atom probe analysis and secondary ion mass spectrometry.* Journal of Alloys and Compounds, (2002). **330**: p. 225-228.
168. Z. Tarzimoghadam, et al., *Multi-scale and spatially resolved hydrogen mapping in a Ni-Nb model alloy reveals the role of the δ phase in hydrogen embrittlement of alloy 718.* Acta Materialia, (2016). **109**: p. 69-81.
169. K. Takai, et al., *Visualization of the hydrogen desorption process from ferrite, pearlite, and graphite by secondary ion mass spectrometry.* Metallurgical and Materials Transactions a-Physical Metallurgy and Materials Science, (2002). **33** 8: p. 2659-2665.
170. B. Gault, et al., *Atom Probe Microscopy*. (2012): Springer.
171. J.A. Spitznagel, et al., *Deuterium and Helium Trapping at Tic Particles in Ferritic Steel.* Journal of Nuclear Materials, (1984). **122** 1-3: p. 252-253.
172. G. Sundell, et al., *Direct observation of hydrogen and deuterium in oxide grain boundaries in corroded Zirconium alloys.* Corrosion Science, (2015). **90**: p. 1-4.
173. Y.J. Kim, et al., *Direct Atomic-Scale Imaging of Hydrogen and Oxygen Interstitials in Pure Niobium Using Atom-Probe Tomography and Aberration-Corrected Scanning Transmission Electron Microscopy.* Acs Nano, (2013). **7** 1: p. 732-739.
174. Y.J. Kim and D.N. Seidman, *Atom-Probe Tomographic Analyses of Hydrogen Interstitial Atoms in Ultrahigh Purity Niobium.* Microscopy and Microanalysis, (2015). **21** 3: p. 535-543.
175. R. Gemma, et al., *APT analyses of deuterium-loaded Fe/V multi-layered films.* Ultramicroscopy, (2009). **109** 5: p. 631-636.
176. R. Gemma, et al., *Analysis of deuterium in V-Fe5at.% film by atom probe tomography (APT).* Journal of Alloys and Compounds, (2011). **509**: p. S872-S876.
177. R. Gemma, et al., *Visualization of deuterium dead layer by atom probe tomography.* Scripta Materialia, (2012). **67** 11: p. 903-906.
178. J. Takahashi, et al., *The first direct observation of hydrogen trapping sites in TiC precipitation-hardening steel through atom probe tomography.* Scripta Materialia, (2010). **63** 3: p. 261-264.
179. S.S. Hong, et al., *Residual gas survey of stainless steel 304 extreme high vacuum chamber with hot cathode ionization gauge.* Measurement, (2008). **41** 9: p. 1026-1031.
180. M.K. Gupta, et al., *Hydrogen in Stainless Steel as killing agent for UHV: A review.* Materials Today-Proceedings, (2015). **2** 4-5: p. 1074-1081.
181. P.A. Redhead, *Hydrogen in vacuum systems: An overview.* Hydrogen in Materials and Vacuum Systems, (2003). **671**: p. 243-254.
182. G. Sundell, et al., *Hydrogen analysis in APT: Methods to control adsorption and dissociation of H-2.* Ultramicroscopy, (2013). **132**: p. 285-289.
183. R.P. Kolli, *Controlling residual hydrogen gas in mass spectra during pulsed laser atom probe tomography.* Advanced Structural and Chemical Imaging, (2017). **3** 1: p. 10.
184. X. Zhu, et al., *Hydrogen trapping sites and hydrogen-induced cracking in high strength quenching & partitioning (Q&P) treated steel.* International Journal of Hydrogen Energy, (2014). **39** 24: p. 13031-13040.

185. X.Y. Cheng, et al., *Direct observation of hydrogen-trapping sites in newly developed high-strength mooring chain steel by atom probe tomography.* Progress in Natural Science-Materials International, (2013). **23** 4: p. 446-452.
186. X. Zhu, et al., *Improved resistance to hydrogen embrittlement in a high-strength steel by quenching-partitioning-tempering treatment.* Scripta Materialia, (2015). **97**: p. 21-24.
187. T.F. Kelly and D.J. Larson, *Atom Probe Tomography 2012.* Annual Review of Materials Research, Vol 42, (2012). **42**: p. 1-31.
188. R.K.W. Marceau, *Atomic-scale analysis of light alloys using atom probe tomography.* Materials Science and Technology, (2016). **32** 3: p. 209-219.
189. A.T. Paxton and I.H. Katzarov, *Quantum and isotope effects on hydrogen diffusion, trapping and escape in iron.* Acta Materialia, (2016). **103**: p. 71-76.
190. E. Serra, et al., *Hydrogen isotopes transport parameters in fusion reactor materials.* Journal of Nuclear Materials, (1998). **255** 2-3: p. 105-115.
191. J. Chene and F. Martin, *Isotopic tracing of hydrogen transport and trapping in nuclear materials.* Philosophical Transactions of the Royal Society a-Mathematical Physical and Engineering Sciences, (2017). **375** 2098.
192. R.K.W. Marceau, et al., *Understanding the detection of carbon in austenitic high-Mn steel using atom probe tomography.* Ultramicroscopy, (2013). **132**: p. 239-247.
193. J. Takahashi, et al., *Quantitative analysis of carbon content in cementite in steel by atom probe tomography.* Ultramicroscopy, (2011). **111** 8: p. 1233-1238.
194. M. Thuvander, et al., *Quantitative atom probe analysis of carbides.* Ultramicroscopy, (2011). **111** 6: p. 604-608.
195. H.S. Kitaguchi, et al., *Quantitative analysis of carbon in cementite using pulsed laser atom probe.* Ultramicroscopy, (2014). **147**: p. 51-60.
196. G. Miyamoto, et al., *Quantitative measurement of carbon content in Fe-C binary alloys by atom probe tomography.* Scripta Materialia, (2012). **67** 12: p. 999-1002.
197. H. Suzuki and K. Takai, *Summary of Round-robin Tests for Standardizing Hydrogen Analysis Procedures.* Isij International, (2012). **52** 2: p. 174-180.
198. R.A. Karnesky, et al., *Imaging and quantification of hydrogen isotope trapping.* Sandia report, (2012). **SAND2012** 8539.
199. J. Takahashi, et al., *Direct observation of hydrogen-trapping sites in vanadium carbide precipitation steel by atom probe tomography.* Scripta Materialia, (2012). **67** 2: p. 213-216.
200. J.H. Muller, et al., *A cryogenic scanning force microscope for the characterization of frozen biological samples.* Applied Physics a-Materials Science & Processing, (2003). **76** 6: p. 893-898.
201. A. Stintz and J.A. Panitz, *Cluster Ion Formation in Isothermal Ramped Field-Desorption of Amorphous Water Ice from Metal-Surfaces.* Surface Science, (1993). **296** 1: p. 75-86.
202. A. Stintz and J.A. Panitz, *Imaging Atom-Probe Analysis of an Aqueous Interface.* Journal of Vacuum Science & Technology a-Vacuum Surfaces and Films, (1991). **9** 3: p. 1365-1367.
203. J.A. Panitz and A. Stintz, *Imaging Atom-Probe Analysis of a Vitreous Ice Interface.* Surface Science, (1991). **246** 1-3: p. 163-168.
204. M. Koyama, et al., *Martensitic transformation-induced hydrogen desorption characterized by utilizing cryogenic thermal desorption spectroscopy during cooling.* Scripta Materialia, (2016). **122**: p. 50-53.

205. A. Nishimoto, et al., *Detection of Charged Hydrogen in Ferritic Steel through Cryogenic Secondary Ion Mass Spectrometry.* Isij International, (2015). **55** 1: p. 335-337.
206. R.G. Cortes, et al., *On the Determination of Grain-Size Distributions from Intercept Distributions.* Journal of Materials Science, (1985). **20** 8: p. 2997-3002.
207. R. Gomer, *Field emission and field ionization*. (1961), Cambridge, Mass.: Harvard University Press ; London : Oxford University Press.
208. M.K. Miller, *Atom-probe tomography : the local electrode atom probe*. (2014), New York: Springer. pages cm.
209. D.J. Larson, et al., *Local Electrode Atom Probe Tomography: A User's Guide*. 1 ed. (2013): Springer-Verlag New York. XVII, 318.
210. D. Haley, et al., *Guided mass spectrum labelling in atom probe tomography.* Ultramicroscopy, (2015). **159**: p. 338-345.
211. P.A. Redhead, *Hydrogen in Vacuum Systems: An Overview*, in *AIP Conference Proceedings*. (2003). p. 243-254.
212. B. Gault, et al., *Advances in the reconstruction of atom probe tomography data.* Ultramicroscopy, (2011). **111** 6: p. 448-457.
213. L. Yao, *A filtering method to reveal crystalline patterns from atom probe microscopy desorption maps.* MethodsX, (2016). **3** Supplement C: p. 268-273.
214. B. Gault, et al., *Advances in the calibration of atom probe tomographic reconstruction.* Journal of Applied Physics, (2009). **105** 3.
215. A.J. London, *Irradiation damage of oxide dispersion strengthened steels*, in *Department of Materials*. (2015), University of Oxford. p. 99.
216. B.P. Geiser, et al., *Spatial distribution maps for atom probe tomography.* Microscopy and Microanalysis, (2007). **13** 6: p. 437-447.
217. C.A. Williams, et al., *Defining clusters in APT reconstructions of ODS steels.* Ultramicroscopy, (2013). **132**: p. 271-278.
218. O.C. Hellman, et al., *Efficient sampling for three-dimensional atom probe microscopy data.* Ultramicroscopy, (2003). **95** 1-4: p. 199-205.
219. O.C. Hellman, et al., *Analysis of three-dimensional atom-probe data by the proximity histogram.* Microscopy and Microanalysis, (2000). **6** 5: p. 437-444.
220. J.M. Hyde, et al., *A sensitivity analysis of the maximum separation method for the characterisation of solute clusters.* Ultramicroscopy, (2011). **111** 6: p. 440-447.
221. A.J. London, et al., *Effect of Ti and Cr on dispersion, structure and composition of oxide nano-particles in model ODS alloys.* Acta Materialia, (2015). **97** Supplement C: p. 223-233.
222. S.S.A. Gerstl and R. Wepf, *Methods in Creating, Transferring, & Measuring Cryogenic Samples for APT.* Microscopy and Microanalysis, (2015). **21** S3: p. 517-518.
223. G. Caruso and M.T. Porfiri, *ICE layer growth on a cryogenic surface in a fusion reactor during a loss of water event.* Progress in Nuclear Energy, (2015). **78**: p. 173-181.
224. C.E. Bryson, et al., *Sublimation Rates and Vapor-Pressures of H2o, Co2, N2o, and Xe.* Journal of Chemical and Engineering Data, (1974). **19** 2: p. 107-110.
225. R.B. Bird, et al., *Transport phenomena*. 2nd rev. ed. ed. (2007), New York ; Chichester: J. Wiley.
226. J. Crank, *The mathematics of diffusion*. 2nd ed. ed. (1979), Oxford: Clarendon Press.

227. S. Sakakibara, et al., *Determination of Impurities in Titanium Carbide and Titanium Nitride by Inductively Coupled Plasma Atomic Emission-Spectrometry.* Analyst, (1989). **114** 12: p. 1663-1666.
228. H.W. Yen, *TEM Investigation on the Interphase Precipitation of Nanometer-sized Carbides in Advanced Ultra High-Strength Steels*, in *Department of Materials*. (2011), Natioanl Taiwan University: Taiwan. p. 264.
229. S. Mukherjee, et al., *Clustering and precipitation processes in a ferritic titanium-molybdenum microalloyed steel.* Journal of Alloys and Compounds, (2017). **690**: p. 621-632.
230. X.X. Yu, et al., *Ab initio investigations of the phase stability in tantalum carbides.* Acta Materialia, (2014). **80**: p. 341-349.
231. S. Yamasaki and H.K.D.H. Bhadeshia, *M4C3 precipitation in Fe-C-Mo-V steels and relationship to hydrogen trapping.* Proceedings of the Royal Society a-Mathematical Physical and Engineering Sciences, (2006). **462** 2072: p. 2315-2330.
232. W.Y. Choo and J.Y. Lee, *Hydrogen Trapping Phenomena in Carbon-Steel.* Journal of Materials Science, (1982). **17** 7: p. 1930-1938.
233. F.G. Wei, et al., *Precise determination of the activation energy for desorption of hydrogen in two Ti-added steels by a single thermal-desorption spectrum.* Metallurgical and Materials Transactions B-Process Metallurgy and Materials Processing Science, (2004). **35** 3: p. 587-597.
234. F. Jambon, et al., *Mechanism of hydrogen absorption during the exposure of alloy 600-like single-crystals to PWR primary simulated media.* Journal of Nuclear Materials, (2011). **414** 3: p. 386-392.
235. S. Tacke, et al., *A Versatile High-Vacuum Cryo-transfer System for Cryo-microscopy and Analytics.* Biophysical Journal, (2016). **110** 4: p. 758-765.
236. T.L. Martin, et al., *Comparing the Consistency of Atom Probe Tomography Measurements of Small-Scale Segregation and Clustering Between the LEAP 3000 and LEAP 5000 Instruments.* Microsc Microanal, (2017). **23** 2: p. 227-237.
237. G.L. Kellogg and T.T. Tsong, *Pulsed-Laser Atom-Probe Field-Ion Microscopy.* Journal of Applied Physics, (1980). **51** 2: p. 1184-1193.
238. A.J. London, et al., *Single-Ion Deconvolution of Mass Peak Overlaps for Atom Probe Microscopy.* Microscopy and Microanalysis, (2017). **23** 2: p. 300-306.
239. M. Meisnar, et al., *Atom probe tomography of stress corrosion crack tips in SUS316 stainless steels.* Corrosion Science, (2015). **98**: p. 661-671.
240. L.M. Gordon and D. Joester, *Nanoscale chemical tomography of buried organic-inorganic interfaces in the chiton tooth.* Nature, (2011). **469** 7329: p. 194-197.
241. E.M. Peterman, et al., *Nanogeochronology of discordant zircon measured by atom probe microscopy of Pb-enriched dislocation loops.* Science Advances, (2016). **2** 9.
242. W. Sha, et al., *Some Aspects of Atom-Probe Analysis of Fe-C and Fe-N Systems.* Surface Science, (1992). **266** 1-3: p. 416-423.

Appendix

1. Fracture mode

Transgranular and intergranular fracture modes in materials are frequently studied by fractography. As shown in Figure 83(a), intergranular fracture occurs when grain boundaries are weaker than grains. Hence a crack propagates along grain boundaries during tensile testing resulting in the featured fracture surface shown in (b). The occurrence of intergranular fracture generally accompanies with a macroscopic observation of brittle failure, given that crack propagation will be rapid once the yield strength of grain boundaries has been reached. In contrast, transgranular fracture as shown in Figure 84(a) occurs when grains yield earlier than grain boundaries, so the crack propagates directly through the grains. Transgranular fracture can originate from both ductile and brittle failures which require to be inspected in fractographic analysis. Ductile transgranular fracture is typically associated to the dimpled feature shown in Figure 84(b), whereas in the case of brittle transgranular fracture, flat and quasi-cleavage features as Figure 84 (c) and (d), respectively, would be observed under the microscope.

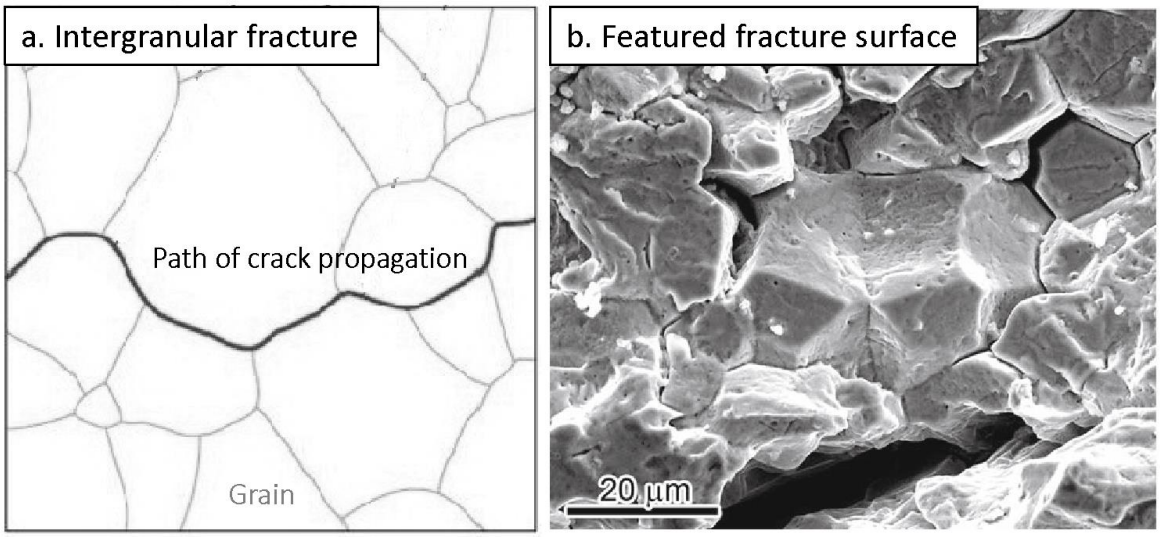

Figure 83 –Intergranular fracture (a) schematic and (b) example SEM image of pure iron from [19]

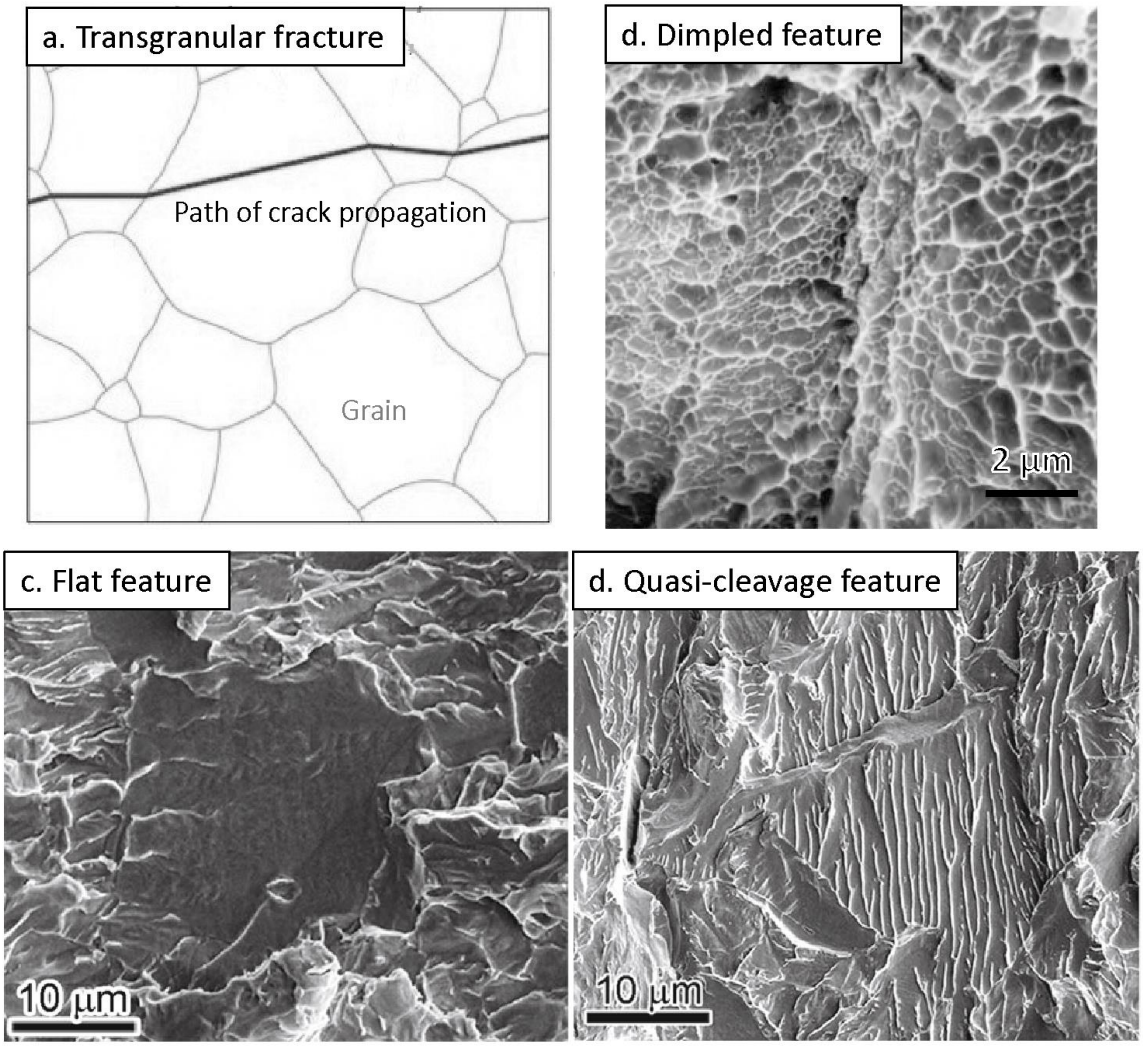

Figure 84 – Transgranular fracture (a) schematic (b)-(d) example SEM images of dimpled, flat, and quasi-cleavage features from low-strength pipeline steels in [119] and [19]

2. Iron loss and carbon peak overlaps in mass spectra

The solid dots in Figure 85(a), (b), and squares in c show that at about or above 60K the carbon concentrations obtained by APT deviate less from the nominal composition, as compared to the results at lower temperatures. Interestingly, in the low-temperature measurements, carbon concentration apparently exceeds the nominal value. This phenomenon was found to be related to the losses in the detection of iron ions, due to the pile-up effect (as described in Section 2.2.4.2). This decreases the apparent amount of iron and therefore increases apparent concentrations of the solute elements, including carbon

[192, 193, 196]. Figure 85 shows the trend of iron content as a function of varying the sample temperature. It can be seen that iron concentration decreases with lowering the temperature and this decrease leads to the increases of the concentrations of other elements (such as manganese in Figure 85(a)). Figure 85(c) confirms the trend of higher multi-hit rate of iron in various content of iron at lower temperatures with parameter α, where α is subjected to the probability of multiple events of iron.

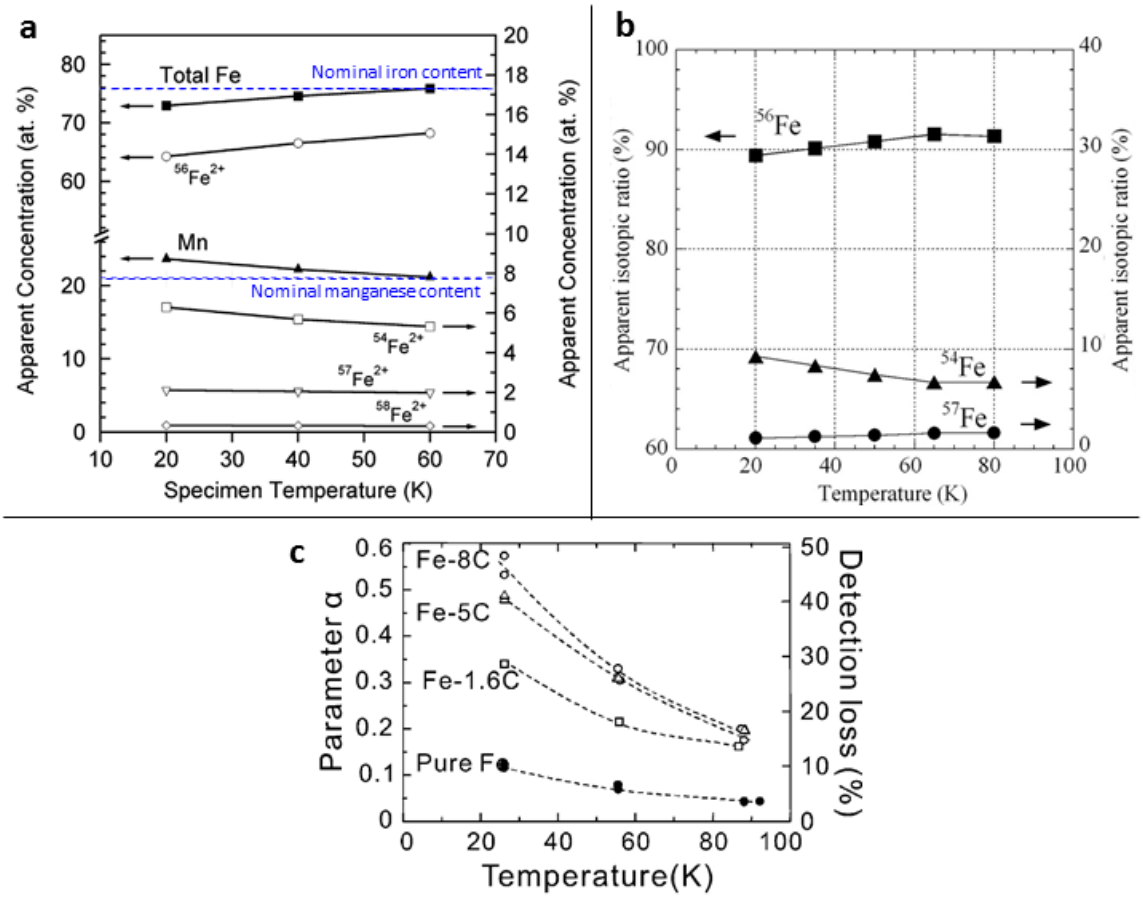

Figure 85 - Detected iron contents at corresponding cryo-stage temperatures (a) of austenitic steel [192], (b) of cementite [193], and (c) of carbon-solutionised ferrite [196], showing an observation of iron shortage at low temperatures of APT experiemnt

Another source of inaccuracy in APT measurement of carbon content is mislabelling of peaks related to carbon ion species in the mass-to-charge-state ratio spectrum [242]. Regardless of the use of voltage- or laser-pulsing atom probe, carbon is known to field evaporated in the form of complex ions, including monomer (C), dimer (C_2), trimer (C_3),

and tetramer (C_4) [242]. Each type of complex ion can be observed in multiple charge states (+1, +2, +3, or rarely +4) and combination of isotopes (^{12}C or ^{13}C), as listed in Table 10 in the order of their relative abundances. As such, the issue arises that the mass-to-charge-state ratios of $^{12}C_2^+$ and $^{12}C_4^{+2}$ are both at 24 Da [242]. Therefore, the apparent amount of carbon associated to the 24 Da peak could be miscounted if it was solely assigned to either $^{12}C_2^+$ or $^{12}C_4^{2+}$. This miscounting can be corrected by consideration of the relative isotopic abundances and analysis of the next most common isotopes of $^{12}C_2^+$ and $^{12}C_4^{+2}$ adjacent to the 24 Da peak, namely peaks associated to $^{13}C^{12}C^+$ at 25 Da and $^{13}C^{12}C^{12}C^{12}C^{2+}$ at 24.5 Da (as seen in Table 10), if these peaks are discernible [193]. This enables the relative contributions to the 24 Da peak to be deconvolved. However, this correction alone was found not being able to sufficiently correct the deviation of carbon content, which implies other sources contributed to this error [193, 194].

Species	Combination	Relative abundances (%)	Mass-to-charge ratios		
			1 +	2 +	3 +
C	^{12}C	98.89	12	6	4
	^{13}C	1.11	13	6.5	4.33
C_2	$^{12}C^{12}C$	97.79	24	12	8
	$^{12}C^{13}C$	2.20	25	12.5	8.33
	$^{13}C^{13}C$	0.01	26	13	8.67
C3	$^{12}C^{12}C^{12}C$	96.71	36	18	12
	$^{12}C^{12}C^{13}C$	3.26	37	18.5	12.33
	$^{12}C^{13}C^{13}C$	0.03	38	19	12.67
	$^{13}C^{13}C^{13}C$	0.0001	39	19.5	13
C4	$^{12}C^{12}C^{12}C^{12}C$	95.63	48	24	16
	$^{12}C^{12}C^{12}C^{13}C$	4.29	49	24.5	16.33
	$^{12}C^{12}C^{13}C^{13}C$	0.07	50	25	16.66
	$^{12}C^{13}C^{13}C^{13}C$	0.0005	51	25.5	17
	$^{13}C^{13}C^{13}C^{13}C$	1.4×10^{-6}	52	26	17.33

Table 10 - Possible carbon ions in APT and their corresponding relative abundances [242]

3. Experimental procedure of Dry Cryo-Transfer

A. <u>Preparation:</u>

a. Personal protection: goggles, cryo-gloves, lab coat, ventilation (open ALL windows)
b. Attach right-hand glove to plastic bag
c. Check whether the vents on glove box are well-taped

d. Make sure cryo-block and cryo-puck are clean and DRY
e. Prepare 2x2 litre of LN_2
f. Turn off loadlock turbo pump but DO NOT open it
g. Locate cryo-puck and its allen key at proper place for later sample loading

B. Connect glove box to LEAP 3000

a. Align glove with glove box to proper height, then attach bag to loadlock
b. Partially tape the bag's opening to glove box but leave sufficient room in the opening for later LN_2 box's loading

C. Pre-cool cryo-block

a. Put cryo-block (WITHOUT cryo-puck), and block hat (open end up), in the LN_2 box
b. Pour LN_2 into the LN_2 box
c. When still cooling the block and hat, top up LN_2 (if they are not fully immersed)
d. Place block hat over block when stabilised

D. Conduct liquid charging

E. (Must be quick) Remove the charged samples and load them into cryo-puck; give them a gentle spray with N_2 to remove residual heavy water

F. Cool the charged samples

a. (cryo-gloves on) Plunge cryo-puck into LN2 with tweezer, and load the puck on one of the slot in cryo-block (slot A is recommended)
b. Lock the puck in when stabilised

G. Seal glove box

a. Put silica gel, hygrometer, and short threaded rod into glove box
b. Check that amount of LN_2 is sufficient to keep cryo-block fully immersed for up to 1hr (top up if necessary), then load the whole container into glove box.
c. Seal glove box with tape
d. **(optional)** Connect compressed air pipe to the plastic bag, vent the glove box on the other side

H. Keep monitoring Relative Humidity (RH) until plateau reached (ideally at 1%)

I. Load the charged samples into LEAP
a. Fully open loadlock and load cryo-block
b. Via view port, match the pin and Teflon insulating notch
c. Remove block hat with threaded rod
d. Close loadlock and pump
J. After loading the sample to analysis stage, remove cryo-block from loadlock safely with threaded rod and place it at a proper place to warm up

K. Sublimation cleaning of ice contamination

a. Loadlock vacuum will go down quickly due to the presence of cryo-object
b. Move cryo-block to buffer, as the pressure of two chambers are close enough ($\sim 10^{-7}$)
c. Use transfer rod to take out cryo-puck and then move cryo-block back to loadlock
d. Close ion pump in analysis chamber, open the valve, and load the sample to analysis stage in order to record the as-loaded sample status
e. Remove the sample from analysis chamber for dehydration in buffer
f. Mind and record buffer pressure carefully: the pressure going up means dehydration is beginning, dropping back down to 10-7~10-8 means dehydration is over
g. Load to analysis chamber for APT experiment